University of Strathclyde

Engineering

University of Strathclyde

Department of Chemical and Process Engineering

Development of New Materials for Intermediate-Temperature Solid Oxide Fuel Cells

by

Christophe T. G. Petit

A thesis presented in fulfilment of the requirements for the degree of Doctor of Philosophy

2013

Declaration of Authors Rights

This thesis is the result of the author's original research. It has been composed and written by the author and has not been previously submitted for examination which has led to the award of a degree.

Tuesday, 29 October 2013

Associated Publications

Accepted for Publication

Petit, CTG; Lan, R; Cowin, PI; Tao, SW "Structure and conductivity of strontium-doped cerium orthovanadates $Ce_{1-x}Sr_xVO_4$ ($0 \leq x \leq 0.175$)" *J. Solid State Chem.* 2010, **183 (6)**, 1231-1238

Zhang, L; Lan, R; Petit, CTG; Tao, SW "Durability study of an intermediate temperature fuel cell based on an oxide-carbonate composite electrolyte" *Int. J. Hydrogen Energy* 2010, **35 (13)**, 6934-6940

Petit, CTG; Lan, R; Cowin, PI; Irvine, JTS; Tao, SW "Novel redox reversible oxide, Sr-doped cerium orthovanadate to metavanadate" *J. Mater. Chem.* 2011, **21 (2)**, 525-531

Petit, CTG; Lan, R; Cowin, PI; Kraft, A; Tao, SW "Structure, conductivity and redox stability of solid solution $Ce_{1-x}Ca_xVO_4$ ($0 \leq x \leq 0.4125$)" *J. Mater. Sci.* 2011, **46 (2)**, 316-326

Petit, CTG; Lan, R; Cowin, PI; Irvine, JTS; Tao, SW "Structure, conductivity and redox reversibility of Ca-doped cerium metavanadate" *J. Mater. Chem.* 2011, **21 (24)**, 8854-8861

Amar, IA; Lan, R; Petit, CTG; Arrighi, V; Tao, SW "Electrochemical synthesis of ammonia based on a carbonate-oxide composite electrolyte" *Solid State Ionics* 2011, **182 (1)**, 133-138

Cowin, PI; Lan, R; Petit, CTG; Zhang, L; Tao, SW "Conductivity and stability of cobalt pyrovanadate" *J. Alloys Compd.* 2011, **509 (10)**, 4117-4121

Cowin, PI; Lan, R; Zhang, L; Petit, CTG; Kraft, A; Tao, SW "Study on conductivity and redox stability of iron orthovanadate" *Mater. Chem. Phys.* 2011, **126 (3)**, 614-618

Cowin, PI; Petit, CTG; Lan, R; Irvine, JTS; Tao, SW "Recent progress in the development of anode materials for solid oxide fuel cells" *Adv. Energy Mater.* 2011, **1 (3)**, 314-332

Amar, IA; Lan, R; Petit, CTG; Tao, SW "Solid-state electrochemical synthesis of ammonia: a review" *J. Solid State Electrochem.* 2011, **15 (9)**, 1845-1860

Amar, IA; Petit, CTG; Zhang, L; Lan, R; Skabara, PJ; Tao, SW "Electrochemical synthesis of ammonia based on doped-ceria carbonate composite electrolyte and perovskite cathode" *Solid State Ionics* 2011, **201 (1)**, 94-100

Petit, CTG; Alsulaiman, MSA; Lan, R.; Tao, SW "Direct synthesis of Ni nanoparticles by a non-aqueous sol-gel process" *Nanosci. Nanotechnol. Lett.* 2012, **4 (2)**, 136-141

Petit, CTG; Tao, SW "Structure and conductivity of praseodymium and yttrium co-doped barium cerates" *Solid State Sci.* 2013, **17**, 115-121

Cowin, PI; Petit, CTG; Lan, R; Schascke, CJ; Tao, SW "Structure and conductivity of rutile niobium iron titanate" *Solid State Ionics* 2013, **236**, 48-53

Petit, CTG; Alsulaiman, MSA; Lan, R.; Mann, G; Tao, SW "Synthesis and characterisation of Ag nanoparticles by a non-aqueous sol-gel process" *J. Nanosci. Nanotechnol.* 2013, **13**, 5445-5451

Petit, CTG; Tao, SW "Structural, thermal and electrical properties of Bi and Y co-doped barium zirconium cerates" *Ionics* 2013, accepted, in press, DOI: 10.1007/s11581-013-0990-2

Submitted for Publication

Petit, CTG; Schaschke, CJ; Tao, SW "Effects of cobalt addition on the structural, thermal and electrical properties of praseodymium-yttrium co-doped barium cerates" *Solid State Sci.* 2013

Acknowledgments

My first thanks go to my supervisor Prof. Shanwen Tao for providing me with the great opportunity to study as a PhD student at Heriot-Watt and then at Strathclyde University. It has been a few long years where the knowledge brought forward was of great help and contributed to this successful achievement.

I also would like to thank all the members of the fuel cell group, especially Peter I Cowin for the helpful and wide discussions on all sides of fuel cell technology and for reading all those papers before submission. Particular thanks to Gregory Mann, Ibrahim A Amar, Lei Zhang and Lynsey Anderson for providing me with an enjoyable and pleasant working atmosphere. Thanks also go to Marian Millar at Heriot-Watt University for the collection of XRD and SEM data during the first year of study and to Dr Arno Kraft, my second supervisor at Heriot-Watt University, for his kindness and help whenever I needed it. Thanks also go to the members of the solid-state group and polymer group at Heriot-Watt particularly Steven, Sarah, Jack and Vijay as we had mostly known each other since undergraduate levels and to most people of the postgraduate community at Strathclyde that will recognise themselves for some enjoyable time over these past years whether during good or less good periods.

Finally, special thanks to my family and friends outside university circles for always believing and supporting me at great length and to my lovely wife, simply for being there.

Content

List of Figures

List of Tables

List of Equations

Acronyms and Abbreviations

AC-IS	Alternating Current – Impedance Spectroscopy
AFC	Alkaline Fuel Cell
APU	Auxiliary Power Unit
BCY	Yttrium-doped Barium Cerate
BCZs	Barium Cerates and Zirconates
BCZY	Yttrium-doped Barium Cerium Zirconate
	Yttrium-doped Barium Zirconium Cerate
BiMeVOX	Bismuth Metal Vanadates
CPE	Constant Phase Element
D	Diffusion coefficient
DEFC	Direct Ethanol Fuel Cell
DMFC	Direct Methanol Fuel Cell
DPB	Double Phase Boundary
DSC	Differential Scanning Calorimetry
DTA	Differential Thermal Analysis
EC	Equivalent Circuit
EM	Electron Microscopy
EDS	Energy Dispersive X-ray Spectroscopy
EIS	Electrochemical Impedance Spectroscopy
FC	Fuel Cell
FLW	Finite Length Warburg
GDC	Gadolinium-Doped Ceria
GSAS	General Structure Analysis System
IT-SOFC	Intermediate Temperature – Solid Oxide Fuel Cell
IR	Infrared
J	Diffusion flux
j	Imaginary unit
k_B	Boltzmann constant
LCO	Lanthanum Chromite
LSCF	Lanthanum Strontium Cobalt Ferrite
LSCM	Lanthanum Strontium Manganese Chromite
LSF	Lanthanum Strontium Ferrite

LSGM	Lanthanum Strontium Gallate Magnesite
LSM	Lanthanum Strontium Manganite
LST	Lanthanoids-doped Strontium Titanate
LSTM	Lanthanum Strontium Titanium Manganite
MCFC	Molten Carbonate Fuel Cell
MIEC	Mixed Ionic Electronic Conductor
OCV	Open Circuit Voltage
ORH	Oxidation Reaction of Hydrogen
ORR	Oxygen Reduction Reaction
PAFC	Phosphoric Acid Fuel Cell
PEMFC	Polymer Electrolyte Membrane Fuel Cell
	Proton Exchange Membrane Fuel Cell
PXRD	Powder X-Ray Diffraction
QPE	Q-based (Constant) Phase Element
REE	Rare-Earth Elements
RFC	Regenerative Fuel Cell
RT	Room Temperature
SDC	Samarium-Doped Ceria
SEM	Scanning Electron Microscope
SSZ	Scandium-Stabilised Zirconia
SOFC	Solid Oxide Fuel Cell
SPU	Stationary Power Unit
SSCF	Strontium Samarium Cobalt Ferrite
STA	Simultaneous Thermal Analysis
STO	Strontium Titanate
TCE	Thermal Coefficient of Expansion
TEM	Transmission Electron Microscope
T	Absolute temperature (K)
TGA	Thermo Gravimetric Analysis
TPB	Triple Phase Boundary
XRD	X-Ray Diffraction
YDC	Yttrium-Doped Ceria
YST	Yttrium-doped Strontium Titanate
YSZ	Yttrium Stabilised Zirconia

δ	Hyper/hypo- stoichiometry in oxides
φ	Phase angle shift
λ	Mean free path
	Wavelength of a particle
ν	Jumping frequency
θ	Incident Angle
ρ_{calc}	Calculated density
ρ_{exp}	Experimental density
ρ_{rel}	Relative density
σ_{elec}	Electronic conductivity
σ_{ionic}	Ionic conductivity
Σ	Warburg constant
τ	Time constant/relaxation of an RC system
	Goldschmidt tolerance factor
ω	Angular frequency
Ω	Ohm

Abstract

In this thesis, the main focus of the work is the development of novel materials for intermediate-temperature solid oxide fuel cells (IT-SOFCs) with an aim of showing suitability and compatibility with fuel cell system environment. Fuel cell fabrication was briefly encountered to test appropriateness with existing fuel cell element standards (yttrium-doped zirconia as electrolyte for high temperature operation and gadolinium-doped ceria for IT-SOFCs) but due to the lack of appropriate component, extensive tests to determine full potential were not carried out. Methods such as solid-state reaction and sol-gel process were adopted for the synthesis of the materials and solid-solution limits were determined for the orthovanadate compounds studied. These latter were then reduced to their metavanadate counterpart in order to establish a possible cyclability between the two oxygenated forms that could be exploited in fuel cell mechanisms. Doped version of the former and latter with alkaline-earth elements were found to greatly increase stability and conductive behaviour while maintaining appropriate densification through the formation of closed pores in the orthovanadate structure allowing the metavanadate to benefit from increased conductance.

Electrolyte studies were also carried out based on doped barium yttrium cerate/zirconate structures however compounds synthesised exhibited inappropriate properties for use in IT-SOFCs despite some interesting behaviours that would be a benefit in high-temperature electrolysers.

1. Introduction and theory

As far as from the beginning of the industrial revolution, voices and ideas have been expressed, precepts and predictions set regarding the effects of human activities on the Earth's climate. Mostly unfounded at the start, based on superstition or non-facts, these opinions were disregarded and forgotten as technology and "innovation" prevailed above all. In the last decades however, Mankind – perhaps for the first time – realised that the impact of human activities on our climate was a reality. After the discovery of the Antartic ozone hole[1] at Halley by the British Antartic Survey (BAS) in 1985, energy activists and environmental scientists had suddenly the attention their predecessors could have only dreamed of. Concerns were then again expressed and led to the first Vienna Conference (VC) the same year that resulted in the Vienna Convention for the Protection of the Ozone Layer (entry into force, 09/1988). It was the first of a series of international treaties and agreements aiming to reduce, confine and/or eliminate human influences on our climate.

Since then, the Montreal Protocol, the Kyoto Protocol and the annual Conferences of the Parties (COP) were ratified, with the most recent, the COP-18 that took place in Doha, Qatar in November-December 2012. Aimed at setting new targets from 2012 onwards – when the initial commitment period under the Kyoto Protocol expires – a large place is given to renewable green energies. Those include but are not limited to, wind and underwater turbines, solar panels or bio-fuels. Despite their considered 'green' character, most renewable energies are difficult to implement, for various reasons ranging from lack of appropriate infrastructures to low power outputs and high costs.

Until those processes are fully controlled, optimised and implemented in order to provide low cost, readily available high output energies, technologies already known but in need of improvements are the simplest, easiest and quickest way to reduce human greenhouse gases emissions. One example is the Fuel Cell (FC).

In the following sections, FCs will be described with an emphasis on Solid Oxide Fuel Cells (SOFCs) before current materials and required properties are explored and finishing with the overall objectives.

1.1. Fuel Cell

Fuel cells are electrochemical devices that convert the energy of a fuel directly into electricity and are composed of an anode (–), an electrolyte and a cathode (+). There are currently a large variety of fuel cell systems (Table 1.1) under development or improvement including but not limited to the Regenerative Fuel Cell (RFC) used in electrolysers, the Alkaline Fuel Cell (AFC), the Phosphoric Acid Fuel Cell (PAFC), the Polymer Electrolyte Membrane Fuel Cell (PEMFC), the Direct Methanol Fuel Cell (DMFC), the Molten Carbonate Fuel Cell (MCFC) and the Solid Oxide Fuel Cell (SOFC). Only the last four are described here, as the first two are based on no particular design and can be described generally from other systems.

Type	Electrolyte	Temperature of operation	Carrier
AFC	KOH (lq)	< 120 ºC	OH^-
PAFC	H_3PO_4(lq)	180-200 ºC	H^+
PEMFC	Ion exchange membrane	< 120 ºC	H^+
MCFC	Molten CO_3^{2-}	~650 ºC	CO_3^{2-}
SOFC	Ceramics	500 – 1000 ºC	O^{2-} or H^+

Table 1.1 Major types of fuel cells

1.1.1. Polymer Electrolyte Membrane Fuel Cell

First used in the sixties as part of NASA's Gemini Project, PEMFCs are FC based on a proton conducting electrolyte membrane. In order to operate, the electrolyte must be a good conductor of protons, have no electrical conductivity, be impermeable and dense to avoid gas crossover. A chemically inert character is also required to sustain reduction and oxidation at the cathode and at the anode interfaces respectively.

Relatively easy to implement, due to its mild operating conditions (medium range of pressure and temperature compared to other FC systems), it is compactable in such way to form stacks of hundreds of individual units. To date, the most commonly used membranes are based on perfluorosulfonic acid polymers (such as Nafion® by DuPont, Flemion® by Asahi Glass or Aciplex® by Asahi Kasei) operating under water saturation to ensure permeability to protons. Depending entirely on temperature-resistance and water management, researchers have – in recent years – focussed on

developing new polymer membranes as reported in a review by Lee *et al.*[2]. A notable example is the fluorohydrogenate ionic liquid-based gel-type membrane[3] operating without humidification, thereby, opening the door for use at higher temperature.

Despite encouraging results on the range of operability, one of the major drawbacks of PEMFCs is the requirement for platinum catalysts in order to split both hydrogen and oxygen molecules. According to spectroscopic measurements, the dissociation energies of molecular oxygen[4] and hydrogen[5] are 498.4 and 436.0 kJ mol^{-1} respectively, however currently employed platinum catalysts do not manage to split the former as well as the latter and are therefore used at the cathode rather by default than being chosen for providing the best catalytic activity.

1.1.1.1. Direct Methanol Fuel Cell

DMFCs are a type of PEMFC which, as the name indicates uses methanol as fuel instead of molecular hydrogen. Their functionality relies on the same principles as for PEMFCs with methanol being converted into carbon dioxide and hydrogen ions at the anode while oxygen is converted to water from reaction with permeated protons at the cathode. Despite recent improvements[6], DMFCs have a low efficiency due to low operating temperatures requiring very active catalysts and methanol permeation[7-9], hence only a very low concentration of methanol can be used (about 0.5 M generally[10]). Moreover, some theoretical aspects are still unclear as underlined by Nordlund *et al.*[11] when showing that a large portion of CO_2 is in fact not transported out of the system by the liquid flow but permeates to the cathode through the membrane forming gas bubbles.

Due to high costs, low efficiency and the toxicity of cross-diffusion of methanol, research has also begun on Direct Ethanol Fuel Cells (DEFCs) but as for DMFCs in the early 1990s, DEFCs are currently inefficient from a power density point of view[12].

1.1.2. Molten Carbonate Fuel Cell

MCFCs are high temperature FCs operating above 600 ºC and based on a molten mixture of carbonate salts. At such temperatures, the salts are softened and a high ionic mobility throughout the electrolyte is achieved; fuel reforming is unnecessary and

natural gas and coal-based fuels can be used directly and non-precious metals are as efficient as noble ones[13-15]. Producing heat as a by-product of electricity generation, the efficiency of MCFCs can be greatly ameliorated if this latter is captured and used in other processes, hence, the mainly stationary character associated with such systems.

Practicality is, however, a major drawback as long times are needed to reach operating temperature.

1.1.3. Solid Oxide Fuel Cell

SOFCs are fuel cells operating over a wide range of temperatures (currently from 600 º to 1000 ºC) with a wide variety of fuels (H_2 from direct or indirect reforming of various hydrocarbons, straight-chain alcohols, ammonia, etc...) in which the main feature is a solid oxide electrolyte, schematised in Figure 1.1.

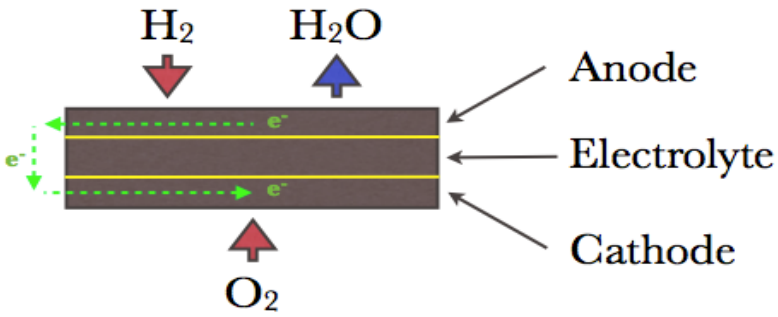

Figure 1.1 Schematic of a SOFC based on an O^{2-} ion conducting electrolyte

SOFCs are based on the transfer of oxygen ions (or protons) – acting as charge carrier – from the cathode (Equation 1.1) to the anode (Equation 1.2) with reactions described as follows (Equation 1.3 overall based on an O^{2-} ion conducting electrolyte):

$$O_2 + 4e^- \rightarrow 2O^{2-} \qquad \textbf{Eq. 1.1}$$

$$2H_2 + 2O^{2-} \rightarrow 2H_2O + 4e^- \qquad \textbf{Eq. 1.2}$$

$$2H_2 + O_2 \rightarrow 2H_2O \qquad \textbf{Eq. 1.3}$$

Composed solely of solid materials, SOFCs are impervious to gas crossover and yield heat as a by-product. Due, in fact, to being impervious to gas crossover and to

their efficiency to generate electricity (the highest with MCFCs), SOFCs are currently the best candidate for stationary applications – as Stationary Power Units (SPU) – which require high-power outputs or power generation for large-scale industrial plants. In contrast to other FC systems, SOFCs are relatively tolerant to fuel poisoning in part due to their high temperature operating conditions. However, such extreme conditions also have major disadvantages including mainly high costs, long starting times and/or slow response to energetic requirements.

Credited for the first applicable Nernst[16] engine* using a zirconia-based electrolyte, Baur and Preis[17] triggered interest that has only intensified since. In fact, one reason for the abundant research is driven by the encouraging perspective that the SOFC systems currently used have much scope for improvement in order to yield more affordable and less time-consuming units. For this to occur, new materials operating at lower temperatures – conserving all the required properties – have to be developed.

* sometimes used to describe SOFCs in reference to what is known as the Nernst glower (an obsolete device capable of producing a stream of continuous infrared radiation).

1.2. Materials and required properties

Structurally composed of two ceramic electrodes and an electrolyte, SOFCs are complex systems exhibiting various properties within each of its components, mostly in antagony between each other. The following sub-sections deal with the required properties for each constituent of the FC as well as a review of currently used materials in each area.

1.2.1. Electronic and ionic conductivity

Electronic conductivity in materials can be generally defined as the ability to conduct electrons through a flow of moving charges, generating a current. All materials for FCs can be classified as being either conductors (such as metals with $10^{-1} \leq \sigma_{elec}$ ($S.cm^{-1}$) $\leq 10^{5}$)[18], insulators (like plastics and glasses with σ_{elec} ($S.cm^{-1}$) $< 10^{-12}$)[18] or semiconductors (exhibiting properties between the two other classes with $10^{-5} \leq \sigma_{elec}$ ($S.cm^{-1}$) $\leq 10^{2}$)[18].

Electronic conduction in conductors (like metals) – also known as metallic conductivity – arises – according to band theory – from the overlap of the valence and conduction band forming a partially filled (and partially empty) large band[19]. In semiconductors and insulators, a band gap forms a physical barrier between the two aforementioned bands resulting in an almost fully unoccupied conduction band leading to high electronic resistivity (with higher practical effects in insulators as the gap is larger). Within the semiconducting family, intrinsic and extrinsic semiconductors can be distinguished (with transition from one state to the other possible at high temperatures). The former being characteristic of an extremely pure, impurity-free semiconductor whose conductance depends solely on band gaps and thermally activated motion of electrons; and the latter, resulting from the introduction of dopants into the lattice causing defects referred as *n*-type (introduction of electrons into the conduction band) or *p*-type (introduction of 'holes' into the valence band). While largely considered independent of temperature in metals (as the presence of the overlap band is unaffected), the electronic conduction is greatly influenced by temperature in semiconductors as – referring to band theory – the excitation of electrons to the conduction band is mainly due to thermal activation and governed by an Arrhenius-type

equation for conductivity. Hence, electronic conductance exponentially increases with temperature in semiconducting materials, while in metals it statistically decreases due to reduced electron flow from electron-phonon collisions[20, 21].

Ionic conduction in materials is defined by the ability of ions to migrate within a lattice by jumping to equivalent vacant sites thus transporting the electrical current[22]. It is mathematically defined by Equation 1.4 with σ_{ionic} the ionic conductivity, z_B the charge number of the ionic species B, F the Faraday constant (96485 C mol^{-1}) and, μ_B the electric mobility of species B,

$$\sigma_{ionic} = |z_B| F \mu_B \qquad \textbf{Eq. 1.4}\ [23]$$

As for electronic conductors, ionic conducting materials can be sorted in three classes: ionic crystals (with $10^{-18} \leq \sigma_{ionic}$ (S.cm^{-1}) $\leq 10^{-4}$)[18], solid electrolytes and strong liquid electrolytes (with $10^{-3} \leq \sigma_{ionic}$ (S.cm^{-1}) $\leq 10^{1}$)[18]. Allowing conduction to take place by acting as charge carrier, anions and/or cations movement within a lattice occurs through empty crystallographic positions (naturally present or introduced by doping) or voids and channels. Ionic conduction in SOFCs is extensively linked to the Triple Phase Boundary (TPB) concept[24]. It holds that the Oxidation Reaction of Hydrogen (ORH) and the Oxygen Reduction Reaction (ORR) solely occur at specific spatial positions where the electrolyte, gas, and catalytic regions are electrically connected. The TPB concept is especially important since at the current state of SOFC technologies, efficiency limitations are mainly due to reaction kinetics, thus increasing the TPB area by any factor would, at least, improve the reaction kinetics by the same said factor.

1.2.2. Chemical and catalytic activity

Chemical reactivity/instability is an important aspect of SOFC components as it governs durability and constitutes the most critical challenge for SPUs[25]. Ideally, no inter-component activity is wanted, however, materials currently employed are subject to high diffusion and poisoning. Several factors are responsible, namely temperature[26, 27], an oxygen-rich atmosphere[26, 28] and simple acid-base relations[29]. The most common types of degradation encountered consist of microstructural changes[30] including cracking, change in porosity and coarsening, delamination and change induced by

poisoning (sulphur-containing species[31, 32], chromium-containing species[28], others[33-35]). In theory, pure hydrogen is – chemically speaking – the ideal fuel for FC, however, current infrastructure, supply and production of high purity hydrogen gas is limited and implementation at low costs is hardly seen feasible in such a state. Other fuels can be used, as seen previously with DMFCs, DEFCs and/or MCFCs, but these use catalysts to convert the fuel directly or indirectly into hydrogen. Precious metal catalysts (Pt, Pd, Au) are currently used for these latter FC electrodes but their costs and the reforming process implied somewhat undermine the overall efficiency of these FCs.

Thus, research on new materials for SOFC components currently under development are designed in such a way as to incorporate active catalytic sites within their structures.

1.2.3. Thermal and redox stability

As SOFCs operate at very high temperatures, both the electrolyte and the electrodes have to resist thermal cycles in order to operate durably as thermomechanical stability is vital for use of SOFCs as Auxiliary Power Units (APU) in transportation for example[25]. The most accurate measure of thermal stability is achieved by comparing Thermal Coefficients of Expansion (TCE) expressed in Equation 1.5 for solids as the specific change in volume per change in temperature at constant pressure with α_V the volumetric expansion coefficient, V the volume of material, ∂V the change in volume and, ∂T the change in temperature (linear TCEs are sometimes also used but as a volume has three linear and usually orthogonal components – at least under isotropic conditions – volumetric TCEs are preferred since offering more perspective):

$$\alpha_V = \frac{1}{V}\left(\frac{\partial V}{\partial T}\right)_{P=cst} \qquad \textbf{Eq. 1.5}\ [36]$$

As some materials may expand/contract more than others upon heating/cooling cycles, it is essential to match the TCEs of components connected together to avoid irreversible damage to the structural integrity of the cell and a substantial drop in efficiency.

As part of its normal operation routine, each component of a SOFC is subject to either an oxidising and/or a reducing atmosphere at any given time. Redox stability – unnoticeable changes of the physicochemical and structural properties of a material upon periodic reduction and oxidation – is particularly crucial at the anode as this constitutes the physical location subject to subsequent reduction and oxidation[37]. Effects can be variable, from simple TCE-induced cracking and delamination, to incomplete red/ox processes, to difficult to explain drop in efficiency and conductivity resulting in a major increase of ohmic resistance[38].

Materials able to sustain repeated thermal and redox cycling are therefore necessary in order to operate SOFCs at their highest efficiencies; however, only a few materials to date have been discovered that exhibit all the necessary properties cited above.

1.2.4. Cathode materials

As the electrode in contact with air, cathode materials have less stringent requirements than components for anodes. A potential ceramic for cathodes has to be a good electronic conductor, be thermally stable, exhibit chemical inertia towards the electrolyte and have a high enough porosity to allow oxygen to reach the electrode/electrolyte interface. Concerning ionic conductivity, despite not being required to allow reaction (already occurring at the TPB without ionic conduction), a material with both electronic and ionic conductivity would lead to the ideal model given in Figure 1.2 with a specific area for ORR represented by a Double Phase Boundary (DPB) where the interface of an oxygen-impregnated cathode with the electrolyte is fully used in the kinetics of the reaction.

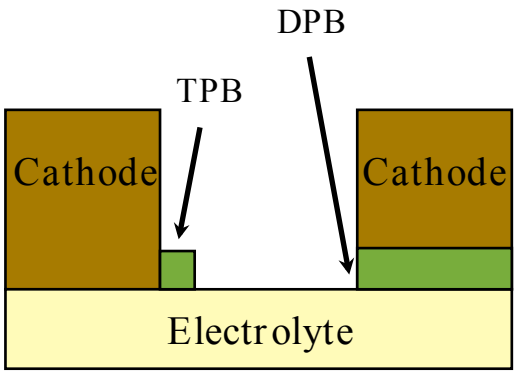

Figure 1.2 Schematic of the reaction sites in cathodes

Commonly used cathode materials are mostly perovskite (ABO_3) or double perovskite ($A'A''B'B''O_6$ where *A'* and *A''* and *B'* and *B''* may differ or not) structures.

1.2.4.1. Perovskite-type cathodes

The most commonly used cathode material is Lanthanum Strontium Manganite (LSM). It is mainly an electronic conductor and is – practically speaking – the best choice for SOFCs operating at 700-900 ºC due to high catalytic activity helping the ORR high electronic conductivity, a thermal stability and chemical inertia towards all common electrolytes including Yttrium-Stabilised Zirconia (YSZ). However, at lower temperatures, its cathodic polarisation is substantial with its total conductivity dropping from >1 S cm^{-1} at 1000 ºC to 5 x 10^{-4} S cm^{-1} at 500 ºC[39].

Lanthanum Strontium Ferrite (LSF) was more recently discovered, it shows real promise as a Mixed Ionic Electronic Conductor (MIEC)[40, 41] and its reaction with YSZ was found to be avoidable by adding a layer of Samarium-Doped Ceria (SDC)[42].

Cobalt containing perovskites also constitute promising materials due to their increased catalytic activity and their MIEC character allowing them to be used in combination with doped-ceria based SOFCs at temperatures below 700 ºC as these latter require high catalytic activity; however, the cobalt doping is limited – for structural reasons – since a large amount would induce a mismatch of TCEs. Strontium Samarium Cobalt Ferrite $Sr_{0.5}Sm_{0.5}Co_{1-x}Fe_xO_{3-\delta}$ (SSCF)[43] and Lanthanum Strontium Cobalt Ferrite $La_{0.6}Sr_{0.4}Co_{0.2}Fe_{0.8}O_{3-\delta}$ (LSCF)[44] working at 550 ºC with Gadolinium-Doped Ceria (GDC) are good examples of these type of compound with cobalt providing the high catalytic activity and the large iron content preventing a detrimental deviation of the TCE.

1.2.4.2. Double perovskite-type cathodes

Of general formula $AA'Co_2O_{5+\delta}$ (with *A* = Y, Rare-Earth Element (REE) and *A'* = Ba, Sr)[45], double perovskite structure are related to yttrium-barium iron-cuprite $YBaFeCuO_5$ discovered in the late 80's[46]. One example of this family of compounds is the praseodymium barium cobaltite $PrBaCo_2O_5$ represented in Figure 1.3[47] showing the

alternating layered structure of *A*-site metals within the typical octahedron matrix of the perovskite formed by cobalt, the *B*-site metal.

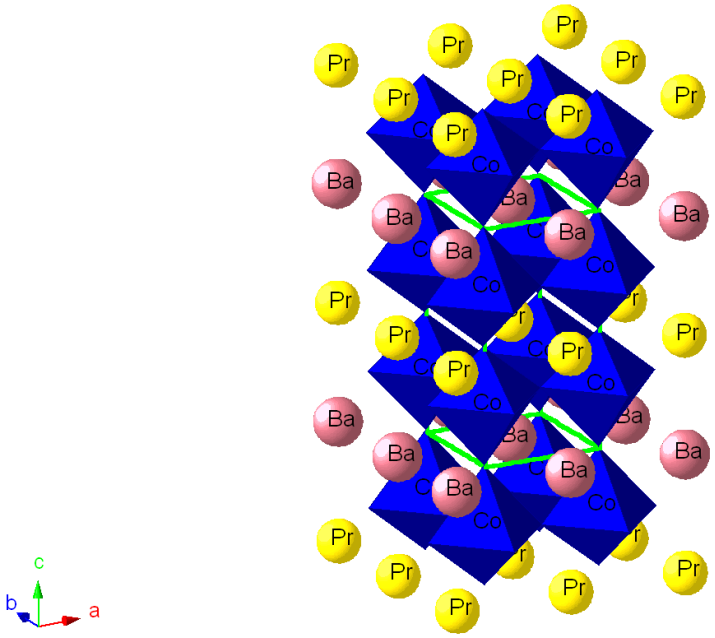

Figure 1.3 Structural representation of $PrBaCo_2O_{5+\delta}$

Despite an acceptable conductivity of 6.6 $S.cm^{-1}$ at 600 ºC[48] and as manganites and ferrites have already been investigated in double perovskite configuration, research has now focussed on cuprates and nickelates[49, 50] due to their ability – and need – to operate at lower temperatures, essentially due to a narrower thermal stability ($LaNiO_3$ decomposes at around 850 ºC)[49].

1.2.5. Electrolyte materials

Electrolyte materials have specific requirements too, including high ionic conductivity to allow the transfer of the charge carrier, the lowest possible or no electronic conductivity to prevent the electrons from passing directly through the electrolyte, redox and thermal stability, chemical inertia towards the electrodes and high density at the minimum thickness to reduce resistive losses. Two main systems of electrolytes are currently in use, fluorite-based compounds[51] like YSZ and GDC and perovskite-based compounds like Magnesium-doped Lanthanum Strontium Gallate (LSGM), Bismuth Metal Vanadates (BiMeVOX)[52] and Barium Cerates and/or Zirconates (BCZs)[53].

1.2.5.1. Fluorite-based systems

Within the fluorite-based family of compounds, ceria and zirconia are the most promising as results with pyrochlores and bismite-based electrolytes were unfortunately disappointing.

Aforementioned, YSZ is the most commonly used electrolyte. It exhibits negligible electronic conduction, a high ionic conductivity and has a lower TCE compared with other electrolytes. It is however reactive with lanthanum-containing perovskites at high temperatures forming resistive layers of lanthanum pyrozirconates[54, 55].

Scandium Stabilised Zirconia (SSZ) is a good alternative to YSZ as being even more conductive at lower temperatures[56] (around 600 ºC) but is a higher cost material. Its highly conductive cubic structure formed at temperature between 500 ºC - 600 ºC from the less conductive yet thermally more stable (at room temperature, RT) β-phase can be stabilised by addition of yttria as dopant[57].

Ceria based compounds like GDC and SDC have the highest known ionic conductivity in the range 550 ºC - 650 ºC and are compatible with LSCF and related perovskite cathodes. One issue is the formation of Ce^{3+} ions under reducing atmosphere making doped-ceria compounds electronically *n*-type conductive, thus, decreasing the FC efficiency due to short circuit[58] but this can be avoided if the temperature is kept below 500 ºC.

1.2.5.2. Perovskite and perovskite-related systems

Within the perovskite family of electrolytes, Lanthanum Gallates are the compounds of choice. Discovered jointly[59, 60], LSGM is the most notable example. Its ionic conductivity is higher than that of YSZ and SSZ; it is unreactive towards lanthanum containing perovskite cathodes but less inert than YSZ with current nickel cermet anodes. Also, doubts still persist regarding its chemical stability for high

temperature SOFCs as surface morphology changes were observed under reducing atmosphere at 1000 ºC[61].

BCZs – part of what could be called the $AB_{1-x}M_xO_{3-\delta}$ family of compounds with M, some trivalent element and δ, the oxygen deficiency – also constitute an important part of the studies carried out on proton and MIECs and materials based on alkaline and alkaline-earth cerates and zirconates have therefore intensively being investigated as providing the most interesting performance in terms of protonic conductivity[29, 62-67]. Partial substitution of the cerium atom with a trivalent atom – mostly done with yttrium, gadolinium or ytterbium – causes oxygen vacancies resulting in *p*-type electronic conduction especially at high temperatures (Equation 1.6) and gives rise to a mixed ionic/electronic conduction in water-containing oxygen and hydrogen-rich atmospheres (Equation 1.7).

$$\frac{1}{2}O_2(g) + V_O^{\cdot\cdot} \leftrightarrow 2h^{\cdot} + O_O^{x} \qquad \textbf{Eq. 1.6}$$

$$O_O^{x} + V_O^{\cdot\cdot} + H_2O_{(g)} \leftrightarrow 2(OH)_O^{\cdot} \qquad \textbf{Eq. 1.7}$$

The Kröger-Vink notation[68] is used to describe lattice spatial position and electrical charge for point defect species in crystals and is conventionally formatted as E_{Site}^{Charge} where *E* is an atom (O, Ni, Cu, H, etc…), a vacancy (*V*), an electron (*e*) or electron hole (*h*); the '*Charge*' represented by x if null, by ˙ if positively charged and by ´ if negatively charged; and, the '*Site*' representing the physically occupied lattice site and thus annotated by either an atom or a lattice interstitial (i). Hence, $V_O^{\cdot\cdot}$ would be described as a doubly positively charged vacancy on an oxygen lattice site.

Although barium cerates (BCs) are much higher conductors than their zirconate equivalents, the latter are still favoured due to the instability of the former in water and carbon dioxide containing atmospheres[69, 70]. A recent study however demonstrated that with only 10% of zirconium doping, a 20% yttrium BCs could remain stable at 500 ºC in 2% CO_2-H_2 as well as in 15% H_2O-H_2 without any decomposition and while exhibiting a higher conductivity below 550 ºC than the most commonly used electrolytes, namely GDC and YSZ[71].

BCZs also have the advantage of being able to be used as electrode components in high temperature hydrolysers due to the protonic nature of their ionic conductance if, while exhibiting high ionic conductivity, the electronic contribution is deemed too important, thus lowering their potential use as electrolytes.

1.2.6. Anode materials

To be considered as a potential fuel electrode, a material needs to be thermally, chemically and redox stable, have both high electronic and ionic conductivity and exhibit uniform porosity for gas flow. Many different materials have been investigated as potential anode materials with a large array of both successes and failures as noted in diverse reviews[72-77]. Due to the required properties, metals have always been considered as the best candidates for SOFC anodes.

1.2.6.1. Nickel cermets

Anodes made of nickel are currently the most used with YSZ electrolyte. While TCE mismatch makes them chemically incompatible in pure form, composite materials of Ni metal and YSZ (a cermet) are inert towards YSZ. Despite a very high conductivity of about 1000 $S.cm^{-1}$ at 900 ºC for sintered pellets[78], the major issue is that nickel catalyses the formation of graphite from hydrocarbons[79, 80], is sensitive to sulphur[81] and has poor mechanochemical resistance over time as a consequence of the reduction of catalytic sites thus destroying the anode capacity for use with unreformed fuels.

Reduction of sulphur poisoning can be achieved through the use of 'cleaner' or sulphur-free fuels but this is not economically viable therefore research has focused on developing sulphur-tolerant SOFC components instead of producing high purity fuels. Concerning coking, a lower temperature of operation is a solution but it significantly reduces the efficiency of the FC. Murray *et al.*[82] reported that the use of Yttrium – doped ceria (YDC) as an interlayer between Ni cermets and YSZ allowed direct use of methane with power densities up to 0.37 $W.cm^{-2}$ at 650 ºC suggesting that ceria-based compounds may well be the answer to resolve the major drawbacks of Ni-based anodes[83]. The use of copper as the metal in a ceria cermet may also be considered as ceria would provide the catalytic activity and copper the high electronic conductivity

even if such systems would be required to operate at lower temperature to avoid the melting of copper.

1.2.6.2. Perovskite-type systems

Non-cermet focused research into anode materials is essentially centred on perovskites as replacing, substituting and doping the different cationic sites of the ABO_3 structure is relatively easy to accomplish with a multitude of options. Within the perovskite family, titanates such as Strontium Titanate (STO) pictured in Figure 1.4[47] and Lanthanum Strontium Titanium Manganite (LSTM)[84] and chromites such as Lanthanum Chromite (LCO) and Lanthanum Strontium Manganese Chromite (LSCM)[85] exhibit the most promising properties as they are thermochemically stable under various atmospheres.

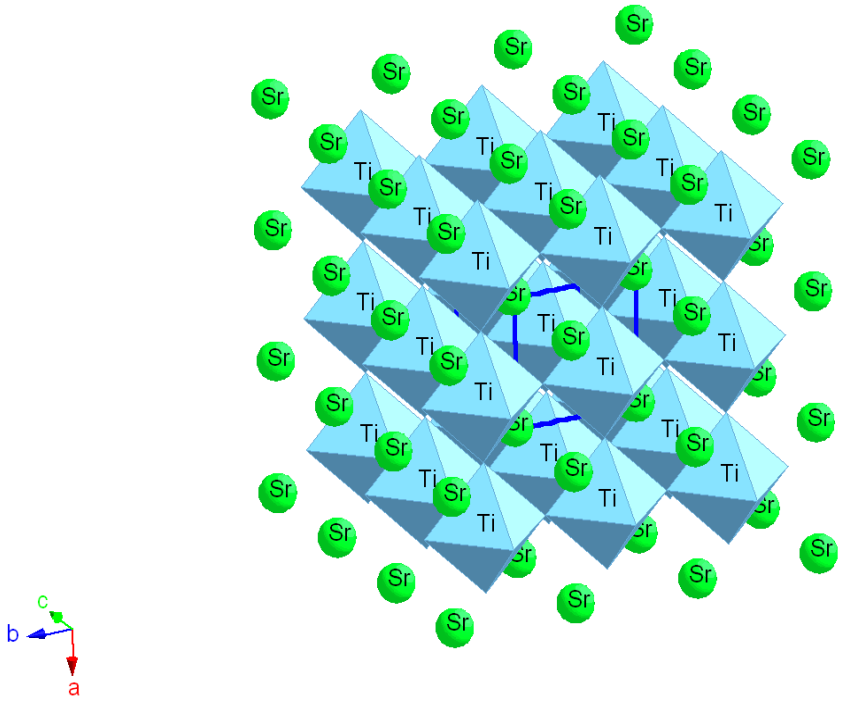

Figure 1.4 Structural representation of $SrTiO_3$

Despite being considered as low electronic conductors in comparison with thermomechanically unstable alternative perovskites like ferrites and cobaltites, STO is known to be a good electronic conductor in a reducing atmosphere and doping of the strontium site with lanthanoids (referred to as Lanthanoids-doped Strontium Titanate, LST) or yttrium (denoted as Yttrium-doped Strontium Titanate, YST) can increase the ionic conductivity[86-90], as does doping of the titanium site with niobium. Doping of both

sites is however difficult to balance as structural constraints favour the formation of impurities (such as yttrium titanates $Y_2Ti_2O_7$ or $YTiO_{2.085}$). Also, STO, LST and YST have a poor catalytic activity for hydrogen but this can be improved by doping with manganese or gallium[91].

Chromites also play an important role, with LCO being one of the most known. LCO induces almost no coking with methane as fuel[92-94] making it greatly advantageous compared to Ni-cermets. Its catalytic activity and electronic conductivity is usually enhanced with alkaline-earth doping (strontium and calcium notably) however compounds like $La_{1-x}Sr_xCrO_{3-\delta}$ and related have demonstrated very high polarisation resistance[94-96]. On the other hand, the first redox stable anode material for SOFC, LSCM – $La_{1-x}Sr_xCr_{1-y}Mn_yO_{3-\delta}$ – is electrochemically active, redox stable, compatible with various electrolytes (having a similar TCE)[73, 97-103] and despite a low ionic transport, electrode polarisation losses can be greatly decreased by the use of ceria- and zirconia-based interlayers[99, 103, 104].

1.2.6.3. Double perovskite-type systems

Double-perovskites such as Sr_2FeMoO_6 – Figure 1.5[47] – have also recently being investigated as exhibiting reasonably good ionic conduction[105, 106].

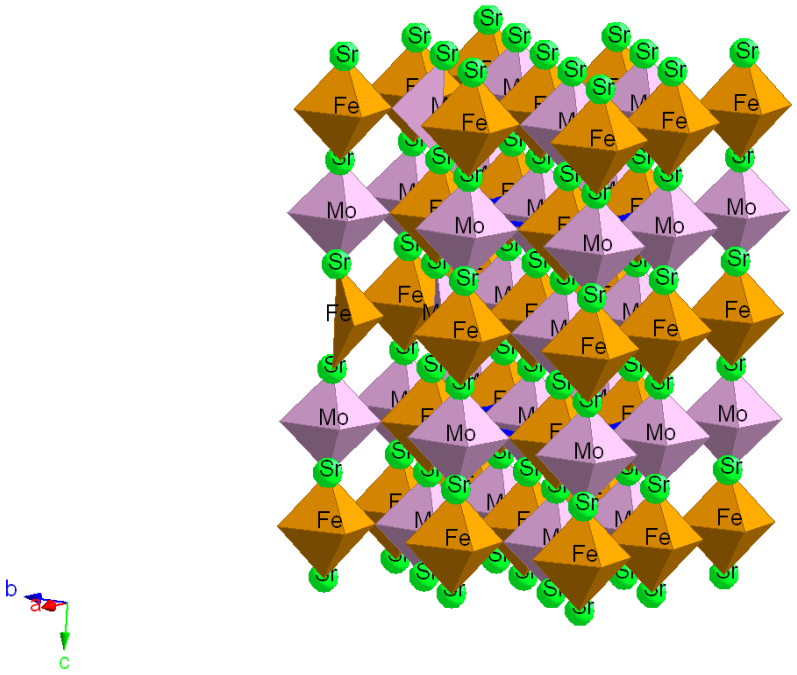

Figure 1.5 Structural representation of Sr_2FeMoO_6

$Sr_2Mg_{1-x}Mn_xMoO_6$ was found to be efficient with methane fuel, tolerant to sulphur – even after prolonged exposure – and redox stable[107, 108]. The efficiency and electronic conduction of this class of compounds can also be enhanced by lanthanum-substitution on the *A*-site[109]. However, despite encouraging new properties, efficiencies achieved by double perovskites are still far from matching those obtained from LSCM or doped-STO.

1.2.7. Defect crystal chemistry

Crystal chemistry is the study of all aspects of crystalline structures and the relation of a crystal's particular physical state with its properties in a solid state. It is used extensively in many areas of science and/or engineering, sometimes unknowingly, and is vital to understand many of the properties exhibited by solids. In inorganic chemistry and materials science, the most interesting topics of crystal chemistry are structure-property relations (thermal properties, diffusion, conductivity, magnetism, etc…), phase transitions, phase diagrams and the possible imperfections (most commonly referred as defect chemistry). This latter is of significant importance in the development of new materials as most newly formed/synthesised structures are often non-stoichiometric on one site at least (*A* and/or *B*-site deficiencies, oxygen hypo/hyperstoichiometry).

1.2.7.1. Defects in ceramics

Point defects in crystals are expressed using the Kröger-Vink notation (as described earlier in section 1.2.5.2). Within the possible types of point defects, ionic defects (Schottky and Frenkel defects) are the most common and important types with electronic defects (electron holes and free electrons) also widely observed in ionic compounds.

1.2.7.1.1. Schottky defects

Unique to ionic compounds, the Schottky defect is the stoichiometric association of anion and cation vacancies. In a fully ionised MX compound, it is formed according

to Equation 1.8 below with A describing where a new lattice site is formed, and Equation 1.9 giving the resulting Schottky defect equation considering that M_M and X_X are considered equivalent to M_A and X_A respectively.

$$X_X + M_M \leftrightarrow V_M''' + V_X^{\cdots} + X_A + M_A \qquad \textbf{Eq. 1.8}$$

$$0 \leftrightarrow V_M''' + V_X^{\cdots} \qquad \textbf{Eq. 1.9}$$

Thus, the concentrations of Schottky defects in MX are given by Equation 1.10, with ΔG_S the Schottky formation free energy; K_S, the reaction constant and k_B, the Boltzmann constant.

$$[V_M'''][V_X^{\cdots}] = K_S = e^{\left(-\frac{\Delta G_S}{k_B T}\right)} \qquad \textbf{Eq. 1.10}$$

1.2.7.1.2. Frenkel defects

Frenkel defects are formed when there is a transfer of an atom from a lattice site to an interstitial site thus creating a vacancy and are the result of thermal vibrations within the lattice. The pair formed by the created vacancy and the occupancy of the interstitial site constitutes the Frenkel defect. Unlike Schottky defects, Frenkel defects do not involve the create and/or migration to new lattice sites; hence, physical structural constraints apply concerning availability and size of the interstitial site. In the case of a metal oxide MO, fully ionised, Frenkel defects can be described from Equation 1.11 and 1.12.

$$O_O^{\mathrm{x}} + M_M^{\mathrm{x}} + V_i \leftrightarrow V_M' + M_i^{\cdot} + O_O^{\mathrm{x}} \qquad \textbf{Eq. 1.11}$$

$$M_M^{\mathrm{x}} + V_i \leftrightarrow V_M' + M_i^{\cdot} \qquad \textbf{Eq. 1.12}$$

Thus, the concentrations of Frenkel defects in MO are given by Equation 1.13, with ΔG_F the Frenkel formation free energy; K_F, the reaction constant and k_B, the Boltzmann constant.

$$[V_M'][M_i^{\cdot}] = K_F = e^{\left(-\frac{\Delta G_F}{k_B T}\right)} \qquad \textbf{Eq. 1.13}$$

1.2.7.1.3. Electronic defects

The electronic order within a solid may be considered perfect only at a temperature of 0 K where electrons all occupy the lowest possible energy levels following Pauli's exclusion principle. The excitation of an electron to a higher energy level thus results in electronic disorder which in ceramic materials is classified as either intrinsic (formation of holes and free electrons) or extrinsic (externally dominated, e.g. non-stoichiometry, solute addition) electronic defects. Intrinsic electronic defects thus consist of electron holes in the valence band and of free electrons in the conduction band. Their concentrations are solely determined by the band gap energy and temperature in relation to the Fermi function, *f (E)*, providing the probability of an electron occupying an energy level *E* given in Equation 1.14 below with E_F, the Fermi level.

$$f(E) = \frac{1}{1+e^{\left[\frac{E-E_F}{k_B T}\right]}} \qquad \textbf{Eq. 1.14}$$

In an intrinsic ceramic, concentrations of free electrons and free electron holes are equal while for extrinsic electronic defects, electronic energy levels are changed thus varying the relative concentrations of free electrons and electron holes. However, their product at any given temperature remains constant and is expressed in Equation 1.15 with E_g, the band gap energy (difference between the conduction band energy level E_c and the valence band energy level E_v); K_E, the reaction constant and k_B, the Boltzmann constant.

$$[e'][h^{\cdot}] = K_E = e^{\left(-\frac{E_g}{k_B T}\right)} \qquad \textbf{Eq. 1.15}$$

1.2.7.1.4. Goldschmidt tolerance factor

In perovskite materials in particular, the incorporation of defects into the lattice and occurring structural distortions deviating from the perovskite primitive cubic unit

cell packing may be evaluated using the Goldschmidt tolerance factor τ. Based on the geometrical packing of charged spheres, it allows to determine whether the resulting level of distortion is low enough to permit formation of the perovskite phase and is given by Equation 1.16 with r_A, r_B and r_O the ionic radii of atoms on site *A*, *B* and *O* respectively.

$$\tau = \frac{(r_A + r_O)}{\sqrt{2}(r_B + r_O)} \qquad \textbf{Eq. 1.16}$$

An ideally packed perovskite structure is primitive cubic (like $BaZrO_3$) and in that case, $\tau \approx 1$. However, most perovskite structures are distorted into rhombohedral, tetragonal and/or orthorhombic systems, often approximated as cubic structures with τ deviating from 1, between 0.8 and 1. After neutron diffraction studies on $BaCeO_3$, four distinct distortion mechanisms were proposed[110] namely; the distortions of the *B*-site octahedra, the displacement of the cation within the *B*-site octahedron, the displacement of the *A*-site cation within the dodecahedron and the tilting of the octahedra relative to one another; the formers being characteristics of ferroelectricity in titanates and the latter of a compound where the *A*-site cation is much smaller than the dodecahedral site, as is the case for barium in barium cerate.

Values obtained for tolerance factors may vary slightly in the literature from authors to authors due to the erroneous use of different atomic coordination numbers having thus different ionic radii values.

1.2.7.2. Imperfections-related properties

Considering that a crystal's physical properties are all related to its specific atomistic structure, the presence and/or absence of imperfections will thus necessarily govern and/or affect some of its properties. While density, fundamental optical absorption and specific heat are rather insensitive to imperfection concentrations; effects on atomic and electronic movements, luminescence and magnetic properties essentially depend on the presence and/or absence of imperfections. It is then obvious that the latter group is best suited to provide information regarding imperfections as the former may require precise analysis in order to evaluate the differences between what is considered a perfect and a less perfect crystal.

1.2.7.2.1. Atomic movement

Atom and ion migration in crystals always occurs because of point defects, whether these involve primitive ones as vacancies or interstitials, or combinations. When direct exchange of two atoms occurs, it is commonly supposed to happen without involving defects which may only be considered true if the situation in which both atoms have left their respective initial site is ignored. In fact, many mechanisms could be considered, e.g. one atom could move into an interstitial site in order for the other atom to occupy its site or both atoms could leave their sites at the same time forming a transition state. Considering these scenarios for example, both involve point defects; namely the association of a vacancy and an interstitial in the former and a transition state in the latter.

Atomic migration over large distances may occur via two distinct phenomena, through diffusion – which may occur in both neutral and charged defects (and is discussed further later) – and through ionic conduction, which requires an effective charge[111]. Experimentally, diffusion coefficients (from creep or precipitation[112]), thermoelectric power (exhibited by ionic conductors) or Hall voltage (shown for sodium in sodium chloride[113]) may be obtained, providing direct information regarding the migration and concentration of imperfections.

1.2.7.2.2. Electronic movement

As noted previously, electronic conduction does not occur at 0 K as perfect electronic order is achieved. However, the presence of free electrons or electron holes in the lattice will allow electronic movements. For the simple case of crystals having only one type of current carriers (holes or free electrons), the thermoelectric power and the Hall effect are straightforwardly related to the concentration of carriers and the sign of these effects essentially provides evidence of whether holes or free electrons are involved, i.e. a negative Hall effect indicates holes are current carriers while a positive Hall effect indicates free electrons are current carriers. Electrical conductivity measurements allow both the concentration and the mobility of the carriers to be determined. Therefore, by combining conductivity and Hall voltage measurements, the

mobility can be obtained, however limited by various scattering processes and affected by temperature.

1.2.7.2.3. Heat conduction

Heat may be conducted through imperfections in two manners; firstly if moving in a temperature gradient, defects somehow transport energy (observed in lead compounds PbS and PbTe[114] and PbSe[115]) or secondly through intrinsic crystal heat conductivity, i.e. phonons scattering at imperfections. This latter mechanism is predominant at low temperatures as typical temperature dependence exists for each type of defects. Evaluating these temperature dependences may then provide information about atomic as well as electronic defects[116-119] as has been shown for indium antimonide[120].

1.2.7.2.4. Solid state diffusion

In its general form, diffusion is described by a gross diffusion coefficient *D* (Fick's first law of diffusion[121] – Equation 1.17 with *J*, the diffusion flux; *D*, the diffusion coefficient; *c*, the concentration gradient of the considered atoms and *x*, the position of the atoms) which is defined by differentiating the relation connecting the considered particle current with their concentration gradient; simplified to Fick's second law of diffusion[121] – Equation 1.18 where *t* is the time – if *D* is independent of *c*.

$$J = -D\frac{\partial c}{\partial x} \qquad \textbf{Eq. 1.17}$$

$$\frac{\partial c}{\partial t} = D\frac{\partial^2 c}{\partial x^2} \qquad \textbf{Eq. 1.18}$$

The relation between *D* as described in Fick's laws (Equations 1.17 and 1.18) and the processes by which diffusion occurs is never simple, however, *D* is always dependent on concentration and might thus assume negative values.

In crystals, two types of diffusion may occur: self-diffusion (movement of atoms constituting the structure, which may involve chemical changes or not; in which case tracers are used to detect diffusion) or diffusion of foreign constituents (such as the diffusion of calcium atoms in sodium chloride crystals), both being plausible as a result of either imperfection interactions and/or electric fields (this latter only occurring when

charged particles are considered). Diffusion always involves either interstitial atoms or vacancies or a combination of these defects. Ring diffusion for example – exchange of two or more neighbouring atoms – is theoretically plausible, but although it is rarely observed, it can be treated as the combination of an interstitial and a vacancy being formed prior to the exchange (as discussed in an earlier part on atomic movements). The simplest case would then concern diffusion of neutral/charged interstitials where diffusion conditions are such that charge effects are negligible. Under these conditions, Fick's first law would be respected and D (both for vacancies and interstitials) would solely depend on geometry and the jump frequency ν corresponding to the number of random migration made by diffusing particles per second.

1.2.7.2.4.1. Correlation effects

At any time where diffusion occurs by movement of two species, the relation between D and atomic jumps is complicated by the dependency of the various jumps with each other; i.e. correlation effects governed by correlation factors (f) do exist and apply to vacancy and interstitial diffusion (both for tracers and foreign atoms) but not to pure interstitial diffusion. Many interstitialcy mechanisms are possible, involving either collinear or back jumps as found for silver halides[122-124] or being a combination of jumps by multiple atoms in which case the correlation factor is driven by the ratio of each atom's jump frequencies as shown for alkali halides in a cation-anion vacancy pair diffusion mechanism[125].

Correlation factors for single atom diffusion only depend on the structure of the crystal and have been calculated for several compounds for vacancy diffusion, collinear, non-collinear and mixed interstitialcy mechanisms[122, 126-128]. In cases where the diffusion mean free path is a multiple of the smallest atomic hopping distance, correlation factors will have a tendency to equal one and correlation effects will become negligible or even disappear completely.

1.2.7.2.4.2. Nernst-Einstein relation

For charged point defects, movements within the crystals are possible through either diffusion or conduction which added to each other represent the equilibrium

potential. The conductivity resulting from a point defect is expressed in terms of charge and mobility (Equation 1.4). On the other hand, Einstein's kinetic theory relation links mobility of charges (μ_B) with diffusion (D_B) and is expressed in Equation 1.19 for a charged particle B with *R*, the ideal gas constant and *F*, the Faraday constant.

$$D_B = \frac{\mu_B RT}{z_B F} \qquad \textbf{Eq. 1.19}$$

Combining Equation 1.4 and Equation 1.19, the diffusion coefficient can be expressed in terms of the ionic conductivity as,

$$D_B = \frac{\sigma_{i,B} RT}{{z_B}^2 F^2} \qquad \textbf{Eq. 1.20}$$

According to Kohlrausch's law, the limiting ionic conductivity of a strong electrolyte is equal to the sum of contributions from its constituent ions. By substituting Kohlrausch's law with an ionic conductivity rearrangement of Equation 1.20, the Nernst-Einstein equation is obtained as shown in Equation 1.21 with ${\Lambda_B}^0$, the limiting molar conductivity; n_+, D_+ and z_+, the number, diffusion coefficient and charge of the cations respectively and n_-, D_- and z_-, the number, diffusion coefficient and charge of the anions respectively.

$${\Lambda_B}^0 = (n_+ D_+ {z_+}^2 + n_- D_- {z_-}^2)\frac{F^2}{RT} \qquad \textbf{Eq. 1.21}$$

Some electrolytes exhibit very large ionic conductivities, which may be explained either by the presence of a large number of ions with normal mobility or a moderate concentration of mobile species with very large mobility. In this latter case, the large mobility may be due to a larger mean free path λ compared to the smallest atomic hopping distance *a* giving $\lambda = na$ with *n* an integer very much larger than one. In a vacancy diffusion mechanism, this would have the effect of neglecting the correlation factor and *f* would tend to one. However, as an *n*-fold jump would only move a tracer by the distance *a*, an additional factor *f'* equaling n^{-1} in the expression of the self-diffusion must be added. For interstitial diffusion, an enlarged mean free path affects both diffusion and conductivity in the same way, thus both *f* and *f'* are equal to one.

1.2.7.3. Sintering and grain growth

Sintering is a thermal technique used as a means of densification and grain growth. It may be applied to a large quantity of materials and is mainly carried out either in the solid or liquid phase (other types do exist but are either combinations and/or are derived from the two main ones). Depending on the desired process and components used, a specific sintering procedure is required in order to obtain the desired structure and/or properties, i.e. presence or absence of grain boundaries, size of grains, porosity.

Sintering is driven by the diminution in total interfacial energy within a structure. For a compacted powder, this energy is expressed as γS as shown in Equation 1.22 below with γ, the specific interface energy and S, the total interface area of the compacted powder and where the first term is due to densification and the second to grain growth.

$$\Delta(\gamma S) = S\Delta\gamma + \gamma\Delta S \qquad \textbf{Eq. 1.22}$$

In solid state sintering, the change in interfacial energy relates to the substitution of solid/void interfaces by solid/solid interfaces as illustrated schematically in Figure 1.6. Considering that the total interfacial energy for powder sintering is in the order of a few Joules per mole – a considerably small amount compared to other chemical/physical processes – it is then necessary to know the involved variables in order to control them and obtain the desired level of densification and grain growth thus giving the desired microstructure. Sintering variables may be sorted into two categories; namely physical/chemical variables and process variables: physical variables being the state of the powder used, its initial grain size, the shape and distribution of the particles, etc…; chemical variables being the powder's composition, its stoichiometry, the presence/absence of sintering aids, etc. and the process variables corresponding to sintering temperature, dwelling times, heating/cooling rates, pressures, etc.

As the dwelling times are increased during sintering, the average particle size of the sintered materials increases, either normally, where a simple and homogeneous distribution of grain sizes with sintering time is obtained or abnormally, where a matrix of very small grains is formed in conjunction with extremely large particles. Factors

affecting the rates of densification and grain growth are clearly unique, thus control or predominance of one or the other will directly affect the sintering process: densification depends on lattice and grain boundary diffusion while grain growth relies on surface and gas phase diffusion, evaporation/condensation and boundary mobility. The contribution of lattice and gas diffusion for example is inversely proportional to the cube of the pore size while for condensation, the dependence to the pore size is only to the square therefore as the pore size decreases the contribution of all these factors is increasing. Under ideal conditions, all pores are situated at the grain boundary and therefore move along this latter as the grains are growing, however if the boundary mobility is much larger than the pore mobility, some of these will get trapped inside grains and form pore/boundary separations, indicative of the limit of densification in sintering. When such a problem does occur, if it is known (verifiable by SEM or TEM), it is best if the sintering process (i.e. the heating programme) is completed as any additional dwelling at high temperature will only increase grain sizes without any gain in overall density.

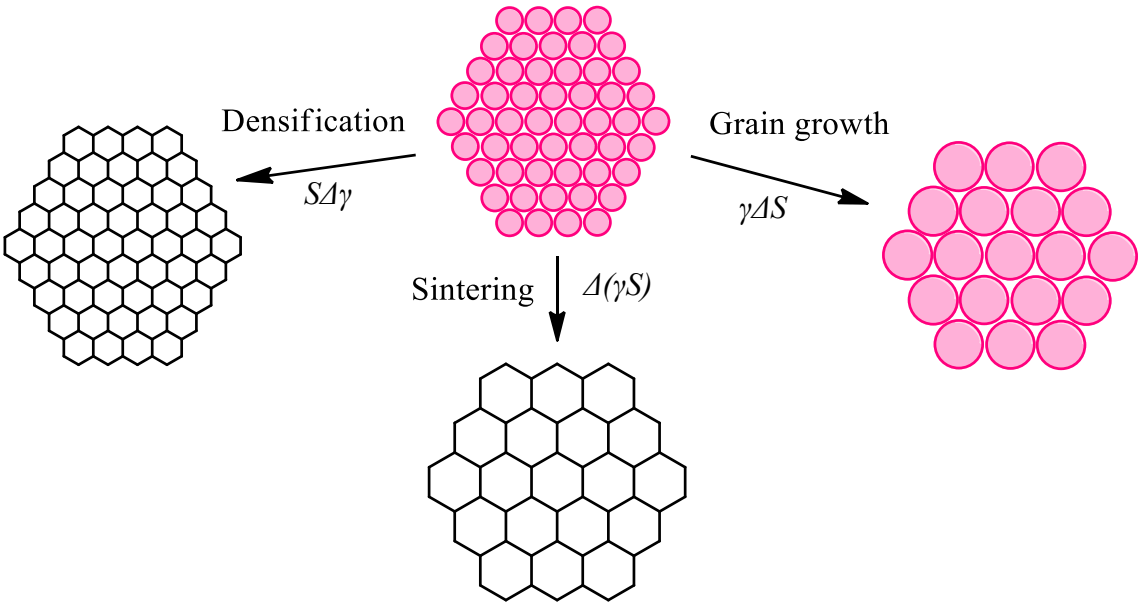

Figure 1.6 Basic solid state sintering phenomena

1.3. Objectives

As aforementioned, there has been considerable amount of work carried out in order to yield high performance, efficient components for SOFC, with some degree of success[72-77]. However, current systems based on Ni-cermets or Ni-composite electrodes suffer from numerous counterproductive effects, mechanical, thermal or chemical. The use of pure metallic compounds also brings into the discussion the matter of costs. Indeed, in the case of PEMFCs, the greatest disadvantage to their full-scale mass industrial production has been the cost associated with the use of noble metal catalysts. Ceramic materials such as perovskite-based and related compounds exhibit the most interesting properties as alternative materials for SOFC electrodes (LSCF, BSCF for cathodes and LSCM, doped-STO for anodes) and as proton-conductor electrolytes (BCZs).

Vanadate compounds such as BiMeVOX electrolytes have shown to exhibit very high ionic conductivities at lower temperatures, a rare and important characteristic not found in many currently used anode materials. Incompatible with most common electrodes, BiMeVOX are still an interesting area of study as their vanadium content boosts the catalytic activity of such species however studies of such systems in a fuel cell environment (part of a functioning electrodes-electrolyte structure) has for now been unsuccessful (due entirely to their high chemical reactivity at interfaces).

Rare-earth and alkaline-earth vanadates in pure or doped forms also constitute an important family of compounds to be researched. Lanthanoids vanadates in general have proven to be very interesting compounds exhibiting properties that have often been overlooked. Some aspects have been well studied but not applied to SOFCs at all thus, specific properties may be put to good use in well designed compounds in order to yield very efficient, stable and durable materials. However, keeping in mind the overall costs of material development, systematic studies were aimed at cerium vanadates and this for multiple reasons. Firstly, the chemistry of lanthanum vanadates was generally understood and its stability in respect of its conductive behaviour was in question, secondly, as doping with an alkaline-earth element was desirable in order to induce a charge imbalance (to provide ‘natural’ oxygen vacancies, which is more likely with cerium due to correspondence of ionic radii) and thirdly, as thermodynamic properties

are more favourable for cerium than for lanthanum (phases containing cerium melt, soften and form at lower temperatures and have generally a higher expansion coefficient than those containing lanthanum). Moreover, studies carried out on zircon type cerium-containing compounds had been overlooked as to their application to the field of SOFC, hence cerium vanadium oxide studies constitute the core of the electrode section discussed in Chapter 3 as well as the main objective of this thesis.

Proton-conductors on the other hand are a vivid field of study with a seemingly endless possibility of plausible elemental combinations within the base formed by BCZs compounds. $BaCeO_3$ is one of the oldest proton conductor electrolyte known. Since its discovery, an uncountable amount of studies have been carried out and most have suffered from one issue: its stability in humid environment. A number of doping agents and substitution elements have been used with some successes but in majority, the pure barium cerium oxide compound remains an unstable, uncontrolled material. Considering all the available dopant/sintering aid/stabiliser available, a couple of these possibilities were explored as shown in Chapter 4 and mixed results were obtained; nonetheless, the understanding and advances in knowledge is undeniable.

The overall aim of this project is thus to investigate appropriate materials for IT-SOFCs meeting all fundamental requirements to achieve good cell performance and stability at a lower temperature than existing FC systems.

2. Experimental

2.1. Syntheses

In order to synthesise the desired material, many different procedures can be used including standard ceramic, wet chemical, sol-gel, combustion and/or co-precipitation reaction methods. Only the employed methods are described below with full experimental details given for each studied components in their respective chapters.

2.1.1. Solid state reaction

The most common and simplest method of synthesis is the solid state reaction, often referred to as 'shake and bake' or 'heat and beat'. It is a high temperature method (typically 500 º - 2000 ºC) that can be used with any non-volatile compounds to yield the desired product and follows the steps illustrated in Figure 2.1 below.

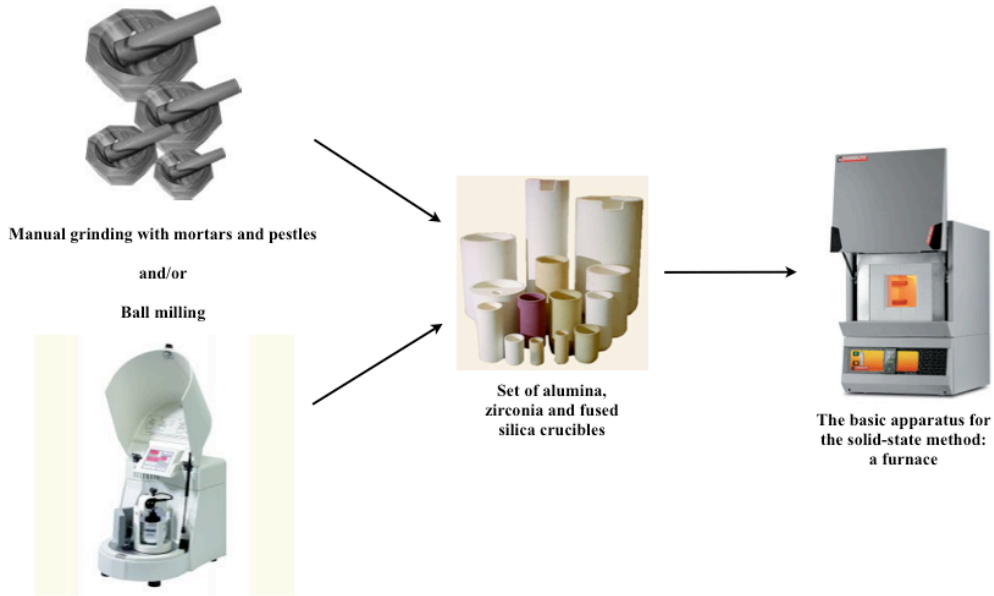

Figure 2.1 Schematic of a solid-state reaction

It is based on known stoichiometric amounts of each reactant, homogenisation of the mixture followed by firing at a defined temperature for a specific time. A homogeneous mix is essential and is usually achieved with a mortar and a pestle, however smaller particle sizes can be obtained with a ball miller. Homogeneity can indeed be improved by ball milling and pressing the mixture of powders into pellets can

maximise the number of crystallite faces in direct contact thus requiring less cycles of grinding/firing to obtain a single phase product. A large amount of crucible types are commonly used for the firing step including but not limited to porcelain, corundum, platinum, iridium and/or nickel crucibles. All have their own specificity and range of operability and can be employed opened or capped.

2.1.2. Co-precipitation reaction

The co-precipitation of solids is a basic synthetic method that relies on the precipitation character of solutes depending on the dissolution conditions. In a typical reaction, stoichiometric amounts of soluble salts are dissolved in a medium before being precipitated by addition of the required agent to induce the desired precipitation e.g. if nitrates are used as the soluble salts with water as the medium and hydroxides are wanted as the precipitate, the required agent would be diluted ammonia. The precipitates are usually stirred and aged for some time before being filtered, washed to prevent any unreacted starting materials being trapped in the suspension, dried and then calcined to yield a ceramic powder. Due to space distribution and physical state of the reactants during the synthesis, ceramic powders obtained from co-precipitation reactions have a much smaller average particle size than powders prepared by the conventional ceramic method.

2.1.3. Sol-gel reaction

Another useful method is the sol-gel reaction. It has the advantage of having no filtering and washing step as is the case in co-precipitation avoiding the possibility of changing the stoichiometry by washing off unreacted products. In detail (Figure 2.2), the sol-gel process involves the dissolution of a stoichiometric amount of the desired nitrates, oxalates and/or hydroxides into a medium (water in most of the cases) to obtain a solution (hence the ‘sol’ step); followed by a gentle heat treatment to evaporate the solvent and form a gel; and finally, another heating step at much higher temperature to form the desired ceramic powder (but still at lower temperature than for conventional ceramic synthesis).

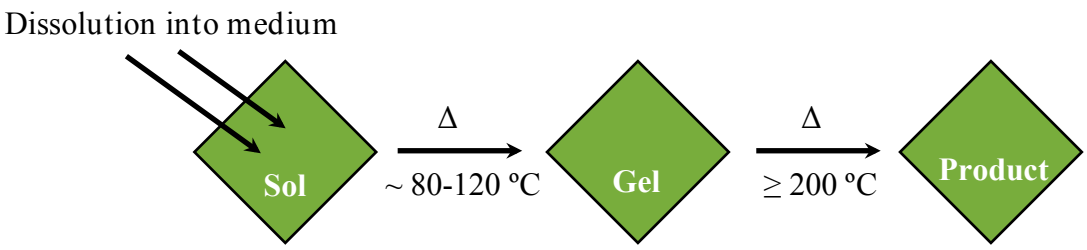

Figure 2.2 Synthesis steps in the sol-gel method

As is the case for co-precipitation, the fact that products are formed directly from previously dissolved reactants, the average particle size is much smaller with a sol-gel reaction than it is from conventional high temperature solid state synthesis.

2.2. Characterisation

In order to characterise the synthesised materials, Powder X-Ray Diffraction (PXRD) is used to determine the phase in relation with Rietveld analysis using GSAS for phase refinement correlations. Simultaneous Thermal Analysis (STA) and dilatometry are used to determine the thermal properties. Electron Microscopy (EM) is employed to examine the microstructure. Electrochemical Impedance Spectroscopy (EIS) and DC conductivity measurements allow electrical properties of the materials to be determined.

2.2.1. Powder x-ray crystallography (PXRD)

PXRD is a fast, non-destructive analytical tool enabling the characterisation of samples, essentially providing information on unit cell dimensions. X-rays were discovered in 1895 by Wilhelm Röntgen[129, 130]. An electrically heated filament, emitting electrons and accelerated by a high potential difference are colliding with a water-cooled target metal (usually copper or molybdenum), as illustrated in Figure 2.3[131].

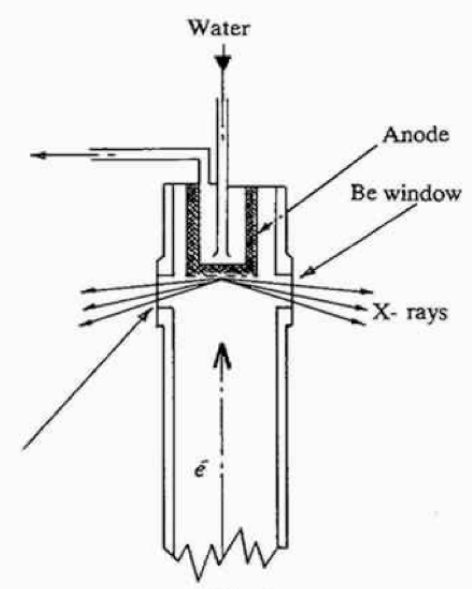

Figure 2.3 Schematic of the section of an X-ray generating tube

A continuous spectrum of what is called 'white' X-radiation is then emitted and superimposed with sharp, intense, very closely spaced doublets of X-ray peaks (K_α and K_β) as depicted in Figure 2.4[131]. These lines occur due to a two-stage process where

firstly an electron from the X-ray generator collides with and knocks out an electron from the innermost *K* shell (*n*=1) from an atom of the target metal and secondly, an electron from a higher shell decreases in energy and fills the vacancy created thereby emitting an X-ray photon.

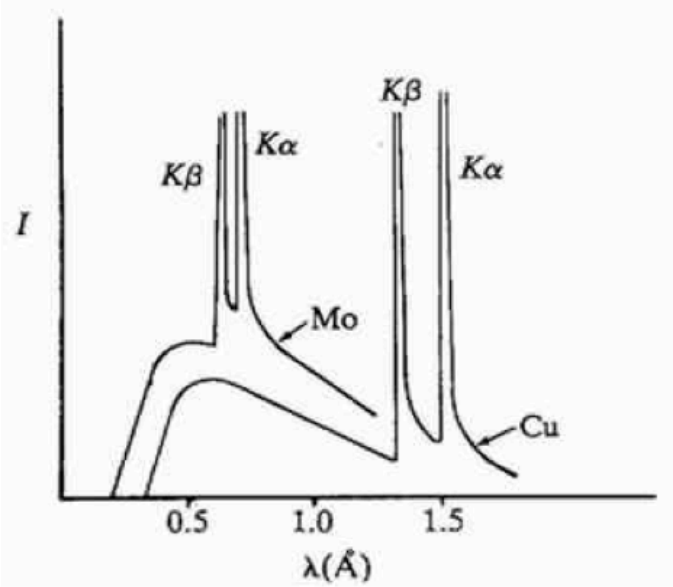

Figure 2.4 An X-ray emission spectra (Cu and Mo combined)

Electrons descending from the *L* shell (*n*=2) produce the K_α lines and electrons from the *M* shell (*n*=3) give the K_β lines. As in theory monochromatic radiation is required for XRD, K_β lines are usually filtered out either by using a filter of an element adjacent (*Z*-1) to the target metal or by reflecting the generated beam of X-rays from a plane of a single crystal, conventionally graphite. Thus, nickel and niobium can effectively filter out the K_β lines of copper and molybdenum respectively; and titanium and iron the K_β lines of chromium and iron respectively when these latter are used as target metals.

In 1912, Max von Laue discovered that crystals were acting as diffraction gratings for X-ray radiation in accordance with the 3-D spacing arrangements of crystalline planes[132]. PXRD and more generally XRD is based on the constructive interference of the crystal being analysed with monochromatic X-rays and if Bragg's Law is satisfied (Equation 2.1 below[132]), a diffracted ray can be detected.

$$n\lambda = 2d_{hkl}sin\theta_{hkl} \qquad \textbf{Eq. 2.1}$$

The Bragg equation[133] relates the spacing between the crystal planes, d_{hkl}, to the particular Bragg angle, θ_{hkl} at which reflections from these planes are observed and is graphically explained in Figure 2.5. By demonstration, if ray A is scattered by the atom at X and the ray B at Y, constructive interference can only be obtained if the path lengths of the interfering beams only differ by an integral number of wavelengths. Therefore, if XG and XH are drawn at right angles to the waves, the path length difference between the two rays AD and BE is equal to the sum of GY and YH. But it can be seen that GY is equal to YH which is in turn equal to $d\sin\theta$, so the difference in path length must be equal to twice $d\sin\theta$. If this must then be equal to an integer of wavelength, n, in order to obtain constructive interference and if the wavelength of the X-rays is λ, the Bragg law is verified.

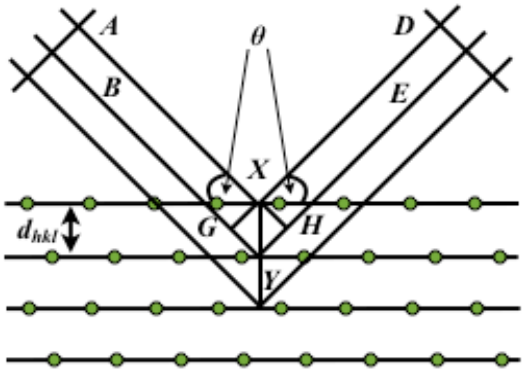

Figure 2.5 Bragg reflection from a set of crystal planes with a spacing d_{hkl}

Practically speaking, a crystal can be X-rayed in generally speaking two manners, either in transmission mode or in reflection mode. In transmission XRD experiments, the incident X-ray beam is not reflected but instead travels through the sample, where diffraction then takes place. Light atom materials, like purely pharmaceutical compounds should always be measured in transmission mode, as in standard reflection geometry, large specimen displacement would occur and the compounds would literally be transparent for X-rays.

In reflection mode, usually referred to as the Bragg-Brentano geometry (Figure 2.6[134]), two different configurations can be used: the θ:θ or the 2θ:θ setup. These in fact only differ in data collection procedures. In a θ:θ goniometer, samples are maintained in a fixed horizontal position and both the X-ray tube and detector simultaneously move

over a θ angular range whereas in the 2θ:θ configuration, the X-ray tube is stationary while the sample holder and the detector simultaneously move by a θ and 2θ angle respectively. There is in essence no fundamental difference between the two configurations even if the former is usually preferred to the latter, essentially since at high theta values, small or loosely packed samples have a tendency to shear off the sample holder. Figure 2.6 below corresponds to the Bragg-Brentano reflection geometry in a θ:θ configuration with from left to right: the X-ray source, the automatic aperture slit, the sample mounted on a holder, the automatic anti-scatter and the receiving slit, respectively, and the detector.

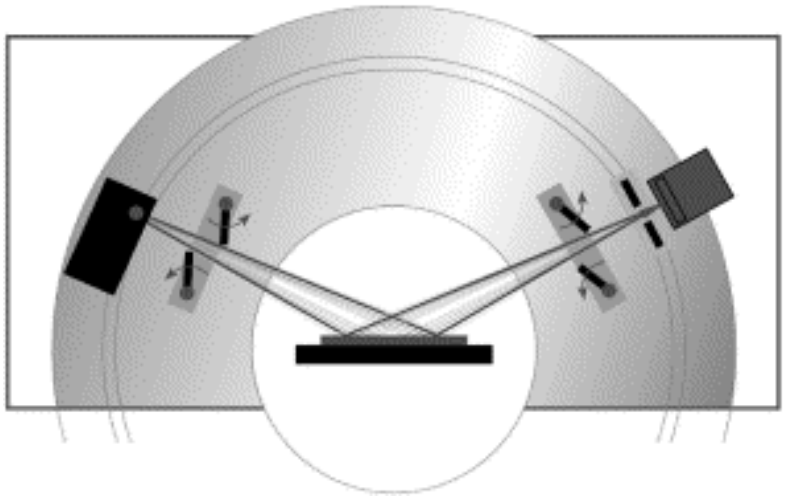

Figure 2.6 Bragg-Brentano geometry in θ:θ configuration

Once processed and quantified over a range of 2θ angles, all possible diffraction directions within the lattice should statistically be attained and conversion to *d*-spacing allows precise identification of the crystal analysed as each mineral has a unique set of diffraction lines.

In the case of a high symmetry system (like the three cubic Bravais lattices), very few peaks occur in the PXRD pattern and as these are often well resolved and well separated, it is then relatively simple to accurately measure their position and intensity. Using absences due to lattice centring and systematic absences due to screw axes and glide planes, the obtained reflections can be indexed and the structure analysed solved. Less symmetrical structures produce much more complicated, overlapped reflections, and it therefore becomes impossible to quantify to any acceptable degree of accuracy the intensities of individual peaks. To resolve that issue from powder diffraction data, a

method known as Rietveld analysis was developed[135]. A series of different software then followed, based on the model devised by Rietveld. One of these programs, GSAS[136] – General Structure Analysis Software – allows the processing and analysis of both single crystal and powder diffraction data obtained either with X-rays or neutrons in a more convenient, efficient and robust way than the original Rietveld program, which was mainly developed for the analysis of structural magnetic peaks obtained from neutron diffraction data.

All programs however share the same concepts and methodologies and treat the diffraction data in the same manner by interpretating both the line intensities and line positions in order to analyse the overall line profiles, operation rendered necessary by the extensive overlap of reflections in – crystallographically speaking – low symmetry lattices. Starting from a trial structure, a powder diffraction profile is calculated and compared with the measured profile. The structure is then gradually modified by changing atomic positions and peak profiles and refined using a least-squares method until a best-fit match with the measured pattern is obtained. A series of statistical constants, *R* factors and a difference plot of the two patterns allow the validity of the structure to be assessed. Best results are obtained if the trial structure used as a starting point is estimated from a known structure; that is if the crystal for which the refinement is being carried out only differs from one element or two from the structure used as model. This is particularly important for novel materials that do not simply involve variations of dopant concentrations on particular sites as would be the case in an ABO_3/$AA'BO_3$ known/unknown couple.

Another application that can provide useful information from PXRD is the use of the Scherrer equation to calculate the particle size of the analysed materials (considering that these are of a nano-scale level) and is given by the following expression[137] (Equation 2.2), where τ is the size of the crystallite; *K*, the shape factor (usually 0.9); λ, the wavelength of the X-ray; $B_{observed}$ and $B_{resolution}$, the full width at half maximum in radians and θ, the Bragg angle.

$$\tau = \frac{K\lambda}{\sqrt{B^2_{observed} - B^2_{resolution}}\cos\theta} \qquad \textbf{Eq. 2.2}$$

Calculations are usually carried out on multiples of the strongest reflections in order to obtain the most accurate values. Highly crystalline compounds/powders produce more reliable results due to a better profile and signal to noise ratio from PXRD.

2.2.2. Simultaneous Thermal Analysis (STA)

STA is a combination of both Differential Scanning Calorimetry (DSC) and Thermo Gravimetric Analysis (TGA) in one unique instrument allowing heat and mass differences to be monitored at the same time during a thermal cycle. Two sample crucibles (varying in materials depending on the sample to be analysed) are heated and/or cooled at a given rate in a controlled environment (air or oxygen for oxidising atmosphere; nitrogen or argon for inert conditions and hydrogen or mixtures of hydrogen/argon/nitrogen for reducing environment). The so-called reference sample consists of a standard of known thermal behaviour (an empty crucible of pure platinum or platinum-rhodium-10 alloy during calibration) while the sample to be analysed is contained in the second crucible. Any difference in the thermal response of the two samples results in a temperature difference delta, between the two crucibles. These may be caused by dissimilarity in specific heat, occurrence of an endo- or exothermic reaction and/or a phase change. Simultaneously, the micro-balance system incorporated measures any change in mass of the specimen as a function of temperature thus displaying both weight-loss and differential calorimetric curves.

The obtained traces can then be studied to determine temperature related characteristics of materials, i.e. water-related losses or gains, volatile organics or ash content and/or decomposition or melting temperature with an example shown in Figure 2.7. This example shows the weight loss occurring during conversion of nickel oxide to nickel metal under reducing conditions with a weight loss of around 23 % between 100 ºC - 500 ºC corresponding to the molecular loss of an oxygen atom. While in this particular plot, the DSC only shows broad endothermic peaks (one below 300 ºC and one above 300 ºC) and therefore mainly serves as a confirmation that the weight loss observed is real and not due to any balance vibrational inaccuracy, it has an extremely important role in identifying melting temperatures or the presence of a melting phase in

the analysed samples, when present, as described in Figure 2.8 (analysis performed from RT to 600 ºC at 5 ºC min^{-1} with a sampling rate of 1 per sec).

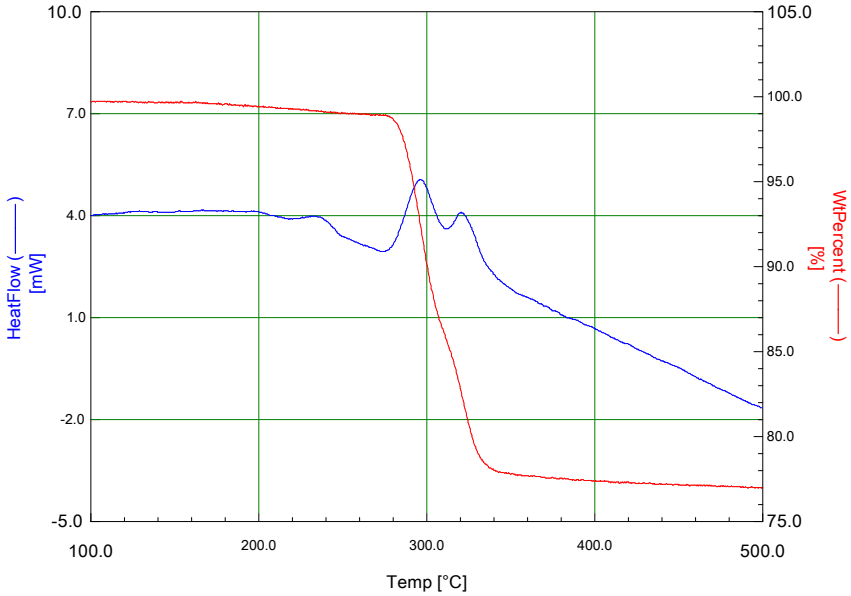

Figure 2.7 TG/DSC curves for nickel oxide in 5% H_2-Ar

In this latter, a pure sample of zinc is used as standard and the DSC trace recorded, showing the physical transition from a solid phase to a liquid phase with a peak at 424.8 ºC and a crystallisation on cooling at 413.1 ºC, which is in accord with a melting point of 419.5 ºC in the literature at ± 1% error. Additionally, the TG trace shows no sign of weight loss. Since experimental error was shown to be rather small under the conditions of this melting/crystallisation standard, these settings were used as default for all experiments throughout this thesis.

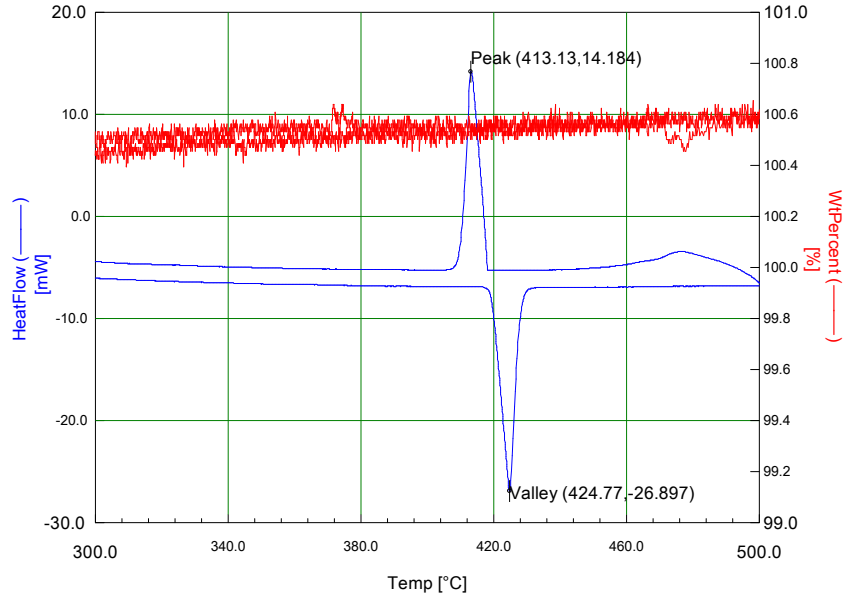

Figure 2.8 TG/DSC curves of pure zinc in flowing air

2.2.3. Dilatometry

Dilatometry is a thermoanalytical technique used to measure the expansion or shrinkage of solids, powders, pastes and liquids subjected to a negligible load while being treated in a controlled temperature/time program. Fully understanding thermal behaviours can provide insight into diverse property-affecting processes such as the influence of additives and raw materials, densification, sintering, reaction kinetics and/or phase transitions, etc.

Dilatometry can be applied to solid samples but also to powders, pastes and even liquids by the intermediate of appropriate attachments. It can also be used to carry out rate-controlled sintering studies in fields such as advanced ceramics and/or powder metallurgy.

Pushrod dilatometry allows the determination of dimensional changes versus temperature or time in a special ceramic holder within a sliding furnace undergoing a controlled temperature program. When performing an analysis, a pushrod is positioned directly in contact with the sample and transmits the length change to a Linear Variable Displacement Transducer (LVDT). As length variations occur during heat treatment, the LVDT core is displaced and an according output signal proportional to the displacement is recorded. The temperature program is controlled via the use of a thermocouple located either near the furnace's heating element or the sample even though the latter is more accurate as uniform temperature distribution may not be guaranteed depending on the instrumental design. As the sample holder and the front part of the pushrod are exposed to the same temperature program as the sample, expansion is also occurring. It is therefore necessary to correct the raw dilatometer data in order to obtain a true set of sample behaviour data. This latter can be achieved either by the application of tabulated expansion data or by using a previously recorded correction curve in order to eliminate systematic error.

Once the dilatometric measurement has been carried out, the thermal coefficient of expansion can be extracted using Equation 1.5 and compared to available existing values.

2.2.4. Electron Microscopy (EM)

Similar in principle to an optical microscope, EM uses an electron beam as a radiation source instead of visible light as is the case in conventional microscopes in order to visualise objects at a much higher resolution and depth. This difference is fundamental *per se* as it constitutes the only limitation of light microscopes to their electron equivalents and can be explained using Abbe's Law (Equation 2.3) with *d*, the resolution; λ, the wavelength of the radiation used; *n*, the index of refraction of the medium through which the radiation travels and α, the aperture angle.

$$d = \frac{0.612\lambda}{n \sin \alpha} \qquad \textbf{Eq. 2.3}$$

Abbe's equation states that the microscope's resolution is roughly equal to the half of the wavelength used. Thus, by using blue-green light at 400 nm, objects apart more than 200 nm would be fully resolved and distinct while objects closer together than 200 nm would result in the fusing of image details.

Electrons, on the other hand have a much smaller wavelength in accord with de Broglie's equation (Equation 2.4) with λ, de Broglie's wavelength; *h*, Planck's constant (6.62 x 10^{-34} kg m^2 s^{-1}); *p*, the electron's relativistic momentum; m_e, the electron's mass (9.11 x 10^{-31} kg); *e*, the elementary charge (1.60 x 10^{-19} coul) and *U*, the electric potential to which electrons are accelerated.

$$\lambda = \frac{h}{p}$$

$$with\ p = m_e\sqrt{\frac{2eU}{m_e}} \qquad \textbf{Eq.2.4}$$

$$\lambda = \frac{h}{\sqrt{2m_e eU}}$$

It results that at an accelerating voltage of 20 kV, the wavelength of the electron emitted is 8.6 x 10^{-12} m (8.6 pm or 0.086 Å) allowing high resolution imaging to be carried out.

There are two types of EM of similar importance commonly used, the Scanning Electron Microscope (SEM) and the Transmission Electron Microscope (TEM). SEM allows surface detection of defects and/or cracks whereas TEM is used to look through the analysed sample, essentially providing first hand in-depth morphological information, also involving more stringent sample preparation procedures than SEM.

2.2.4.1. Scanning Electron Microscope (SEM)

Generally speaking, the configuration of an SEM could be described as a particular type of electron gun aimed at the sample to be analysed, whose produced beam passes through multiple electron lenses and a scanning system before signal current collection and amplification; all occurring in a very high vacuum environment. SEM analysis is thus performed by collision of a beam of accelerated electrons with atoms that make up the sample (Figure 2.9) and detection of the resulting emitted radiation.

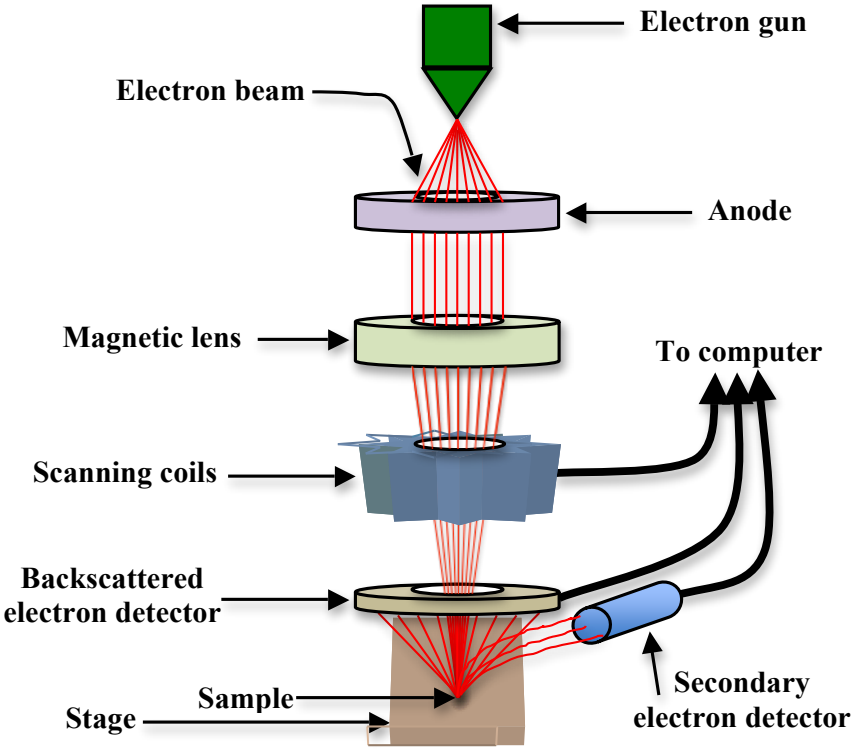

Figure 2.9 Schematic of the beams path through the SEM column

Generated by a filament, usually a loop of tungsten which functions as the cathode within the tungsten hairpin gun, the electron beam is accelerated by the

attractive forces of the anode. A proportion of these pass right by the anode and continue down the column into the magnetic lens. Having both a radial and a longitudinal component, only electrons travelling down the axis will not be affected by the magnetic field as in that case, the radial forces from all sides of the lens will be equal. Off-axis electrons however, will spiral about the optic axis due to unequal forces. Energised by varying the voltage produced by the scan generator, the scan coils create a magnetic field which allows the beam to be deflected back and forth in a controlled manner. The electron beam then hits the sample, producing a number of radiations (Figure 2.10 – electron based in red and photon based in blue). Electrons emitted are collected by a secondary or backscatter detector, converted and amplified in order to be viewed on a monitor.

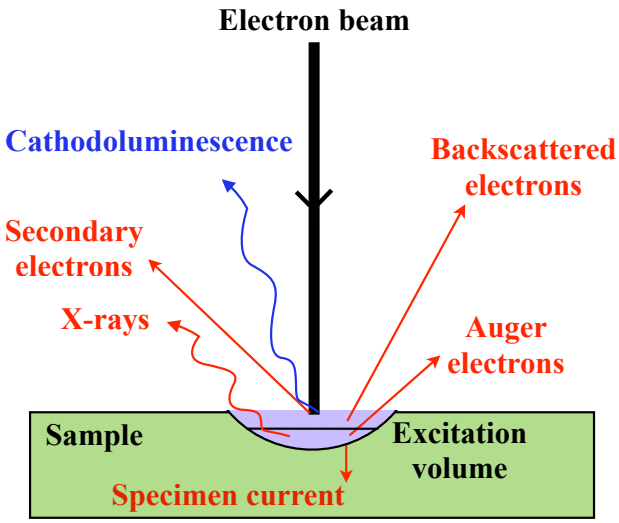

Figure 2.10 Schematic of electron/specimen interactions in SEM

Each interaction produced provides its own set of information. The cathodoluminescence and the specimen current provide electrical information, backscattered and secondary electrons provide topographical information and X-rays and auger electrons provide compositional information through thickness and surface sensitivity respectively.

On a practical point of view, the number of lenses used depends solely on the magnification required. Specimens to be tested have to be stable and electrically conductive (either naturally if of metallic nature or experimentally by applying a gold coating so as to prevent charging up the sample during analysis) and adjustments to the electron gun alignment as well as vibration of less than one hertz are vital to ensure image clarity, beam stability and maximum intensity.

2.2.5. Infrared spectroscopy

Infrared spectroscopy (IR) is one of the most useful and powerful analytical techniques to identify organic and inorganic chemicals. It can be applied to solids, liquids and gases by the use of different attachments. Solids are analysed either in powder form (in Attenuated Total Reflectance mode, ATR) or in pellet form, embedded in a KBr matrix (in Fourier transform Infrared, FT-IR). Liquids on the other hand are either simply deposited on the crystal in ATR mode or squeezed between two crystals in FT-IR. Gases on the other hand are enclosed within a chamber.

In FT-IR, a beam composed of a range of light frequencies is passed through a sample and the absorption of infrared radiation by the sample is measured. Due to IR radiation, the molecules forming the material are excited into a higher vibrational state and the absorbed radiation wavelength is characteristic of the analysed chemical bond i.e. atom species, bonding types and vibration mode (stretch, scissor, wag, twist and rock). The chemical bonds in a molecule can thus be clearly identified by interpreting the infrared absorption spectrum.[138] In ATR, the principle is similar to FT-IR however the beam of radiation is not put through the sample but reflects at its surface, which is in contact with the ATR crystal.

To identify an unknown material or to ascertain the presence or absence of an impurity, the obtained absorption spectrum is compared with standard spectra stored in databases or with a spectrum of a known compound in a spectral library. Absorption bands in the range of 4000–1500 cm^{-1} are normally due to functional groups (e.g., -OH, C=O, N-H, CH_x, etc.). The 1500–400 cm^{-1} range is called the fingerprint region. Absorption bands in this latter region are generally due to intra-molecular phenomena and are highly specific to a particular material. The configuration and arrangement of aromatic rings (e.g. *para*-, *meta*-, *ortho*-) for example can be defined and/or verified just by looking at the fingerprint region and compared with databases. The spectra of inorganic compounds though are usually much simpler to interpret.

2.2.6. Ultra-Violet Visible absorption spectroscopy (UV-Vis)

UV-Vis spectroscopy exploits the area of the electromagnetic spectrum situated at a lower wavelength from the visible area compared to IR situated at the other end.

Absorption spectroscopy depends solely on the capacity of molecules to absorb ultraviolet or visible light and is defined in Beer's Law as being proportional to the path length and the concentration of the absorbing species i.e. absorbance is increasing as the attenuation of the beam is increasing.

Fundamentally, absorption of *UV-Vis* radiation corresponds to the excitation of outer electrons, of which three types of electronic transition can be considered. Firstly, transitions involving π, σ and *n* electrons, secondly, transitions involving charge-transfer electrons and thirdly, transitions involving *d* and *f* electrons. Different molecules will absorb radiation of different wavelengths but – as in IR – an absorption spectrum will show bands corresponding to structural groups within the molecule.

The information contained in the spectra can then be used in many ways; one particular – which is often employed in solid-state chemistry – is the Tauc plot[139]. A Tauc plot is used to determine optical band gap in amorphous thin films and is a function of quantity of light energy versus light energy.

A modified Tauc plot can be used to determine band gap energies in dissolved medium and is graphically represented in Figure 2.11 where the band gap energy can be read on the abscissa (plotting details and equations given in section 3.1.3.1).

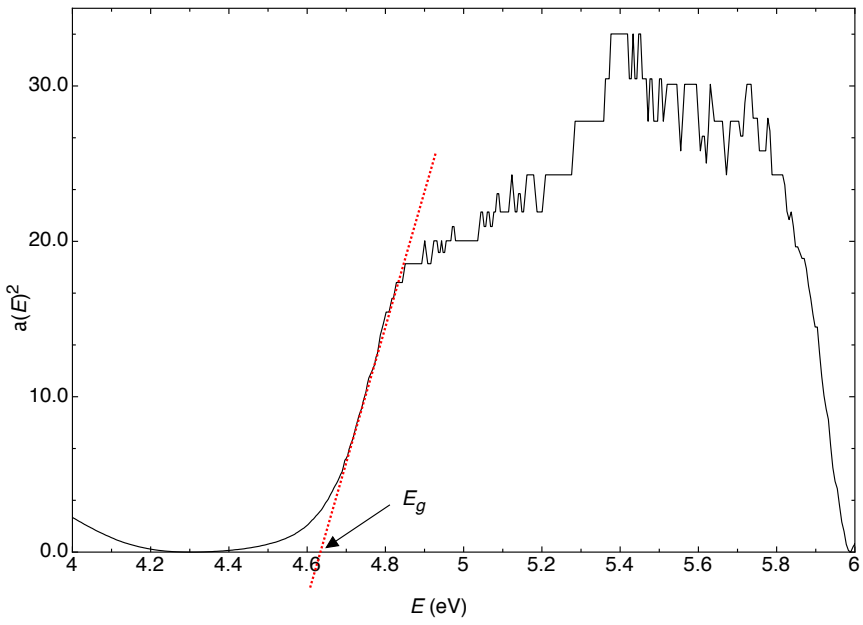

Figure 2.11 Modified Tauc plot of $CeVO_4$

2.2.7. Electrochemical Impedance Spectroscopy (EIS)

Within the family of electrochemical methods available, distinction is made between time domain (such as cyclic voltammetry) and frequency domain methods (like Electrochemical Impedance Spectroscopy – EIS). While the former is commonly used and well established in various fields, the latter is the most used in SOFC studies. EIS has the advantage of measuring a system in thermodynamic equilibrium over a very large frequency range (μHz to GHz nowadays) with very few minor limitations (the equipment constitutes an onerous investment; very low frequencies are more difficult to measure; and, while the measurement is relatively easy, the analysis requires a certain level of experience).

From a mathematical point of view the impedance (resistance in a circuit) is derived from Ohm's Law and represented – when supplied through Alternating Current (AC), hence AC-IS – by Equation 2.5 with its inverse being the admittance (conductivity in a circuit) by Equation 2.6[140].

$$Z(\omega) = \frac{V(\omega)}{I(\omega)} = \frac{V_0 e^{j\omega t}}{I_0 e^{j(\omega t+\varphi)}} = \frac{V_0}{I_0}(\cos\varphi - j\sin\varphi) \qquad \textbf{Eq. 2.5}$$

$$with\ j = \sqrt{-1}\ and\ \omega = 2\pi f$$

$$Y(\omega) = \frac{1}{Z(\omega)} \qquad \textbf{Eq. 2.6}$$

Graphically, the impedance is represented as a Nyquist complex plane plot where both real and imaginary components are displayed according to Equations 2.7 and 2.8 respectively and as represented in Figure 2.12.

$$Z_{real} = Z' = |Z|\cos\varphi \qquad \textbf{Eq. 2.7}$$

$$Z_{imaginary} = Z'' = -j|Z|\sin\varphi \qquad \textbf{Eq. 2.8}$$

In some cases, impedance results are better represented in form of a Bode plot which shows both the absolute resistance and the angular phase as a function of frequency. Bode graphs are often used to gain more accurate information about phenomena encountered when overlapping processes are occurring and is illustrated in Figure 2.12 (B).

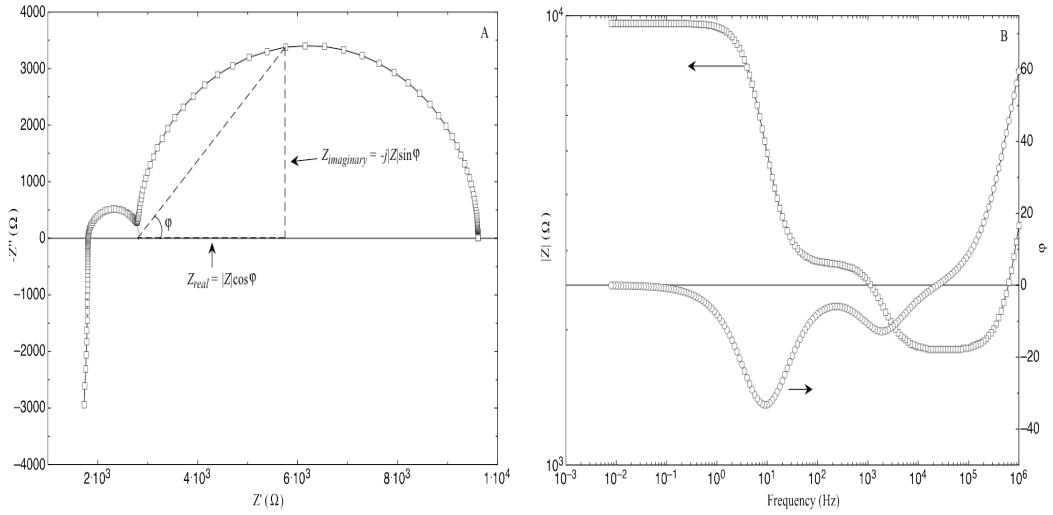

Figure 2.12 Impedance with a 1kΩ resistor in (A) Nyquist plot and in (B) Bode plot

The simplest elements measurable from AC-IS are:

- the overall resistance Z_t = R, representing the electronic and ionic conductivity and the charge transfer resistance

- the capacitance Z_c $(\omega) = (j\omega C)^{-1}$, which can correspond to the redox, dielectric or adsorption capacitance and can be differentiated from its value (Table 2.1)[141]

- the inductance *I*, an electromagnetic force induced by a change in electronic current which opposes that particular change and caused by instrumental issues, broken leads and short circuits

- the Warburg impedance, Z_w which is a kind of resistance to mass transfer and is caused by diffusion to and from the electrode, extending to infinity. Experimentally, it is observed as a line at 45º at high frequencies and is characteristic of dominant ionic

conduction. Finite length diffusion can also occur and appears as a high frequency semicircle

Not all impedance plots show an ideal behaviour however, and complex responses, difficult to analyse are often obtained. This can be often be rationalised by non 45º Warburg's or depressed capacitance and is due to fractal behaviour, that is, the closer it is looked at the less linear it appears.

Non-ideal capacitances are therefore corrected by a Constant Phase Element (CPE) of the form $Z_{CPE}(\omega) = Q^{\circ}(j\omega)^{-n}$ where Q° has the value of admittance Y_{CPE} at ω equals 1 rad.s^{-1}.

Capacitance value (F)	Source or related phenomenon
10^{-12}	Geometric / Bulk
10^{-11}	Minor secondary phase
10^{-11}-10^{-8}	Grain boundaries
10^{-10}-10^{-9}	Bulk ferroelectric
10^{-8}-10^{-7}	Double layer / space charge
10^{-8}-10^{-5}	Surface charge / "adsorbed species"
10^{-7}-10^{-5}	Sample electrode interface
10^{-4}	Electrochemical reaction
1-100	'Closed' pores (chemical capacitance)
~ 1000	'Stoichiometry' changes

Table 2.1 Classification of capacitance value and associated phenomenon

In order then to analyse virtually any impedance spectra, a model is simulated using electrical circuits. The model contains plausible processes occurring within the analysed systems and makes uses of ideal physical elements; namely, inductance (L), resistance (R), capacitance (C), Warburg (W), CPEs (Q). One simple example is the inductance pattern presented in Figure 2.13 in both Nyquist and Bode representation. This behaviour is observed when short circuits occur or if a sample exhibits pure metallic conduction; thereby giving an impedance response similar to the one obtained

by measuring the impedance of a straight wire of conductive nature such as gold, silver and/or platinum. The corresponding equivalent circuit (EC) is given in Figure 2.14.

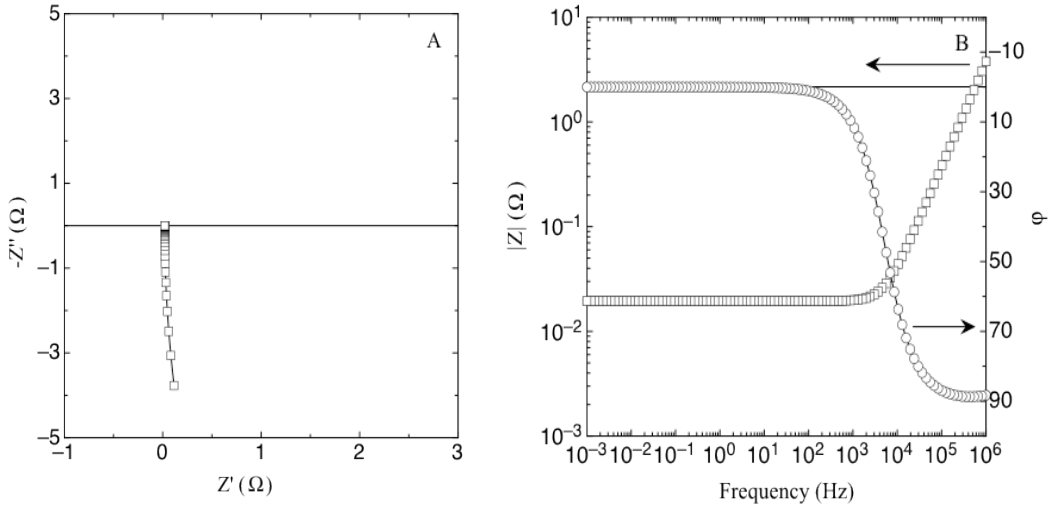

Figure 2.13 Schematic of inductance in (A) Nyquist plot and in (B) Bode plot

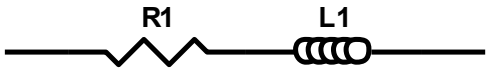

Figure 2.14 Equivalent circuit corresponding to inductance observed

2.2.7.1. Equivalent circuit model

In the same manner as modelling is applied to XRD analysis, fitting the impedance data obtained with a simulated set is possible using an EC model. Models are built according to phenomena that are thought to be happening within the studied systems in order to offer a reasonable explanation as to why the measured patterns are observed. Hence, phenomena happening at the same time are represented in parallel while those occurring one after another are drawn in series. Difficulties are to be expected when overlapping processes are occurring as a multitude of different circuits can then give identical spectra. This latter point is however not restricted to cases of overlapping impedance semicircles, but may also happen due to physical limitation of the measurement where an inductance-like spectrum is obtained due to the system being more conductive than the medium used in the instrument for conduction, thus producing a response which corresponds to an instrumental short-circuit phenomenon often occurring at very high frequencies, >5 x 10^5 Hz. The closer a simulated system is from

the phenomena occurring in the measured system the better the fit. Conventional writing does apply in the form of a circuit description code, thus allowing ECs to be suitable for computer processing with parallel operations bounded by square brackets "[ ]" while distinctive series operations are bounded by standard brackets "( )".

Most frequently used elements are listed in Table 2.2 along with their correlated impedances. Two different types of CPE and Warburg impedances are given as these describe different phenomena. W_s and W_o only differ by the manner their graphical complex plane representation ends, hence the difference between the hyperbolic tangent and cotangent in their mathematical impedance expression with *P* and *T*, diffusion parameters fixed to 0.5 and $\frac{L^2}{D}$, respectively, in case of a Finite Length Warburg (FLW) with *L*, the effective diffusion thickness and *D*, the effective diffusion coefficient of the particle.

Element	Code	Impedance
Capacitor	C	$\frac{1}{j\omega C}$
CPE #1	Q	$\frac{1}{T(j\omega)^P}$
CPE #2 (QPE)		$\frac{1}{(j\omega Q)^n}$
Inductor	L	$j\omega L$
Resistor	R	R
Warburg (short circuit terminus)	W_s	$\frac{R}{[jT\omega]^P}\tanh([jT\omega]^P)$
Warburg (open circuit terminus)	W_o	$\frac{R}{[jT\omega]^P}\mathrm{ctnh}([jT\omega]^P)$

Table 2.2 Common equivalent circuit elements and corresponding impedance

In a more general manner, Z_w can also be expressed using the Warburg constant, Σ with *D*, C^b and *O* and *R* representing the diffusion coefficient, the bulk concentration and the oxidised and reduced forms respectively, as described in Equation 2.9 or, if

limited to high frequencies by removing the hyperbolic tangent and cotangent contributions with Z_0, a closely related expression of Σ as described in Equation 2.10.

$$Z_w = \frac{\Sigma}{\sqrt{\omega}} - j\frac{\Sigma}{\sqrt{\omega}} = \frac{\Sigma(1-j)}{\sqrt{\omega}} \qquad \textbf{Eq. 2.9}$$

$$with\ \Sigma = \frac{RT}{n^2F^2A\sqrt{2}}\left(\frac{1}{\sqrt{D_O}C_O^b} + \frac{1}{\sqrt{D_R}C_R^b}\right)$$

$$\boldsymbol{Z_w = \frac{Z_0}{\sqrt{j\omega}}} \qquad \textbf{Eq. 2.10}$$

Concerning CPEs, CPE #1 and #2 are simply written in different format (CPE #2 adopts Dr. B. A. Boukamp EQUIVCRT program nomenclature) so that parameters *n* and *P* are identical and parameters *Q* and *T* may be translated using a power *n*. The main difference therefore resides in the values of the two parameters during simulation rather than due to fundamentals. If *n* and/or *P* are equal to -1, 0, 0.5 and 1, respectively, it is common practice to consider these particular CPEs as respectively an insulator, a resistor, a Warburg and a capacitor as their equations coincide. However, if *n* is very close to 1, the CPE has a capacitor-like behaviour but the phase angle is not 90˚. This latter is in fact constant and somewhat lower than 90˚ over the entire range of frequencies and should be considered as being a depressed capacitor-like semicircle.

Some common ECs with their impedance in complex plane are presented in Figure 2.15 and 2.16 and show respectively, R(C), RC and C(RC) systems in Figure 2.15 (A), (B) and (C) and (LR)(RC)(RC), W_s(RC) and W_o(RC) in Figure 2.16 (A), (B) and (C) respectively. Values given in the ECs fitting lists are in ohms (**Ω**) for resistors (includes Warburg parameter R), in Farads (F) for capacitors (includes Warburg parameter T) and in Henries (H) for inductors; also note, Warburg's parameter P is dimensionless as simply being an integer number.

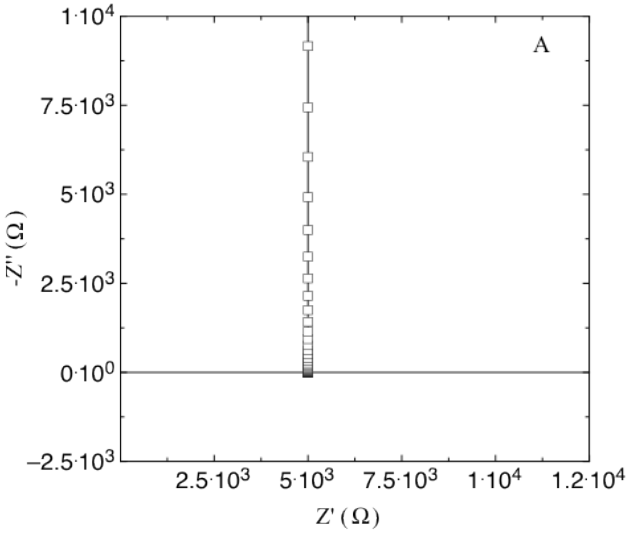

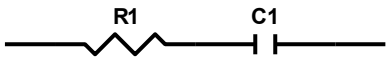

Element	Freedom	Value
R1	Fixed(X)	5000
C1	Fixed(X)	1E-05

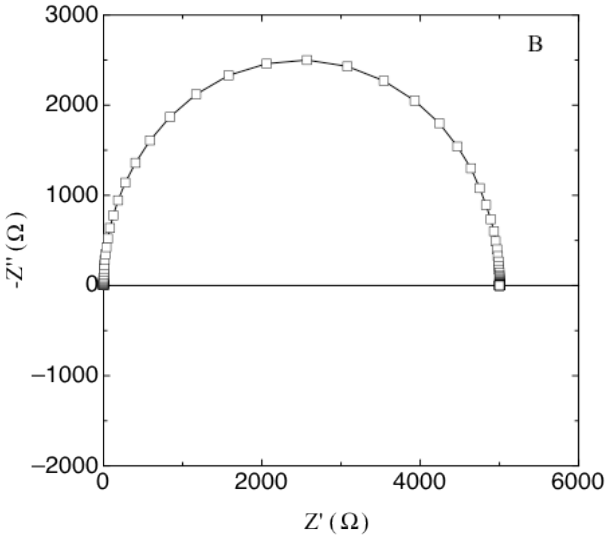

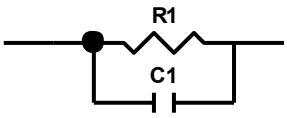

Element	Freedom	Value
R1	Fixed(X)	5000
C1	Fixed(X)	1E-07

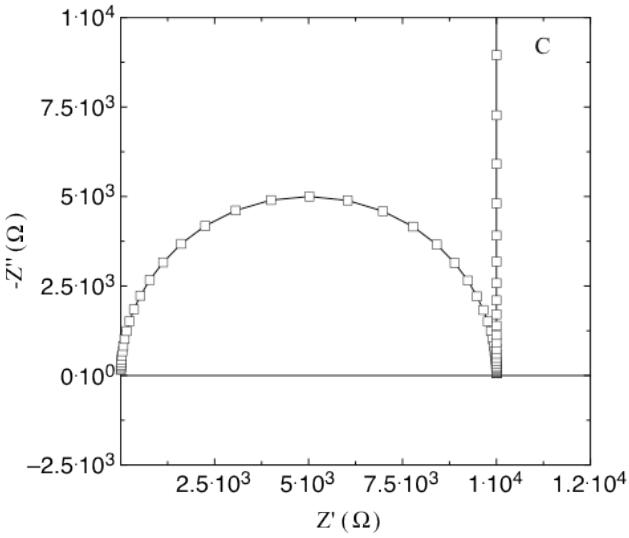

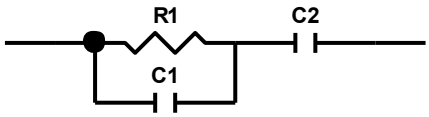

Element	Freedom	Value
R1	Fixed(X)	10000
C1	Fixed(X)	1E-09
C2	Fixed(X)	0.0001

Figure 2.15 Common ECs with representation in the complex plane

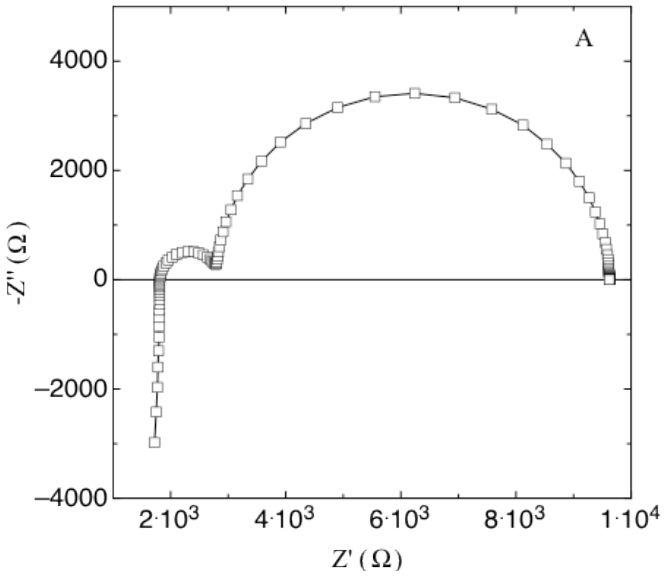

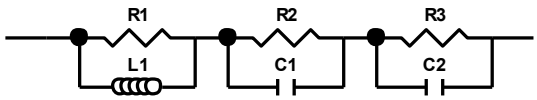

Element	Freedom	Value
R1	Fixed(X)	1807
L1	Fixed(X)	0.000475
R2	Fixed(X)	995
C1	Fixed(X)	1E-07
R3	Fixed(X)	6815
C2	Fixed(X)	4.72E-06

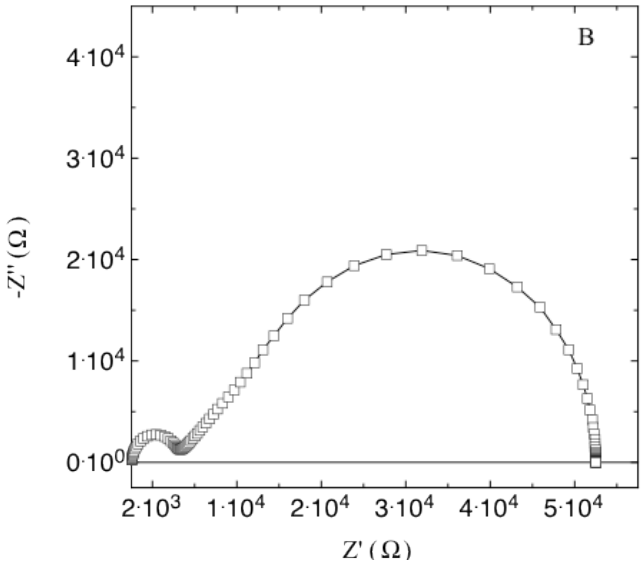

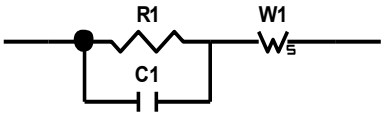

Element	Freedom	Value
R1	Fixed(X)	5000
C1	Fixed(X)	1E-09
W1-R	Fixed(X)	50000
W1-T	Fixed(X)	0.1
W1-P	Fixed(X)	0.5

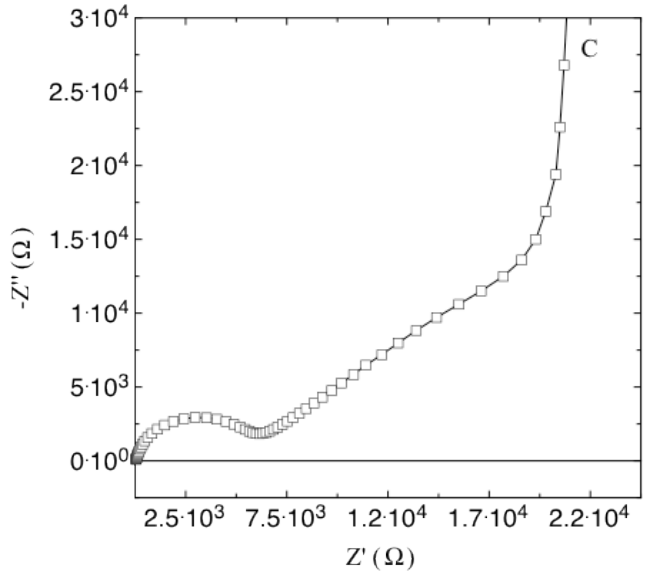

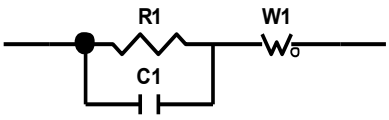

Element	Freedom	Value
R1	Fixed(X)	5000
C1	Fixed(X)	3E-09
W1-R	Fixed(X)	50000
W1-T	Fixed(X)	0.1
W1-P	Fixed(X)	0.5

Figure 2.16 Complex plane representation with ECs of real systems

2.2.7.2. Application of impedance spectra to fuel cells

When applied to individual components of a fuel cell, information obtained from direct current method measurement (DC) is often inaccurate unless the component has a high conductivity (> 1 $S.cm^{-1}$) and is almost never appropriate in case of dominant ionic conduction (like an electrolyte since this would result in a total conductivity lesser than 1 $S.cm^{-1}$). Moreover, if geometric and grain boundary responses are to be differentiated from the main electrode response, AC-IS is necessary. In that case, three points of resistance have to be considered namely, the bulk, the grain boundary (for ceramic-based materials only, i.e. PEMFCs do not exhibit this feature) and the electrode as described in Figure 2.16 (resistance values are given in Ω, capacitances in F, QPE (Q-based CPE) Q parameter in F^n and QPE *n* parameter is dimensionless). In an ideal circuit of a single material bounded by two identical electrodes (Figure 2.17), all resistances will be observed with no overlap; however, in 'real' circuits, RC overlap of different processes will occur with some not being observed due to equipment limitations (mainly because of too high frequencies or inductance).

The total conductivity of a system is defined by the combination of the bulk and the grain boundary resistances (300 Ω for the system shown in Figure 2.17).

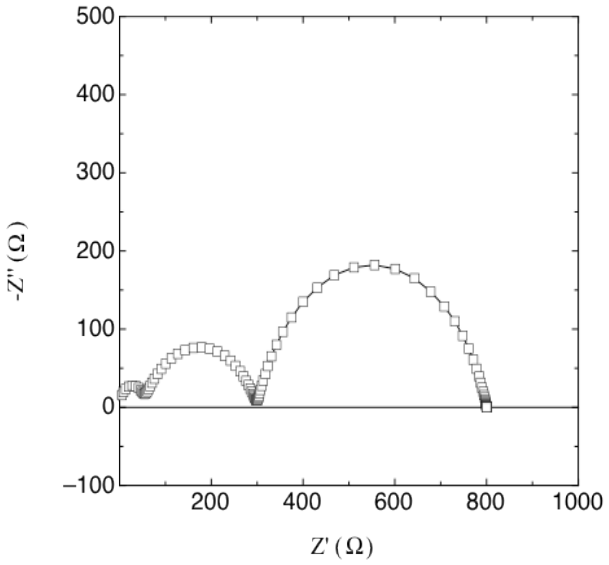

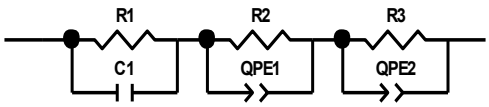

Element	Freedom	Value
R1	Fixed(X)	50
C1	Fixed(X)	1E-12
R2	Fixed(X)	250
QPE1-Q	Fixed(X)	1E-11
QPE1-n	Fixed(X)	0.7
R3	Fixed(X)	500
QPE2-Q	Fixed(X)	1E-06
QPE2-n	Fixed(X)	0.8

Figure 2.17 Impedance response of an ideal three resistances circuit in the complex plane

In SOFCs, the three main resistances observed are the anode, the electrolyte and the cathode in a manner described by the EC in Figure 2.18. Anodic and cathodic resistances (labelled R_{ct} as 'resistances to charge transfer') normally overlap each other unless their time constants (commonly denoted τ as being the transport process occurring when placing a resistor and a capacitor in parallel) differ significantly; however, individual anodic/cathodic behaviour may be elucidated by using a symmetrical FC. Electrodic resistance is also likely to be much higher than that of the electrolyte due to ORH and ORR kinetics.

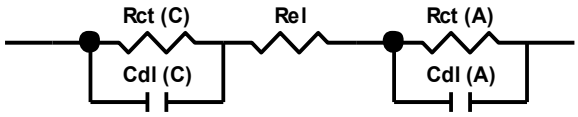

Figure 2.18 General EC for FCs

In PEMFCs, the impedance spectra is dominated by cathodic features due to fast ORH at the anode and high, medium and low frequency phenomena can be observed:

- At high frequency, internal ohmic resistance and contact capacitance in case of a granular electrode structure or limited proton transfer in the electrolyte
- At medium frequency, cathodic loss caused by interfacial kinetics of ORR
- At low frequency, mass transport resistance expressed by open- or closed-circuit termini (W_o or W_s)

In practical terms, AC-IS can be measured in three different ways with their own level of accuracy and are schematically displayed in Figure 2.19. From left to right; the two-electrode measurement, where the influence of cabling is non-negligible (around 6 Ω for 100 kHz and 10 μH); the pseudo 4-point measurement, where inductance is eliminated but an additional capacitance of coaxial cables still exists (twisted cables in the cell reduces the inductance further) and the true 4-point measurement, essential for accurately probing voltages of mixed conductors even though spurious capacitances are still possible[142].

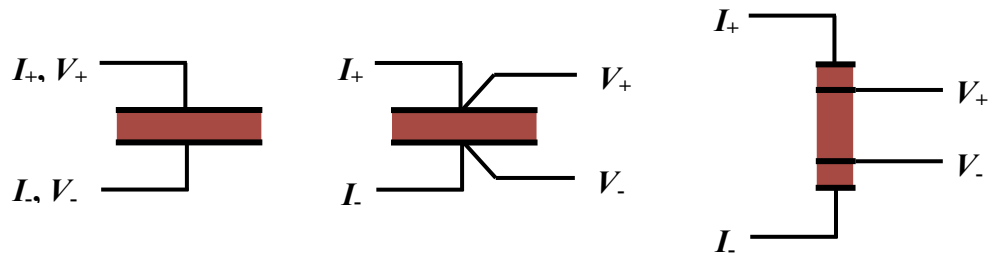

Figure 2.19 Cell connections in AC-IS measurement

EIS is then undoubtedly a very powerful tool; providing more visual information than time domain methods; with analytical expressions almost always available and the ability to analyse very complex systems[143]. With the same configuration, the conductivity can be measured by dc methods, i.e., by applying a constant current through the cell then measuring the voltage drop between the two electrodes, the resistance can be calculated from Ohm's Law and the conductivity via the surface-resistance relation; namely conductivity (σ) is equal to the quotient of the sample thickness (L in mm) by the product of the sample surface area (A in cm^2) and its resistance (R in Ω) as descripted in Equation 2.11 and with it's inverse being the resistivity (ρ in Ω cm).

$$\sigma = \frac{L}{A \cdot R} \qquad \rho = \frac{1}{\sigma}$$

Eq. 2.11

3. Potential of $CeVO_x$ as SOFC electrodes

First studied in the 1950s as part of investigations to determine precise crystal structures[144], atomic arrangements in chemical series and ionic radius of crystals comprising heavy metals[145], Rare-Earth Vanadates ($REVO_4$) have been intensively studied in the last two decades, in particular lanthanoid orthovanadates ($LnVO_4$) and metavanadates ($LnVO_3$) due to the interesting physical properties exhibited by those compounds (luminescence, Jahn-Teller phase transitions, *etc*).

3.1. Cerium orthovanadates

3.1.1. Background

Among the $REVO_4$ exhibiting an ABO_4 structure, two main crystal structures are observed: tetragonal zircon[146] and monoclinic monazite[147]. More generally, larger lanthanoid ions prefer the monazite type while smaller lanthanoids crystallise in the zircon type[148]; thereby, monazite is the most common REE bearing mineral. Interestingly, cerium (III) orthovanadate ($CeVO_4$), which according to phase diagrams is located at the boundary of Zircon (Z) – shown in Figure 3.1 – and Monazite (M) – shown in Figure 3.2 – types, exhibit three polymorphic forms with the pseudo-octahedral looking-like structure of tetragonal Scheelite (S) – shown in Figure 3.3 – in addition to the (Z) and (M) type forms.

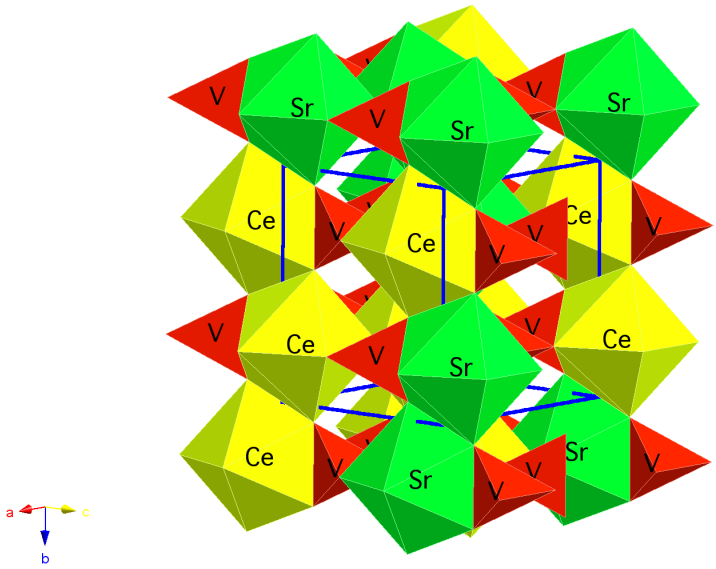

Figure 3.1 Structural representation of $(Ce,Sr)VO_4$ (Z)

Structurally speaking, $CeVO_4$-(Z) is composed of tetragonal bisphenohedra of VO_4, edge-linked to CeO_8 triangular dodecahedra along the c-crystal axis, and VO_4 tetrahedra corner-linked with CeO_8 dodecahedra along the *a*- and *b*-crystal axes. Additionally, channels along the *c*-crystal axis, octagonal in shape, allow the insertion of lithium ions and the use of cerium vanadates in catalytic processes for example[149-151].

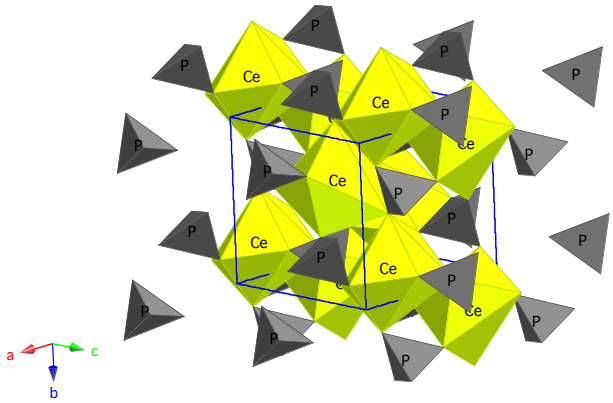

Figure 3.2 Structural representation of $CePO_4$ (M)

In the first studies of heavy metal orthovanadates ($HMVO_4$), researchers started to focus on crystal structures and group theory, looking for answers to explain the specific characteristics obtained when heavy metals and less generally RE elements of the f-block (lanthanoids and actinoids) were mixed with orthovanadates. Based on a synthetic protocol previously established[152], Milligan and Vernon[144] reported structural studies on a group of fifteen $HMVO_4$ among which thirteen were lanthanoids. They demonstrated using X-ray diffraction lines obtained, that the crystals had crystallised in the body-centred tetragonal system, space group $I4_1/amd$.

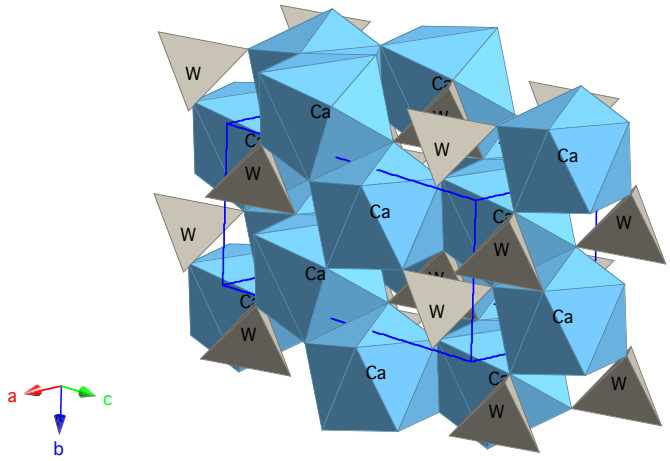

Figure 3.3 Structural representation of $CaWO_4$ (S)

The first study on the electrical and thermal behaviour of $CeVO_4$ as well as infrared studies was reported by Rao and Palanna[153] in 1995, more than twenty years after the IR study of the isostructural $LaVO_4$[154]. Whereas $CeVO_4$ in itself is an insulator whether in pure or stoichiometric composition, a *p*-type semiconductive behaviour between RT and 800 ºC was observed. An explanation given to account for the *p*-type conduction in the lattice was that among the Ce^{3+} ions, coexisted a few number of Ce^{4+} ions and that therefore the conduction was occurring via thermally activated motions of ions on equivalent sites.

In 1999, two linked studies were published on the electrochemical character of $CeVO_4$, the first by Krašovec *et al.*[155] focussed on the cerium/vanadium oxide interface ion-storage films and the second by Picardi *et al.*[156] looked at optically passive $CeVO_4$ counter-electrodes. Electrochemically, it was found that $CeVO_4$ films behave in the same manner as crystalline V_2O_5 films. Electrochemical measurements could not establish any contribution of redox processes involving cerium ions, agreeing with a structure of $CeVO_4$ containing only Ce^{3+} and V^{5+} ions.

Catalytic properties of $CeVO_4$ were also investigated by Coronado *et al.*[157] and by Mahapatra *et al.*[150, 158]. It was found that vanadia surfaces were highly dispersed on ceria in VO_x/CeO_2 catalytic systems and that the product distribution of these latter tends to become similar with $CeVO_4$ structural features as the vanadia load was increased. This behaviour was believed to arise from the existence of a V^{5+}–O–Ce^{3+} bond in both $CeVO_4$ and ceria-supported vanadia. The presence of this particular bond was observed at temperatures as low as 300 ºC while the catalytic range of operation for the oxidation of ethane in that study was from 450 ºC to 610 ºC. Moreover, unlike other supported vanadia catalysts, it was found that the redox cycle occurring during ethane oxidative dehydrogenation reaction appeared to be due, in ceria-supported vanadia, to the presence of cerium sites near vanadium sites; further indicating that vanadium may be regulating cerium oxygen site lability. This would be of great significance by allowing the formation and the growth of $CeVO_4$ directly from V/CeO_2 catalytic systems at temperatures lower than those achieved up-to-date in air.

In the last decade, doped *RE*VO_4 have also being studied, particularly lanthanide and cerium orthovanadates doped with other *RE*[159] or with elements like calcium[151, 160-164], iron[151, 165, 166], bismuth[163, 164] or strontium[160-162, 164] notably.

3.1.2. Experimental

3.1.2.1. Materials and properties

Cerium dioxide (CeO_2 Alfa-Aesar, 99.9% REO), vanadium pentoxide (V_2O_5 Aldrich, 99.6+% metals basis), calcium carbonate ($CaCO_3$ Alfa-Aesar, ACS 99.0% min) and strontium carbonate ($SrCO_3$ Aldrich, 99.95% metal basis) were used as received.

Pure, non-doped cerium orthovanadates were synthesised by a solid-state method using CeO_2 and V_2O_5 as cerium and vanadium sources. Stoichiometric amounts of the respective oxides were fired at 800 ºC at a heating rate of 5 ºC min^{-1} for a dwelling time of 50 hrs. $Ce_{1-x}Sr_xVO_4$ compounds were synthesised by a solid-state method using CeO_2, V_2O_5 and $SrCO_3$ as cerium, vanadium and strontium sources and $Ce_{1-x}Ca_xVO_4$ compounds were synthesised using CeO_2, V_2O_5 and $CaCO_3$ as cerium, vanadium and calcium sources.

For the Sr-doping syntheses, stoichiometric amounts of the respective oxides were fired at 950 ºC at a heating rate of 5 ºC min^{-1}, maintained for 66 hrs and cooled down to RT at the same rate of 5 ºC min^{-1}. Powders were then re-ground and fired at 1000 ºC at a heating rate of 5 ºC min^{-1}, dwelled for 72 hrs before being quenched. x was varied from 0.1 to 0.4 and a pure phase was obtained with $x \leq 0.175$.

For the Ca-doping syntheses, stoichiometric amount of the respective oxides were fired at 850 ºC or at 900 ºC – depending on the doping factor – at a heating rate of 5 ºC min^{-1} and maintained for 66 hrs. x was varied from 0.1 to 0.7 and a pure phase was obtained with $x \leq 0.4125$.

3.1.2.2. Characterisation and conductivity

3.1.2.2.1. UV-vis absorption

The band gaps at RT of all synthesised compounds were determined graphically from spectra obtained using a UV–vis spectrophotometer (Shimadzu UV-2550) operating with UVProbe® software.

3.1.2.2.2. Powder x-ray diffraction

X-ray data were collected on a Bruker-AXS (D8 Advance) machine, controlled by DIFFRACT$^{plus\ TM}$, in the Bragg-Brentano reflection geometry with a Cu Kα source, fitted with a LynxEye^{TM} detector.

Absolute scans in the 2θ range of 5-85º with step size of 0.009º and time step of 61.6 s or 123.2 s were used during data collection.

3.1.2.2.3. Thermal analysis

Thermogravimetry and differential scanning calorimetry (TG/DSC) analyses were performed using a Stanton Redcroft STA/TGH series STA 1500 operating through a Rheometric Scientific system interface controlled by the software RSI Orchestrator up to 1000 ºC (calcium-doped) and 1200 ºC (non-doped and strontium-doped) at 5 ºC min^{-1} for analyses in air and up to 750 ºC at 5 ºC min^{-1} for reduced atmosphere analyses.

3.1.2.2.4. Scanning electron microscopy

SEM pictures were taken with the use of a Quanta 3D FEG scanning electron microscope (FEI Company) with usual voltages of 10 kV and 10 pA.

3.1.2.2.5. Conductivity

Total conductivity measurements were carried out using a computer-controlled Solartron Analytical® SI 1260 impedance/gain phase analyser over a frequency range of 1 MHz to 0.01 Hz and a temperature range of 600 ºC (700 ºC for Ca-doped in air) to RT (~ 25 ºC) and impedance data were recorded with the Solartron Impedance Measurement software, SMaRT^{TM}.

Sample powders were pressed into pellets and sintered at temperatures depending on the sample themselves for 12 hrs (650 ºC for $CeVO_4$, 850 ºC for Ca-doped and 900 ºC for Sr-doped). The relative densities of the samples were ~ 75-86%. Pellets were coated with silver paste for measurements in air and with platinum paste for measurements in 5% H_2-Ar dried through a 98% solution of H_2SO_4. Pellets coated

with silver paste were directly fitted into the measuring apparatus while platinum coated samples were fired at 850 ºC at a rate of 5 ºC min^{-1}, dwelled for two hrs and cooled down before being used for pseudo 4-probe AC-IS. Measurements in air were carried out on heating and those in reduced atmosphere on cooling after stabilisation was achieved. The sample dwelled at each temperature for at least 30 mins to reach a stabilised state before conductivity measurements.

3.1.2.2.6. Hydrogen/Air electrochemical cell measurement

Pellets used for cell measurements were coated with platinum electrodes and fired at 850 ºC for 1 hr in air. Dry 5% H_2-Ar is passed through 98% H_2SO_4 before feeding the anode side of the cell while the cathode is exposed to ambient air. The Open Circuit Voltage (OCV) of the electrochemical cell was measured using a Solartron 1287 electrochemical interface controlled by CorrWave/CorrView® for automatic data collection.

3.1.2.2.7. Dilatometry

Dilatometric measurements were carried out using a Netzsch DIL 402 PC running under Proteus® software up to temperature of 1000 ºC in flowing air (50 ml min^{-1}) with a ramp up and down of 5 ºC min^{-1} on selected samples.

3.1.3. Strontium-doped cerium orthovanadate results and discussion

3.1.3.1. Crystal structure

Single phase powders of strontium-doped cerium orthovanadate were obtained up to a doping of 17.5% with strontium pyrovanadate ($Sr_2V_2O_7$) forming as secondary phase when doping exceeding 17.5% (Figure 3.4 (a) and (b)). Rietveld refinements were carried out using GSAS[136] with both structural and shape profile parameters being varied with initial values for the zircon structure used as mentioned in the literature[148]. Wyckoff sites assigned to Ce and Sr, V and O were 4*a*, 4*b* and 16*h*, respectively. Vanadium and oxygen were considered with full occupancies during the refinement processes whereas cerium and strontium occupancies were varied in accordance with

the stoichiometry. A typical GSAS refinement pattern for $Ce_{0.95}Sr_{0.05}VO_4$ is shown in Figure 3.5 with the experimental (crossed) and calculated (solid line) profiles and the differential at the bottom of the pattern. The refined parameters are listed in Table 3.1 and 3.2.

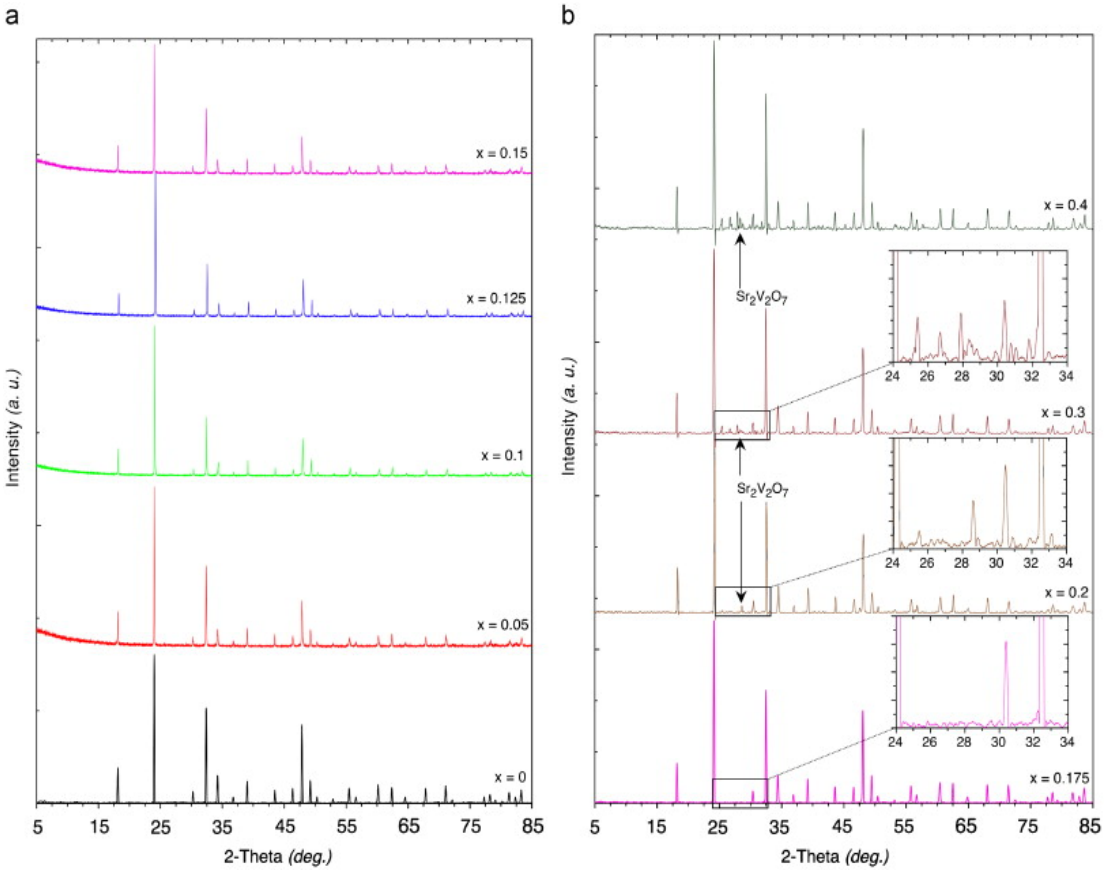

Figure 3.4 XRDs of $Ce_{1-x}Sr_xVO_4$ with (a) $0 \leq x \leq 0.15$ and (b) $0.175 \leq x \leq 0.4$

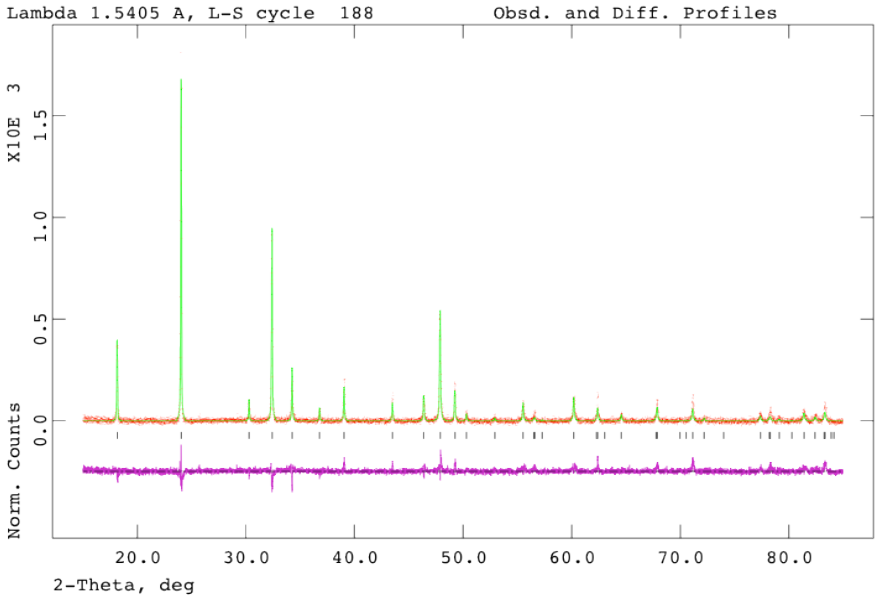

Figure 3.5 Representation of a typical GSAS refinement for $Ce_{0.95}Sr_{0.05}VO_4$

Crystallographic parameter	$CeVO_4$	$Ce_{0.95}Sr_{0.05}VO_4$	$Ce_{0.9}Sr_{0.1}VO_4$
r Ln^{3+} (VIII) (Å)	1.143[167]		
λ (Å)	1.5405		
Crystal system	Tetragonal		
Space group	$I4_1/amd$		
a (Å)	7.4004 (1)	7.3940 (1)	7.3779 (2)
c (Å)	6.4982 (6)	6.4972 (2)	6.4905 (2)
V (Å^3)	355.88 (5)	355.21 (3)	353.30 (1)
ρ_{calc} (g.cm^{-3})	4.7601	4.7200	4.6962
Rp (%)	7.9	11.6	10.9
wRp (%)	10.0	14.8	13.8
χ^2	1.400	1.453	1.494

Table 3.1 Crystallographic refinement parameters of $Ce_{1-x}Sr_xVO_4$ with $0 \leq x \leq 0.1$

Crystallographic parameter	$Ce_{0.875}Sr_{0.125}VO_4$	$Ce_{0.85}Sr_{0.15}VO_4$	$Ce_{0.0.825}Sr_{0.175}VO_4$
r Ln^{3+} (VIII) (Å)	1.143[167]		
λ (Å)	1.5405		
Crystal system	Tetragonal		
Space group	$I4_1/amd$		
a (Å)	7.3733 (1)	7.3690 (2)	7.3670 (3)
c (Å)	6.4914 (2)	6.4886 (3)	6.4894 (1)
V (Å^3)	352.91 (1)	352.35 (1)	352.20 (2)
ρ_{calc} (g.cm^{-3})	4.6767	4.6595	4.6367
Rp (%)	11.6	9.6	8.3
wRp (%)	14.9	12.8	10.6
χ^2	1.898	2.707	1.299

Table 3.2 Crystallographic refinement parameters of $Ce_{1-x}Sr_xVO_4$ with $0.125 \leq x \leq 0.175$

All single phase powders obtained (up to the solid solution limit of $x = 0.175$) exhibited a zircon tetragonal structure, crystallising in the space group $I4_1/amd$. As

shown in Table 3.1 and 3.2, the unit cell volume is decreasing as the dopant concentration is increased. However, while *a* is decreasing through the whole series, *c* slightly increases after a minimum at $x = 0.1$ (as represented in Figure 3.6).

This behaviour can be explained by the distortions occurring as a consequence of the insertion of strontium ions. Indeed, Sr^{2+} ions are much larger than Ce^{3+} ions (1.40 and 1.143 Å respectively)[167]. One could then argue this difference should influence the observed average bond lengths within the unit cell, but as shown in Table 3.3, Ce/Sr–O and V–O interatomic distances keep decreasing as the dopant concentration is increased.

However, while decreasing, V–O bond lengths correlate with the ionic bond length of 4–2-coordinated V^{5+}–O^{2-} couple, whereas Ce/Sr–O bond lengths are not representative of the 8–2-coordinated Ce^{3+}/Sr^{2+}–O^{2-} couple. In fact, these are smaller than expected if it is considered that the insertion of larger ions into the lattice –where all cerium sites are occupied by Ce^{3+} ions– should increase the interatomic distances between cerium and oxygen. As this is not the case, the possibility of the formation of Ce^{4+} ions to compensate the charge loss introduced by the insertion of a 2^{+} ion may be considered.

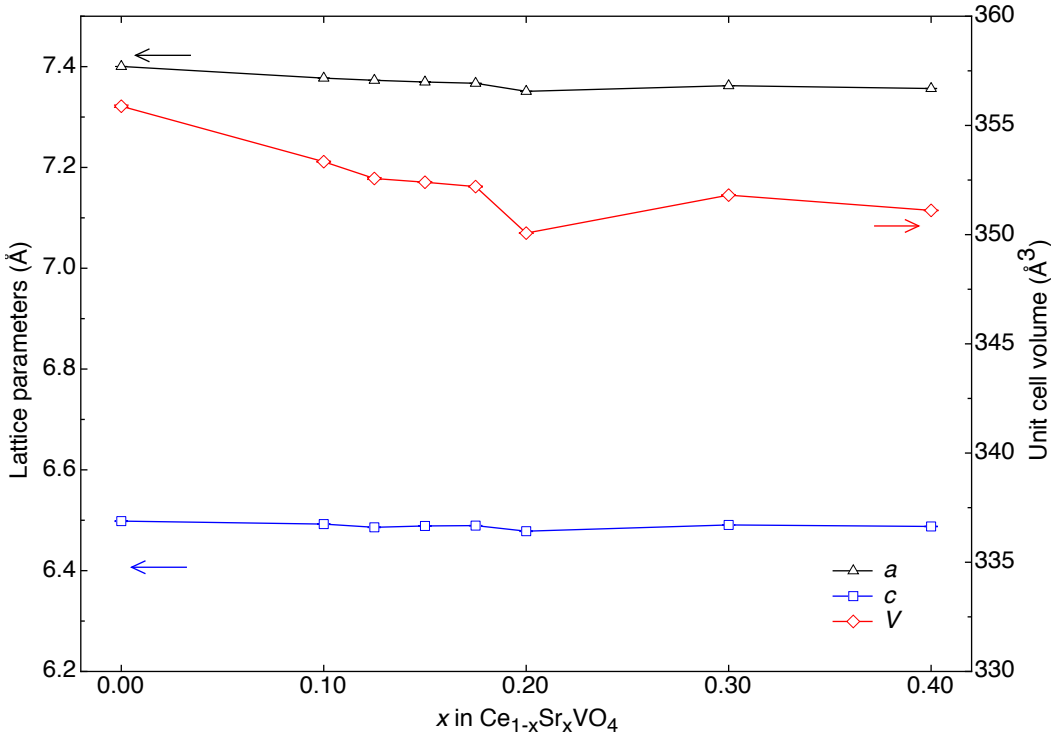

Figure 3.6 Lattice parameters and volume reduction in $Ce_{1-x}Sr_xVO_4$ with $0 \leq x \leq 0.4$

By considering the average bond lengths of Ce–O as being an average of both Ce^{3+}–O^{2-} and Ce^{4+}–O^{2-} combinations, the fraction of Ce^{4+} ions present in each compound can be determined using Equations 3.1 and 3.2 below. From Equation 3.1 the fraction of Ce^{4+} ions (y_{sp}) occupying the Ce-site within the structure that are actually occupied by cerium atoms can be calculated; whereas Equation 3.2 provides the overall fraction of Ce^{4+} ions (y_o) contained within each compound considering the total number of Ce-sites, even if some are in fact occupied by strontium atoms (with *b.l.* standing for *bond length*).

$$y_{sp_{Ce_{1-x}Sr_xVO_4}}(\%) = \frac{\left[\frac{(Ce-O\ b.l.)-(Sr^{2+}-O^{2-}b.l.)\times x}{1-x}\right]-(Ce^{3+}-O^{2-}b.l.)}{(Ce^{4+}-O^{2-}b.l.)-(Ce^{3+}-O^{2-}b.l.)}\times 100 \qquad \textbf{Eq. 3.1}$$

with $(Sr^{2+}-O^{2-}b.l.) = 2.61$ Å , $(Ce^{3+}-O^{2-}b.l.) = 2.493$ Å,

$(Ce^{4+}-O^{2-}b.l.) = 2.32$ Å

$$y_{o_{Ce_{1-x}Sr_xVO_4}}(\%) = y_{sp_{Ce_{1-x}Sr_xVO_4}}\times(1-x) \qquad \textbf{Eq. 3.2}$$

Once the fraction of Ce^{4+} is determined, it can be used in the crystal electroneutrality law[162] in order to determine the hyperstoichiometric factor of oxygen δ within $(Ce^{3+}_{1-y}Ce^{4+}_{y})_{1-x}Sr_xVO_{4\pm\delta}$ using Equation 3.3,

$$\delta = \frac{y_{sp}-x-xy_{sp}}{2} \qquad \textbf{Eq. 3.3}$$

Average bond lengths obtained from the refinements are listed in Table 3.3 with the Ce-O bond lengths averaged between Ce-O1 and Ce-O2 interatomic distances.

It can be seen that the overall fraction of Ce^{4+} ions is comprised between 5% in non-doped cerium orthovanadate and just below 22% at the doping limit. It can also be noticed that the major increase is occurring from a state where the dopant is absent to a

state where the doping level is 0.1. This kind of trend, suggestive of a plateau concentration of Ce^{4+} reflects on the variations of Ce/Sr–O bond lengths as well as on the variations of the lattice parameter *a*.

	$x = 0$	$x = 0.05$	$x = 0.1$	$x = 0.125$	$x = 0.15$	$x = 0.175$
Ce-O (Å)	2.4839 (2)	2.4825 (1)	2.4782 (3)	2.4773 (2)	2.4760 (2)	2.4758 (1)
V-O (Å)	1.7115 (1)	1.7105 (1)	1.7076 (2)	1.7071 (2)	1.7062 (1)	1.7060 (2)
y_{sp} (%)	5.26 (1)	9.95 (2)	17.01 (4)	20.03 (3)	23.49 (5)	26.40 (3)
y_o (%)	5.26 (2)	9.45 (2)	15.32 (3)	17.53 (2)	19.97 (1)	21.78 (3)
δ	0.03 (4)	0.02 (2)	0.02 (4)	0.01 (4)	0.01 (1)	0.02 (1)

Table 3.3 Average bond lengths, Ce^{4+} ions and oxygen δ in $Ce_{1-x}Sr_xVO_4$ with $0 \leq x \leq 0.175$

Values for the hyperstoichiometry of oxygen are very limited in Sr-doped compounds ranging from +0.03 to +0.02; indicating the presence of hyperstoichiometric anions within the lattice.*

Band gap energy values for Sr-doped compounds, determined from UV-Visible absorption spectra are shown in Table 3.4. Graphically, band gap energies are determined using Equation 3.4, assuming Equation 3.5.

$$\alpha(E)_{measured} = -\frac{1}{d}\ln\left(\tau_{normalised}(E)\right) \qquad \textbf{Eq. 3.4}$$

with $\alpha\,(E)_{\text{measured}}$, the absorption coefficient; *d*, the sample thickness and τ, the normalised transmittance energy.

$$\alpha(E) \propto \sqrt{E - E_g} \qquad \textbf{Eq. 3.5}$$

with E_g, the band gap energy.

* Hyperstoichiometric values for oxygen ions were not taken into account in the GSAS refinement processes due to the lack of accuracy of the XRD data for such small variations. Neutron-scattering experiments could help to resolve this matter but were not performed.

According to Equation 3.5, $\alpha(E)$ has a square-root dependence on E. Consequently, $\alpha(E)^2$ has a linear dependence on E. Thus, plotting $\alpha(E)^2$ against E and extrapolating the linear measurement to zero, the value of the band gap is obtained.

More in details, solutions of known concentration were prepared for each sample represented in Figure 3.7. UV scans were performed and data obtained were used to determine E_g through a multi-steps procedure involving conversion of absorbance into transmittance, normalisation, the determination of energy values in electron volt from the wavelengths, the calculation of $\alpha(E)$ and subsequently of $\alpha(E)^2$ from Equation 3.4 and the extraction of the band gap energy values from the plots of $\alpha(E)^2$ against E. The values obtained from the extrapolation – tabulated in Table 3.4 – show that at RT, $Ce_{1-x}Sr_xVO_4$ with $0 \leq x \leq 0.175$ compounds are insulators, as expected.

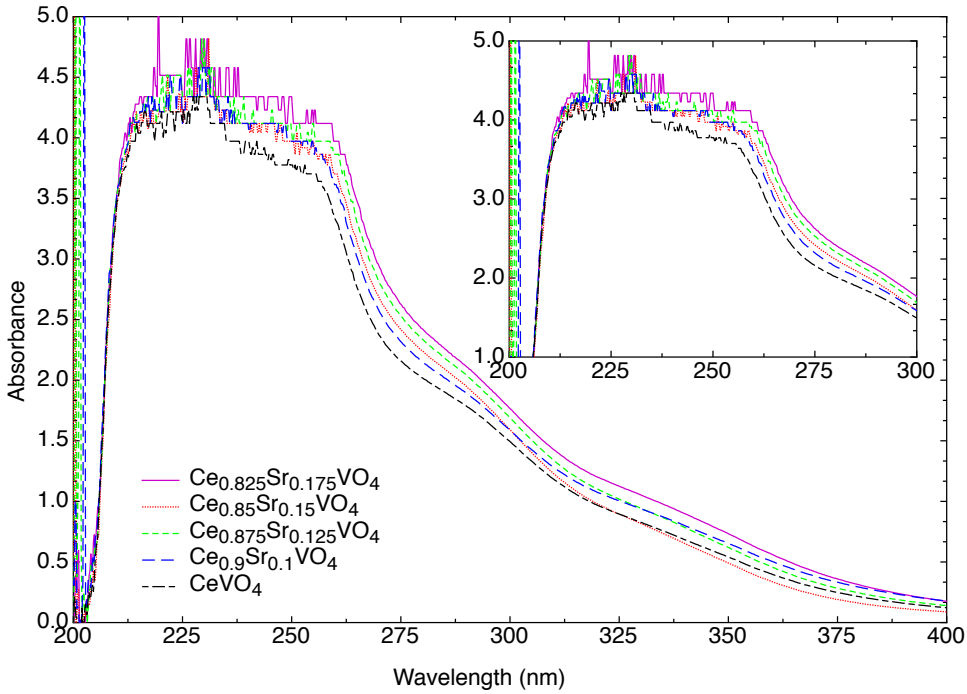

Figure 3.7 UV-vis absorbance spectra of $Ce_{1-x}Sr_xVO_4$ with $0 \leq x \leq 0.175$

Composition	E_g (eV)
$CeVO_4$	4.635 (2)
$Ce_{0.95}Sr_{0.05}VO_4$	4.630 (1)
$Ce_{0.9}Sr_{0.1}VO_4$	4.615 (3)
$Ce_{0.875}Sr_{0.125}VO_4$	4.580 (4)
$Ce_{0.85}Sr_{0.15}VO_4$	4.590 (1)
$Ce_{0.825}Sr_{0.175}VO_4$	4.555 (3)

Table 3.4 Band gap energies of $Ce_{1-x}Sr_xVO_4$ with $0 \leq x \leq 0.175$

3.1.3.2. Thermal analysis

Thermal stability of the compounds was verified by carrying out TG/DSC measurements in both air and 5% H_2-Ar with traces shown in Figure 3.8 and 3.9 respectively for the non-doped and 17.5% doped cerium orthovanadate.

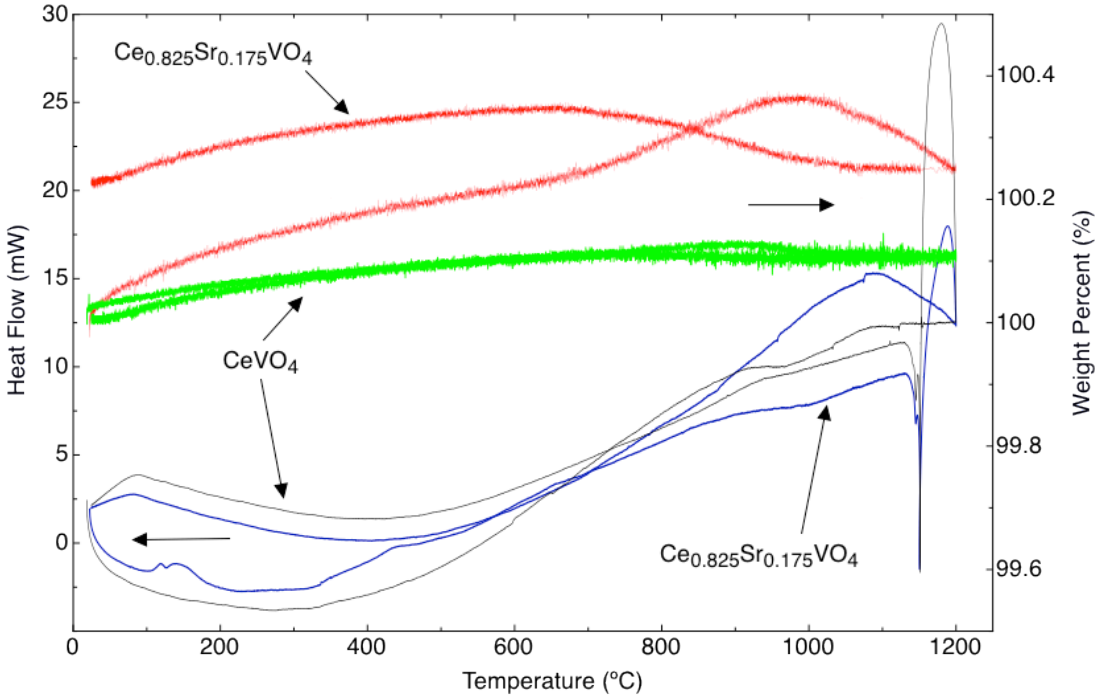

Figure 3.8 TG/DSC curves in air of $CeVO_4$ and $Ce_{0.825}Sr_{0.175}VO_4$

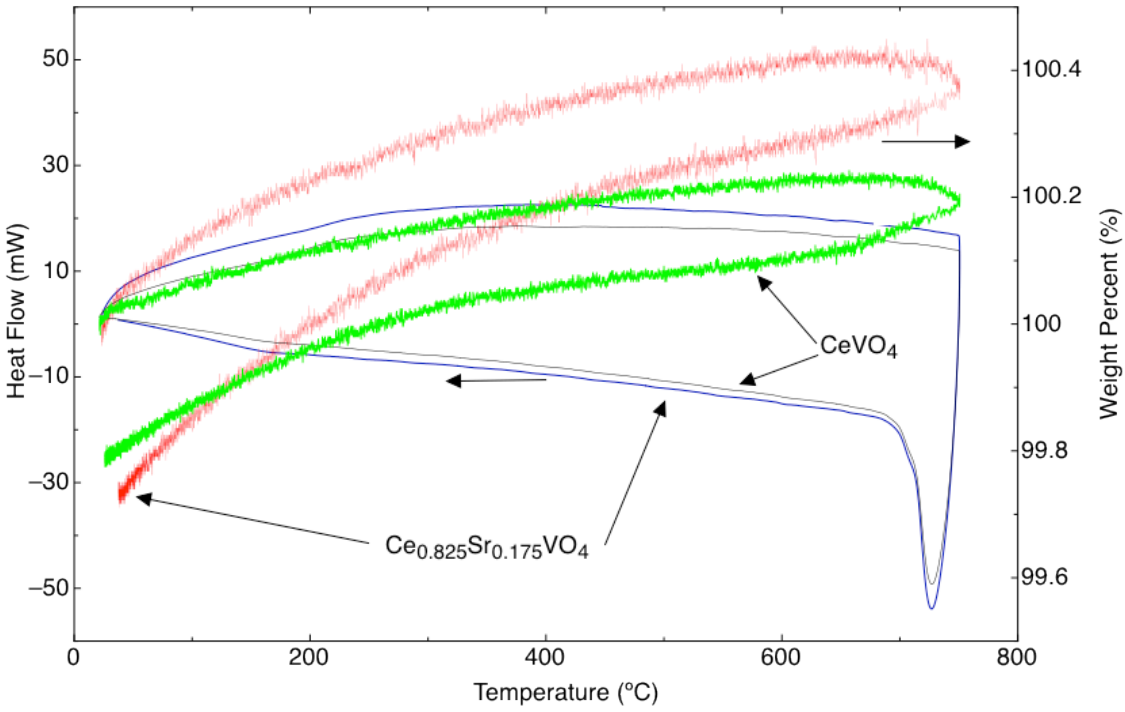

Figure 3.9 TG/ DSC curves in 5% H_2-Ar of $CeVO_4$ and $Ce_{0.825}Sr_{0.175}VO_4$

As can be seen, there is no significant change in weight as observed for similar compounds by Tsipis *et al.*[161] with small variations for the doped sample due to the decomposition of the zircon tetragonal structure forming cerium oxide as suggested by Tsipis *et al.*[162] through the transformation of the zircon phase into the scheelite phase of cerium orthovanadate. The absence of weight losses in reduced atmosphere suggests that within the considered range of temperature, no transformation occurs and the compounds can therefore be considered as being fully stable in both oxidising and reducing atmosphere within the studied range of temperatures.

3.1.3.3. Microstructure

Microstructurally speaking, the doping with strontium and the sintering of the corresponding pellets results in densification values high enough to be mechanically sound (as no cracking is observed) and porous enough to allow reactivity as shown in Figure 3.10 by SEM images.

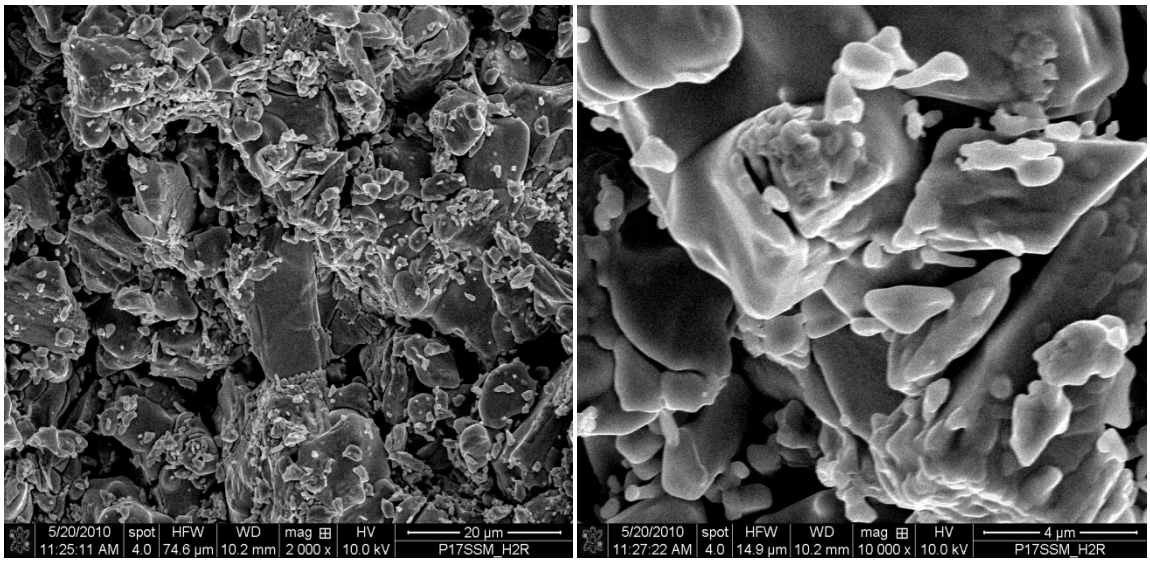

Figure 3.10 SEM images of $Ce_{0.825}Sr_{0.175}VO_4$ at magnification x2000 and x10000

3.1.3.4. Conductivity

Values obtained from the conductivity measurements were used to plot the natural logarithm of the product of the conductivity with temperature expressed in $S.K.cm^{-1}$ against the quotient of a thousand over temperature expressed in K^{-1}. This Arrhenius type plot allows the extraction of the activation energy from the slope of the

line obtained and the Arrhenius pre-exponential factor from the intercept as expressed in the following equations:

$$slope = -\frac{E_a}{R} \qquad \textbf{Eq. 3.6}$$

with R = gas constant

$$intercept = \ln A$$

Conductivity results expressed in the form of Arrhenius plots are shown in Figure 3.11 and 3.12 for $Ce_{1-x}Sr_xVO_4$ compounds in air and 5% H_2-Ar respectively and the activation energies are listed in Table 3.5.

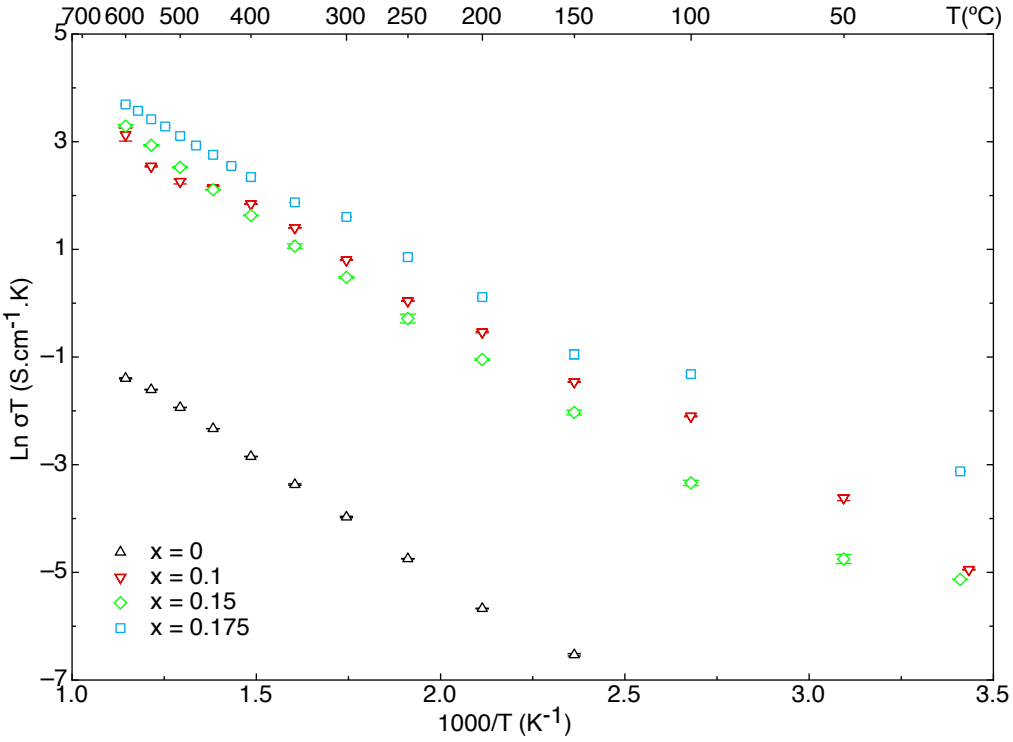

Figure 3.11 Arrhenius plots of the conductivity in air of $Ce_{1-x}Sr_xVO_4$ with $0 \leq x \leq 0.175$

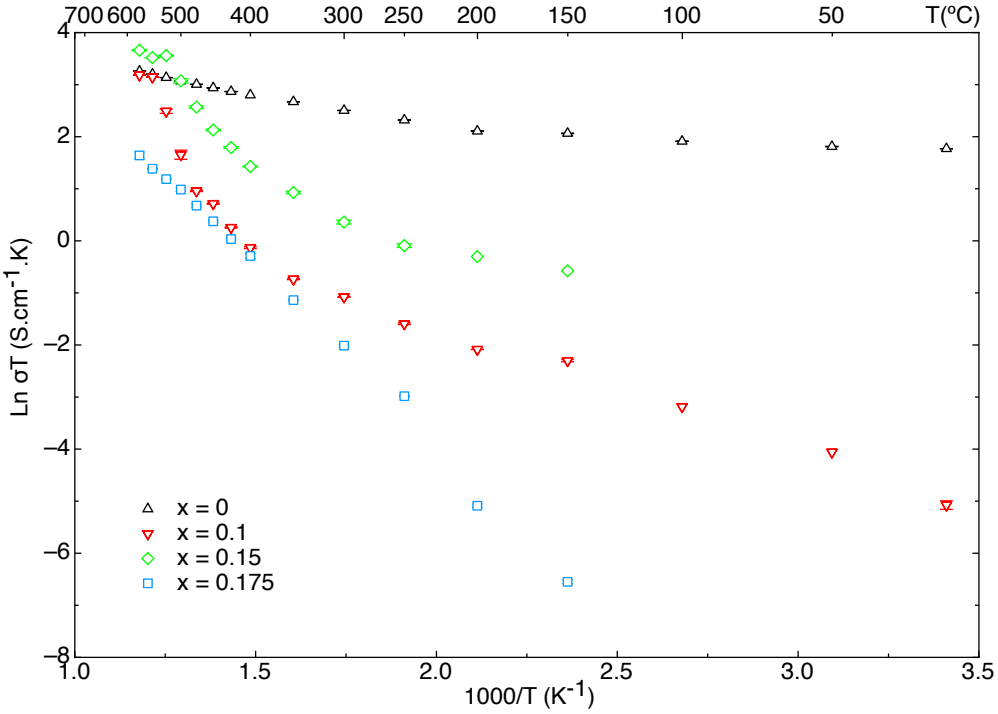

Figure 3.12 Conductivity plots in 5% H_2-Ar of $Ce_{1-x}Sr_xVO_4$ with $0 \leq x \leq 0.175$

E_a in kJ.mol^{-1} A in S.K.cm^{-1}			$x = 0$	$x = 0.1$	$x = 0.15$	$x = 0.175$
Air		E_a	36.3 ± 0.3	28.3 ± 0.4	32.3 ± 0.7	25.4 ± 0.2
		A	38.4 ± 1.1	878.80 ± 0.4	1654.5 ± 1.2	1254.5 ± 1.0
dry 5% H_2-Ar	High Temp.	E_a	10.6 ± 0.2	115.2 ± 7.5	75.2 ± 6.5	49.2 ± 1.3
		A	112.3 ± 1.0	$3.7.10^8$ ± 3.1	$2.4.10^6$ ± 2.8	$5.0.10^3$ ± 1.0
	Low Temp.	E_a	2.3 ± 0.2	20.7 ± 0.7	12.4 ± 1.8	NA
		A	14.8 ± 1.1	30.9 ± 1.2	17.7 ± 1.5	NA
	Approx. Temp. Border (°C)		575	575	525	NA

Table 3.5 Arrhenius constants and activation energies in $Ce_{1-x}Sr_xVO_4$*

It can be seen in Figure 3.11, that the doping of $CeVO_4$ with strontium did improve the conductivity of the compounds in comparison with the non-doped sample independently of the temperature. Variations of conductivity values within the doped

* E_a and A values in air (extracted from the slope and the intercept of results exhibiting no phase transition) correlate to the values obtained in 5% H_2–Ar at high temperature. Low temperature values in 5% H_2–Ar have no correlations in air.

compounds were found to be very small indicating that the conductivity increase is independent of the dopant concentration.

$Ce_{1-x}Sr_xVO_4$ compounds with $0 \leq x \leq 0.15$ were found to be stable in air up to the measured temperature of 600 ºC, exhibiting a metallic behaviour around 550 ºC (Figure 3.13). Consequently, activation energies for samples in air (Table 3.5) were found to be similar while still lower for doped species compare to $CeVO_4$.

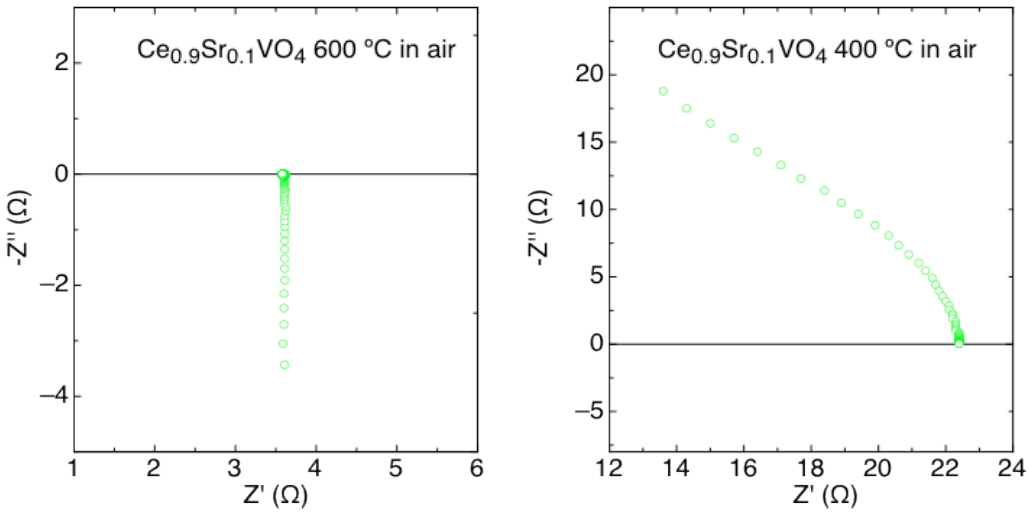

Figure 3.13 Emphasis of *p*-type conduction in $Ce_{0.9}Sr_{0.1}VO_4$ in air

Considering measurements in dry 5% H_2-Ar, it can be observed in Figure 3.12 that the general conductivity of doped $CeVO_4$ compounds were similar or increased; ranging from 30 to 45 $mS.cm^{-1}$ at reduced oxygen pressure compared to around 30 $mS.cm^{-1}$ in air. The maximum conductivity of $CeVO_4$ at 600 °C jumps from 0.3 to 30 $mS.cm^{-1}$ in air and in dry hydrogen atmosphere, respectively, indicating *n*-type conduction which could be related to the reduction of Ce^{4+} or/and V^{5+} cations. While the dopant concentration had little influence on the conductivity in air, it can be observed that in reduced atmosphere the higher the doping level, the lower the overall conductivity at a temperature below 500 °C. In comparison with values in air, the lower conductivity of Sr-doped $CeVO_4$ in reducing atmosphere tends to indicate *p*-type conduction at low pO_2, as it is the case in a similar compound, $CeNbO_{4+\delta}$ [168]. Reversible phase transitions were observed for all compounds at temperatures between 200 and 400 ºC resulting in an observed metallic behaviour during conductivity measurements at about 550 ºC which corresponds to a transition from a semi-conductive to a purely metallic state (Figure 3.14).

All samples within the solid solution limit were found to be redox stable during conductivity measurements up to 600 °C with an example given in Figure 3.15. As can be seen, patterns of $Ce_{0.825}Sr_{0.175}VO_4$ are almost unchanged upon reduction and the sample can therefore be considered as being redox stable below 600 °C. Its lattice expansion on reduction is believed to be due to the reduction of both cerium and vanadium ions because both the Ce–O and V–O bond lengths increased in the reduced sample. The bond lengths extracted from the pattern are 2.5248 Å for Ce–O (average) and 1.7309 Å for V–O compared with 2.4758 Å for Ce–O (average) and 1.7060 Å for V–O before the conductivity measurement.

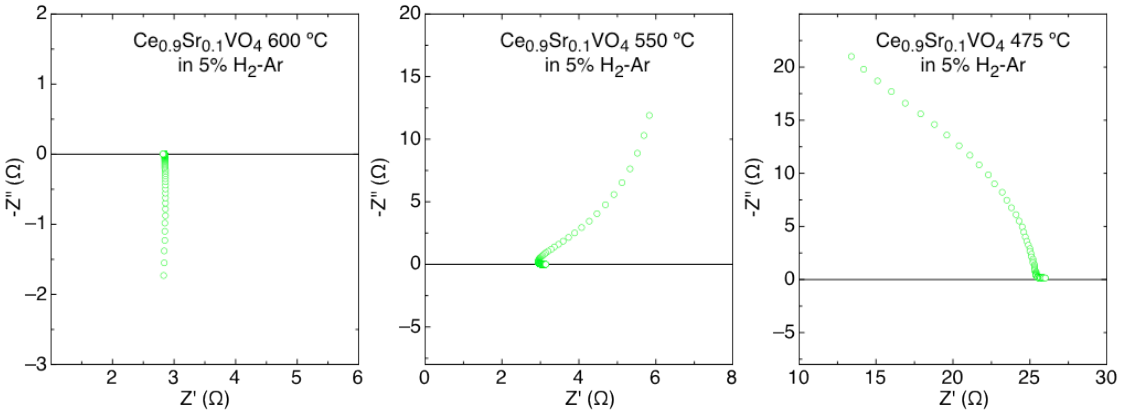

Figure 3.14 Emphasis of *p*-type conduction in $Ce_{0.9}Sr_{0.1}VO_4$ in 5% H_2-Ar

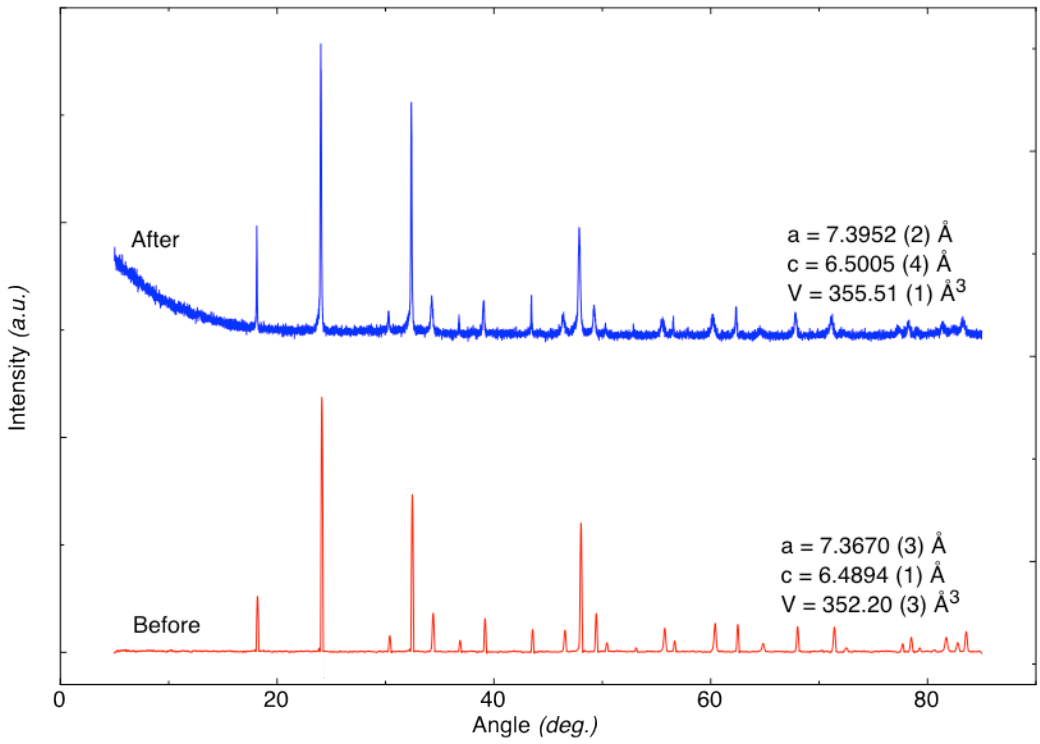

Figure 3.15 XRD pattern of $Ce_{0.825}Sr_{0.175}VO_4$ before/after measurement in dry 5% H_2-Ar

Concerning activation energies in reduced atmosphere (Table 3.5), values found were lower at low temperatures and higher at high temperatures than in air. Comparatively, while all activation energies in air for doped compounds were lower than for $CeVO_4$; in reduced atmosphere, either at high or low temperature, $CeVO_4$ constants were lower than all others in accordance with conductivity variations; also indicating that the dopant concentration has little effect on conductivity values in air but does in reduced atmosphere. Indeed, variations percentages in reduced atmosphere of 35 to 40% are obtained for high and low temperatures whereas the difference in air is only about 12%.

3.1.3.5. Dilatometry

Considering the mechanical compatibility of these materials with other plausible cell components, thermal expansion measurements of previously densified ceramics were carried out in air using dilatometry, Figure 3.16 illustrates the $\Delta L/L_0$ values obtained using a 5 ºC min^{-1} heating rate in the 25 ºC to 1000 ºC range for a characteristic Sr-doped cerium orthovanadate and $Y_{0.2}Zr_{0.8}O_2$ (8YSZ) synthesised via low-temperature carbon growth[169]. The strontium-containing and pure orthovanadate compounds were sintered at 1025 ºC for 18 hrs prior to analysis.

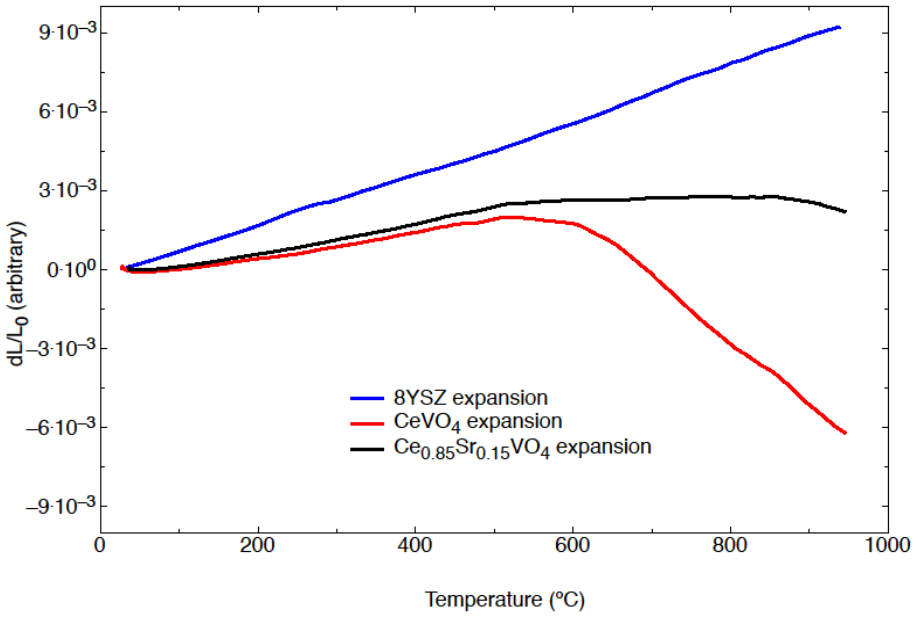

Figure 3.16 Dilatometric measurement in air up to 1000 ºC of selected doped cerium vanadate and 8YSZ as standard

The calculated thermal coefficients obtained were $3.4x10^{-6}$ (RT to 550 ºC) and $-20x10^{-6}$ K^{-1} (550 to 1000ºC) for $CeVO_4$, $4.6x10^{-6}$ K^{-1} (RT to 550 ºC) and $-0.8x10^{-6}$ K^{-1} (550 to 1000 °C) for $Ce_{0.85}Sr_{0.15}VO_4$ and $10x10^{-6}$ K^{-1} for 8YSZ (RT to 1000ºC) which correlates with the observation of Tsipis *et al.*[161, 162] ($5.73x10^{-6}$ and $5.64x10^{-6}$ K^{-1} respectively between RT and 550 °C) that noticed an initial anisotropic thermal expansion followed by a linear increase before an unexplained zero and negative expansion although no phase transitions were noted from high temperature XRD. The differences observed with the values from Tsipis are due to differences in sample density as in Tsipis study, samples exhibited an above 99% density, achievable only by sintering at temperature above a phase change which was not carried out in this case. Negative TCE is an unusual property that has been previously utilised in order to yield zero expansion composite materials such as Invar, an iron nickel alloy synthesised by Charles E. Guillaume in 1896 with uniquely low TCE[*170]. However in the interfacial layered mode of a fuel cell stack, TCE mismatch cannot be utilised in such ways as the occurrence of cracking and delamination is the only certain result.

3.1.4. Calcium-doped cerium orthovanadate results and discussion

3.1.4.1. Crystal structure

Single-phase powders of $Ce_{1-x}Ca_xVO_4$ were obtained up to x = 0.4125 (Figure 3.17), for higher x values, a second phase corresponding to $Ca_2V_2O_7$ was formed indicating that the solid solution limit in $Ce_{1-x}Ca_xVO_4$ series lies between x = 0.4125 and x = 0.425. Rietveld refinements were carried out in the same manner as for $Ce_{1-x}Sr_xVO_4$ with Ca replacing Sr. The refined parameters are listed in Table 3.6 for $Ce_{1-x}Ca_xVO_4$ and the average bond lengths in Table 3.7 (averaged between Ce-O1 and Ce-O2 as for Sr-doped compounds).

The tetragonal system exhibited by $CeVO_4$ with a zircon type structure was found to be also exhibited in the calcium doped system. Increasing the dopant level up to the solid solution limit decreases the size of the primary unit cell as shown by the decreasing values of the lattice parameters (Figure 3.18). As the ionic radius of Ca^{2+}

[*] The Nobel Prize in Physics 1920 was awarded to Charles Edouard Guillaume "*in recognition of the service he has rendered to precision measurements in Physics by his discovery of anomalies in nickel steel alloys*".

(1.12 Å) is smaller than that for Ce^{3+} (1.143 Å) for a coordination number of eight[167], replacing Ce^{3+} ions by Ca^{2+} ions should not cause any significant lattice contraction if the charge of the cerium ions remained unchanged. However, continuous lattice contraction was observed when more calcium was introduced in the lattice (Figure 3.18). This reduction in size may be due to the formation or the transformation of some components of the lattice into smaller counterparts; namely the formation of Ce^{4+} in order to balance the charge animosity introduced by doping with Ca^{2+} as the ionic size of Ce^{4+} ions is only 0.97 Å when eight-coordinated[167].

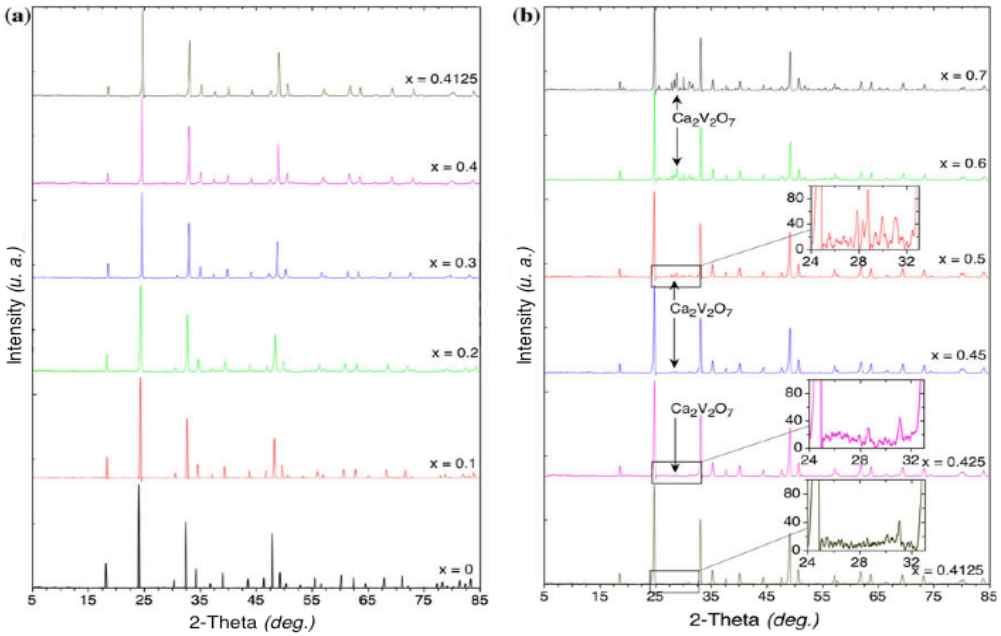

Figure 3.17 XRD patterns of $Ce_{1-x}Ca_xVO_4$ with (a) $0 \leq x \leq 0.4125$ and (b) $0.4125 \leq x \leq 0.7$

Crystallogr. parameter	$x = 0$	$x = 0.1$	$x = 0.2$	$x = 0.3$	$x = 0.4$	$x = 0.4125$
r Ln^{3+}(VIII) (Å)	1.143[167]					
λ (Å)	1.5405					
Crystal system	Tetragonal					
Space group	$I4_1/amd$					
a (Å)	7.4004 (1)	7.3706 (1)	7.3145 (1)	7.2483 (3)	7.2314 (2)	7.2150 (1)
c (Å)	6.4983 (6)	6.4879 (1)	6.4525 (2)	6.4129 (3)	6.4084 (3)	6.4027 (2)
V (Å^3)	355.88 (5)	352.45 (2)	345.22 (1)	336.91 (4)	335.11 (4)	333.30 (3)
ρ_{calc} (g.cm^{-3})	4.7601	4.6179	4.5222	4.4365	4.2621	4.2604
Rp (%)	7.88	8.15	7.78	8.89	9.27	6.80
wRp (%)	10.00	10.44	9.74	12.94	12.06	9.01
χ^2	1.463	1.722	1.343	2.081	1.913	1.870

Table 3.6 Crystallographic refinement parameters of $Ce_{1-x}Ca_xVO_4$ with $0 \leq x \leq 0.4125$

	$x = 0$	$x = 0.1$	$x = 0.2$	$x = 0.3$	$x = 0.4$	$x = 0.4125$
Ce-O (Å)	2.4839 (2)	2.4675 (2)	2.4595 (1)	2.4401 (1)	2.4360 (2)	2.4318 (1)
V-O (Å)	1.7115 (1)	1.7045 (2)	1.6949 (1)	1.6815 (3)	1.6788 (2)	1.6759 (2)

Table 3.7 Average bond lengths in $Ce_{1-x}Ca_xVO_4$ with $0 \leq x \leq 0.4125$

The charge compensation in $Ce_{1-x}Ca_xVO_4$ could occur in two ways: (a) the formation of oxygen deficient oxides with the charge for cerium ions remaining at 3+, which might lead to lattice expansion due to the formation of oxygen vacancies which is inconsistent with the observed lattice contraction; (b) some Ce^{3+} ions are converted to Ce^{4+} ions with the oxygen content remaining stoichiometric or with an oxygen excess. It has been reported from results on the structure and electrical properties of Ca-doping in $CeVO_4$ that there is a moderate oxygen excess in the lattice, leading to an interstitial mechanism[161]. Therefore it is likely that an oxygen excess solid solution was formed when doped with calcium. The general formula of the compounds can then be written as $(Ce^{3+}{}_{1-y}Ce^{4+}{}_{y})_{1-x}Ca_xVO_{4+\delta}$.

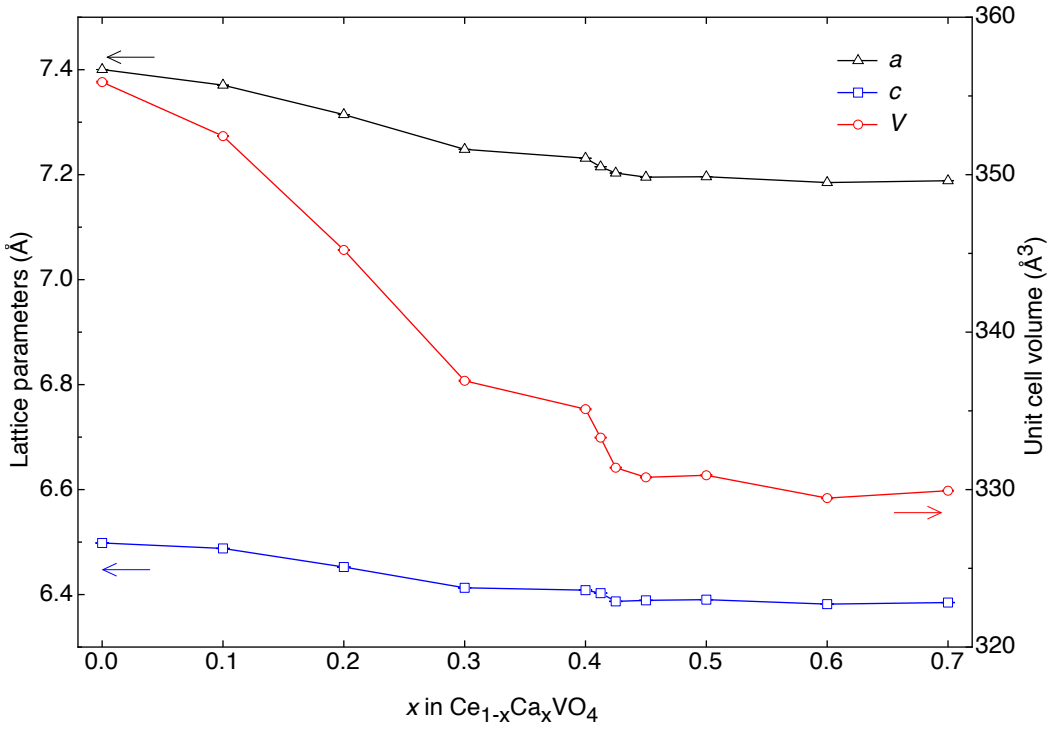

Figure 3.18 Lattice parameters and volume reduction in $Ce_{1-x}Ca_xVO_4$ with $0 \leq x \leq 0.7$

Band gap energy values given in Table 3.8 for Ca-doped compounds were determined from UV-Visible absorption spectra (Figure 3.19) using Equation 3.4 and 3.5 and confirm the insulating character at RT of $Ce_{1-x}Ca_xVO_4$ compounds.

Composition	$x = 0$	$x = 0.1$	$x = 0.2$	$x = 0.3$	$x = 0.4$	$x = 0.4125$
E_g (eV)	4.435 (2)	4.495 (1)	4.440 (3)	4.490 (4)	4.525 (1)	4.520 (3)

Table 3.8 Band gap energies of $Ce_{1-x}Ca_xVO_4$ with $0 \leq x \leq 0.4125$

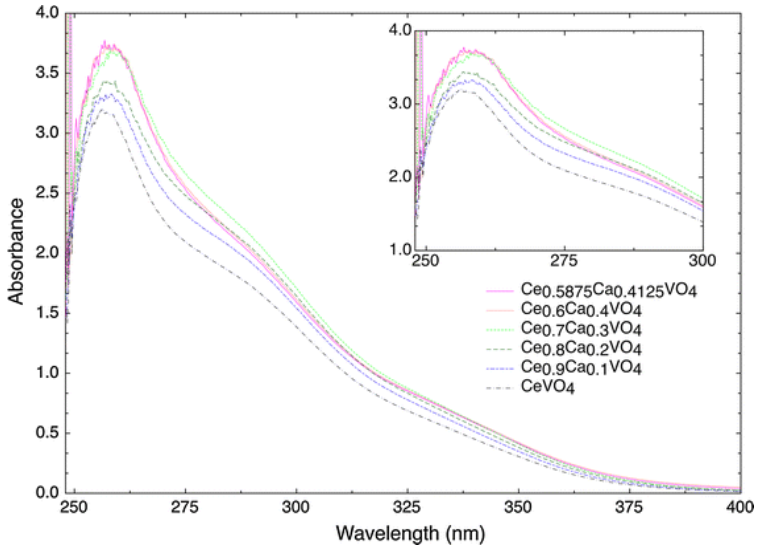

Figure 3.19 UV-vis absorbance spectra of $Ce_{1-x}Ca_xVO_4$ with $0 \leq x \leq 0.4125$

3.1.4.2. Thermal analysis

Thermal stability of the compounds was verified by carrying out TG/DSC measurements in both air and 5% H_2-Ar which are shown in Figure 3.20 and 3.21 respectively for a selection of calcium-doped cerium orthovanadate.

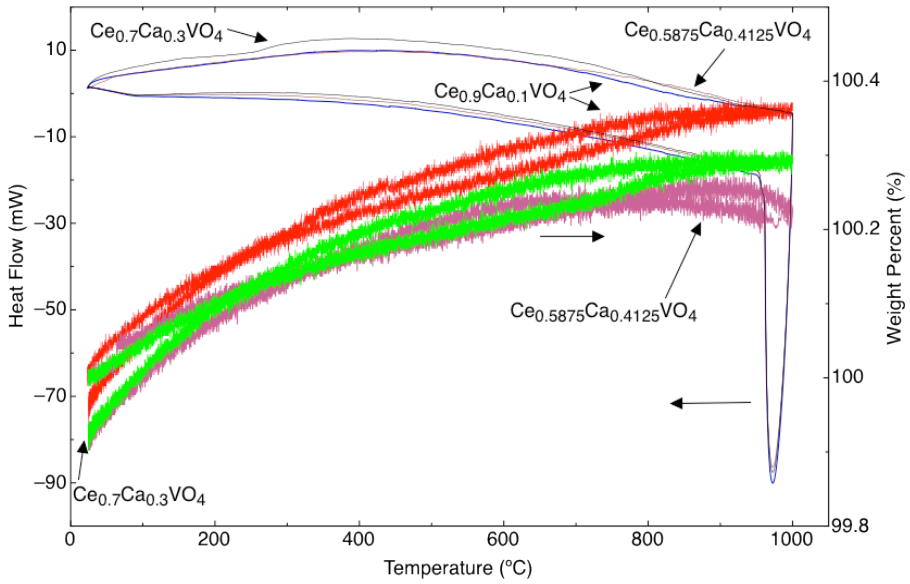

Figure 3.20 TG/DSC curves in air of $Ce_{0.9}Ca_{0.1}VO_4$, $Ce_{0.7}Ca_{0.3}VO_4$ and $Ce_{0.5875}Ca_{0.4125}VO_4$

No significant changes in weight are observed in both atmospheres with the most significant variations due to buoyancy. The compounds can therefore be considered as being stable in both oxidising and reducing atmosphere within the studied range of temperatures.

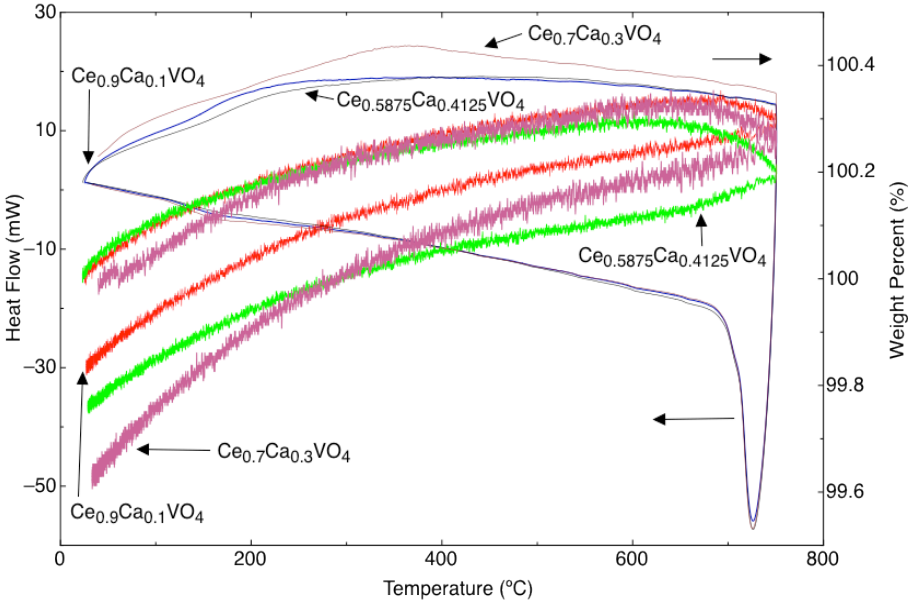

Figure 3.21 TG/DSC curves in air of $Ce_{0.9}Ca_{0.1}VO_4$, $Ce_{0.7}Ca_{0.3}VO_4$ and $Ce_{0.5875}Ca_{0.4125}VO_4$

3.1.4.3. Microstructure

On a microstructural point of view, the doping with calcium and the subsequent sintering into pellets has the same effect as with strontium; namely a high enough density to sustain mechanical strains and stresses and a high enough porosity to allow reactivity as shown by SEM images in Figure 3.22.

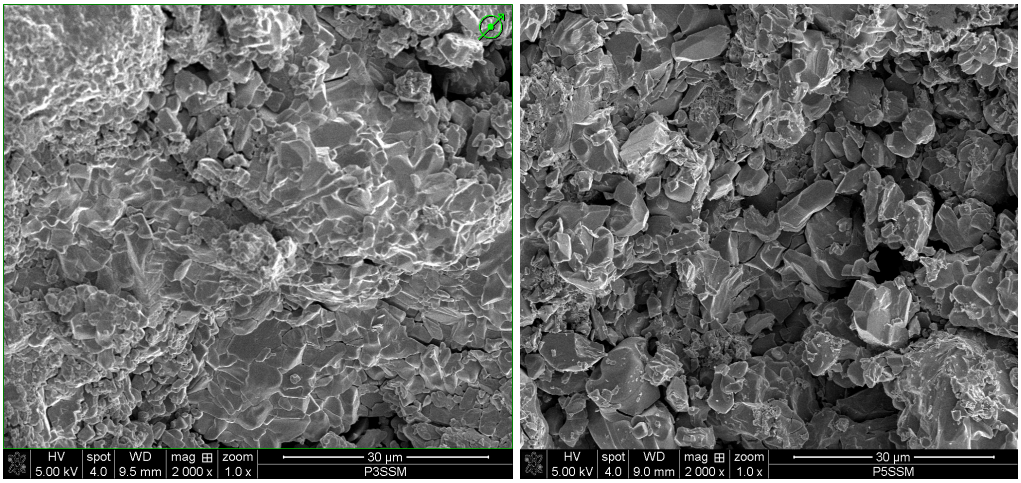

Figure 3.22 SEM images of $Ce_{0.6}Ca_{0.4}VO_4$ (L) and $Ce_{0.7}Ca_{0.3}VO_4$ (R) at magnification x2000

3.1.4.4. Conductivity

Conductivity measurements were carried out in air and in a reducing atmosphere of 5% H_2-Ar. Logarithmic plots of the product of conductivity and temperature against inverse temperature were constructed and are shown in Figure 3.23 and 3.24 for air and reduced atmosphere respectively.

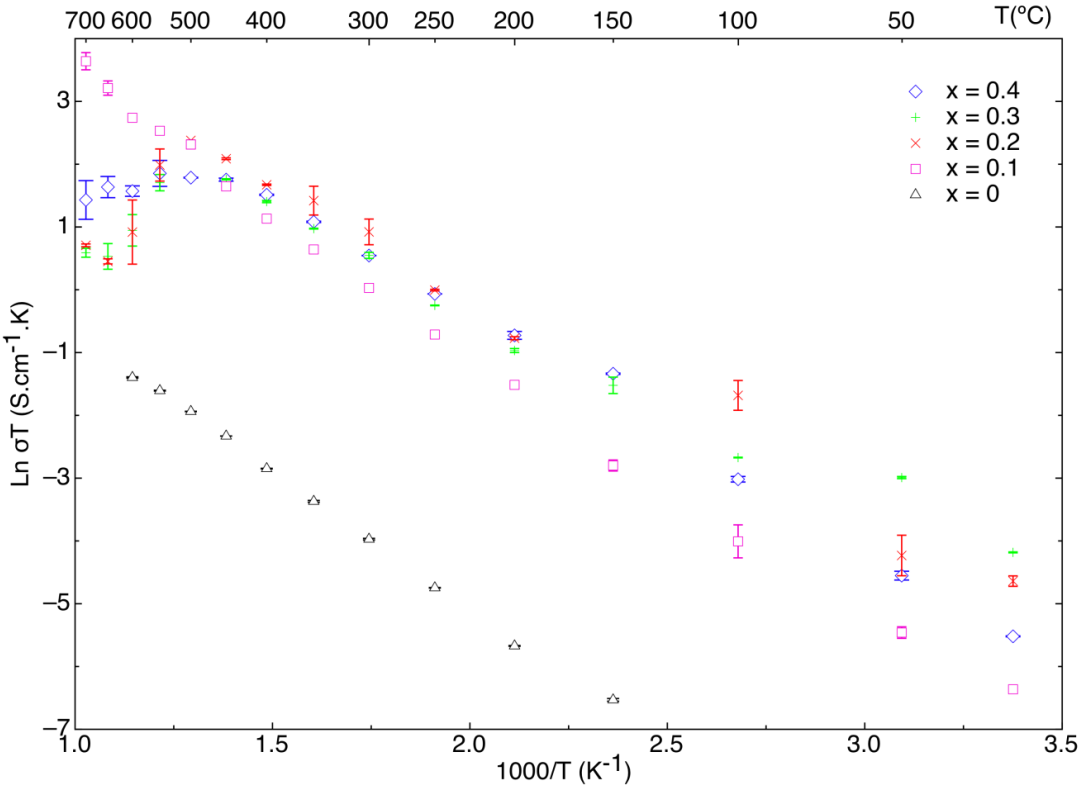

Figure 3.23 Conductivity plots in air of $Ce_{1-x}Ca_xVO_4$ with $0 \leq x \leq 0.4$

Plotted as Arrhenius type plots, activation energies can be extracted from the slope of each series of points while the Arrhenius pre-exponential factor *A* can be determined from the intercept values and tabulated in Table 3.9. It was observed, as shown in Figure 3.23, that the doping of $CeVO_4$ with calcium improved the conductivity of the compounds in comparison with the non-doped sample independently of the temperature.

Samples with $0.2 \leq x \leq 0.4$ did reach a maximum conductivity at 500-550 ºC before decreasing slightly up to 700 ºC. Variations of conductivity values within the doped compounds were found to be very small and the conductivity improvement therefore seems independent of the dopant level (Figure 3.24).

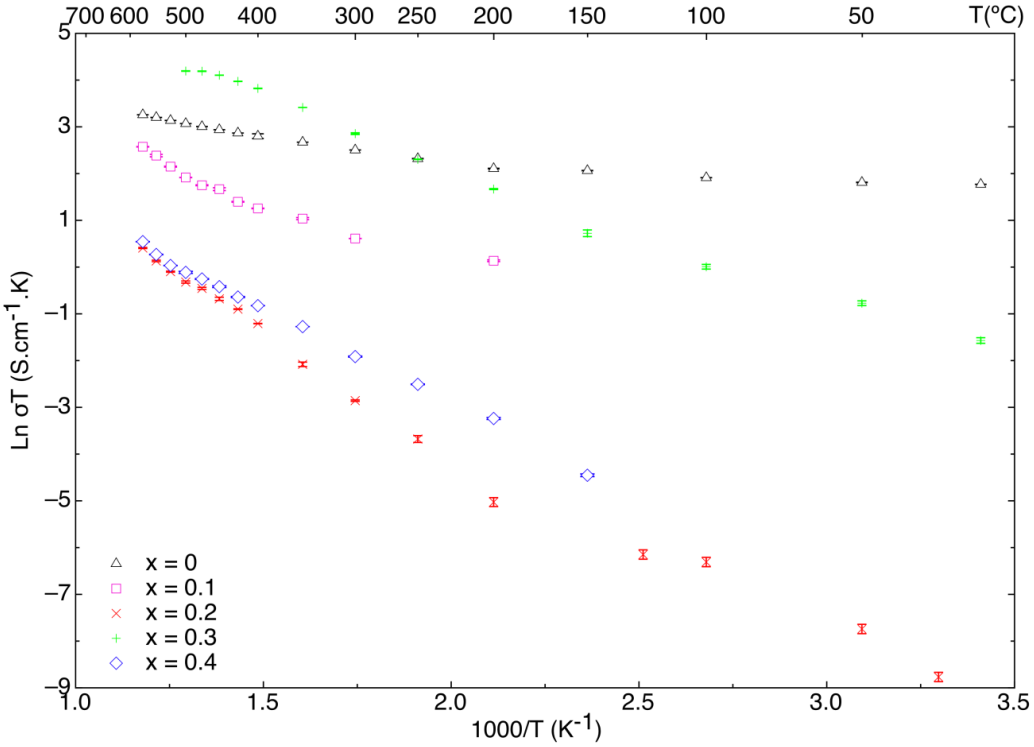

Figure 3.24 Conductivity plots in dry 5% H_2-Ar of $Ce_{1-x}Ca_xVO_4$ with $0 \leq x \leq 0.4$

E_a in kJ.mol^{-1} A in S.K.cm^{-1}			$x = 0$	$x = 0.1$	$x = 0.2$	$x = 0.3$	$x = 0.4$
Air		E_a	36.3 ± 0.3	35.6 ± 0.5	28.4 ± 2.3	25.0 ± 0.8	30.2 ± 5.1
		A	38.4 ± 1.1	2119.6 ± 1.1	891.4 ± 1.3	325.4 ± 1.2	932.7 ± 1.1
dry 5% H_2 - Ar	High Temp	E_a	10.6 ± 0.2	37.6 ± 1.6	47.5 ± 0.6	27.8 ± 0.5	33.5 ± 0.3
		A	112.3 ± 1.0	2562.9 ± 1.3	1279.5 ± 1.1	6001.7 ± 1.1	174.7 ± 1.1
	Low Temp	E_a	2.3 ± 0.2	15.5 ± 0.9	25.0 ± 1.8	18.0 ± 0.6	NA
		A	14.8 ± 1.1	55.1 ± 1.2	4.2 ± 1.8	345.8 ± 1.2	NA
	Approx. Temp. Border (ºC)		575	575	575	575	NA

Table 3.9 Arrhenius constants and activation energies in $Ce_{1-x}Ca_xVO_4$*

$Ce_{1-x}Ca_xVO_4$ compounds with $0 \leq x \leq 0.4$ were found to be stable in air up to the measured temperature of 700 ºC, exhibiting a metallic behaviour at 600 ºC (Figure 3.25). It is likely that a change in the conduction mechanism from a semi-conductor to a

* *As in Table 3.5*

metal is occurring between 500 – 600 ºC, which could be related to the loss of excess oxygen at high temperatures.

Activation energies for samples in air were found to be very similar while still lower for doped species compare to $CeVO_4$. Those variations in activation energies are linked to an increased capability of electron movement allowed by the reduction in size of the lattice parameters created as a consequence of the doping.

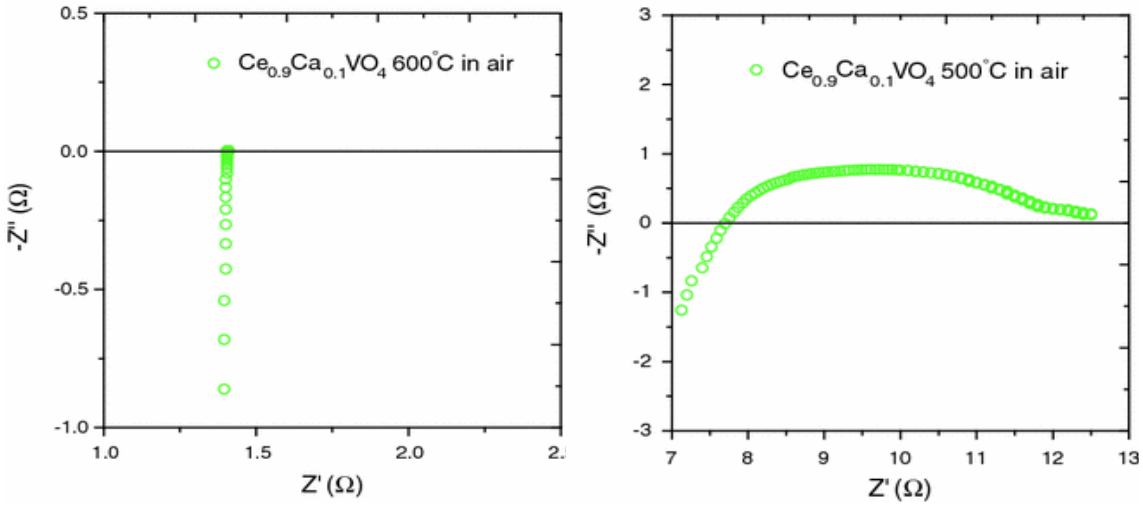

Figure 3.25 Impedance plots of $Ce_{0.9}Ca_{0.1}VO_4$ at 500 and 600 ºC in air

Considering measurements in dry 5% H_2-Ar, it can be observed in Figure 3.24 that the general conductivity of doped $CeVO_4$ compounds were similar or slightly lowered (except for sample $Ce_{0.7}Ca_{0.3}VO_4$ which was increased); ranging from 2 to 15 $mS.cm^{-1}$ at reduced oxygen pressure compared to 3 to 20 $mS.cm^{-1}$ in air. This behaviour is not reproduced with $CeVO_4$ whose maximum conductivity jumps from 0.3 $mS.cm^{-1}$ at 600 ºC in air to 30 $mS.cm^{-1}$ at 600 ºC under reduced atmosphere. While the dopant concentration didn't influence large conductivity variations in air, it can be seen that the matter is singularly different in reducing atmosphere. Indeed, while all Ca-doped species were more conductive than $CeVO_4$ in air across the whole range of temperatures, only sample $Ce_{0.7}Ca_{0.3}VO_4$ is more conductive than $CeVO_4$ at high temperatures in reduced atmosphere. This behaviour can be explained by the oxygen partial pressure dependency of the total conductivity of these compounds introduced with the *p*-type semi-conductive character; as indicated for $CeNbO_4$ by Tsipis *et al.*[168] namely that the total conductivity of $CeNbO_4$ – structurally similar to $CeVO_4$ – decreases consequently when the oxygen partial pressure is very low at high

temperatures. It could also be related to the higher relative density of this sample (86% compare to 80% for $CeVO_4$) which involves that it was not fully reduced even after exposure to 5% H_2-Ar at 600 ˚C for 12 hrs (Figure 3.26).

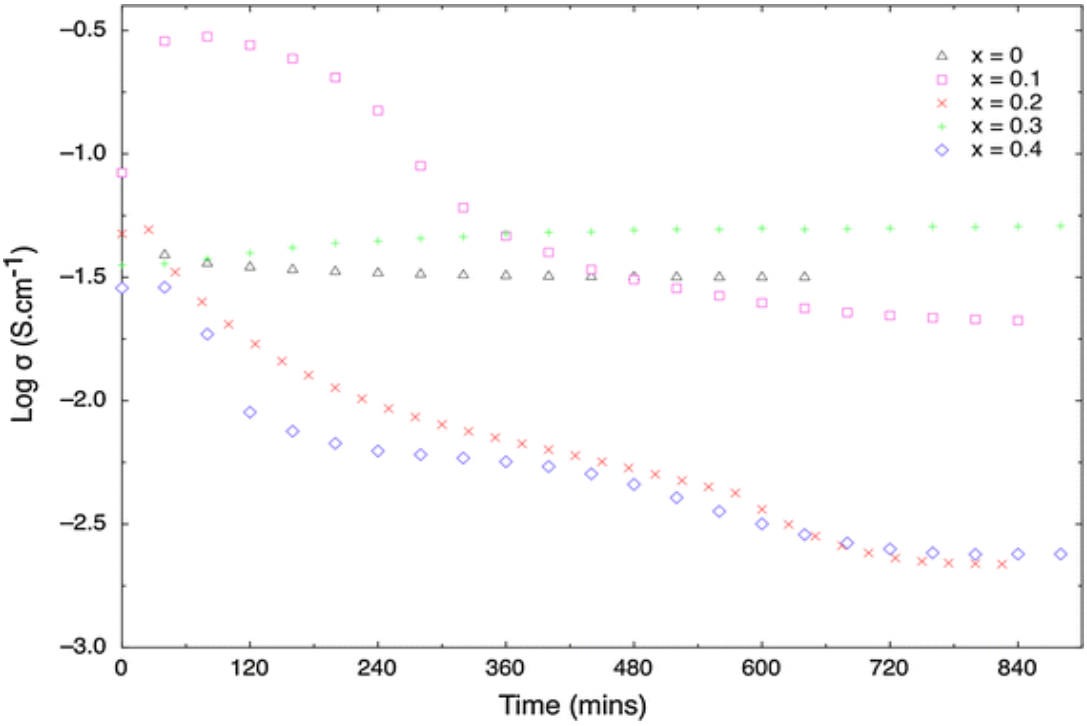

Figure 3.26 Conductivity changes at 600 ˚C in 5% H_2-Ar of $Ce_{1-x}Ca_xVO_4$ with $0 \leq x \leq 0.4$

The decrease in conductivity in 5% H_2-Ar at 600 ˚C (Figure 3.24) is related to the loss of excess oxygen. However, the total conductivity of samples $CeVO_4$ and $Ce_{0.7}Ca_{0.3}VO_4$ did not decrease during the measured 12 h, this could be due to the higher relative densities of these two samples causing slow reduction. Moreover, at 600 ˚C, the conductivities of samples $CeVO_4$ and $Ce_{0.7}Ca_{0.3}VO_4$ do not exhibit obvious change against time (Figure 3.26) with a decrease in conductivity observed in our samples. This could be explained if these two samples have either significant ionic conduction or if the kinetic process to reach equilibrium for reduction is very fast or very slow.

An electrochemical cell was therefore constructed to verify the observed phenomena. An OCV curve is shown in Figure 3.27 after 10 hrs (a) and 18 hrs (b) of anode exposure to dry 5% H_2-Ar. While rather small (0.38 mV after 10 hrs and 0.65 mV after 18 hrs), OCV values of the 5% (H_2-Ar)-Air electrochemical cell do indicate some ionic conduction, even if the electronic contribution is strongly dominating as under the

aforementioned conditions an OCV of ~1.0 V would be expected for a pure ionic conducting electrolyte.

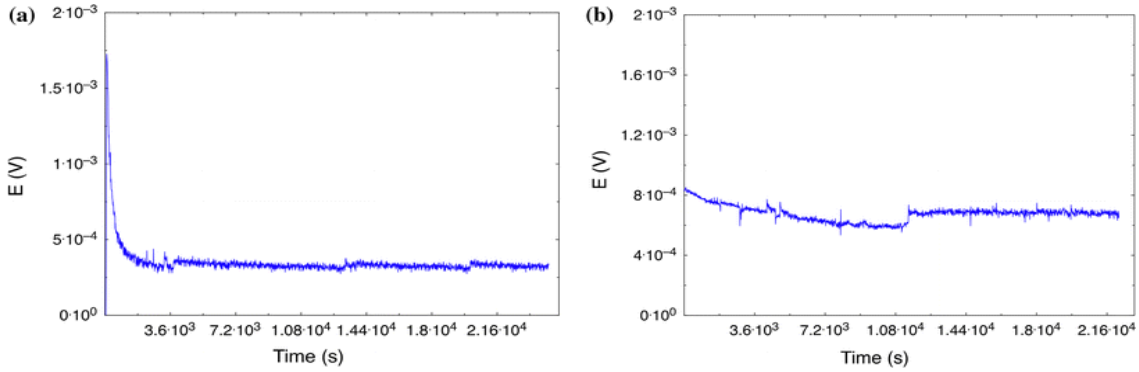

Figure 3.27 OCV plots of a $Ce_{0.7}Ca_{0.3}VO_4$ cell at 600 ºC after (a) 10 hrs and (b) 18 hrs

As shown in Figure 3.28 and 3.29, XRD pattern of samples $Ce_{0.9}Ca_{0.1}VO_4$ and $Ce_{0.8}Ca_{0.2}VO_4$ are almost unchanged upon reduction and can be considered as being redox stable below 600 ºC. The marked peaks are metallic platinum reflections corresponding to the coating agent that could not be removed from the pellets and was therefore re-ground with.

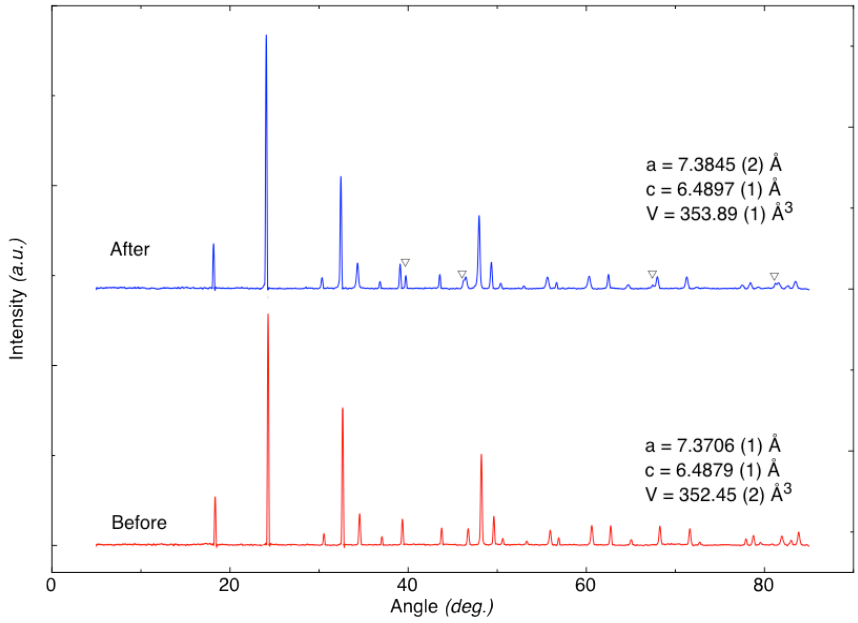

Figure 3.28 XRD pattern of $Ce_{0.9}Ca_{0.1}VO_4$ before and after conductivity measurements in 5% H_2-Ar

For $x > 0.2$, samples were found to be relatively stable to reduced atmosphere treatment with CeO_2 traces detectable as a result of reducing oxygen pressure; process most likely due to traces of CeO_2 present in the product as impurity and intensified by

treatment in H_2 atmosphere. The lattice expansion observed for samples with $x < 0.2$ on reduction is believed to be due to the reduction of both cerium and vanadium ions because both the Ce-O and V-O bond lengths increased in the reduced sample. The bond lengths refined are – for $Ce_{0.8}Ca_{0.2}VO_4$ as an example – 2.4780 Å for Ce-O (average) and 1.7074 Å for V-O compared with 2.4595 Å for Ce-O (average) and 1.6949 Å for V-O before the conductivity measurement. Reversible change in conduction mechanism were observed for all compounds except for sample $Ce_{0.6}Ca_{0.4}VO_4$ at temperatures ~ 575 ºC resulting in an observed metallic behaviour during conductivity measurements as previously stated and illustrated by Figure 3.30.

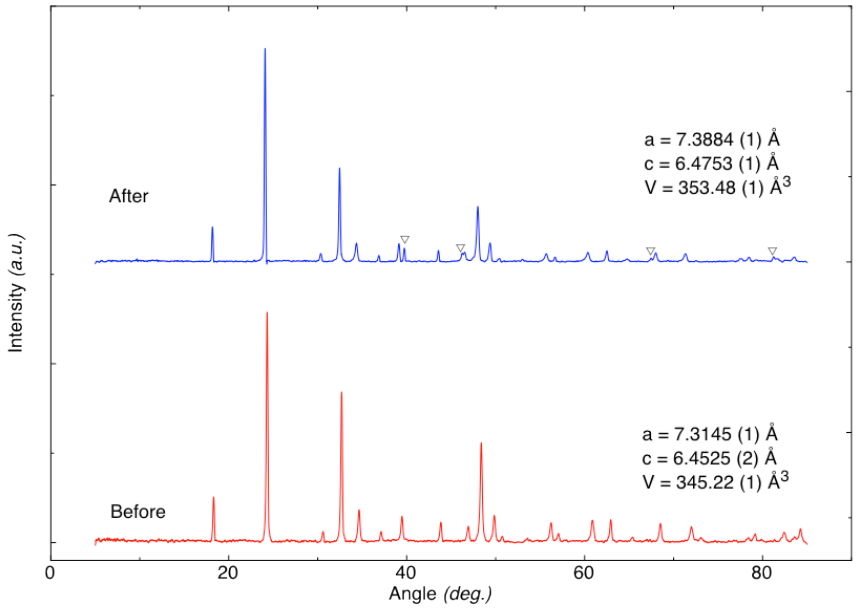

Figure 3.29 XRD pattern of $Ce_{0.8}Ca_{0.2}VO_4$ before and after conductivity measurements in 5% H_2-Ar

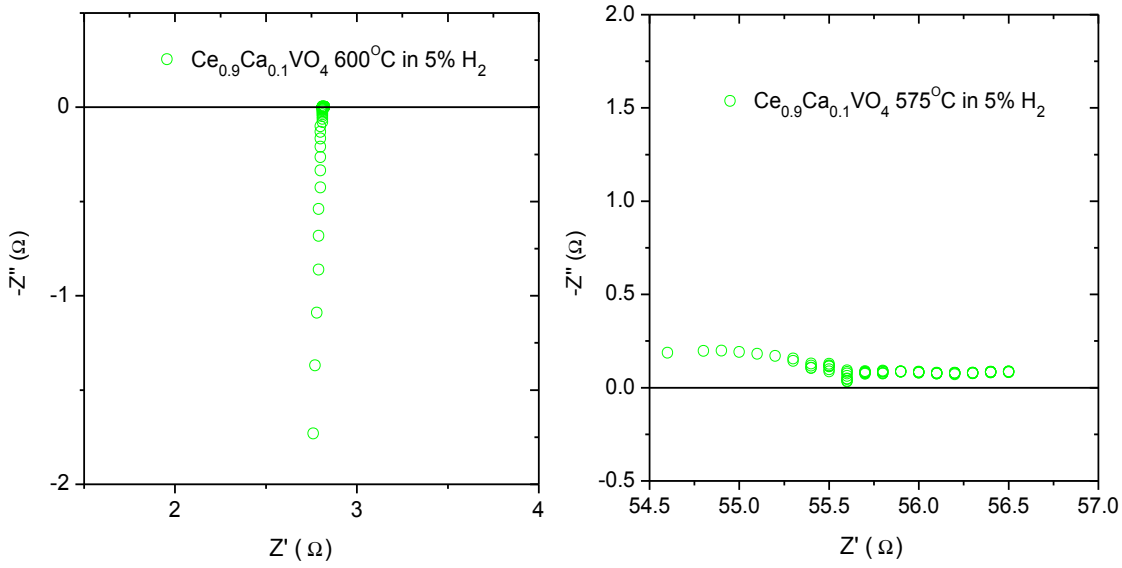

Figure 3.30 Impedance plots of $Ce_{0.9}Ca_{0.1}VO_4$ at 575 and 600 ºC in 5% H_2-Ar

3.1.4.5. Dilatometry

Considering the mechanical compatibility of these materials with other plausible cell components, thermal expansion measurements of dense ceramics were carried out in air using dilatometry. Figure 3.31 illustrates the $\Delta L/L_0$ values obtained using a 5 ºC min^{-1} heating rate in the 25 ºC to 1000 ºC range for a characteristic Ca-doped cerium orthovanadate and 8YSZ synthesised via low-temperature carbon growth[169]. The calcium compound was sintered at 1025 ºC for 18 hrs prior to analysis.

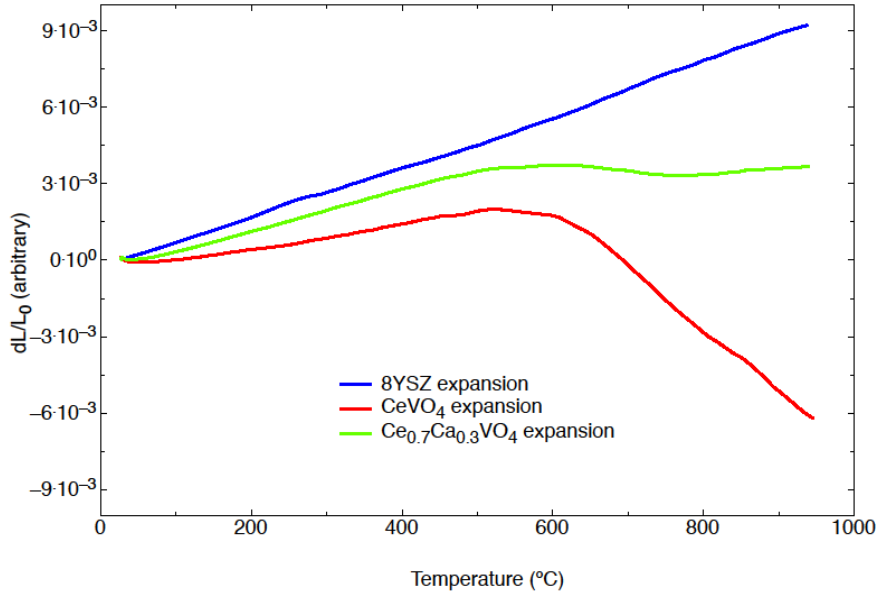

Figure 3.31 Dilatometric measurement in air up to 1000 ºC of selected Ca-doped cerium vanadate and 8YSZ as standard

The calculated thermal coefficients obtained were $3.4x10^{-6}$ (RT to 550 ºC) and $-20x10^{-6}$ K^{-1} (550 to 1000ºC) for $CeVO_4$, $6.6x10^{-6}$ K^{-1} (RT to 550 ºC), $-2.6x10^{-6}$ K^{-1} (600 to 750 ºC) and $2.1x10^{-6}$ K^{-1} (800 to 1000 ºC) for $Ce_{0.7}Ca_{0.3}VO_4$ and $10x10^{-6}$ K^{-1} for 8YSZ (RT to 1000 ºC) which correlates with the observation of Tsipis *et al.*[161, 162] ($5.64x10^{-6}$ K^{-1} for $CeVO_4$ (RT to 550 ºC), Ca-doped not reported at such doping level) that noticed an initial anisotropic thermal expansion followed by a linear increase before an unexplained zero and negative expansion although no phase transitions were noted from high temperature XRD. The value obtained for the calcium doped compound may be put in perspective from the values obtained by Tsipis for 10 and 20 % percent doping with values of expansion decreasing with increasing the dopant concentration; a pattern

also followed here as the TCE for the 30% dopant compound is smaller than the one reported by Tsipis at 20%.

3.1.5. Conclusions

Single phase crystals of $Ce_{1-x}M_xVO_4$ (M = Ca, Sr with $0 \leq x \leq 0.4125$ and $0 \leq x \leq 0.175$ respectively) were synthesised by a standard ceramic technique. All samples were found to exhibit the tetragonal zircon type structure of space group $I\,4_1/amd$. It is believed that the lattice contraction on Sr/Ca-doping is due to the change of charge of cerium ions from Ce^{3+} to Ce^{4+} introducing oxygen hyperstoichiometry.

Conductivity measurements carried out in air and in reduced atmosphere have shown that the improvement in conductivity resulting from the doping is independent of the dopant level as well as of the temperature for the case of air and while $CeVO_4$ exhibits an increased conductivity in reduced atmosphere, doped species total conductivity is globally decreasing except for sample $Ce_{0.7}Ca_{0.3}VO_4$ which exhibit low level ionic conduction in combination with dominant electronic conduction. The relatively low conductivity in a reducing atmosphere will however restrain the application of these materials as anodes for intermediate temperature solid oxide fuel cells and additionally as average expansion coefficients are disadvantageous. Most doped samples (except those forming millesimal amount of CeO_2 as a result of reducing oxygen pressure, phenomenon most likely due to the presence of undetected ceria in the starting material phase rather than real decomposition) are redox stable at a temperature below 600 °C although some lattice expansion was observed which is related to the reduction of both cerium and vanadium ions.

3.2. Cerium metavanadates

3.2.1. Background

Rare-Earth containing structures, such as orthovanadates *RE*VO_4, have been intensively studied[144, 145, 148, 153, 155, 156, 171, 172] with research going back a few decades, especially for lanthanum and cerium orthovanadates. However, the perovskite analogues of the zircon type structures (*RE*VO_3) have only recently been considered as potential anode materials and within these structures lanthanum and cerium vanadates are considered the most promising. It is known that cerium is a good electronic conductor and that vanadium is a good catalyst at intermediate temperatures, hence the recent interest for the magnetic properties of pure or doped $CeVO_3$[173-179]. Some doped-*RE*VO_x has been investigated for orthovanadates[160-162, 164] and for metavanadates[173, 180] but studies on $CeVO_3$ were all centred on temperatures below ambient or above 700 °C.

3.2.2. Experimental

3.2.2.1. Materials and properties

Single-phase powders of orthovanadates from previous work[181, 182] were used as starting materials. Single-phase cerium metavanadates were synthesised by a solid-state method using cerium orthovanadates as cerium and vanadium sources. Sample powders of the respective orthovanadates were pressed into pellets; sintered at temperatures depending on the sample themselves for 12 hrs (850 ºC for $CeVO_4$, 900 ºC for Ca- and Sr-doped $CeVO_4$); coated with platinum paste; fired again at 850 °C at a rate of 5 ºC min^{-1}, dwelled for two hrs and then cooled down to RT before being reduced in 5% H_2-Ar at 900 °C for 5 hrs for strontium-doped and for 15 hrs for calcium-doped and non-doped cerium orthovanadates.

3.2.2.2. Characterisation and conductivity

3.2.2.2.1. Powder X-ray diffraction

X-ray data were collected on a Bruker-AXS (D8 Advance) machine, controlled by DIFFRACT$^{plus\ TM}$, in the Bragg-Brentano reflection geometry with a Cu Kα source

(1.5405 Å) and fitted with a LynxEye™ detector.

Absolute scans in the 2θ range of 5-85º with step size of 0.009º and time step of 61.6s, 123.2s or 2s (longer scans for metavanadates refinements) were used during data collection.

3.2.2.2.2. Thermal analysis

Thermogravimetry and differential scanning calorimetry (TG/DSC) analyses were performed using a Stanton Redcroft STA/TGH series STA 1500 operating through a Rheometric Scientific system interface controlled by the software RSI Orchestrator up to 950 ºC at 5 ºC min^{-1} for analyses in 5% H_2-Ar and up to 700 ºC at 5 ºC min^{-1} in air.

3.2.2.2.3. Scanning electron microscopy

SEM pictures were taken with the use of a Quanta 3D FEG scanning electron microscope (FEI Company) with voltages of 5 or 10 kV and 10 pA.

3.2.2.2.4. Conductivity

Total conductivity measurements were carried out using on one hand, a computer-controlled Solartron Analytical® SI 1287 potentiostat/galvanostat coupled to an SI 1250 frequency response analyser with the Scribner Associates Corrosion Testing software CorrWave® for non- and strontium-doped compounds; and a computer-controlled Solartron Analytical® 1470E Battery Test System with the Solartron Analytical software, CellTest® for calcium-doped compounds; both within a temperature range of 700 ˚C to RT (~25 ˚C). Platinum coated pellets were fitted into the measuring apparatus and measurements were firstly carried out in a reduced atmosphere of 5 % H_2-Ar dried through a solution of 98% H_2SO_4 and secondly in air. Recordings were made on heating/cooling from RT to 700 ˚C after stabilisation was attained at 700 ˚C at a rate of 2 ˚C min^{-1} for $Ce_{0.85}Sr_{0.15}VO_3$ and 1˚C min^{-1} for all other compounds. The temperature was digitally recorded in parallel with the impedance through an Omega HH506RA multilogger thermometer connected to a microcomputer.

3.2.3. Strontium-doped cerium metavanadate results and discussion

3.2.3.1. Crystal structure

Single-phase perovskite structures were obtained for both synthesised metavanadate and Rietveld refinements were carried out with both structural and profile parameters being varied using an orthorhombic unit cell of space group *Pnma* (62) as starting model, as mentioned in the literature[183]. Wyckoff sites assigned to Ce (and Sr), V and O were 4*c*, 4*a* and *8d* and 4*c* respectively. Vanadium and oxygen were always considered – during the refinement processes – with full occupancies, whereas cerium and strontium occupancies were varied in accordance with the stoichiometry. Profile refinements were performed using GSAS[136] after space group determination with TOPAS®. The experimental and calculated profiles are shown in Figure 3.32 and the atomic parameters in Table 3.10.

	Atoms	***x***	***y***	***z***	**Occ.**	U_{iso} **x100**
$CeVO_3$	Ce	0.4631 (1)	0.2500	0.0005 (1)	1	2.4 (1)
	V	0	0	0	1	2.6 (2)
	O (1)	0.2327 (1)	0.0508 (1)	0.2706 (1)	1	9.0 (2)
	O (2)	0.6164 (1)	0.2500	0.5816 (1)	1	29 (2)
$Ce_{0.85}Sr_{0.15}VO_3$	Ce	0.4695 (1)	0.2500	0.0145 (1)	0.85	0.3 (1)
	Sr	0.4695 (1)	0.2500	0.0145 (1)	0.15	0.3 (1)
	V	0	0	0	1	0.1 (1)
	O (1)	0.2148 (1)	0.0158 (1)	0.3107 (1)	1	0.7 (1)
	O (2)	0.5047 (1)	0.2500	0.5459 (1)	1	2.5 (7)

Table 3.10 Atomic positions and thermal factors for $Ce_{0.85}Sr_{0.15}VO_3$ and $CeVO_3$

Regarding oxygen displacement parameters, values obtained are reasonably larger to other elements as in the presence of heavy atoms, XRD is not sensitive enough to accurately measure light atoms like oxygen. Recent and past publications concerning lanthanoid metavanadates all mention that in the case of cerium (and lanthanum) a tetragonal phase is observed depending on the conditions of synthesis[180, 184]. Looking closely at the XRD pattern in Figure 3.32 (A), one could admit that the pattern has non-split intense peaks whereas split ones are common for orthorhombic lanthanoid

metavanadates, however no tetragonal perovskite space group –neither primitive nor body-centred– could be assigned to the data with an acceptable fit. In these experiments, both $CeVO_3$ and $Ce_{0.85}Sr_{0.15}VO_3$ therefore exhibit orthorhombic structure indicating that the structure of non- and Sr-doped $CeVO_3$ may be sensitive to the reduction conditions.

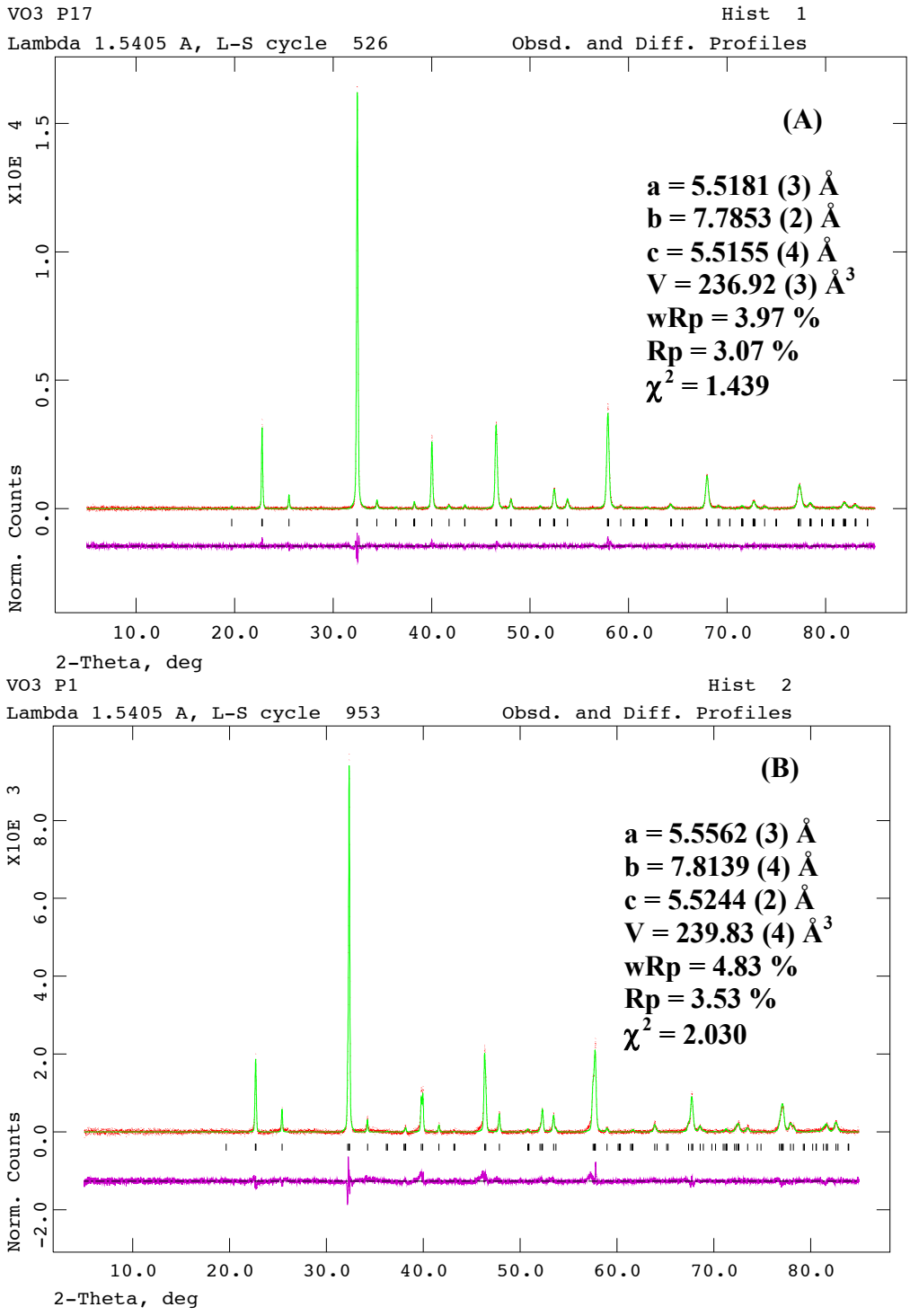

Figure 3.32 GSAS plots of (A) $Ce_{0.85}Sr_{0.15}VO_3$ and (B) $CeVO_3$

XRD analysis was carried out after the conductivity measurements in air to monitor the stability of the perovskite phase and results are shown in Figure 3.33 and Table 3.11. Whereas for $CeVO_3$, the oxidation leads to the formation of a considerable number of different phases including cerium oxides, cerium vanadates and vanadium oxides[185]; the oxidation of $Ce_{0.85}Sr_{0.15}VO_3$ only yields the tetragonal and monoclinic phases of $Ce_{0.85}Sr_{0.15}VO_4$.

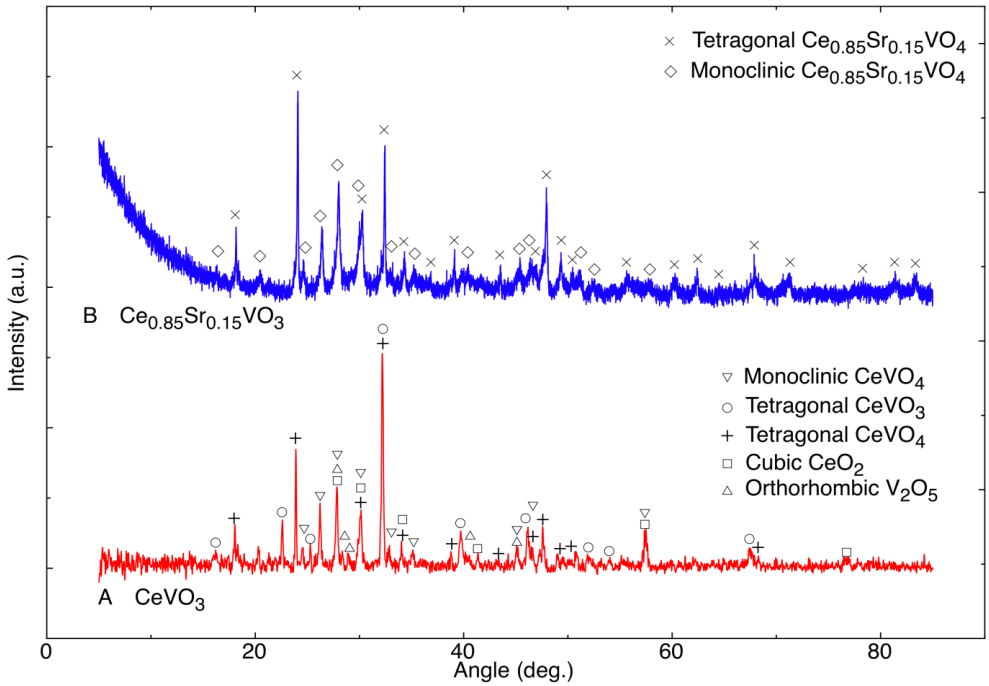

Figure 3.33 XRD patterns of (A) $CeVO_3$ and (B) $Ce_{0.85}Sr_{0.15}VO_3$ after oxidation

	$Ce_{0.85}Sr_{0.15}VO_4$	
Phase	*Monoclinic*	*Tetragonal*
Space Group	$P12_1/n$ (14)	$I4_1/amd$ (141)
a (Å)	6.9928 (3)	7.3687 (5)
b (Å)	7.2293 (4)	7.3687 (3)
c (Å)	6.6788 (2)	6.4882 (2)
$\alpha/\beta/\gamma$ (º)	90 / 105.11 (1) / 90	90 / 90 / 90
V (Å^3)	325.98 (4)	352.26 (3)

Table 3.11 Lattice parameters for $Ce_{0.85}Sr_{0.15}VO_4$ after conductivity measurements

A point worth noting also is that for $CeVO_3$, both cerium metavanadate and orthovanadate phases are present in the oxidised product whereas for the latter, only orthovanadate phases are detected. And if one considers that the monoclinic phase in $Ce_{0.85}Sr_{0.15}VO_3$ is formed when the oxidation process is started at low temperatures, a

long-lasting firing of the metavanadate is likely to yield only the zircon-type tetragonal phase making the process fully reversible. The phase reversibility was tested by reducing the oxidised vanadate from the conductivity test in air with results given in Table 3.12 and 3.13 and in Figure 3.34 (red markers corresponding to the cubic phase of Pt, used as coating agent during conductivity) and 3.35. The Sr-doped compound was found to regain its orthorhombic form making the structural phase process fully reversible making that Sr-doped $CeVO_3$ a better choice than $CeVO_3$ as anode material for SOFCs.

	$Ce_{0.85}Sr_{0.15}VO_3$
Space Group	*Pnma* (62)
a (Å)	5.5047 (3)
b (Å)	7.7827 (4)
c (Å)	5.5521 (2)
V (Å^3)	237.91 (5)
wRp (%)	9.57
Rp (%)	7.47
χ^2	1.322

Table 3.12 Refinement parameters for $Ce_{0.85}Sr_{0.15}VO_4$ after 2nd reduction cycle

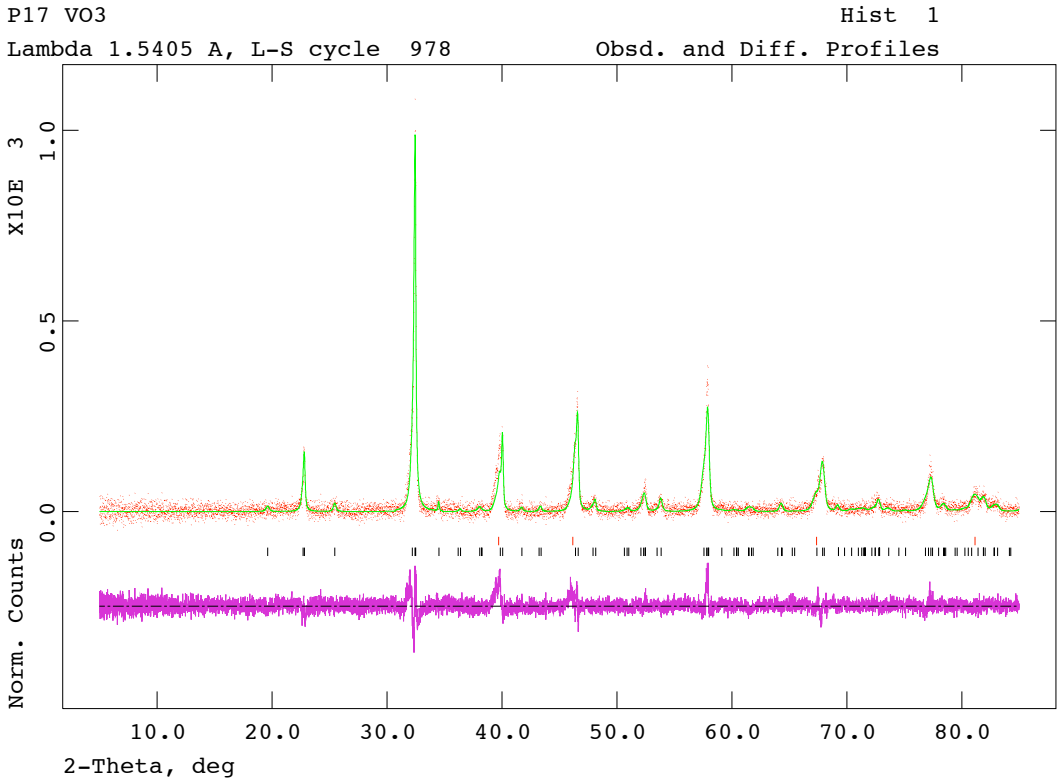

Figure 3.34 GSAS plot of $Ce_{0.85}Sr_{0.15}VO_3$ from reduction after conductivity measurements

	$Ce_{0.85}Sr_{0.15}VO_3$				
Atoms	*x*	*y*	*z*	Occ.	U_{iso} x 100
Ce	0.4723 (1)	0.2500	0.0173 (1)	0.85	2.4 (1)
Sr	0.4723(1)	0.2500	0.0173(1)	0.15	2.4 (1)
V	0	0	0	1	1.9 (1)
O (1)	0.1794 (1)	0.0386 (1)	0.2725 (1)	1	8.4 (1)
O (1)	0.5206 (1)	0.2500	0.5121 (1)	1	8.5 (1)

Table 3.13 Atomic positions and thermal factors for $Ce_{0.85}Sr_{0.15}VO_3$ after second reduction

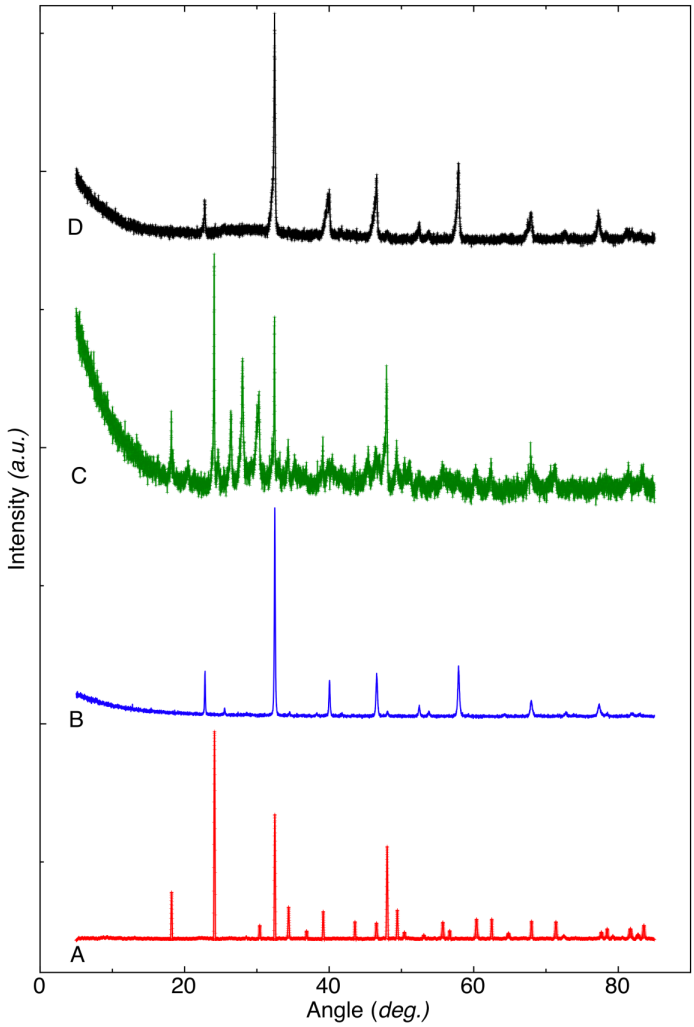

Figure 3.35 XRDs of (A) starting VO_4, (B) as VO_3, (C) after conductivity measurement and (D) re-reduced

3.2.3.2. Thermal analysis

In order to obtain fully reduced samples, TG/DSC curves of the starting materials were beforehand measured in 5% H_2-Ar to assess the necessary range of temperature to

be employed with results shown in Figure 3.36 for $Ce_{0.85}Sr_{0.15}VO_4$. Weight losses observed in 5% H_2-Ar (around 6-6.5 wt %) are due to the loss of oxygen and correlate perfectly with a theoretical weight loss of 6.3 wt % from $CeVO_4$ to $CeVO_3$ and of 6.5 wt % from $Ce_{0.85}Sr_{0.15}VO_4$ to $Ce_{0.85}Sr_{0.15}VO_3$.

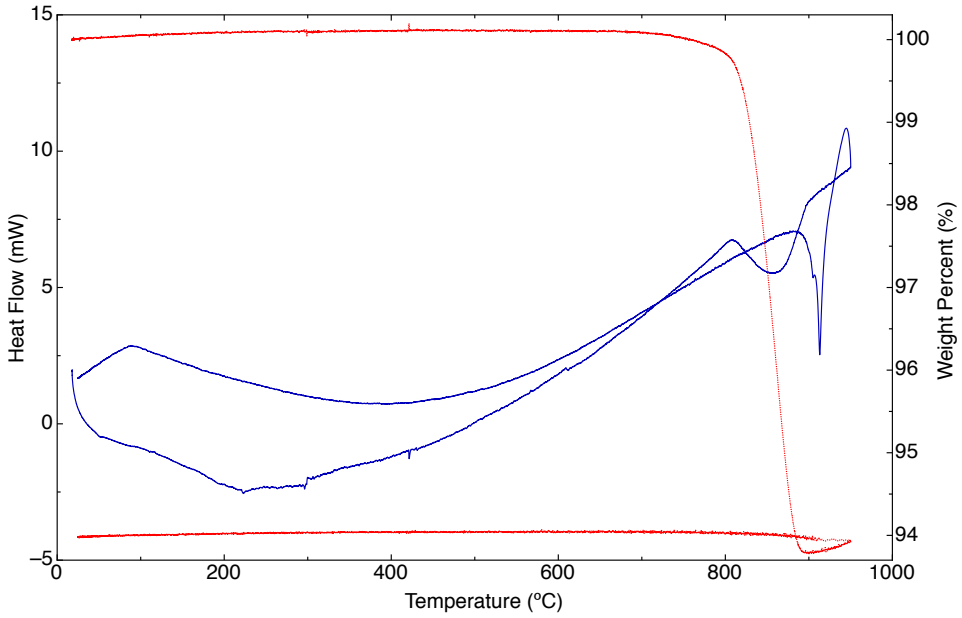

Figure 3.36 TG/DSC of $Ce_{0.85}Sr_{0.15}VO_4$ in 5% H_2-Ar from RT to 950 °C

The thermal stabilities in air of the metavanadates formed were also determined and are shown in Figure 3.37 for $Ce_{0.85}Sr_{0.15}VO_3$ and $CeVO_3$.

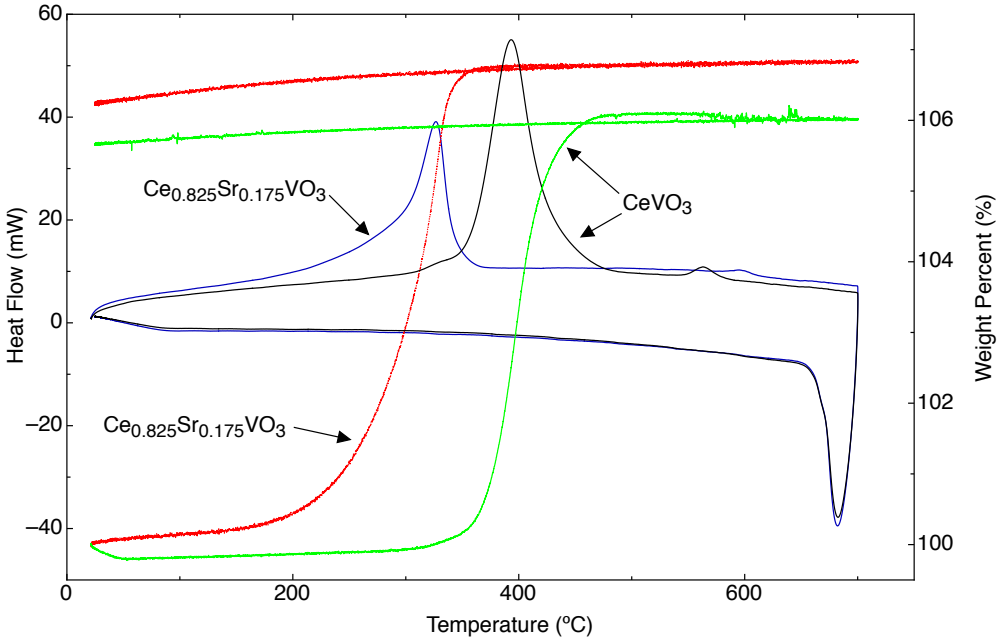

Figure 3.37 TG/DSC of $Ce_{0.85}Sr_{0.15}VO_3$ and $CeVO_3$ in air from RT to 700 °C

Data were recorded up to 700 ºC at a rate of 5 ºC.min^{-1} in order to match the experimental conditions from the conductivity measurements. Upon oxidation, both samples gained weight (around 6.5 wt %), which can be related to the absorption of one oxygen ion. The main difference lies in the oxidation temperature since while the strontium-doped compound is fully oxidised at about 350 ºC, an approximate temperature of 500 ºC is needed for $CeVO_3$ even if in both cases, the oxidation process seems to start at around 200 - 300 ºC. It appears that doping with strontium also changes the kinetics of the oxidation process due to the modification of the surface.

3.2.3.3. Microstructure

In order to examine the microstructure of the material before and after reduction, SEM pictures of the orthovanadate and of the metavanadate were taken for comparison and are shown in Figure 3.38.

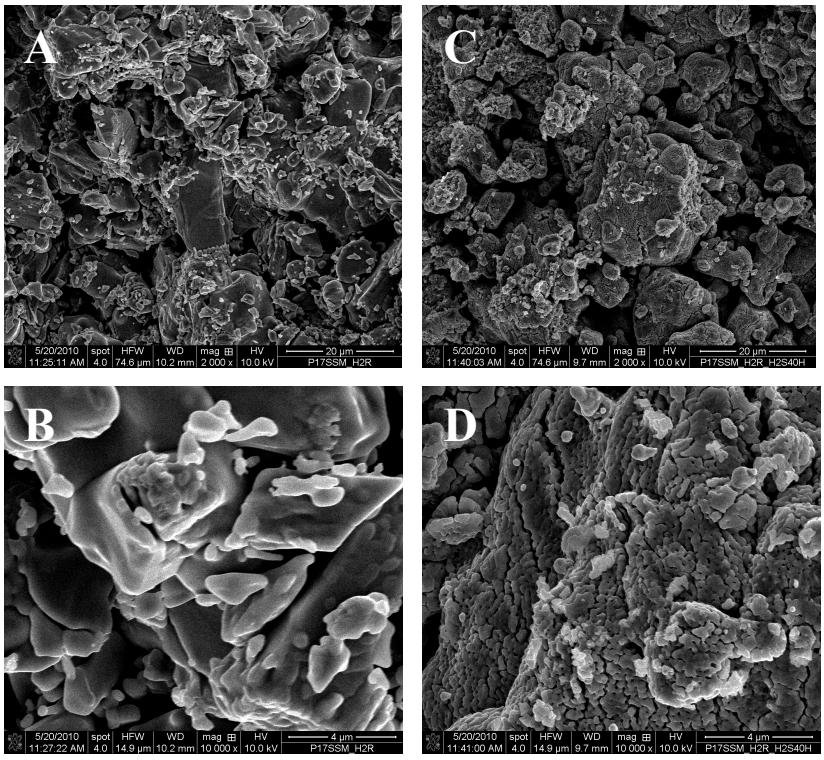

Figure 3.38 SEM images of $Ce_{0.85}Sr_{0.15}VO_x$ at x2000 and x10 000 as ortho (A-B) and meta (C-D)

The pictures of the orthovanadate (A and B) exhibit a well sintered structure of plain particles whereas the same magnification with the metavanadate (C and D) result in an important microporosity (already visible on the x10 000 picture) with channels and void spaces not observed in the orthovanadate (even at x40 000 – Figure 3.39) thus

indicating to be a consequence of the reduction leading to higher conductivity. This phenomenon also confirms that the loss of oxygen happens locally and that the sintering of yielded metavanadate is insignificant, probably caused by its higher melting point. This special property could benefit the redox cyclability when used as anode for SOFCs.

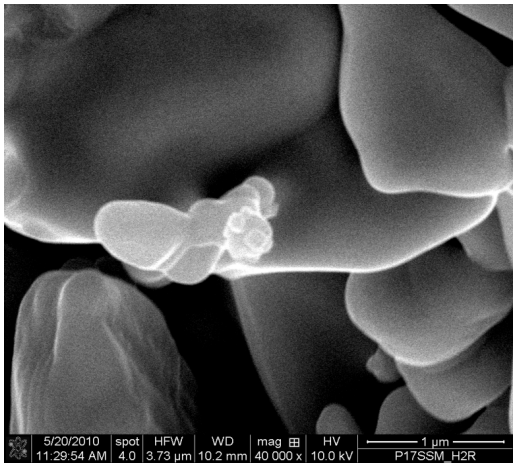

Figure 3.39 SEM image of $Ce_{0.85}Sr_{0.15}VO_4$ at x40 000

3.2.3.4. Conductivity

Values obtained from the impedance measurements and from the temperature recordings were combined to obtain plots of the conductivity against temperature and are shown in Figure 3.40 for $Ce_{0.85}Sr_{0.15}VO_3$ in (a) dry 5% H_2-Ar and in (b) air; and in Figure 3.41 for $CeVO_3$ in (a) dry 5% H_2-Ar and in (b) air.

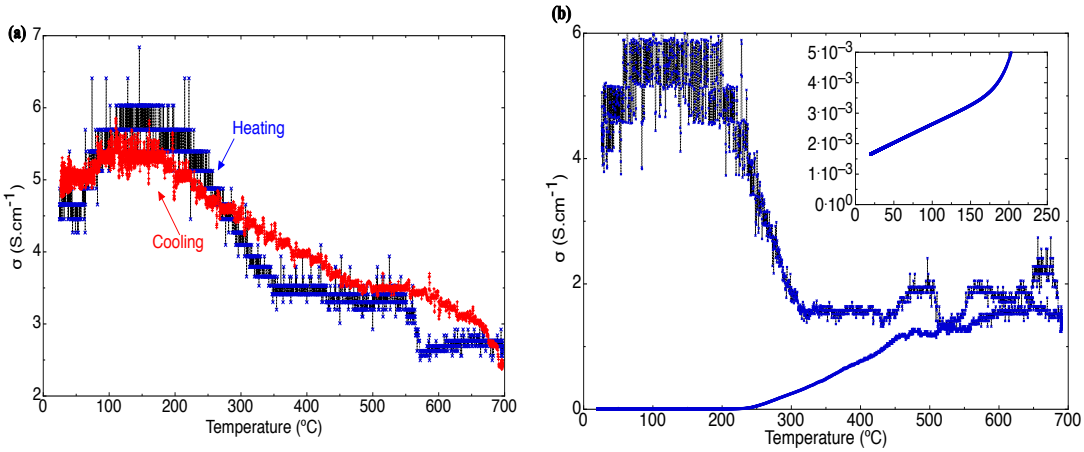

Figure 3.40 Conductivity plots of $Ce_{0.85}Sr_{0.15}VO_3$ in (a) dry 5% H_2-Ar and in (b) air

As shown in Figure 3.40 (a), the conductivity is first improved as the temperature is increased from RT to about 150 ºC then looses half its magnitude while reaching 700 ºC passing from roughly 6 $S.cm^{-1}$ to just below 3 $S.cm^{-1}$.

After a dwell at 700 ºC of 6 hrs, the sample was cooled down and the pattern obtained on heating was reversibly observed on cooling since the conductivity improved from 700 ºC to 200 ºC before decreasing slightly from 150 ºC to RT. This behaviour at low temperatures, corresponding to the transition from a semi-conductive to a metallic character was also observed in air as can be seen on Figure 3.40 (b) and was followed by a rapid decrease upon oxidation starting at 200 ºC, in accordance with the STA data (Figure 3.37).

Moreover and referring to this latter, oxidation to the orthovanadate should be achieved at 350 ºC, however the conductivity was found to stabilise at this same temperature and remain unchanged up to 700 ºC. Its decrease only started on cooling below 600 ºC and dropped sharply by three orders of magnitude from about 1 $S.cm^{-1}$ at 400 ºC to 1 $mS.cm^{-1}$ at RT, reaching a conductivity similar to the one obtained in a previous study[182]. This plateau value could not be rationalised by any means from the diffraction data obtained afterwards since as shown in Figure 3.33, only orthovanadate phases are obtained, exhibiting monoclinic and tetragonal systems. Partial oxidation of the sample would not explain the observed behaviour as the rate of heating used during the conductivity measurements was slower than the one employed for the STA analysis giving a more stabilised character to the values obtained during impedance recordings compared to the oxidation values resulting from the STA analyses. The only plausible reason may therefore be that the re-oxidation process only occurs on the surface, thus not affecting the electrode's interfaces resulting in high conductivity. Upon more cooling, oxidation increases inducing a volume change large enough to expose the electrode's interfaces to air thus resulting in lower conductivity.

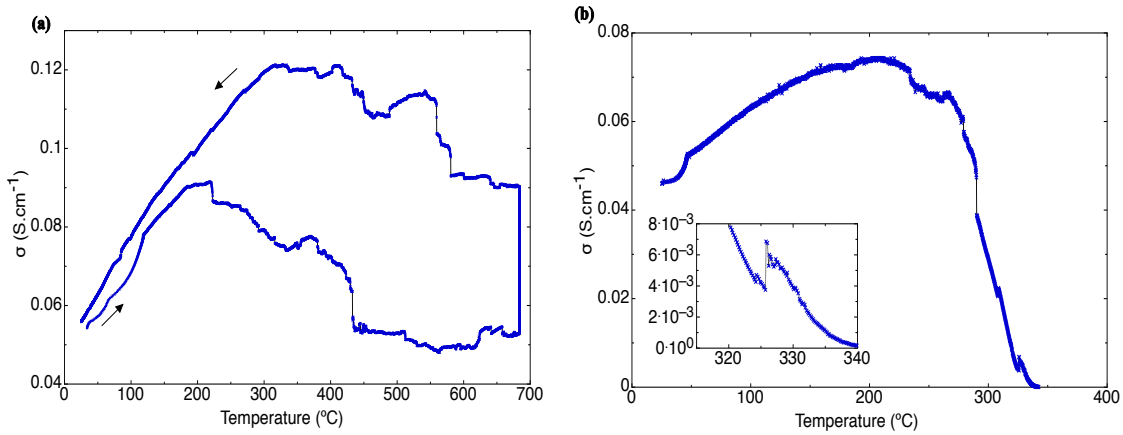

Figure 3.41 Conductivity plots of $CeVO_3$ in (a) dry 5% H_2-Ar and in (b) air

Concerning $CeVO_3$ for the case of dry 5% H_2-Ar (Figure 3.41 (a)), an increase of the conductivity is observed from RT to 220 ºC before a continuous decrease to 440 ºC where the conductivity oscillates around 50 $mS.cm^{-1}$ up to 700 ºC. After a dwell of 12 hrs at this latter temperature, the conductivity is stabilised around 90 $mS.cm^{-1}$. On cooling, an identical pattern is observed, namely a plateau value up to 570 ºC followed by an increase up to 400 ºC where a maximum of 0.12 $S.cm^{-1}$ is attained before a slow decrease to the starting value at RT. The variations in air (Figure 3.41 (b)) repeat the pattern observed for other metavanadates in air or in reduced atmosphere, namely an increase of the conductivity up to a limiting value where it subsequently drops upon oxidation.

The conductivity of $CeVO_3$ in air is lower than in reduced atmosphere from about 10 $mS.cm^{-1}$ at RT and about 20 $mS.cm^{-1}$ around 200 ºC. Beyond that temperature and correlating with the STA data (Figure 3.37), the conductivity sharply drops to 0.3 $mS.cm^{-1}$ at 340 ºC (similar to the value obtained for $CeVO_4$ in [182] under the same conditions) in relation with the oxidation process occurring.

3.2.4. Calcium-doped cerium metavanadate results and discussion

3.2.4.1. Crystal structure

Polycrystalline perovskite structures of $Ce_{1-x}Ca_xVO_3$ were obtained exhibiting orthorhombic and/or monoclinic unit cells of space group *Pnma* (62) and $P2_1/n11$ (14) and are shown in Figure 3.42. The only phase for $x \leq 0.2$ is the orthorhombic form whilst for $x \geq 0.3$, characteristic peaks of both unit cells are found with major phases being the orthorhombic and monoclinic form for $Ce_{0.7}Ca_{0.3}VO_3$ and $Ce_{0.6}Ca_{0.4}VO_3$ respectively.

Rietveld refinements were carried out with both structural and profile parameters being varied. Initial structural and spatial parameters for the orthorhombic perovskite structure with space group *Pnma* (62) were used as mentioned in the literature[183]. Wyckoff sites assigned to Ce (and Ca), V and O were 4*c*, 4*a* and 8*d* and 4*c* respectively. Vanadium and oxygen were always refined with full occupancies, whereas cerium and calcium fractions were varied in accordance with the stoichiometry. Profile refinements were performed using GSAS[136] after space group determination with TOPAS®. The

experimental and calculated profiles are shown in Figure 3.43 with the difference profiles at the bottom and the refinement parameters are shown in Table 3.14. Considering samples with $x \geq 0.3$, refinements using the monoclinic form were attempted however major discrepancies in the unit cell remained for reflections at 2θ values of 23, 32, 47 and 59º corresponding to the orthorhombic strongest peaks. Major phases were therefore assigned, for each composition, on the basis of the observed intensities.

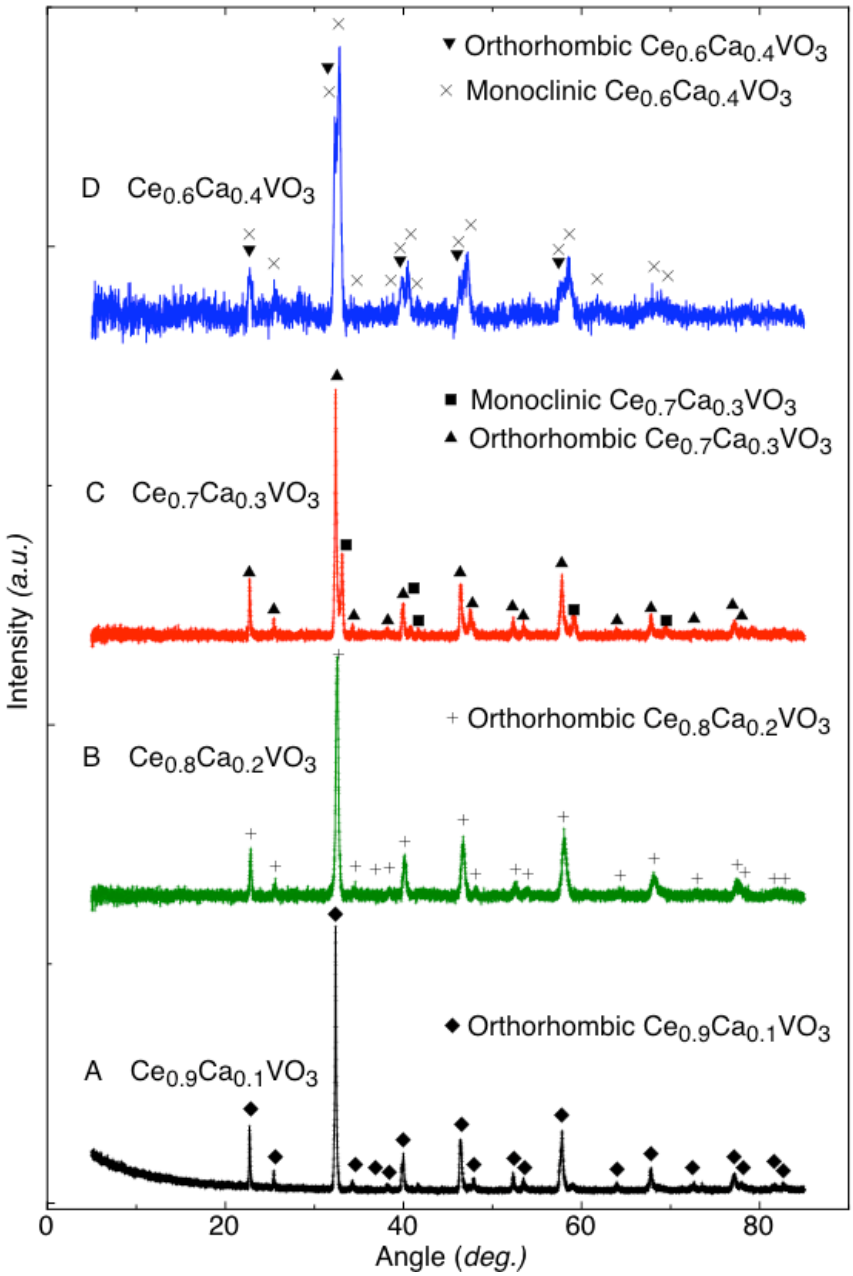

Figure 3.42 XRD patterns of $Ce_{1-x}Ca_xVO_3$ with (A) $x = 0.1$ (B) $x = 0.2$ (C) $x = 0.3$ (D) $x = 0.4$

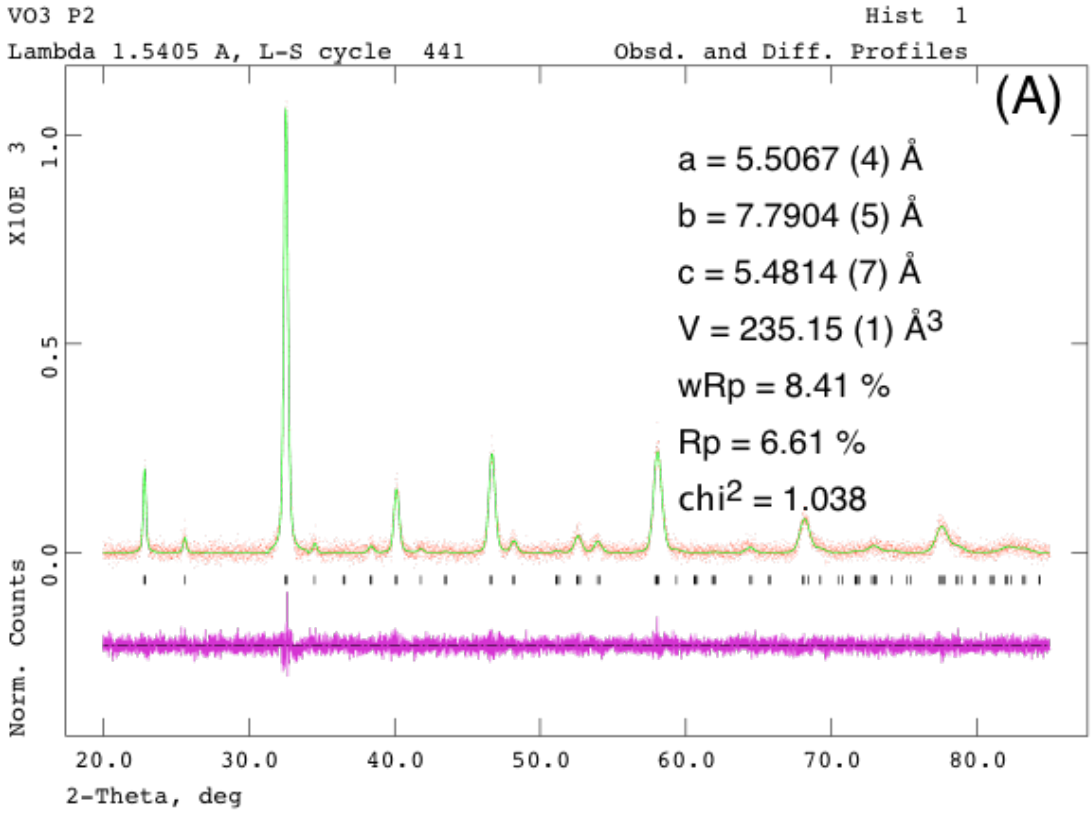

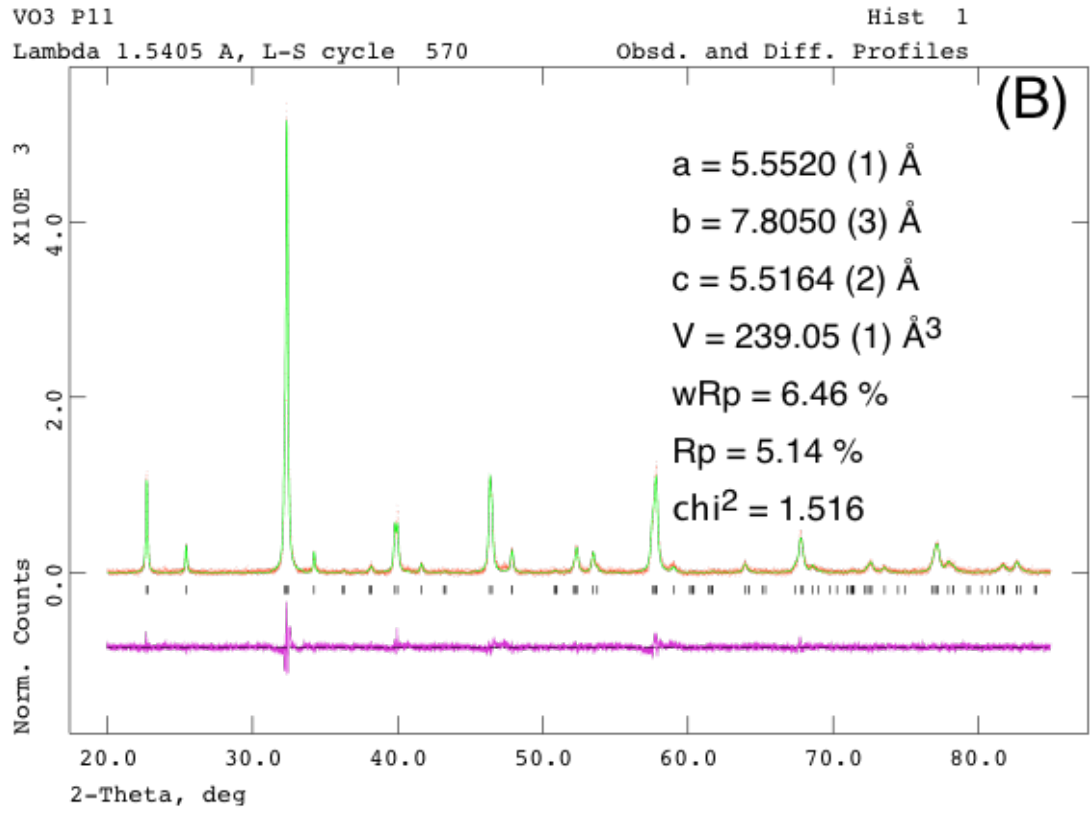

Figure 3.43 GSAS plots of (A) $Ce_{0.8}Ca_{0.2}VO_3$ and (B) $Ce_{0.9}Ca_{0.1}VO_3$

XRD analysis was carried out after the conductivity measurements in air to monitor the stability of the perovskite phase and results are shown in Figure 3.44. Whereas for $Ce_{0.9}Ca_{0.1}VO_3$, the oxidation leads in majority to the formation of the monoclinic phase of the orthovanadate; the oxidation of $Ce_{0.8}Ca_{0.2}VO_3$ and $Ce_{0.7}Ca_{0.3}VO_3$ yield the tetragonal structure of the corresponding orthovanadates and the oxidation of $Ce_{0.6}Ca_{0.4}VO_3$ primarily yields the tetragonal and monoclinic phases of $Ce_{0.6}Ca_{0.4}VO_4$ and $Ca_3(VO_4)_2$. A point worth noting also is that for the $x = 0.1$ sample, both cerium metavanadate and orthovanadate phases are present in the oxidised product whereas for the others, only orthovanadate phases are detected. The high doping level of calcium in the structure of $Ce_{0.6}Ca_{0.4}VO_3$ seems to be the key detrimental factor to its stability and when the oxidation process is started at low temperatures, the monoclinic calcium vanadium oxide phase is simply unconstrained and forms freely.

	Atoms	***x***	***y***	***z***	**Occ.**	U_{iso} **x100**
$Ce_{0.8}Ca_{0.2}VO_3$	Ce	0.4686 (1)	0.2500	0.0086 (1)	0.8	0.4 (1)
	Ca	0.4686 (1)	0.2500	0.0086 (1)	0.2	0.4 (1)
	V	0	0	0	1	0.1 (1)
	O (1)	0.2133 (1)	0.0491 (1)	0.2740 (1)	1	0.9 (1)
	O (2)	0.5094 (1)	0.2500	0.5557 (1)	1	2.6 (1)
$Ce_{0.9}Ca_{0.1}VO_3$	Ce	0.4610 (1)	0.2500	0.0010 (1)	0.9	0.9 (1)
	Ca	0.4610 (1)	0.2500	0.0010 (1)	0.1	0.9 (1)
	V	0	0	0	1	0.2 (1)
	O (1)	0.2316 (2)	0.0492 (1)	0.2835 (1)	1	3.8 (1)
	O (2)	0.5140 (1)	0.2500	0.5783 (1)	1	8.6 (1)

Table 3.14 Atomic positions and thermal factors for $Ce_{0.9}Ca_{0.1}VO_3$ and $Ce_{0.8}Ca_{0.2}VO_3$

Rietveld refinements were carried out with both structural and profile parameters being varied. Initial structural and spatial parameters for the zircon structure were used as mentioned in the literature[148]. Wyckoff sites assigned to Ce and Ca, V and O were 4*a*, 4*b* and 16*h* respectively. Vanadium and oxygen were refined with full occupancies while cerium and calcium fractions were varied in accordance with the stoichiometry.

Profile refinements were performed using GSAS with the experimental and calculated profiles shown in Figure 3.45 (cubic platinum as secondary phase indicated by red markers and difference profiles at the bottom).

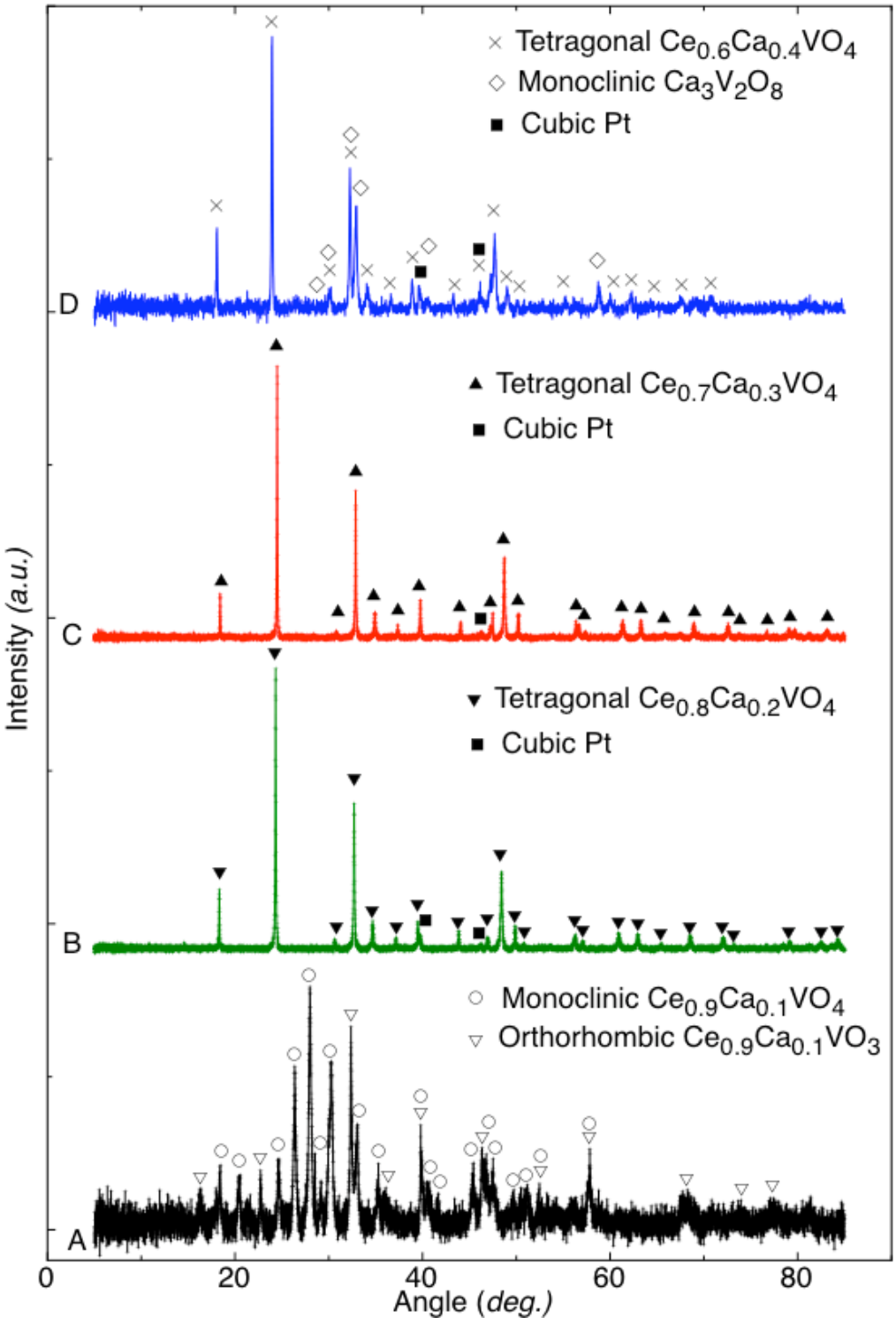

Figure 3.44 XRD patterns of $Ce_{1-x}Ca_xVO_3$ with (A) – (D) x = 0.1 – 0.4 after conductivity measurements

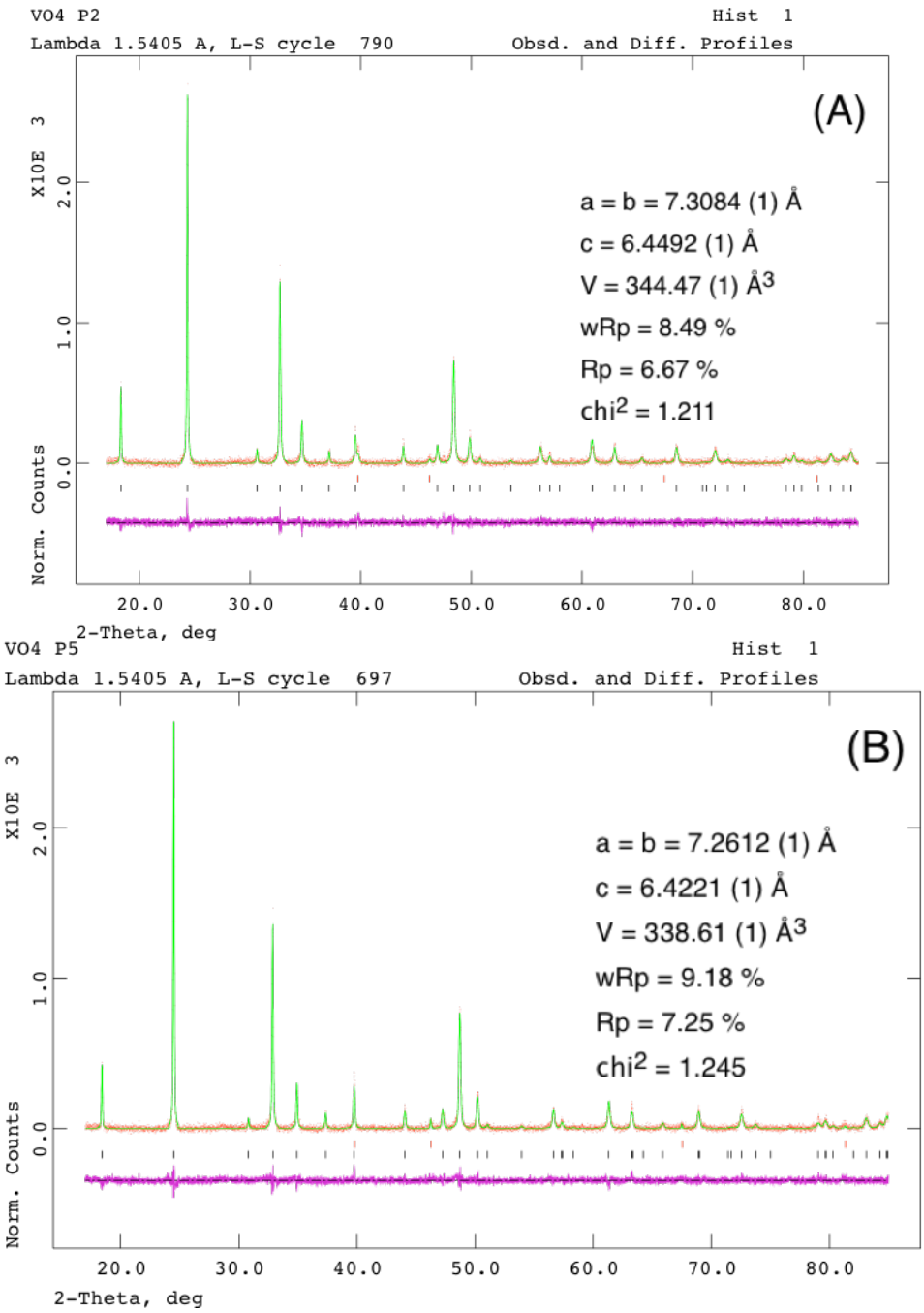

Figure 3.45 GSAS plots of (A) $Ce_{0.8}Ca_{0.2}VO_4$ and (B) $Ce_{0.9}Ca_{0.1}VO_4$

The phase reversibility was tested by reducing the oxidised vanadate from the conductivity test with results given in Figure 3.46 and Table 3.15. The Ca-doped compounds up to $x \leq 0.3$ were found to regain their orthorhombic form making the process fully reversible. One explanation for the single-phase character of $Ce_{0.7}Ca_{0.3}VO_3$ after the second reduction is that experimentally a slightly higher temperature was used namely 925 ºC for 15 hrs instead of the 900 ºC used in the first round of reduction.

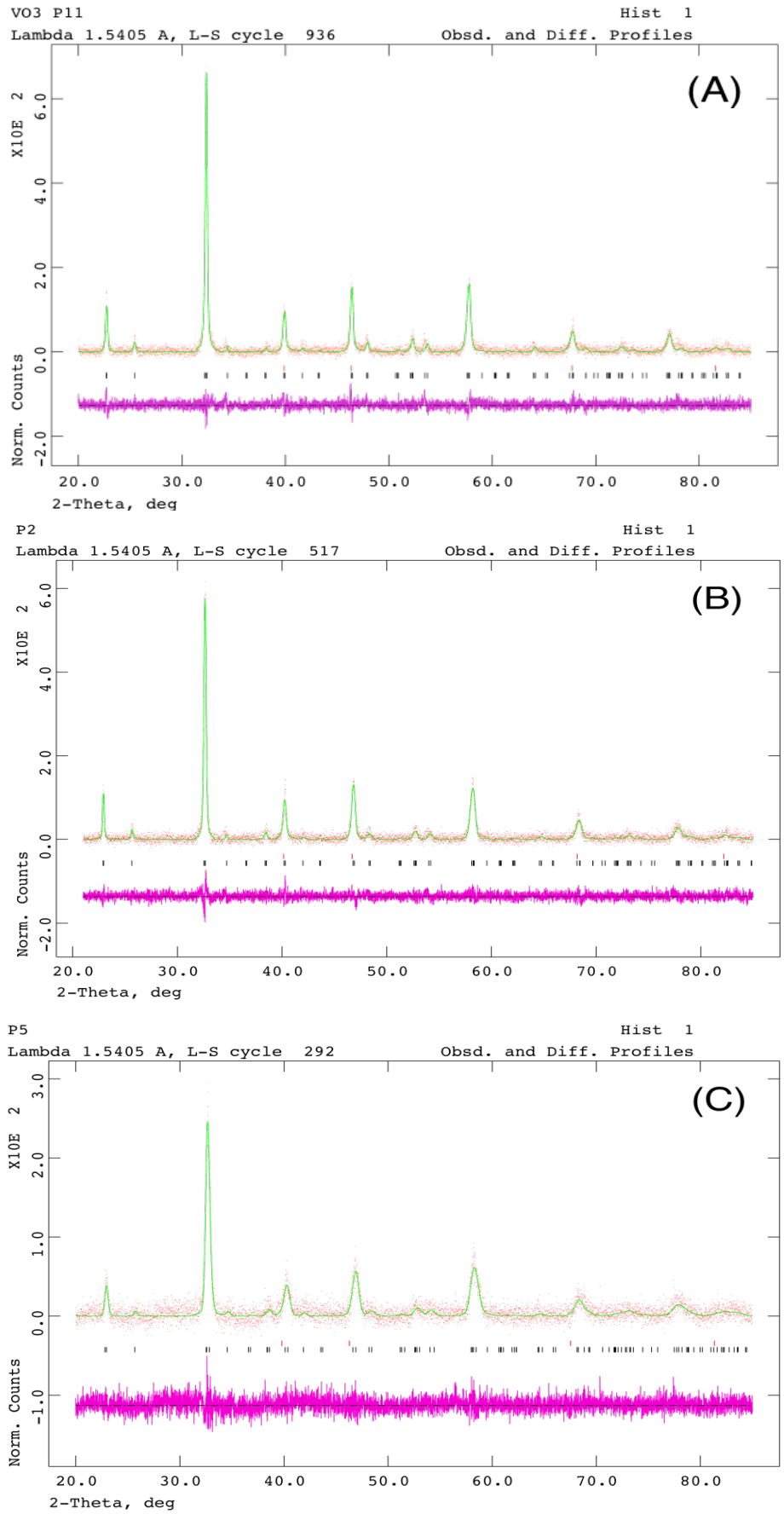

Figure 3.46 GSAS plots of (A) $Ce_{0.8}Ca_{0.2}VO_3$, (B) $Ce_{0.9}Ca_{0.1}VO_3$ and (C) $Ce_{0.7}Ca_{0.3}VO_3$

	$Ce_{0.9}Ca_{0.1}VO_3$	$Ce_{0.8}Ca_{0.2}VO_3$	$Ce_{0.7}Ca_{0.3}VO_3$
Space Group	*Pnma* (62)		
a (Å)	5.5207 (5)	5.4775 (1)	5.4985 (2)
b (Å)	7.8097 (7)	7.7407 (5)	7.7879 (3)
c (Å)	5.5490 (5)	5.4988 (1)	5.4509 (2)
V (Å^3)	239.24 (2)	233.14 (2)	233.42 (1)
wRp (%)	14.06	13.73	13.44
Rp (%)	11.03	10.82	10.57
χ^2	1.141	1.099	1.114

Table 3.15 Refinement parameters of $Ce_{1-x}Ca_xVO_3$ with $0 \leq x \leq 0.3$ after 2nd reduction cycle

3.2.4.2. Thermal analysis

To ensure total reduction of the synthesised samples, thermal analyses of the sintered pellets prior to reduction were carried out in air and in 5% H_2-Ar. Air analyses were carried out up to 1000 ºC at a rate of 5 ºC.min^{-1} and the results obtained were found to be in accord with ref[160] and served as a limiting value for the measurement in hydrogen, carried out up to 950 ºC at the same rate as in air with the same gas flow.

A temperature of 900 ºC was determined as being sufficient to fully reduce all samples as shown in Figure 3.47, even though for the second cycle of reductions, the highest doping stable sample was reduced at 925 ºC allowing formation of a single phase compound (orthorhombic only) in comparison to the two-phase metavanadate (both monoclinic and orthorhombic) obtained after initial reduction. The increase of reduction temperature was rationalise in order to determine if a single phase character could be obtained for the 30 % calcium doped compound in the eventuality that the initial 15 hrs at 900 ºC might have left the sample at an intermediate thermodynamic level where time was long enough to allow VO_3 formation but temperature was too low to solely stabilise the orthorhombic phase. Weight changes observed for calcium-doped compounds were similar in nature to those observed in a previous study on strontium-doped cerium metavanadates[186].

The thermal stabilities in air of the metavanadates formed were also determined and are shown in Figure 3.48. Data were recorded up to 700 ºC at a rate of 5 ºC.min^{-1} in order to match the experimental conditions from the conductivity measurements. Upon oxidation, all samples gained weight (between ~7 and 8 %), which can be related to the absorption of one oxygen ion (theoretically 6.98 to 8.04 % when increasing the dopant level respectively).

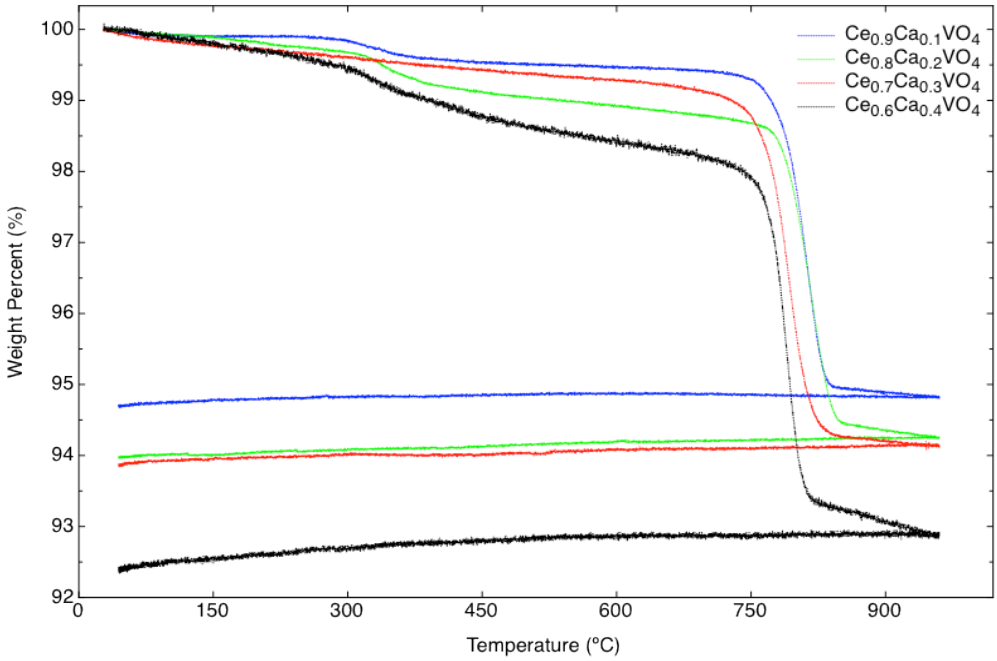

Figure 3.47 TGA curves of $Ce_{1-x}Ca_xVO_4$ in 5% H_2-Ar from RT to 950 ºC

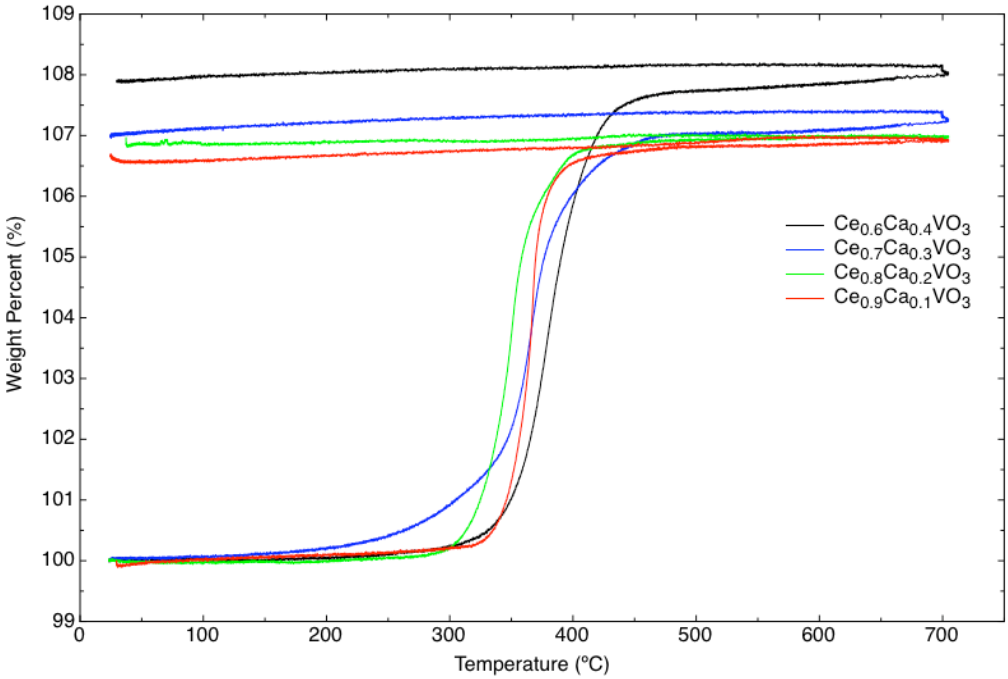

Figure 3.48 TGA curves of $Ce_{1-x}Ca_xVO_3$ in air from RT to 700 ºC

Stabilities with dwellings at 180 ºC were also carried out in order to verify usability below 200 ºC. All samples were analysed under flowing air over 2 hrs at 180 ºC with a 1 ºC.min^{-1} heating/cooling rate. Results obtained are shown in Figure 3.49 and 3.50 for the thermal analyses and Xrd post-analyses respectively.

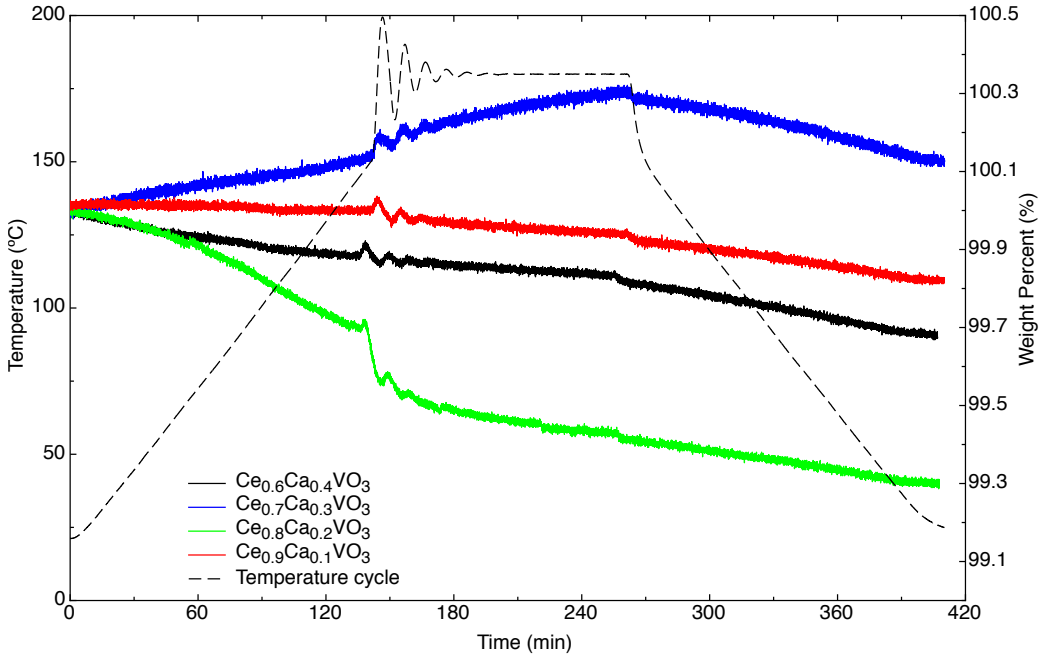

Figure 3.49 TG curves of $Ce_{1-x}Ca_xVO_3$ in air up to 180 ºC with 2 hrs dwell

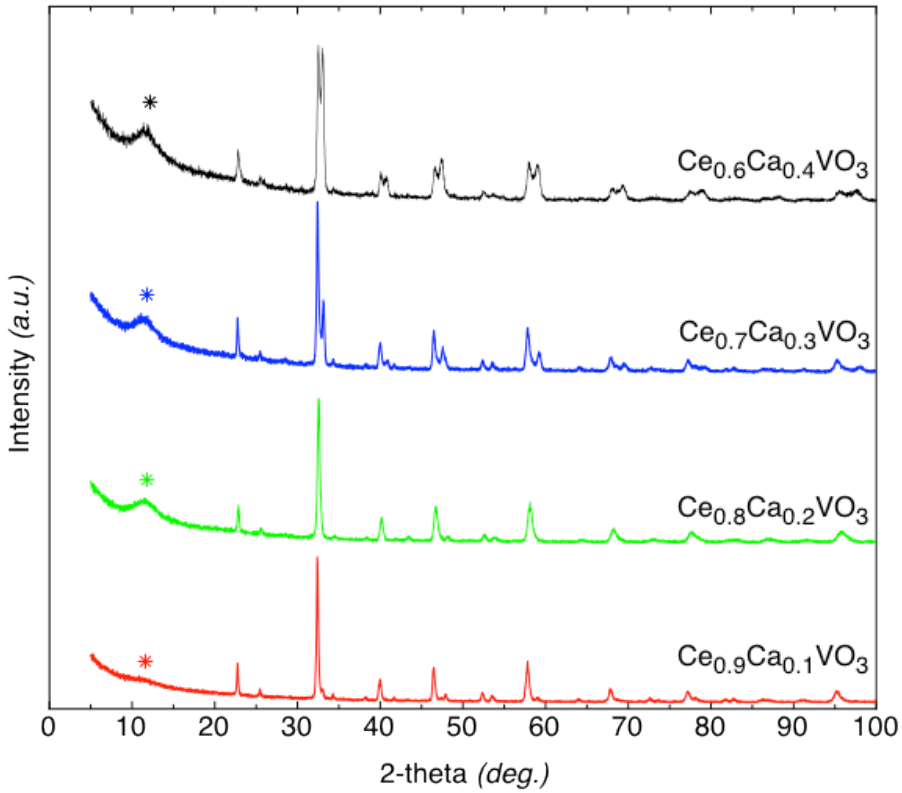

Figure 3.50 XRD of $Ce_{1-x}Ca_xVO_3$ after thermal analysis at 180 ºC with 2 hrs dwell (* grease support peak)

It can be seen that from thermogravimetric and structural analyses after thermal analyse all compounds are stable to air atmosphere up to 180 ºC. Each compound does retain the crystal structure it exhibited prior to thermal analysis, namely orthorhombic for doping lower than 20 % and a mixture of orthorhombic and monoclinic phases for doping level higher than 30 %.

3.2.4.3. Microstructure

Microstructure analysis as a function of the oxygen content was carried out for comparison over the entire cycle of experiment with SEM pictures of the orthovanadates and of the metavanadates shown in Figure 3.51 for the case of $Ce_{0.8}Ca_{0.2}VO_x$.

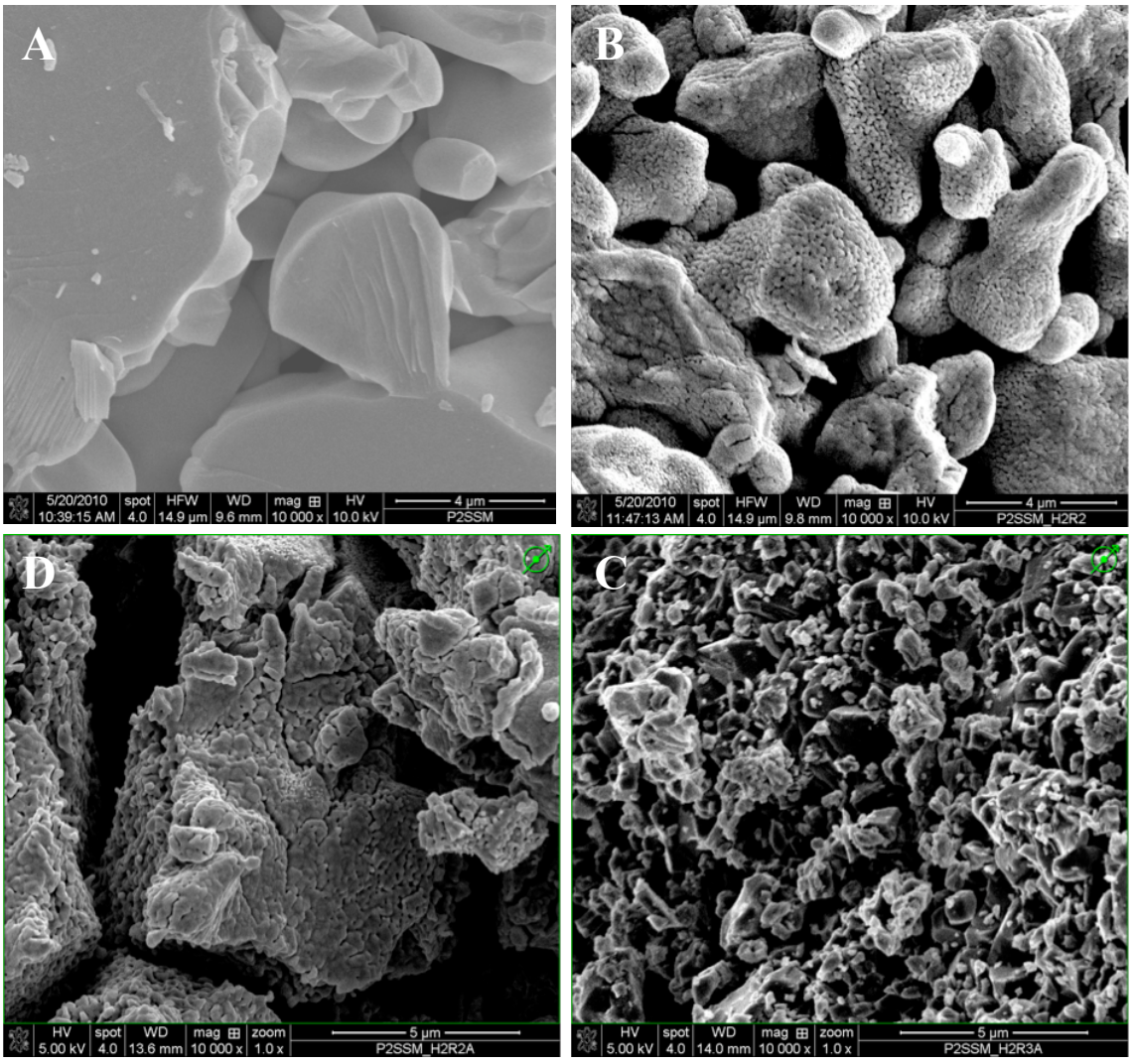

Figure 3.51 $Ce_{0.8}Ca_{0.2}VO_x$ as (A) VO_4, (B) VO_3, (C) after conductivity measurement and (D) back to VO_3

The pictures – all taken at x10000 from the centre of cracked pellets – exhibit a well sintered structure of plain particles in case of the orthovanadate whereas the same magnification with the metavanadate results in an impressive particle microporosity with channels and void spaces not observed in the orthovanadate thus indicating to be a consequence of the reduction leading to higher conductivity. This phenomenon also confirms that the loss of oxygen is happening locally without great densification and/or of porosity thus indicating that the sintering of the yielded metavanadate is insignificant.

This special property has the potential of being beneficial to the redox cyclability if used as an anode for SOFC; and in fact, this is exactly what is happening as after conductivity measurements in air, a sintered – yet with smaller particle size distribution – channels- and voids-free sample is obtained. If re-exposed to a reducing atmosphere for a second cycle, the microporosity is recovered even though this latter property was found to be dependent on time of exposure as illustrated in Figure 3.52 where $Ce_{0.6}Ca_{0.4}VO_x$ is taken as example.

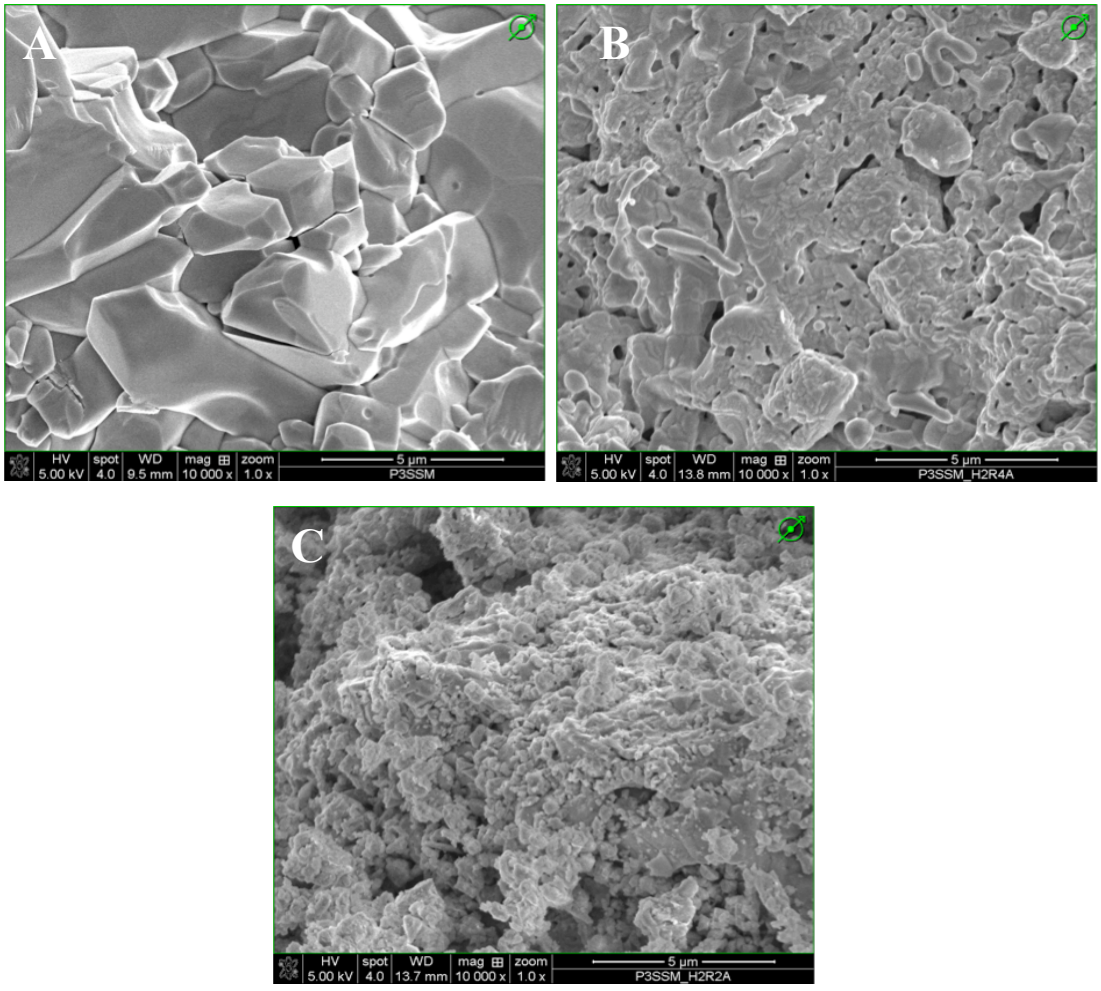

Figure 3.52 $Ce_{0.6}Ca_{0.4}VO_x$ as (A) VO_4, (B) VO_3 and (C) after conductivity measurement in H_2

In its orthovanadate form, particles are plain and have well defined contours, whereas after exposure to 5% H_2-Ar for 55 hrs (15 hrs of initial reduction and 40 hrs during conductivity measurements) the similar microporosity is observed – to a lesser extent however than in Figure 3.51 – with an intermediate porous state obtained after 15 hrs though already in the metavanadate form. The main difference thus resides in the behaviour of the particle shells of the orthovanadates – physically speaking – during reduction and whether their integrity is sustained or not while oxygen is being lost.

3.2.4.4. Conductivity

Impedance measurements and temperature recordings were combined to obtain plots of the conductivity against temperature and are shown in Figure 3.53 for $Ce_{1-x}Ca_xVO_3$ in dry 5% H_2-Ar and in Figure 3.54-56 for $Ce_{1-x}Ca_xVO_3$ in air with decreasing *x* respectively.

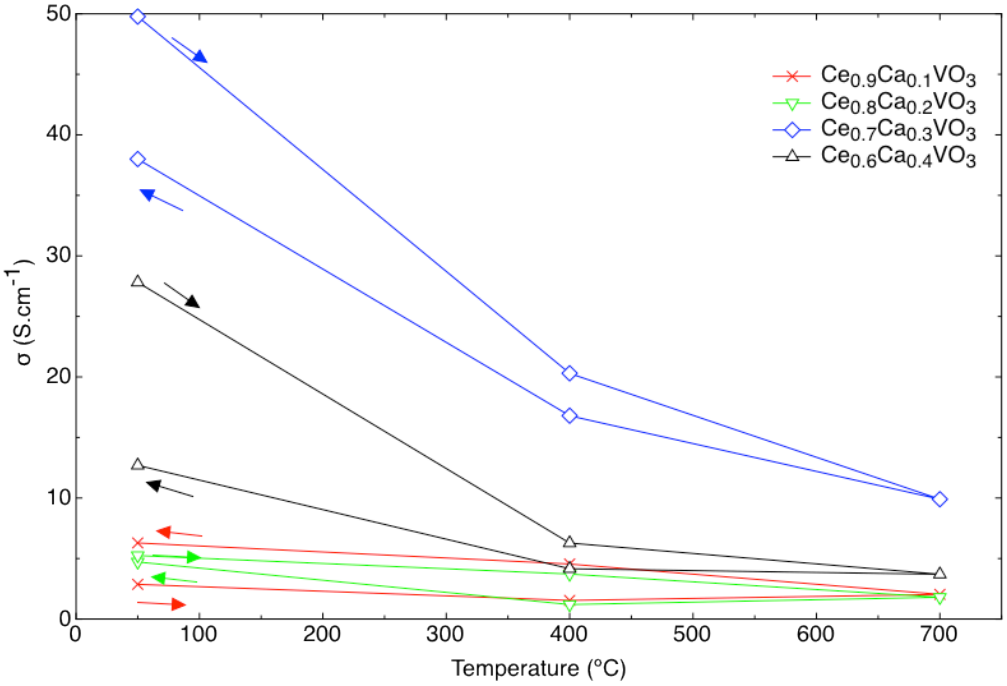

Figure 3.53 Conductivity plots against temperature of $Ce_{1-x}Ca_xVO_3$ in dry 5% H_2-Ar

In reducing atmosphere, the conductivities behave in the same pattern of decreasing magnitude while reaching 700ºC. After stabilisation periods of one day, similar patterns are reversibly observed on cooling as values are improving from 700 ºC to RT, without fully recovering the initial value however probably caused by a too short period of stabilisation at very low temperature. It can be observed that with increased

calcium level, conductivity is also improved with the exception of $Ce_{0.6}Ca_{0.4}VO_3$, which exhibits a lower conductivity than $Ce_{0.7}Ca_{0.3}VO_3$. This is related to the phase composition of those two compounds and the lower conductivity of the monoclinic phase (predominant in $Ce_{0.6}Ca_{0.4}VO_3$) compared to the orthorhombic one. Also, the unusual phenomenon of having a higher conductivity at RT after cooling than before heating for sample $Ce_{0.9}Ca_{0.1}VO_3$ may be explained by the fact that the compounds had already started to reoxidise – partially at least – during the time elapsed from the moment of the reduction and the subsequent X-ray analysis and the following conductivity analysis.

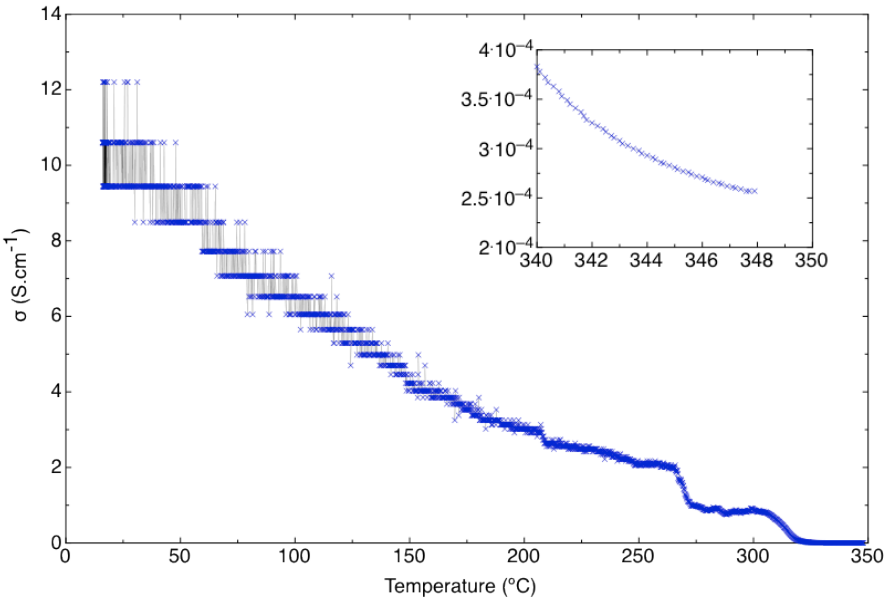

Figure 3.54 Conductivity plot against temperature of $Ce_{0.6}Ca_{0.4}VO_3$ in air

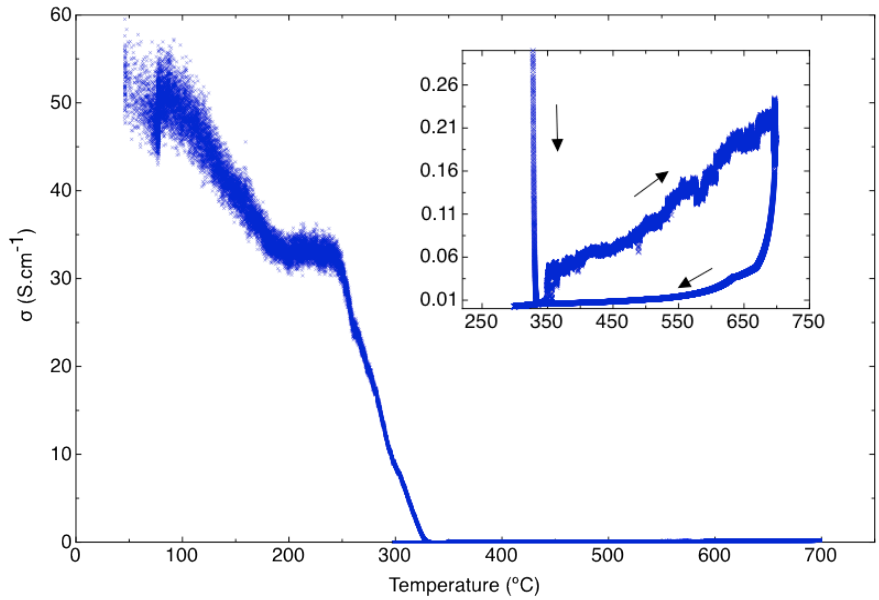

Figure 3.55 Conductivity plot against temperature of $Ce_{0.7}Ca_{0.3}VO_3$ in air

For sample $Ce_{0.6}Ca_{0.4}VO_3$ in air, decreasing conductivity was observed – as can be seen on Figure 3.54 – namely an initial decrease followed by another decrease upon oxidation starting at 200 ºC, in accordance with the STA data (Figure 3.48) with a plateau value at about 275 ºC corresponding to the partial oxidation into calcium vanadium oxide before reaching a value of 0.3 $mS.cm^{-1}$ in accordance to the one obtained in a previous study[181].

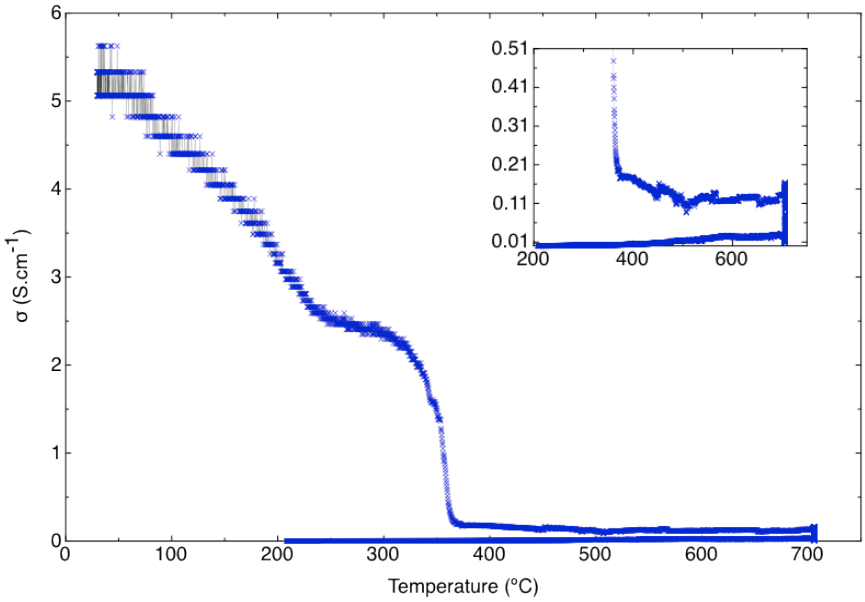

Figure 3.56 Conductivity plot against temperature of $Ce_{0.8}Ca_{0.2}VO_3$ in air

For $Ce_{0.7}Ca_{0.3}VO_3$, the same decreasing conductivity is observed followed by another decrease upon oxidation starting around 200 ºC, in accordance with the STA data (Figure 3.48) with a plateau value this time between 200 and 250 ºC and a low point of 0.01 $S.cm^{-1}$ at 350 ºC before reaching a value of 0.23 $S.cm^{-1}$ at 700 ºC. After a day dwell during which the conductivity had virtually not varied in comparison to the behaviour observed in reduced atmosphere, the conductivity rapidly dropped upon cooling reaching values (<0.005 $S.cm^{-1}$) similar to those obtained in another study[181].

In the case of $Ce_{0.8}Ca_{0.2}VO_3$, again a decrease is observed with a plateau around 250 ºC corresponding to the partial superficial oxidation into orthovanadate before reaching a value of 0.2 $S.cm^{-1}$ from 360 ° up to 700 ºC. After 24 hrs of dwelling at 700ºC, the conductivity decreased upon cooling to reach levels in accordance with orthovanadates obtained in a previous study[181]. Concerning $Ce_{0.9}Ca_{0.1}VO_3$ the variations in air, shown in Figure 3.57 repeat the pattern observed for other metavanadates, namely a generally slow decrease up to about 200 ºC where the conductivity subsequently drops upon oxidation (similar to the value obtained in ref[181] under the same conditions). Also,

whilst all metavanadates have similar or higher values of conductivity at RT in air than final RT conductivities in reduced atmosphere, $Ce_{0.9}Ca_{0.1}VO_3$ is the only one where the increase is that significant.

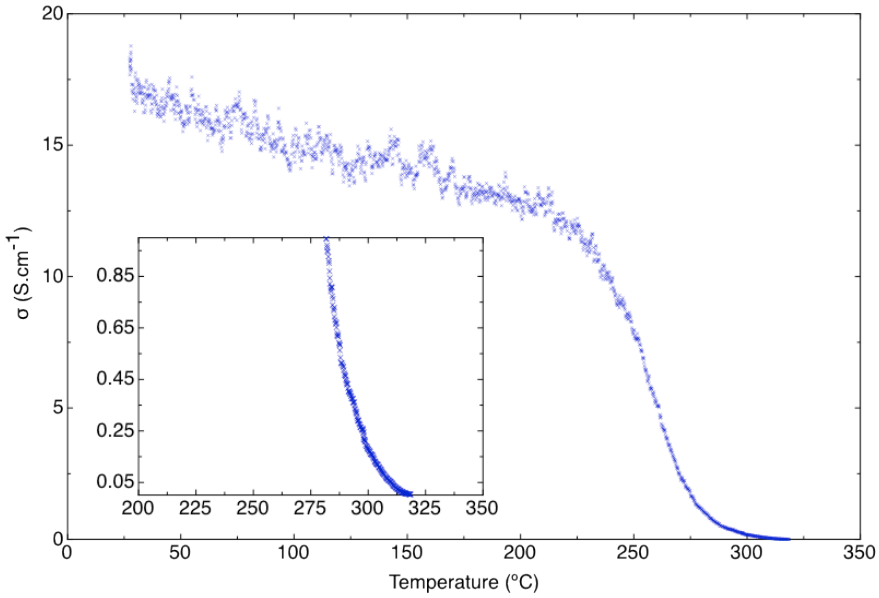

Figure 3.57 Conductivity plot against temperature of $Ce_{0.9}Ca_{0.1}VO_3$ in air

In the same manner as thermal testing was carried out with an isotherm at 180 ºC to evaluate usability as an anode material in low-temperature SOFCs, long lasting conductivity measurements were carried out at the same temperature in air for sample $Ce_{0.7}Ca_{0.3}VO_3$ over a 72 hrs period. The choice of composition was based on overall conductivity values and the stability plot obtained is shown in Figure 3.58 below.

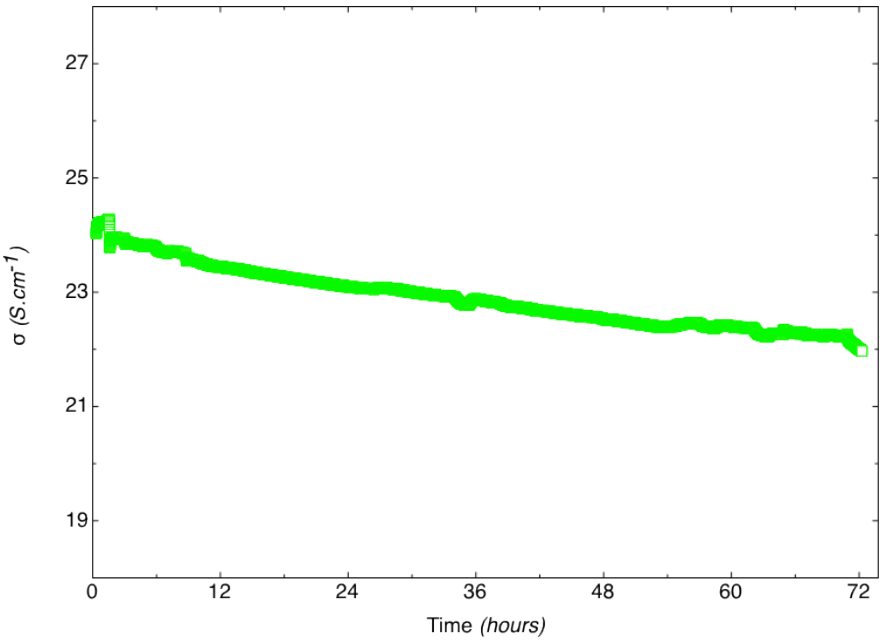

Figure 3.58 Stability plot against time of $Ce_{0.7}Ca_{0.3}VO_3$ in air at 180 ºC

Over the studied period of time, the compound was found to be stable on a practical point of view with conductivity variations lower than 10 %. Even though a decreasing trend is noticeable, it has to be put in context as anode materials are ideally not supposed to be exposed to air (considering that no electrolyte gas diffusion is occurring) while this particular stability test was carried out in static atmospheric environment (a considerable oxygen-rich environment).

3.2.5. Conclusions

Single phase crystals of $Ce_{1-x}M_xVO_3$ (M = Ca, Sr with $0.1 \leq x \leq 0.4$ and $0 \leq x \leq 0.15$ respectively) were synthesised by a standard ceramic technique. All Sr-doped samples were found to exhibit the orthorhombic perovskite structure in space group *P*nma (62) while all Ca-doped samples exhibited orthorhombic – *P*nma (62) – and/or monoclinic – $P2_1/c$ (14) – unit cells. Impedance measurements carried out in air and in reduced atmosphere have shown that the conductivities of Ca/Sr-doped $CeVO_3$ are higher both in air and in dry 5% H_2-Ar compared to $CeVO_3$. This latter actually behaves in the same manner as its orthovanadate conjugate whereas the conductivity of the Ca/Sr-doped compounds was found to be of three orders of magnitude higher in the metavanadate form compared to the orthovanadate counterpart. Moreover, while the oxidation of the reduced $CeVO_3$ and $Ce_{0.9}Ca_{0.1}VO_3$ to $Ce_{0.9}Ca_{0.1}VO_4$ doesn't yield back the zircon structure, in the case of other Ca-doped $CeVO_3$ as well as $Ce_{0.85}Sr_{0.15}VO_3$, a reversible phase transition (with formation of calcium vanadium oxide for $x = 0.4$) has been established. It was therefore concluded that due to the instability of $CeVO_3$ and $Ce_{0.9}Ca_{0.1}VO_3$ upon oxidation leading to a multiple of undesired phases, the formation of $Ca_3(VO_4)_2$ for $Ce_{0.6}Ca_{0.4}VO_3$ and negative TCE, $Ce_{1-x}Sr/Ca_xVO_3$ compounds are not suitable *per se* as anode materials for IT-SOFCs, however the reversible phase transition observed for Ca/Sr-doped metavanadates to orthovanadates and the general character of the compounds investigated may find some use for low temperature fuel cells (< 200 ºC as suggested by stability tests carried out in air for $Ce_{0.7}Ca_{0.3}VO_3$ reflecting usability in an oxygen-rich atmosphere) and/or on an electrolyte-supported cell assembly.

4. Novel proton-conducting electrolyte and potential use in IT-SOFCs

4.1. Background

Proton- and mixed ionic/electronic conducting ceramics have attracted much attention in recent years with the possibility of a wide range of applications including fuel cells, gas sensors and thin films[187].

Among the materials being the focus of attention are cerium and zirconium-based perovskite (ABO_3) in either pure or doped form. Both the *A* and *B* site can be doped with several elements with barium and strontium the most used as on *A*-site element and yttrium or gadolinium as a *B*-site dopant. The structures predominantly studied are based on alkaline and alkaline-earth doping of the *A*-site as providing the most interesting performance in terms of protonic conductivity[29, 62-67, 188, 189]. The doping of the *B*-site with a low-valent atom (yttrium, gadolinium or ytterbium on a cerium site) may generate oxygen vacancies and gives rise to a mixed conduction in water-containing oxygen- and hydrogen-rich atmospheres with predominance of electronic conduction likely at very high temperatures (>700 ºC). Experimentally speaking, barium and strontium cerates exhibit higher total ionic conductivity than their zirconate equivalent with the latter still favoured principally due to their stability in water and carbon dioxide containing atmospheres[69, 70].

A recent study has however demonstrated that 10% zirconium doping was sufficient to stabilise a 20% yttrium $BaCeO_3$ (BCs) up to 500 ºC in CO_2-containing (2%) as well as H_2O-containing (15%) hydrogen without any decomposition and exhibiting a higher conductivity below 550 ºC than the most commonly used electrolytes (GDC and YSZ)[190]. A major disadvantage with the use of zirconate materials is the high sintering temperature required (usually above 1600 ºC for several hrs) while cerate materials tend to sinter earlier (around 1500ºC).

A large amount of studies have therefore being carried out to improve sinterability and lower its temperature using either low-melting point elements (like cobalt, iron, zinc or bismuth...) or by incorporating other elements directly into the lattice [191-197] (with one disadvantage of possibly replacing some lattice atoms by the sintering aid elements like it is the case for zinc in barium zirconates)[196].

Praseodymium-doped compounds were investigated to some extent with the study of Pr/Gd barium cerate as potential cathode materials that required 10 hrs at 1650 ºC to achieve usable density[198] and the recently published Pr-doped barium zirconates sintered 8 hrs at 1600 ºC[199]. Bismuth-doped compounds were investigated to some extent with the study of both zirconate[191] and cerate analogues as potential cathode materials[200] as well as electrolytes[201]. When used as sintering aid by Duval *et al*.[191], 24 hrs sintering at 1720 ºC was insufficient to attain usable density and when introduced in the lattice [200, 202], bismuth was found to greatly influence conductivity towards electronic dominance via *p*-type conduction. The use of cobalt and/or nickel as a dopant or sintering aid has been reported in many yttrium zirconate compounds [203-205] as well as in some cerates [206-208] and all report a lowering of the required sintering temperature to achieve high density, albeit electrical properties are affected. Praseodymium-doped barium cerates on the other hand still require relatively higher sintering temperatures [199, 209] and although a recent study [210] showed that milder conditions could result in high density and thus the effect of cobalt addition on the structural, thermal and electrical properties of Pr-Y co-doped barium cerates were studied.

4.2. Experimental

4.2.1. Materials and properties

Barium carbonate (99% Alfa-Aesar), cerium oxide (99.5% REO Alfa-Aesar), zirconium oxide (99+% Alfa-Aesar), yttrium oxide (99.9% REO Alfa-Aesar), praseodymium oxide (99% REO Alfa-Aesar), cobalt (II/III) oxide (99+% Alfa-Aesar) and bismuth oxide (99.9% Aldrich) for the solid-state syntheses and duty free ethanol (Fisher Scientific) for ball milling were used as received.

Yttria-doped barium cerates were synthesised by solid state reaction after ball milling in duty free ethanol. Typically, stoichiometric amounts of the respective oxides were ball milled for 8 hrs in duty free ethanol at 400 rpm in periods of one hr with inverse rotation and a pause of ten minutes between each repetition using a FRITSCH Pulverisette 6. Powders were then dried, pressed into large pellets and fired twice for 12 hrs at 1100 ºC with heating/cooling rates of 5 ºC min^{-1} with intermediate grinding. Fired powders were then pressed into pellets of diameter 13 mm and sintered at 1400 or 1450 ºC for 6 hrs or 'quick-sintered' at 1500 ºC for 1 hr – namely a direct introduction of the pellet-containing crucible into the furnace at 1500 ºC and subsequent quenching after a dwell time of one hr – depending on the composition for bismuth based compounds (Table 4.1), quick sintered at 1500 ºC for 1 hr for $BaCe_{0.7-x}Zr_yY_{0.3-y-z}Pr_zBi_xO_{3-\delta}$compounds as given in Table 4.2 and fired 1 hr at 1400 ºC or 1500 ºC for cobalt-doped compounds (Table 4.3).

Designation	Composition	Sintering conditions	Relative density
BCYB	$BaCe_{0.7}Y_{0.2}Bi_{0.1}O_{3-\delta}$	Quick sintering 1500 °C, 1 hr	98.4 %
BCZYB_03	$BaCe_{0.7}Zr_{0.1}Y_{0.05}Bi_{0.15}O_{3-\delta}$	1400 °C, 6 hrs	99.9 %
BCZYB_04	$BaCe_{0.6}Zr_{0.1}Y_{0.15}Bi_{0.15}O_{3-\delta}$	1400 °C, 6 hrs	99.9 %
BCZYB_05	$BaCe_{0.6}Zr_{0.1}Y_{0.1}Bi_{0.2}O_{3-\delta}$	1400 °C, 6 hrs	99.9 %
BCZYB_06	$BaCe_{0.6}Zr_{0.1}Y_{0.2}Bi_{0.1}O_{3-\delta}$	Quick sintering 1500 °C, 1 hr	99.6 %
BCZYB_07	$BaCe_{0.5}Zr_{0.1}Y_{0.2}Bi_{0.2}O_{3-\delta}$	1450 °C, 6 hrs	98.5 %

Table 4.1 Designations and sintering conditions of the studied bismuth-doped $BaCeO_3$

Designation	Composition
BCYP	$BaCe_{0.7}Y_{0.2}Pr_{0.1}O_{3-\delta}$
BCZYP15	$BaCe_{0.7}Zr_{0.1}Y_{0.05}Pr_{0.15}O_{3-\delta}$
BCZYP10	$BaCe_{0.7}Zr_{0.1}Y_{0.1}Pr_{0.1}O_{3-\delta}$
BCZYPB	$BaCe_{0.6}Zr_{0.1}Y_{0.1}Pr_{0.1}Bi_{0.1}O_{3-\delta}$

Table 4.2 Detailed description of the $BaCe_{0.7-x}Zr_yY_{0.3-y-z}Pr_zBi_xO_3$ compounds

Designation	Composition	Sintering conditions
BCYP	$BaCe_{0.7}Y_{0.2}Pr_{0.1}O_{3-\delta}$	Quick sintering 1500 °C, 1 hr
BCYP_03	$BaCe_{0.75}Y_{0.05}Pr_{0.15}Co_{0.05}O_{3-\delta}$	1400 °C, 1 hr
BCYP_04	$BaCe_{0.75}Y_{0.075}Pr_{0.15}Co_{0.025}O_{3-\delta}$	1400 °C, 1 hr
BCYP_05	$BaCe_{0.7}Y_{0.175}Pr_{0.1}Co_{0.025}O_{3-\delta}$	1500 °C, 1 hr

Table 4.3 Designation and sintering conditions of the studied cobalt-doped BCs

To prevent barium evaporation at high temperature, pellets were buried into the as-prepared powder. For the conductivity measurements, pellets obtained were coated with platinum paste and fired at 900 ºC for 1 hr with heating/cooling rates of 5 ºC min^{-1}.

4.2.2. Characterisation and conductivity

4.2.2.1. Powder X-ray diffraction

X-ray data were collected on a PANanalytical X'Pert Pro in the Bragg-Brentano reflection geometry with a Ni-filtered Cu Kα source (1.5405 Å), fitted with a X'Celerator detector and an Empyrean CuLFF XRD tube. Absolute scans in the 2θ range of 5-100º with step sizes of 0.0167º were used during data collection.

4.2.2.2. Thermal analysis

TG/DSC analyses were performed using a Stanton Redcroft STA/TGH series STA 1500 operating through a Rheometric Scientific system interface controlled by the software RSI Orchestrator in flowing air and 5% H_2-Ar at a flow rate of 50 ml min^{-1}.

Analyses were also carried out in a wet reducing atmosphere by bubbling 5% H_2-Ar gas through RT water at a flow rate of 50 ml min^{-1}.

4.2.2.3. Scanning electron microscopy

SEM pictures were taken with the use of a Quanta 3D FEG scanning electron microscope (FEI Company) with voltages of 5 kV.

4.2.2.4. Infrared spectroscopy

Infrared scans by Attenuated Total Reflectance (ATR) were acquired with an ABB MB3000 FT-IR laboratory spectrometer fitted with a MIRacle™ single reflection diamond/ZnSe crystal plate in the range 4000 to 600 cm^{-1} and an apodised resolution of 4 cm^{-1}.

4.2.2.5. Dilatometry

Dilatometric measurements were carried out using a Netzsch DIL 402 PC running under Proteus® software up to temperature of 1000 ºC in flowing air (50 ml min^{-1}) with a ramp up and down of 5 ºC min^{-1} on all single phase materials.

4.2.2.6. Conductivity

Total conductivity measurements were carried out using a computer-controlled Solartron Analytical® SI 1260 frequency response analyser within a temperature range of 700 ºC to 300 ºC and impedance data were recorded with the impedance measurement software, SMaRT®. Platinum coated pellets were fitted into the measuring apparatus and measurements were carried out in ambient air and then in a reduced atmosphere of 5% H_2-Ar dried through 98% H_2SO_4 firstly and humidified through a solution of water secondly. Recordings were made on cooling from 700 °C to 300 °C by increment of 50 °C after stabilisation was attained at 700 ºC.

4.3. Pr-doped barium yttrium cerates

4.3.1. Crystal structure

Single-phase perovskite structures were obtained for all samples. Rietveld refinements were carried out with both structural and profile parameters being varied. Initial structural and spatial parameters for the orthorhombic perovskite structure with space group *I mma* (74) were used as mentioned in the literature[211] as providing the best initial fit with the experimental patterns. Wyckoff sites assigned to Ba, Ce (and Zr, Y, Pr, Bi) and O were 4*e*, 4*b* and *8g* and 4*e* respectively. Barium and oxygen were always considered – during the refinement processes – with full occupancies, whereas *B*-site atoms occupancies were varied in accordance with the stoichiometry. Profile refinements were performed using GSAS[136] after space group determination with HighScore Plus. The experimental and calculated profiles are shown in Figures 4.1-4 for BCYP, BCZYP15, BCZYP10 and BCZYPB respectively and the refinement and lattice parameters in Table 4.4.

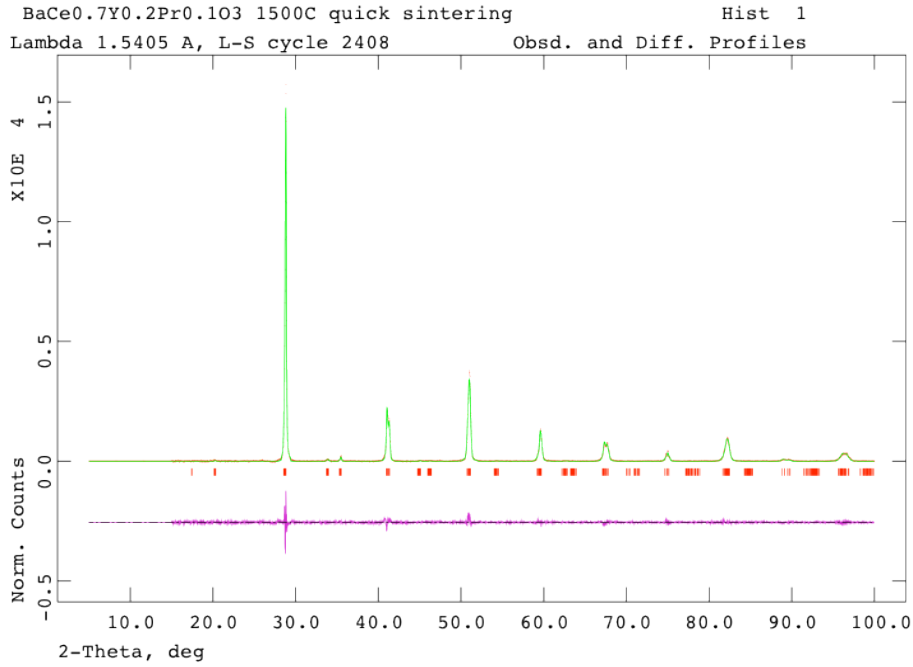

Figure 4.1 GSAS plot of $BaCe_{0.7}Y_{0.2}Pr_{0.1}O_3$

All atoms substituting cerium being on the *B*-site of the perovskite structure, replacing Ce by Zr, Pr and Bi or a mixture of all three has the effect of lowering the average radius of the perovskite *B*-site, optimising its structure towards a smaller spatial

occupation, hence the decrease of lattice parameters and volume observed from the structural refinements. Moreover, this correlation also confirms the results from the refinements as to the incorporation of the diverse dopants into the lattice of the barium cerate in comparison to other perovskite compounds that are densified using low-melting point components as a sintering aid.

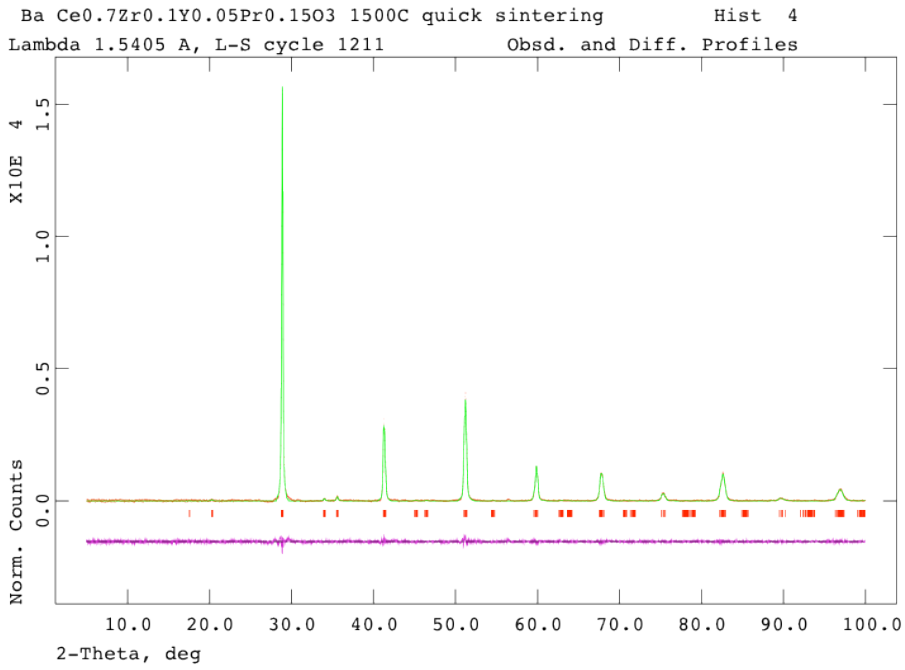

Figure 4.2 GSAS plot of $BaCe_{0.7}Zr_{0.1}Y_{0.05}Pr_{0.15}O_3$

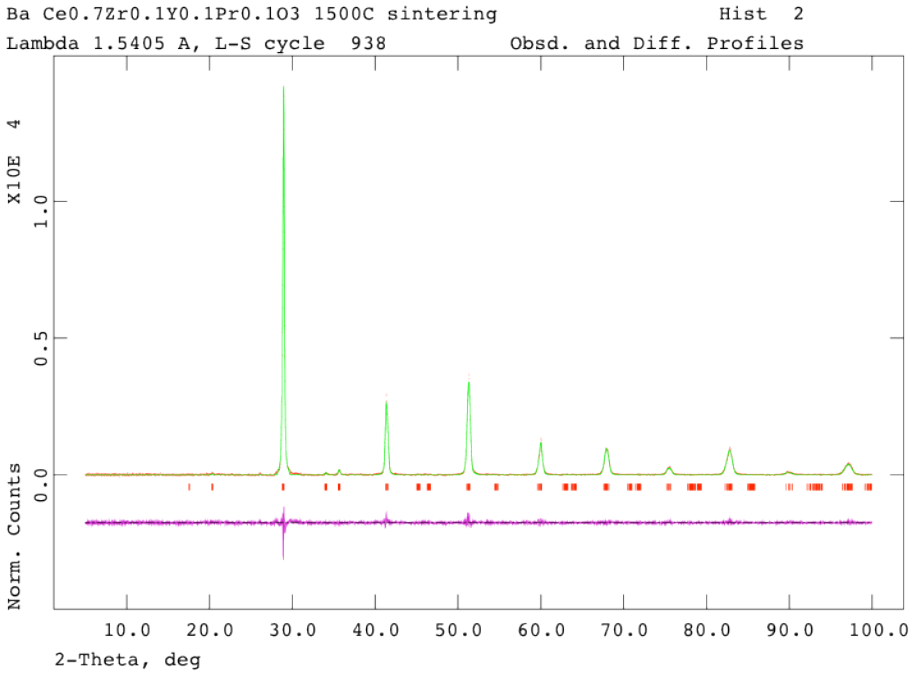

Figure 4.3 GSAS plot of $BaCe_{0.7}Zr_{0.1}Y_{0.1}Pr_{0.1}O_3$

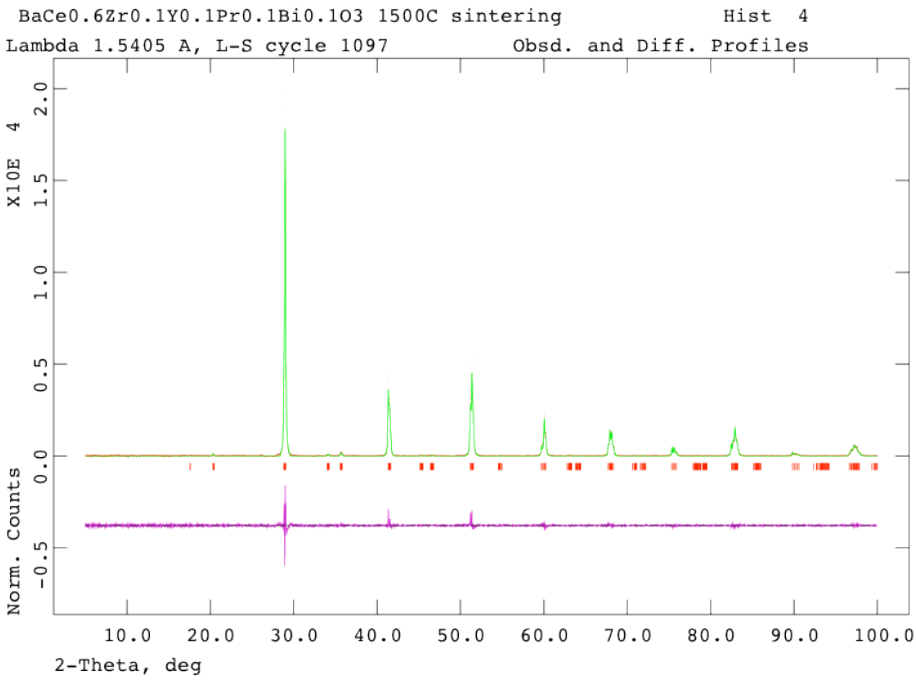

Figure 4.4 GSAS plot of $BaCe_{0.6}Zr_{0.1}Y_{0.1}Pr_{0.1}Bi_{0.1}O_3$

	BCYP	BCZYP15	BCZYP10	BCZYPB
Space Group	*Imma* (74)			
a (Å)	6.2136 (5)	6.1754 (2)	6.1657 (2)	6.1558 (1)
b (Å)	8.7504 (8)	8.7200 (2)	8.0763 (3)	8.6898 (1)
c (Å)	6.2370 (6)	6.2017 (1)	6.1984 (1)	6.1877 (1)
V ($Å^3$)	339.1 (1)	333.9 (1)	332.7 (1)	330.9 (3)
wRp (%)	9.68	7.98	8.41	9.16
Rp (%)	7.49	5.58	6.17	6.95
DWd	1.039	1.139	1.063	1.005
χ^2	2.126	1.887	2.049	2.442
ρ_{calc} ($g.cm^{-3}$)	6.1746	6.3262	6.2976	6.4690
ρ_{exp} ($g.cm^{-3}$)	6.1663	6.3127	6.0897	6.2451

Table 4.4 Refinement parameters for $BaCe_{0.7-x}Zr_yY_{0.3-y-z}Pr_zBi_xO_3$ compounds

XRD analysis was carried out after the conductivity measurements to monitor the stability of the perovskite phase upon exposure to reduced and humidified atmosphere and results are shown in Figure 4.5. All samples retained their orthorhombic forms with the zirconium-free barium cerate ($BaCe_{0.7}Y_{0.2}Pr_{0.1}O_{3-\delta}$)exhibiting a unique additional peak at a 2θ angle of 23.9° marked as * that could not – due to the absence of

other peaks – be assigned to a particular impurity phase and is therefore denoted as unidentified.

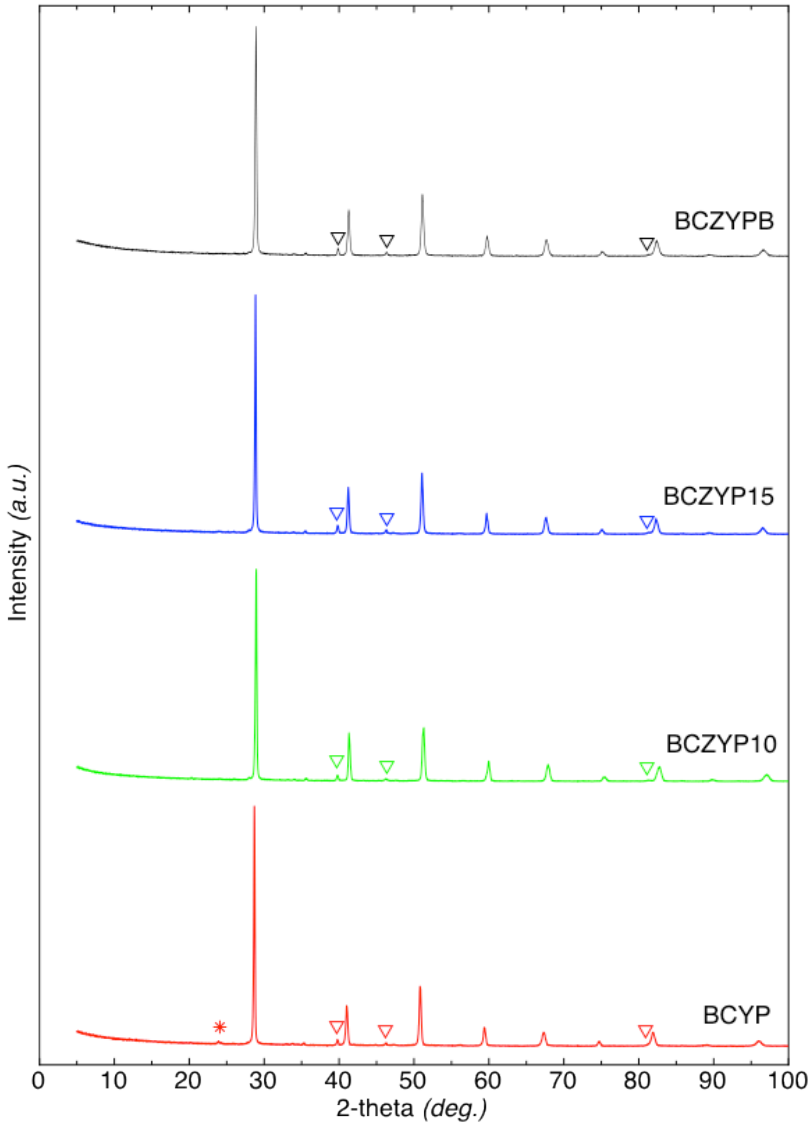

Figure 4.5 XRDs of BCYs after conductivity measurements in air and dry and wet 5% H_2-Ar (triangular marks are electrodic Pt, * unidentified peak)

4.3.2. Thermal analysis

As thermal stability is essential for any type of conductor, TG/DSC curves of the sintered materials were measured in flowing air and 5% H_2-Ar. Measurements in air were carried out up to 1000 ºC at a rate of 5 ºC min^{-1} and the results are shown in Figures 4.6 and 4.7 for the TG and DSC traces respectively. All samples can be considered stable up to the measured temperature, including the Zr-free sample with

weight losses of up to 1% (excluding the high content Pr-doped sample – BCZYP15 – exhibiting a loss of 3.5% after cooling to RT which can be reduced to below 1% by taking aside the region up to 200 ºC). The weight loss of this latter sample below 200 ºC can only be explained through the loss of absorbed water, as the DSC curve obtained for BCZYP15 shows an endothermic peak below 200ºC corresponding with the loss in weight; thus indicating that sample BCZYP15 is more hydrophilic than the other samples.

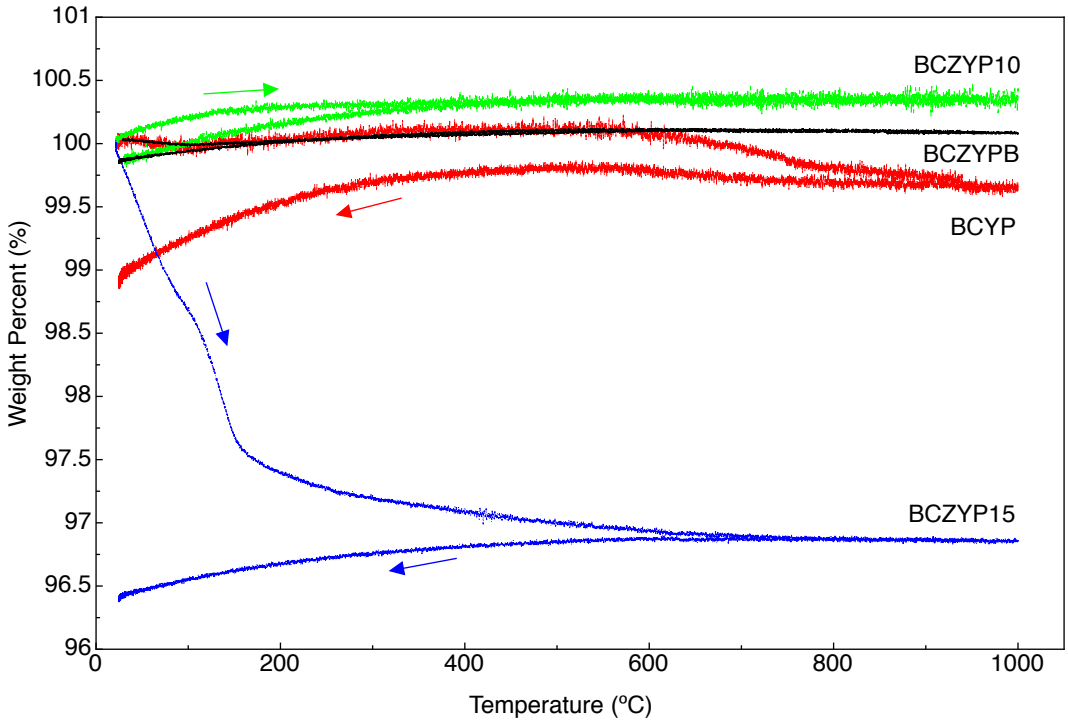

Figure 4.6 TG curves of BCs in air from RT to 1000 ºC

Important information provided in Figure 4.7 is the presence at high temperature of first order phase transitions for all samples except the co-doped Pr/Bi compound ($BaCe_{0.6}Zr_{0.1}Y_{0.1}Pr_{0.1}Bi_{0.1}O_{3-\delta}$). These transitions are fully reversible and may be put in relation with the observed changes in the crystal structure of $BaCe_{0.8}Y_{0.2}O_{2.9}$ (BCY) as a function of temperature as reported by Malavasi *et al.*[211].

In contrast to their conclusions, Pr-doped BCY and BCZY synthesised in this work do not exhibit a monoclinic phase at RT. This difference may be the result of the sintering process used as quenching the samples directly from 1500 ºC may enable the powders to retain a higher symmetry which is confirmed by the Rietveld refinements after sintering in Figures 4.1-4.

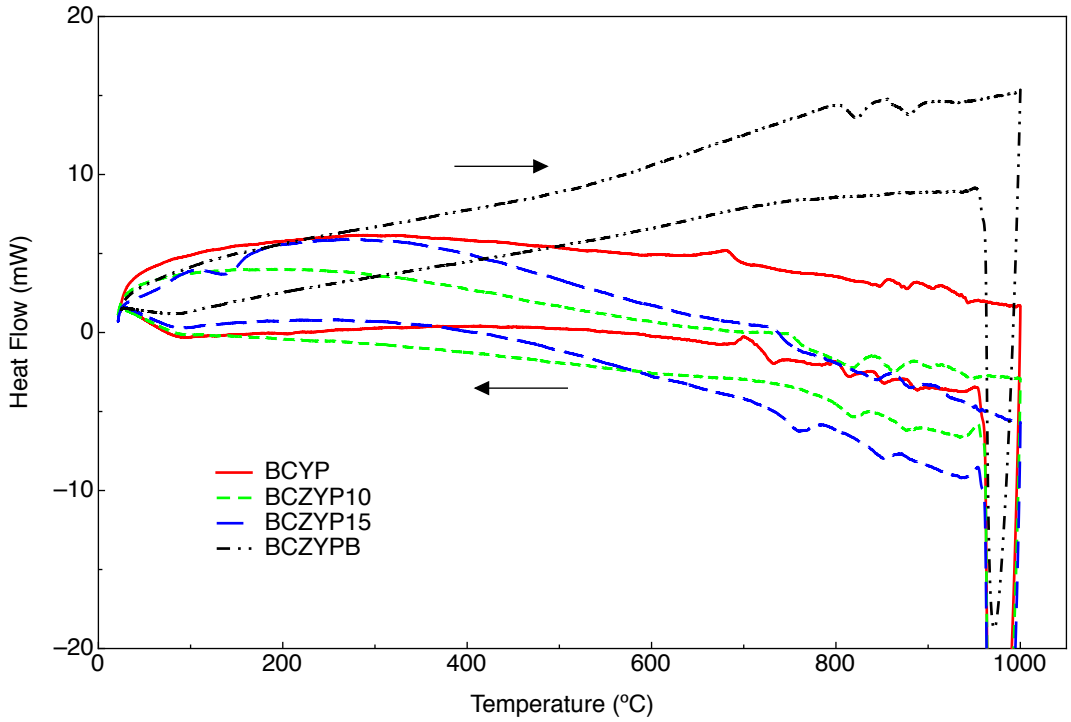

Figure 4.7 DSC curves of BCYs in air from RT to 1000 ºC

Moreover, the reversible nature of these transitions as indicated from the DSC traces suggests that Pr-doped barium cerates retain the orthorhombic morphology even after a relatively slow firing process up to 1000 ºC (5 ºC min^{-1} during STA analysis) at which point the structure has – upon heating and cooling – undergone several phase transformations.

Concerning the Pr/Bi co-doped sample, phase transitions are also observed at high temperature – between 800 and 900 ºC – however, these are non-reversible suggesting a change in symmetry to a more stable crystal system. Indeed, X-ray analysis performed after thermal analysis (Figure 4.8) shows a slight shift at the shoulder of the main reflections and an enhanced splitting of the same peaks; namely at 2θ angles of 41.08º and 41.45º compare to 41.33º, 50.91º and 51.48º instead of 51.41º, 59.60º and 60.12º compare to 59.75º and 60.04º, and so on for peaks around 68º, 75º and 82º. A rapid spacing analysis reveals that the crystal system is now centred monoclinic with a Laue symmetry of 2/m (as reported by Malavasi *et al.*[211]) and the non-reversible phase changes are thus not associated to losses of barium and/or oxygen.

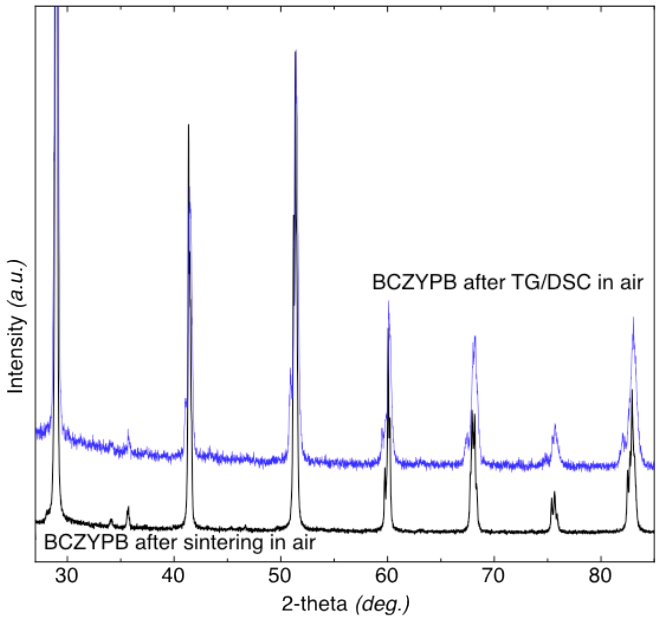

Figure 4.8 XRDs of BCZYPB after sintering and after TG/DSC analysis in air

Measurements in 5% H_2-Ar were carried out up to 800 ºC at a rate of 5 ºC min^{-1} and the results are shown in Figures 4.9 and 4.10 for the TG and DSC traces respectively. Stability for all samples is demonstrated as weight losses do not exceed 1.5% of pre-analysis weights with a loss of absorbed water of up to 0.6% at 150 ºC and formation of oxygen vacancies between 500 and 650 ºC depending on the composition.

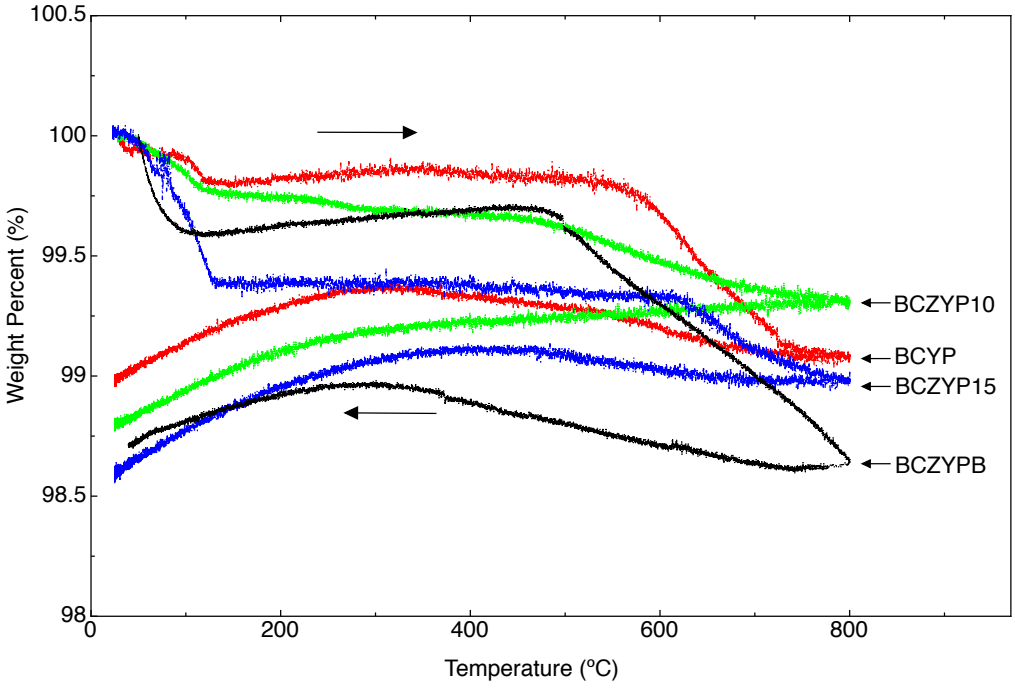

Figure 4.9 TG curves of BCYs in 5% H_2-Ar from RT to 800 ºC

DSC traces do not exhibit – to the same extent – the behaviours observed in air as only one single first order phase transition is noticeable for the Zr-free compound around 700 ºC which matches an identical transition observed in air at the same temperature. This indicates that the observed transitions in the studied compounds are not bound to the atmospheric conditions used but solely on thermodynamic factors.

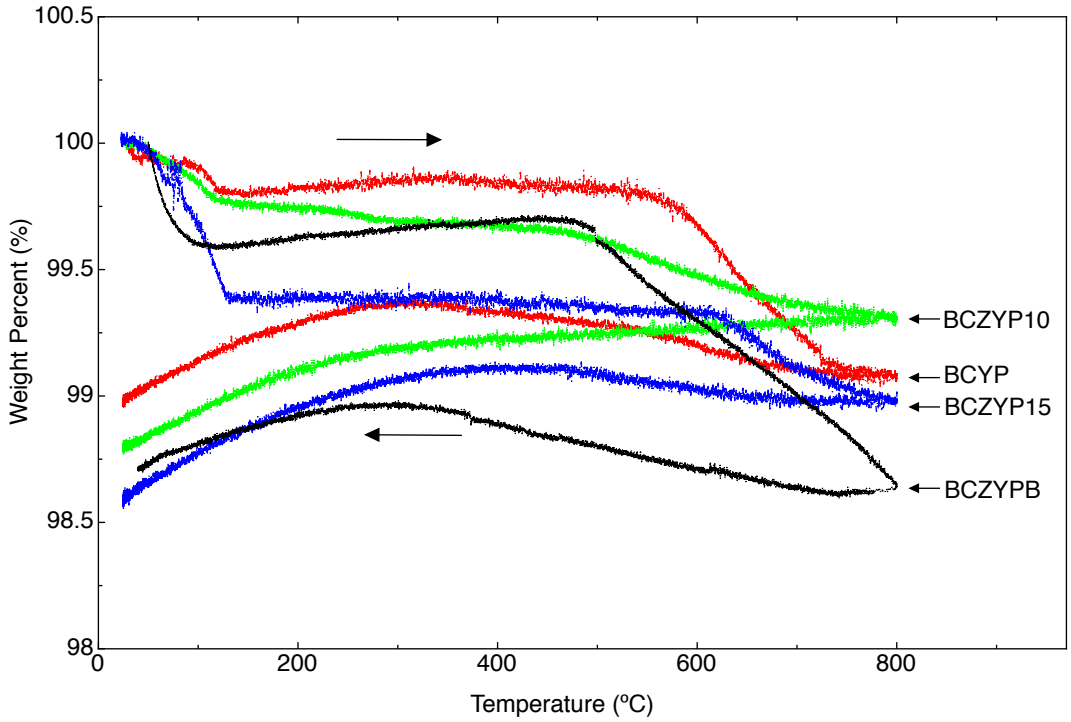

Figure 4.10 DSC curves of BCYs in 5% H_2-Ar from RT to 800 ºC

Analyses in wet 5% H_2-Ar were carried out up to 750 ºC at a rate of 5 ºC min^{-1} and the results are shown in Figures 4.11 and 4.12 for the XRD stabilisation patterns and the TG traces (DSC traces not shown as similar to Figure 4.10) respectively. All compounds except BCZYPB exhibit an overall weight gain from RT up to a region below 600 ºC indicating an uptake of water molecules, a phenomenon observed in many barium cerates[212, 213].

BCZYPB has a rather unchanged behaviour in wet 5% H_2-Ar than in non-humidified 5% H_2-Ar which is as yet unexplained even though the presence of bismuth may have an influence. The uptake of water had also no effect at all on the structure of the compounds as confirmed by XRD analysis after water treatment, and all compounds can therefore be considered as stable in a water-containing atmosphere.

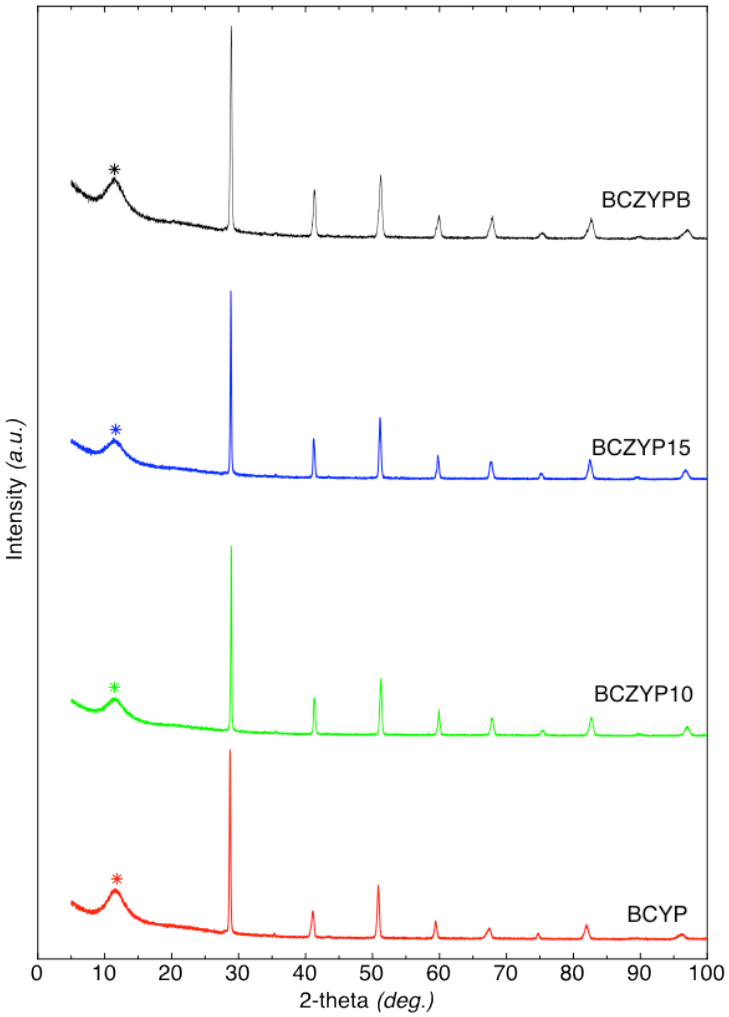

Figure 4.11 XRDs of BCYs after TG/DSC analysis in wet 5% H_2-Ar (* grease support)

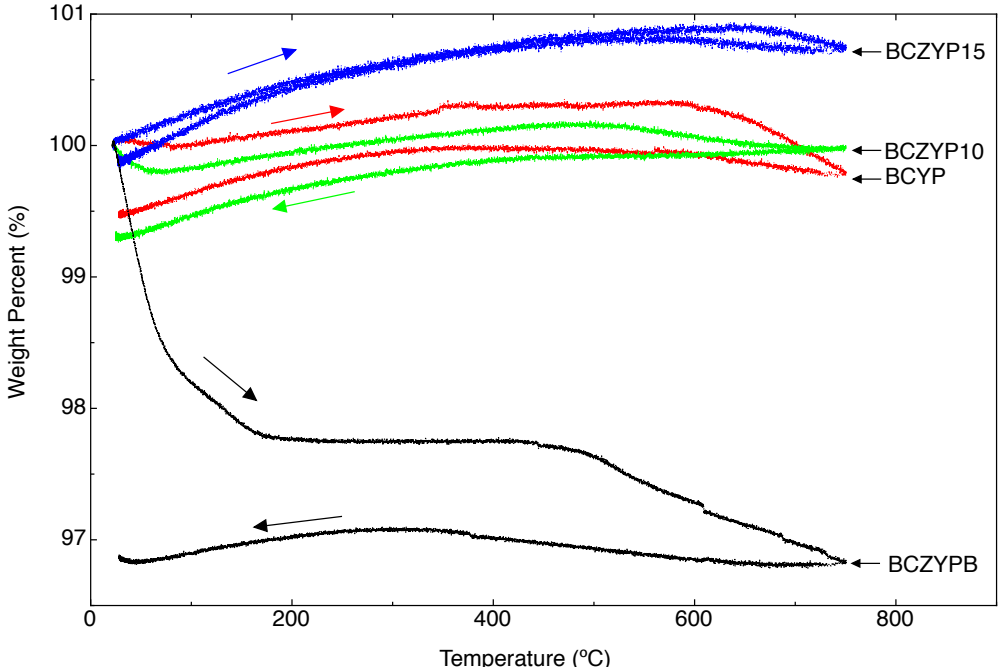

Figure 4.12 TG curves of BCYs in wet 5% H_2-Ar from RT to 750 ºC

4.3.3. Infrared spectroscopy

The biggest current challenge and recurring issue with barium cerate compounds remains the fact that instability in the presence of CO_2 leads to the formation of barium carbonate. To ascertain whether the unidentified peak in the X-ray diffraction pattern after conductivity measurement was due to degradation by contact with CO_2, IR scans were measured on the same powders used for PXRD and results are shown in Figure 4.13. Figure 4.14 represents IR scans of the same compounds after sintering.

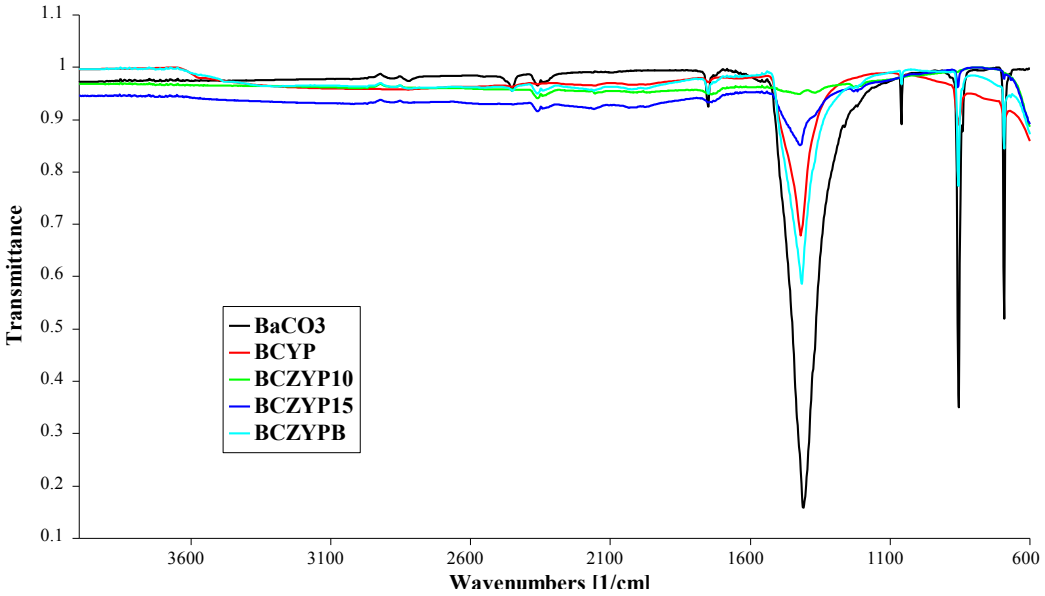

Figure 4.13 IR scans of Pr-doped BCYs after conductivity measurement

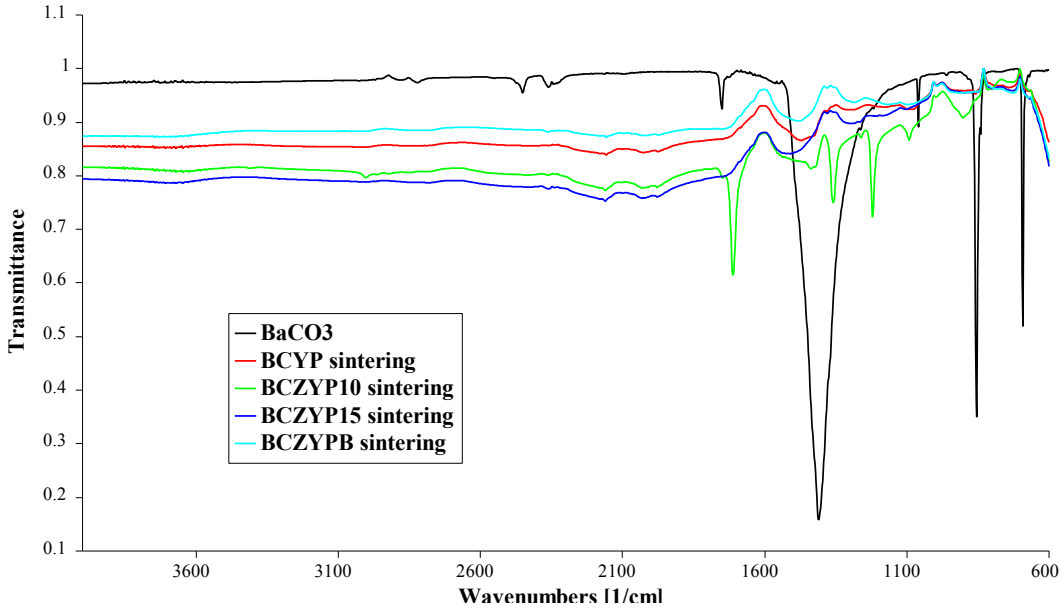

Figure 4.14 IR scans of Pr-doped BCYs after sintering

With a pure sample of barium carbonate taken as comparison, one can clearly see that the major C=O and C–O stretch exhibited by barium carbonate are present in all samples except BCZYP10 after conductivity measurements (Fig. 4.13) while none are present after sintering (Fig. 4.14). The intensity distribution of the main carbonyl peak also provides information on how much carbonate seems to be formed depending on the composition as samples BCZYP10 and BCZYPB for example have a large differential in the carbonyl peak while having equal praseodymium, yttrium and zirconium contents.

4.3.4. Conductivity

Values obtained from the conductivity measurements – performed in air, dry and wet 5% H_2-Ar – were used to plot Arrhenius type plots of the conductivity against inverse temperature and are shown in Figures 4.15-17 for air, dry and wet hydrogen respectively. It can be seen that all the Pr-doped compounds have much higher conductivities over the whole range of temperature than the Pr/Bi co-doped sample in all atmospheres and that within the singly Pr-doped compounds, both the Zr-free and the high Pr-content samples have similar or higher conductivities than the usually accepted base composition for barium cerates, namely a 10% yttrium doping level.

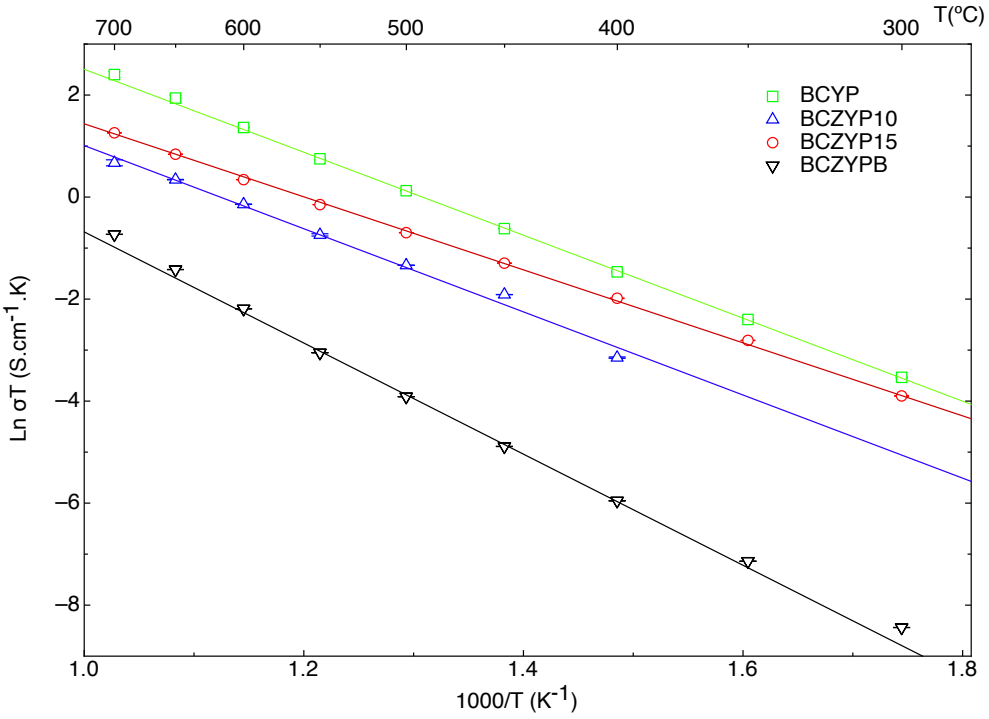

Figure 4.15 Total conductivity of $BaCe_{0.7-x}Zr_yY_{0.3-y-z}Pr_zBi_xO_3$ in static air

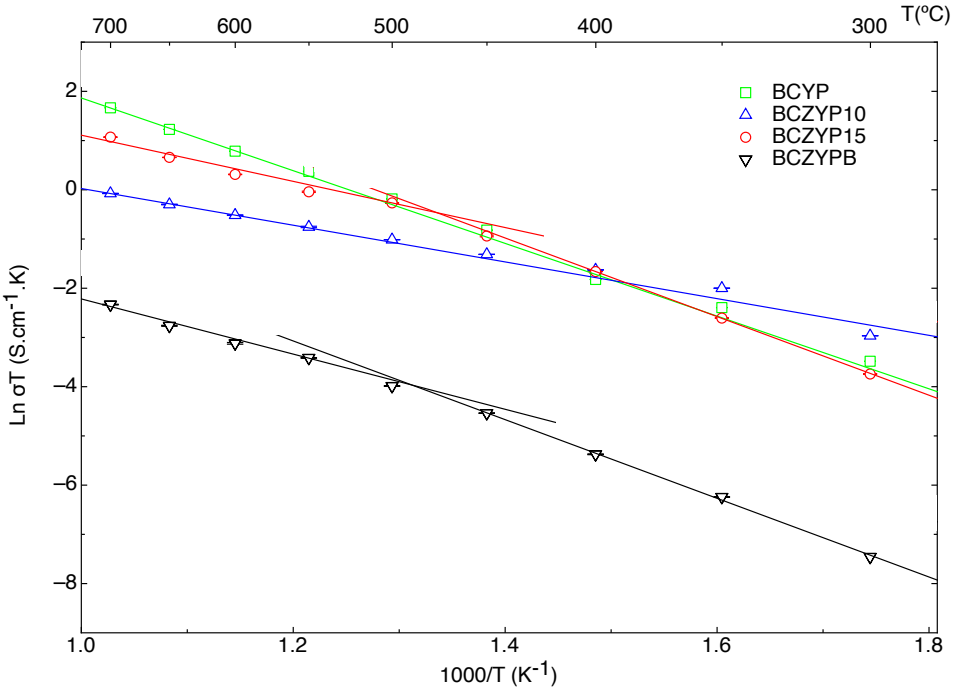

Figure 4.16 Total conductivity of $BaCe_{0.7-x}Zr_yY_{0.3-y-z}Pr_zBi_xO_3$ in dry 5% H_2-Ar

Additionally, in contrast to other reports on barium cerates[211], there is no evident slope change in the conductive behaviour of the Pr-doped yttrium barium cerates for what ambient atmosphere is concerned. In a reducing atmosphere, both wet and dry, a change in slope is at noticeable around 500 ºC for all Zr-containing samples while it is rather unchanged for the Zr-free compound. Total conductivity values therefore obtained at 700 ºC in air for BCYP, BCZYP15, BCZYP10 and BCZYPB are 0.0121, 0.0036, 0.0022 and 0.0005 S cm^{-1} respectively. The conductivity of sample BCYP is comparable to the value obtained by Malavasi *et al.*[211] for $BaCe_{0.8}Y_{0.2}O_{2.9}$ (0.014 S cm^{-1} at 700 ºC in air) that still constitute the best conductivity in air for a barium cerate[53]. In the case of dry and wet reducing atmospheres – in the same order – values obtained are 0.0055 and 0.0047S cm^{-1}, 0.0032 and 0.0058 S cm^{-1}, 0.0011 and 0.0010S cm^{-1}, 0.0001 and 0.0001S cm^{-1} respectively. The unexpectedly low conductance of the co-doped sample cannot be related to the predominant electronic conduction introduced by the addition of bismuth as noted in the study of Hui *et al.*[214] – where it was found that the proton conductivity of $BaCe_{1-x}Bi_xO_3$ decreased significantly with an increased bismuth content and that the total conductivity of the 50/50 sample was almost entirely due to electronic contribution –as if it was the case, differences in conductivity for the co-doped sample between ambient and reduced atmosphere would be greater than the order of five observed. One possibility for the lesser conductivity may be related to the

relative density as can be noted from Table 4.4, samples BCZYPB and BCZYP10 had after sintering slightly lower densities as the other two compounds, around 96% compared to > 99%.

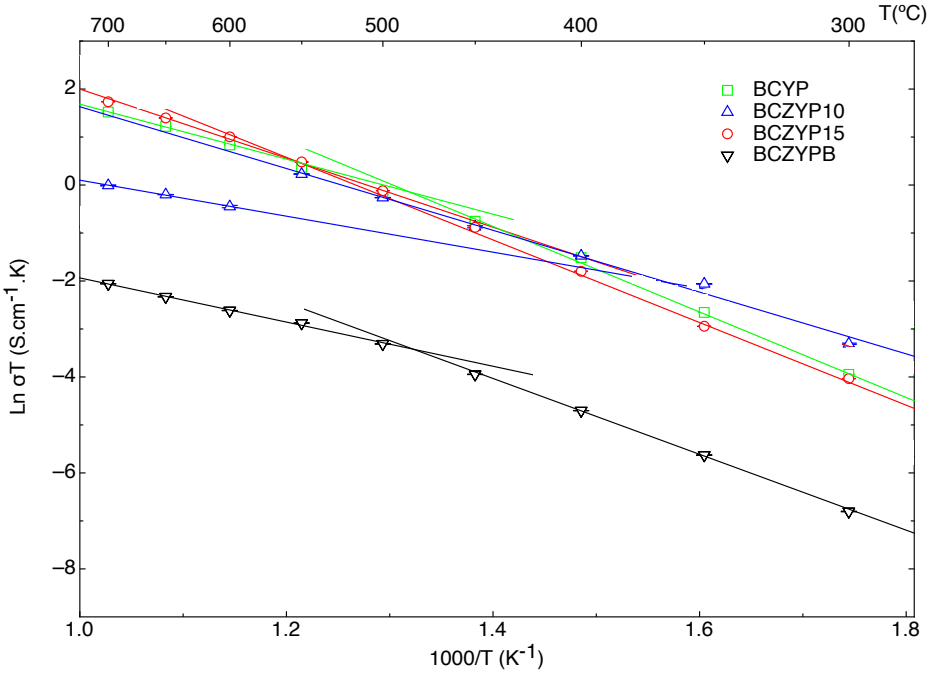

Figure 4.17 Total conductivity of $BaCe_{0.7-x}Zr_yY_{0.3-y-z}Pr_zBi_xO_3$ in wet 5% H_2-Ar

Concerning sample BCZYP15 in particular, one could notice the rather unusual behaviour of a similar or higher conductivity in a wet reducing atmosphere than that in air over the entire range of temperature studied (conductivity data shown in Figure 4.18 for all atmospheres at 700 ºC). This may either be explained by an optimised ratio of yttrium and praseodymium providing the highest conductivity through creation of oxygen vacancies and changes in oxidation number for praseodymium at high temperature on one hand or to a larger water uptake providing more ionic conduction pathways hence increasing mobility of charges and therefore conductivity. This latter is the most likely, firstly since it may also be used to rationalise why the conductivity of sample BCZYP10 suddenly drops from 0.0016 S cm^{-1} at 550ºC to 0.0010 S cm^{-1} at 600ºC and secondly because TG/DSC analysis in wet 5% H_2-Ar (Figure 4.12) confirms the hypothesis. Moreover, a higher conductivity obtained for Pr-doped zirconates in wet hydrogen compare to dry air below 600 ºC by Fabbri *et al.*[199] was also attributed to larger water uptake for these compounds.

In order to establish the stability of the zirconium-free compound with regard to its electrical behaviour as well as to verify the conductive stability of the studied

compounds, conductivity measurements at high temperatures were carried out over a long period of time to allow stabilisation. A stabilisation plot is represented in Figure 4.19 and shows that a time of above 14 hrs is required at 700 ºC to obtain stabilised conductivity values for the Zr-free compound, whose variations are most likely due to loss of oxygen due to prolonged high temperature exposure as measurements in air were carried out under static ambient air rather than under flowing atmosphere.

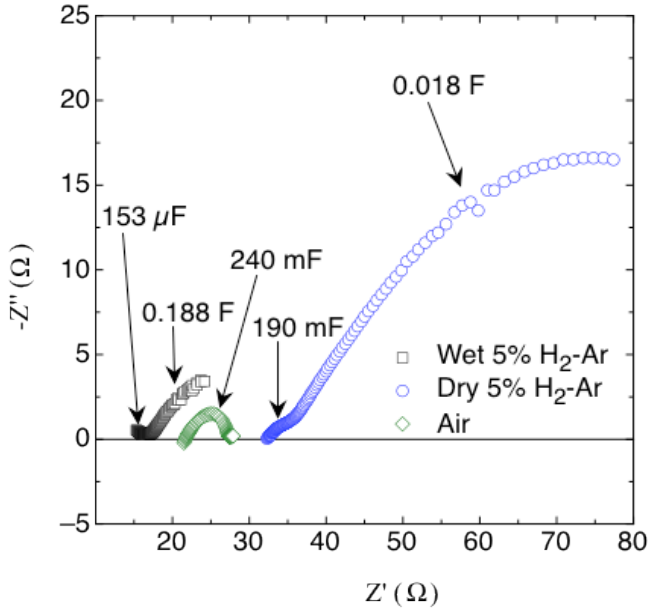

Figure 4.18 AC-IS of BCZYP15 in air, dry and wet 5% H_2-Ar at 700 ºC

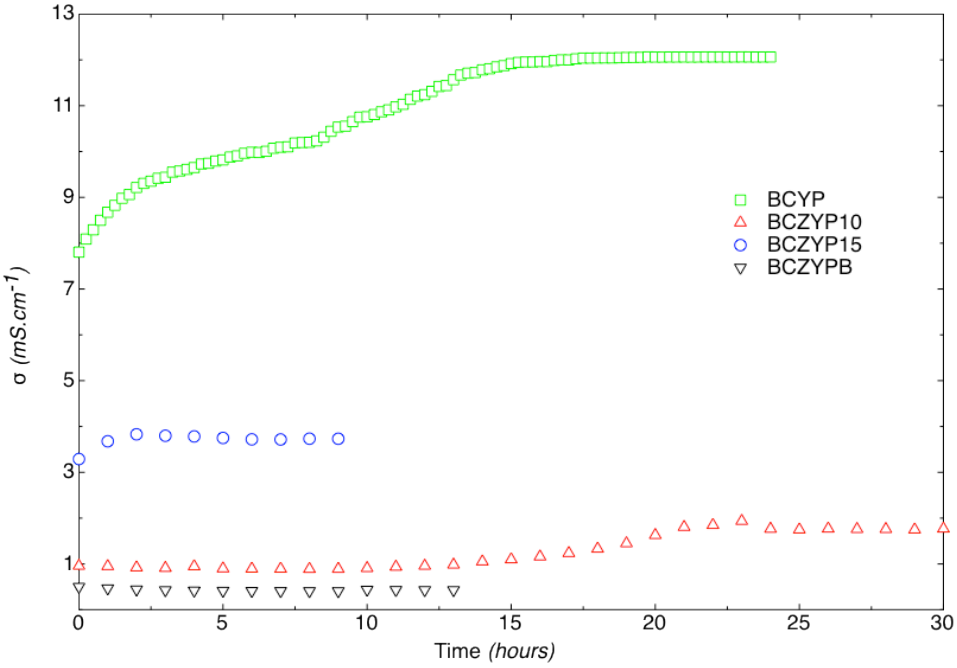

Figure 4.19 Total conductivity stabilisation plot of BCYP in air at 700 ºC

The fact that a stable value is obtained and sustained also indicates that the impurity with the unidentified peak in the X-ray analysis after conductivity –which is likely to be due to the formation of a barium carbonate phase considering results from the IR scans– does not constitute an obstacle to high conductance despite barium carbonate being an insulator. This may be due either to the formation of its latter reaches a maximum due to limited exposure to CO_2 from atmospheric air during measurement and/or because its formation renders the compound passive and thus protects it from further reaction without affecting its conductivity. Moreover, it would constitute a strong argument that while doping with a non-negligible amount of praseodymium (>10%), zirconium is not essential to the stability of the yttrium-doped barium cerate family of compounds both in air and reduced atmosphere, a phenomenon also observed when tantalum[215] is used or when yttrium is completely replaced by gallium[216] or indium[217]. The stability of doped $BaCeO_3$ is thus clearly related to the dopants chosen.

4.4. Bi-doped barium yttrium cerates

4.4.1. Crystal structure

Single-phase perovskite structures were obtained for all samples. Rietveld refinements were carried out with both structural and profile parameters being varied. Initial structural and spatial parameters for the orthorhombic perovskite structure with space group *I mma* (74) were used as mentioned in the literature[211].

Wyckoff sites assigned to Ba, Ce (and Zr, Y, Bi) and O were 4*e*, 4*b* and *8g* and 4*e* respectively. Barium and oxygen were always considered –during the refinement processes– with full occupancies, whereas *B*-site atoms occupancies were varied in accordance with the stoichiometry. Profile refinements were performed using GSAS[136] after space group determination with HighScore Plus. The experimental and calculated profiles are shown in Figures 4.20-25 for BCYB, BCZYB_03 to _07 respectively and the refinement parameters in Table 4.5. Looking at the variations in volume and lattice parameters (decreasing as cerium content is reduced in favour of a mixture of yttrium-bismuth), it is clear that bismuth is not solely acting as a sintering aid but is in fact incorporated into the lattice (based on the ionic sizes of 6-coordinated cerium (IV) at 1.01 Å, yttrium (III) at 1.04 Å and bismuth (V) at 0.9 Å).

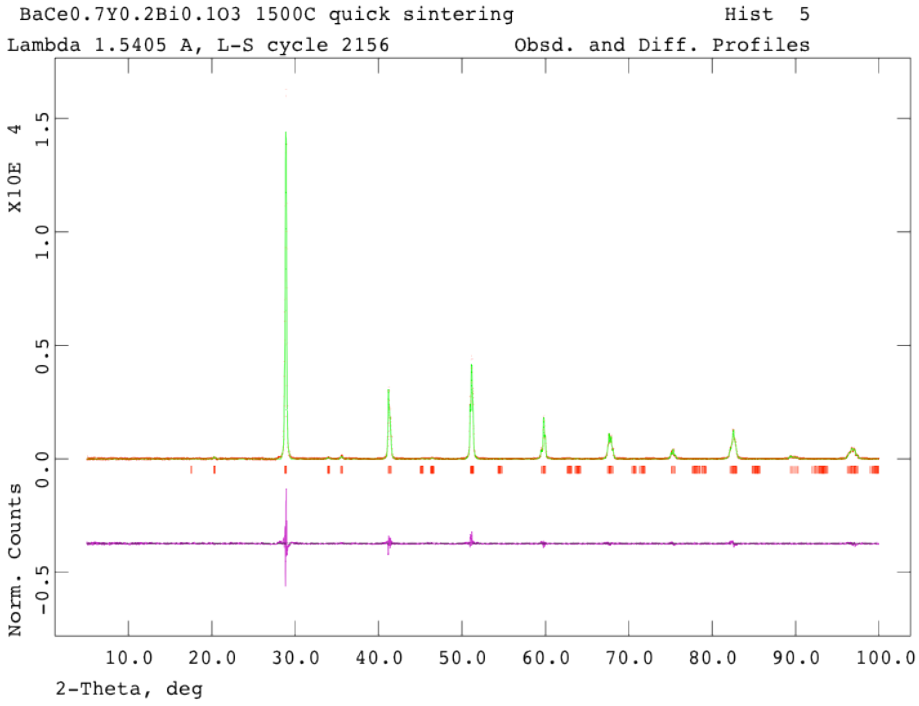

Figure 4.20 GSAS plot of $BaCe_{0.7}Y_{0.2}Bi_{0.1}O_3$

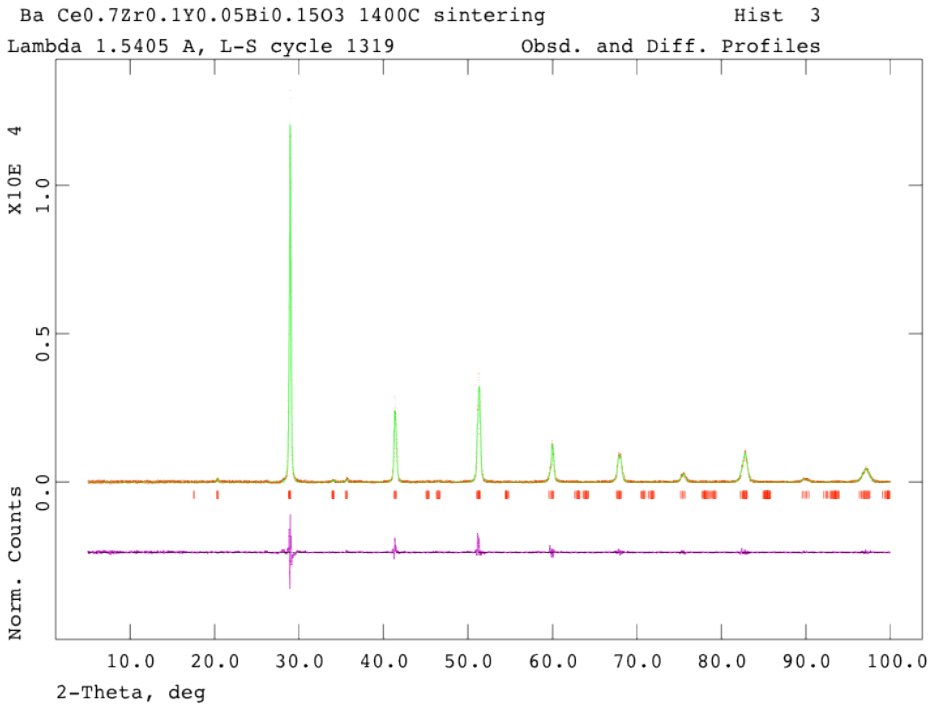

Figure 4.21 GSAS plot of $BaCe_{0.7}Zr_{0.1}Y_{0.05}Bi_{0.15}O_3$

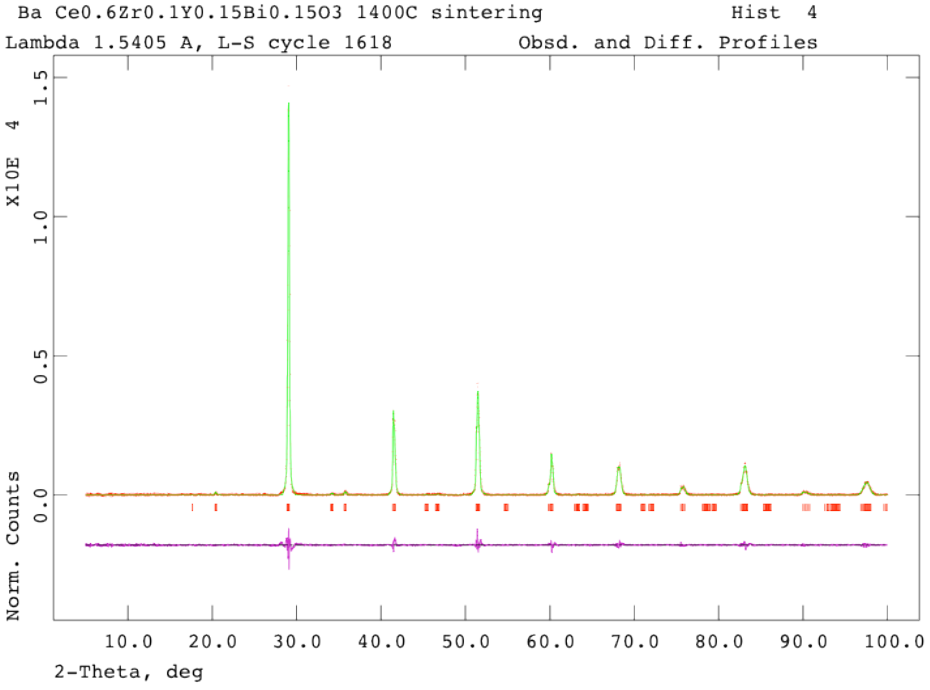

Figure 4.22 GSAS plot of $BaCe_{0.6}Zr_{0.1}Y_{0.15}Bi_{0.15}O_3$

Concerning the sintering, samples containing equal or higher amount of bismuth than yttrium are easily sintered to relative densities >98% at 1400 °C if the overall fraction of bismuth and yttrium is equal to or lower than 0.3 (1450 °C for higher values) while samples containing stoichiometrically more yttrium than bismuth require a quick-sintering process at 1500 °C which involves placing the pellet-containing crucible into a

furnace directly at 1500 °C, dwelling it for one hr and quenching it to RT in air. All pellets obtained through these firings therefore achieve high relative densities. XRD analysis was carried out after the conductivity measurements to monitor the stability of the perovskite phase upon exposure to reduced and humidified atmosphere and results are shown in Figure 4.26.

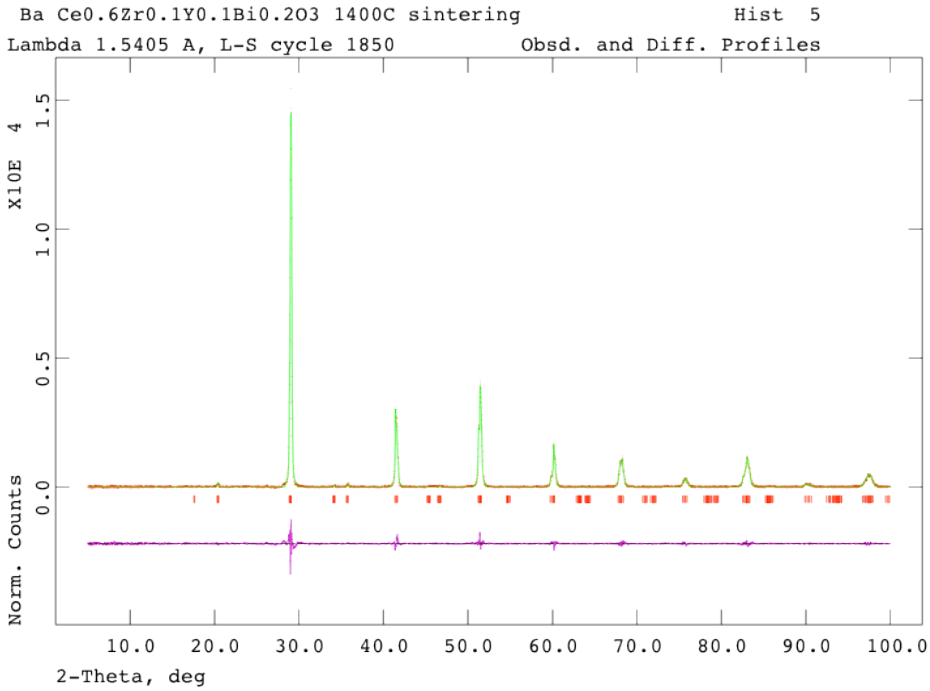

Figure 4.23 GSAS plot of $BaCe_{0.6}Zr_{0.1}Y_{0.1}Bi_{0.2}O_3$

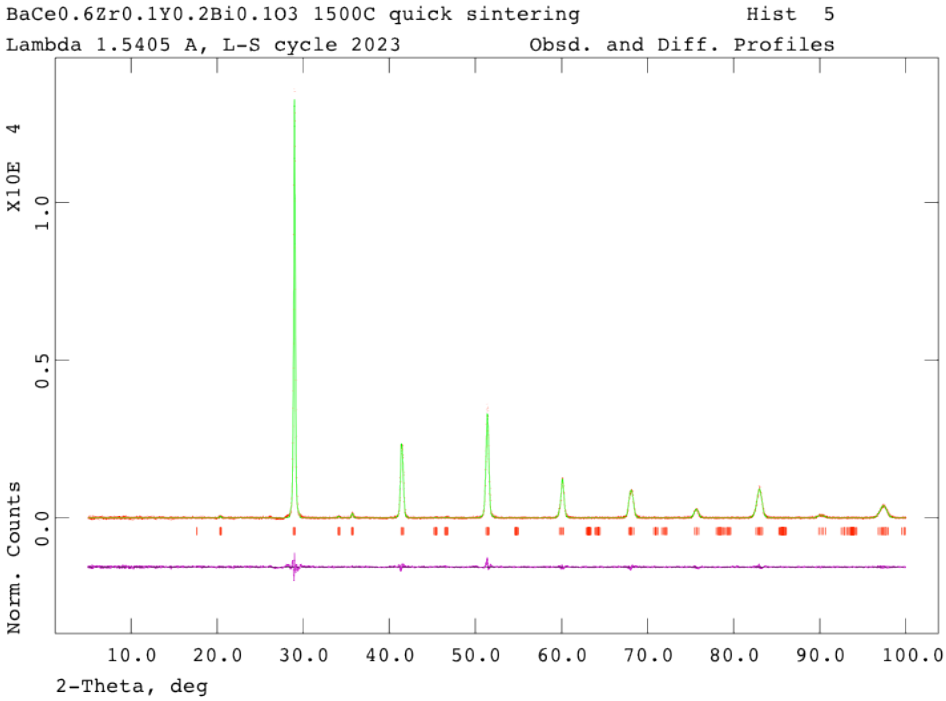

Figure 4.24 GSAS plot of $BaCe_{0.6}Zr_{0.1}Y_{0.2}Bi_{0.1}O_3$

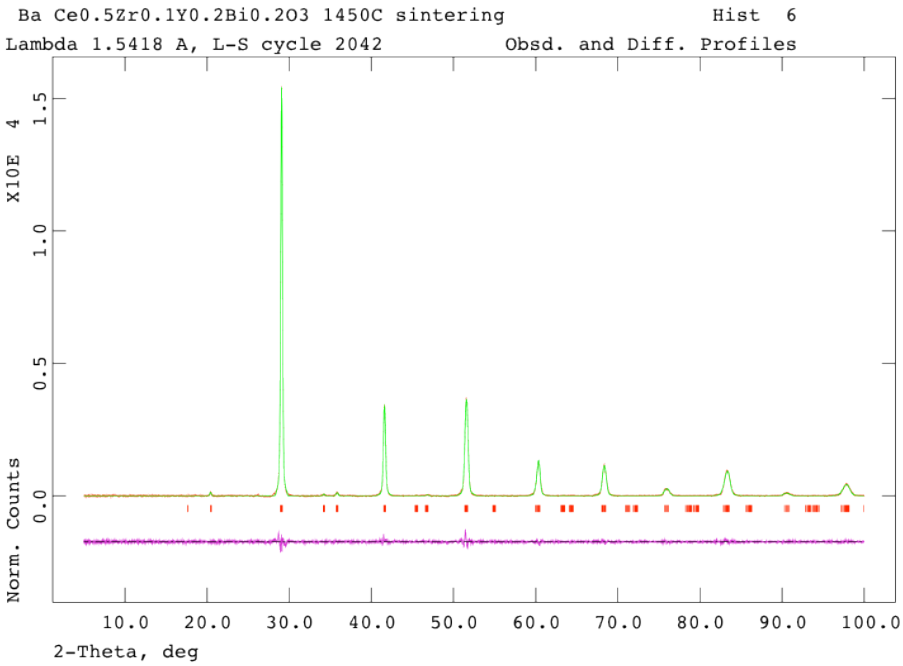

Figure 4.25 GSAS plot of $BaCe_{0.5}Zr_{0.1}Y_{0.2}Bi_{0.2}O_3$

	BCYB	**BCZYB _03**	**BCZYB _04**	**BCZYB _05**	**BCZYB _06**	**BCZYB _07**
Space Group	*Imma* (74)					
a (Å)	6.1792 (1)	6.1675 (3)	6.1459 (3)	6.1511 (4)	6.1535 (2)	6.1313 (2)
b (Å)	8.7155 (1)	8.7096 (1)	8.6783 (6)	8.6850 (6)	8.6833 (2)	8.6714 (3)
c (Å)	6.2068 (1)	6.2013 (2)	6.1774 (3)	6.1847 (4)	6.1804 (1)	6.1677 (1)
V (Å^3)	334.27 (1)	333.11 (1)	329.48 (2)	330.41 (1)	330.24 (1)	327.91 (1)
wRp (%)	9.28	9.05	8.64	8.18	7.29	7.65
Rp (%)	7.04	6.76	6.29	6.04	5.28	5.47
DWd	1.080	1.099	1.074	1.102	1.495	1.111
χ^2	2.249	2.090	2.029	1.913	1.441	1.880
ρ_{calc} (g/cm^3)	6.3994	6.5460	6.5150	6.6174	6.3790	6.5640
ρ_{exp} (g/cm^3)	6.3713	6.5449	6.5080	6.6108	6.3545	6.4665

Table 4.5 Refinement parameters for $BaCe_{1-x}Zr_yY_{0.2-z}Bi_tO_3$ compounds

All samples retained their orthorhombic forms with the two compositions containing comparatively more bismuth than yttrium exhibiting a unique additional peak at a 2θ angle of ~27.2° marked as * that could not – due to the absence of other peaks – be assigned to a particular impurity phase and is therefore denoted as unidentified. In addition, sample BCZYB_05 shows traces of barium carbonate impurity with the presence of its strongest intensity peak around 24°.

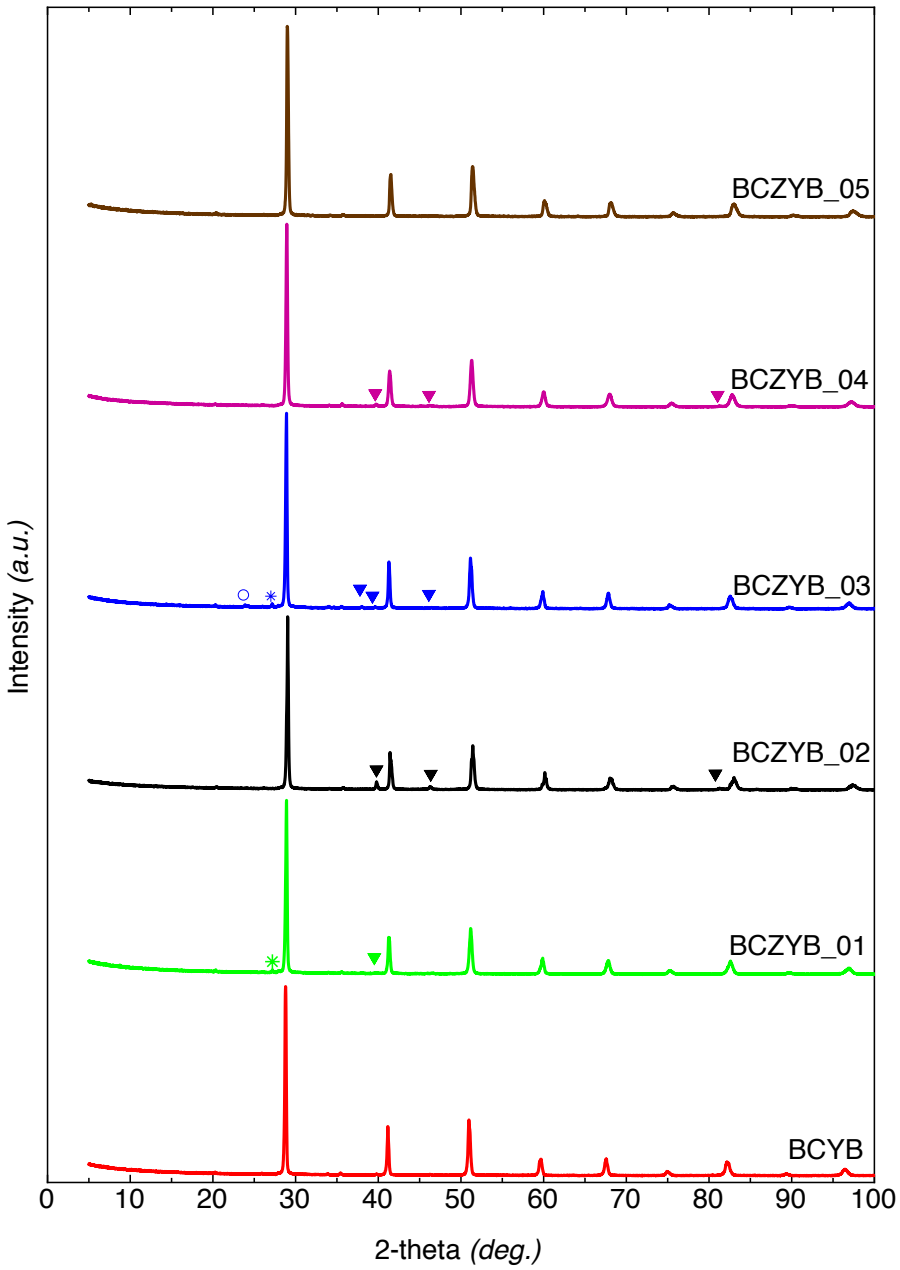

Figure 4.26 XRDs of BCYs after conductivity measurements (▼electrodic Pt, ○ $BaCO_3$)

4.4.2. Thermal analysis

TG/DSC curves of the samples obtained after sintering were carried out to measure the thermal stability in flowing air and 5 % H_2-Ar and are shown in Figures 4.27-28 and 4.29-30 respectively. Figures 4.27 (A) and (B) that present the TG curves of the studied compositions in air, indicate that compounds are stable up to the studied temperature of 1000 °C with overall weight changes not surpassing 1% that can be attributed to the loss of absorbed water for samples in (A) especially.

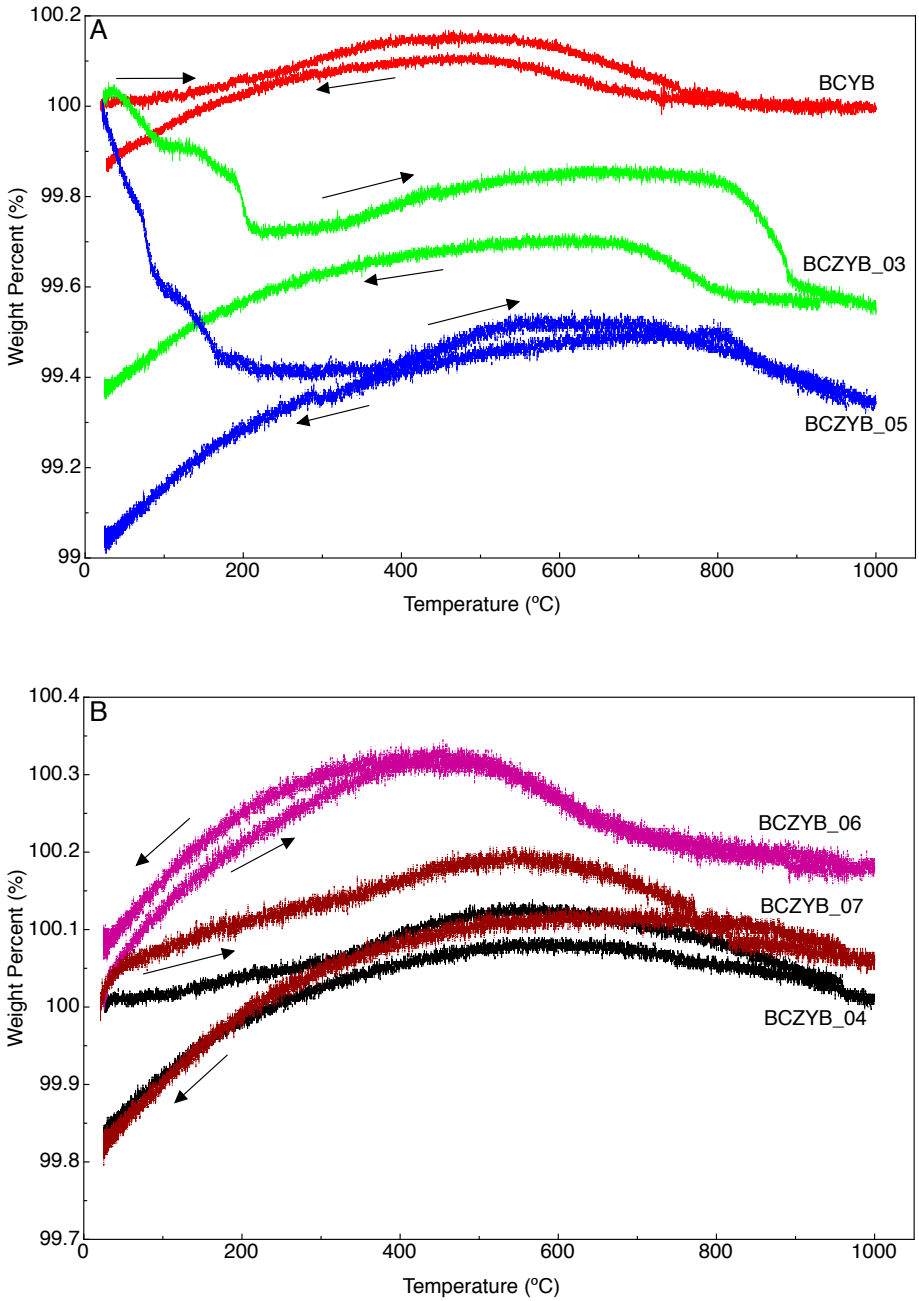

Figure 4.27 (A) and (B) TG curves of BCYs in air from RT to 1000 ºC

DSC curves for air represented in Figures 4.28 (A) and (B) do not show any relevant information undermining stability except for the observed phase transitions at temperatures between 800 °C and 1000 °C in (B) that are non-reversible as not observed on cooling. These phase transitions cannot be rationalised by the sintering process used as those three compositions were sintered under different conditions and require additional investigations to be carried out (high temperature XRD).

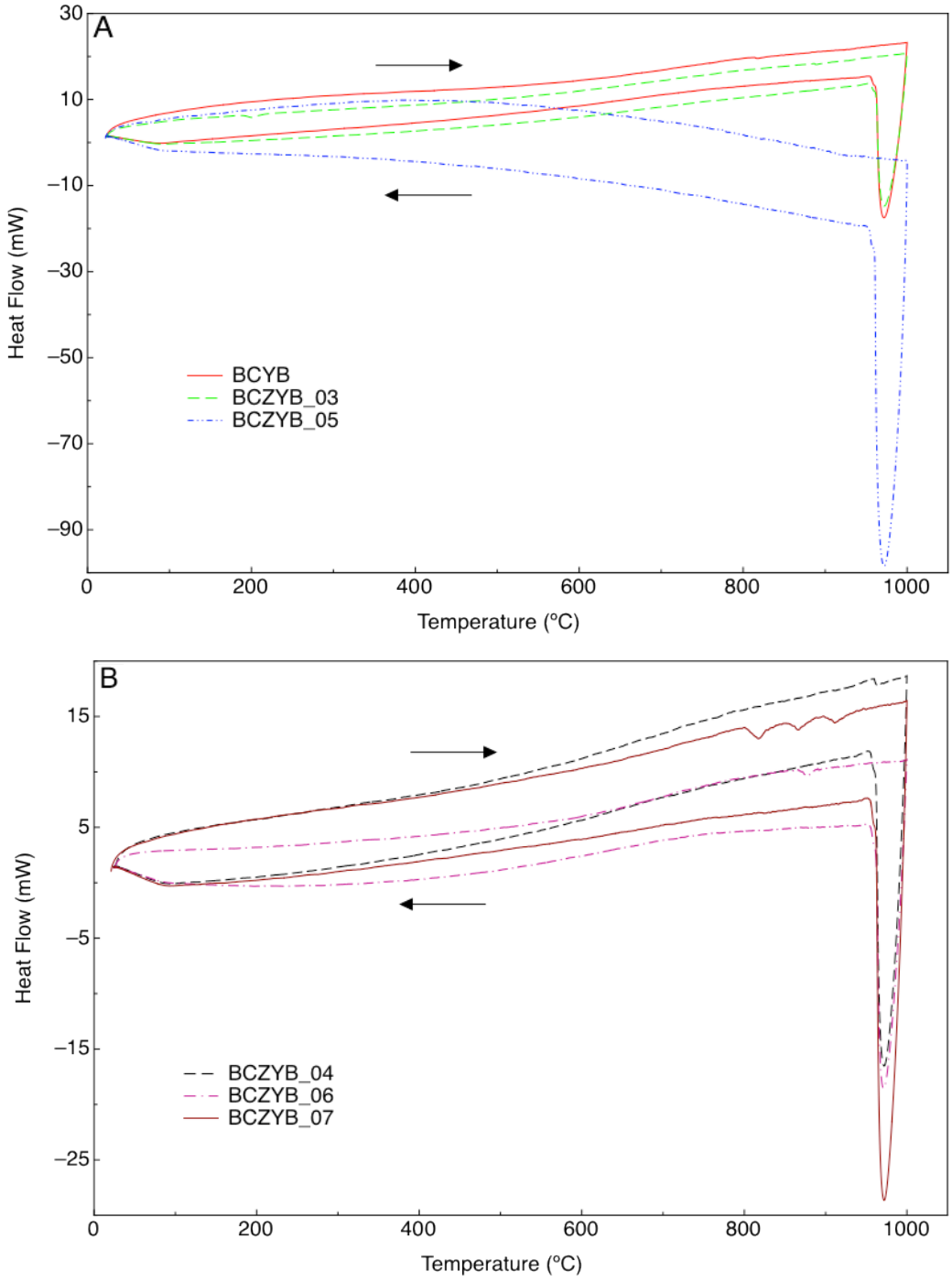

Figure 4.28 (A) and (B) DSC curves of BCYs in air from RT to 1000 °C

In the case of a reduced atmosphere, TG curves shown in Figures 4.29 (A) and (B) indicate that the studied Bi-doped barium cerates are stable in a low oxygen partial pressure environment. Weight losses observed below 200 °C for samples BCZYB_03 and _05 are due to absorbed water while losses for all compounds from 400 °C might be due to loss of oxygen with formation of oxygen vacancies. DSC traces represented in Figures 4.30 (A) and (B) do not show any of the phase transitions observed in air as analyses where only carried out up to 800 °C compared to 1000 °C in air.

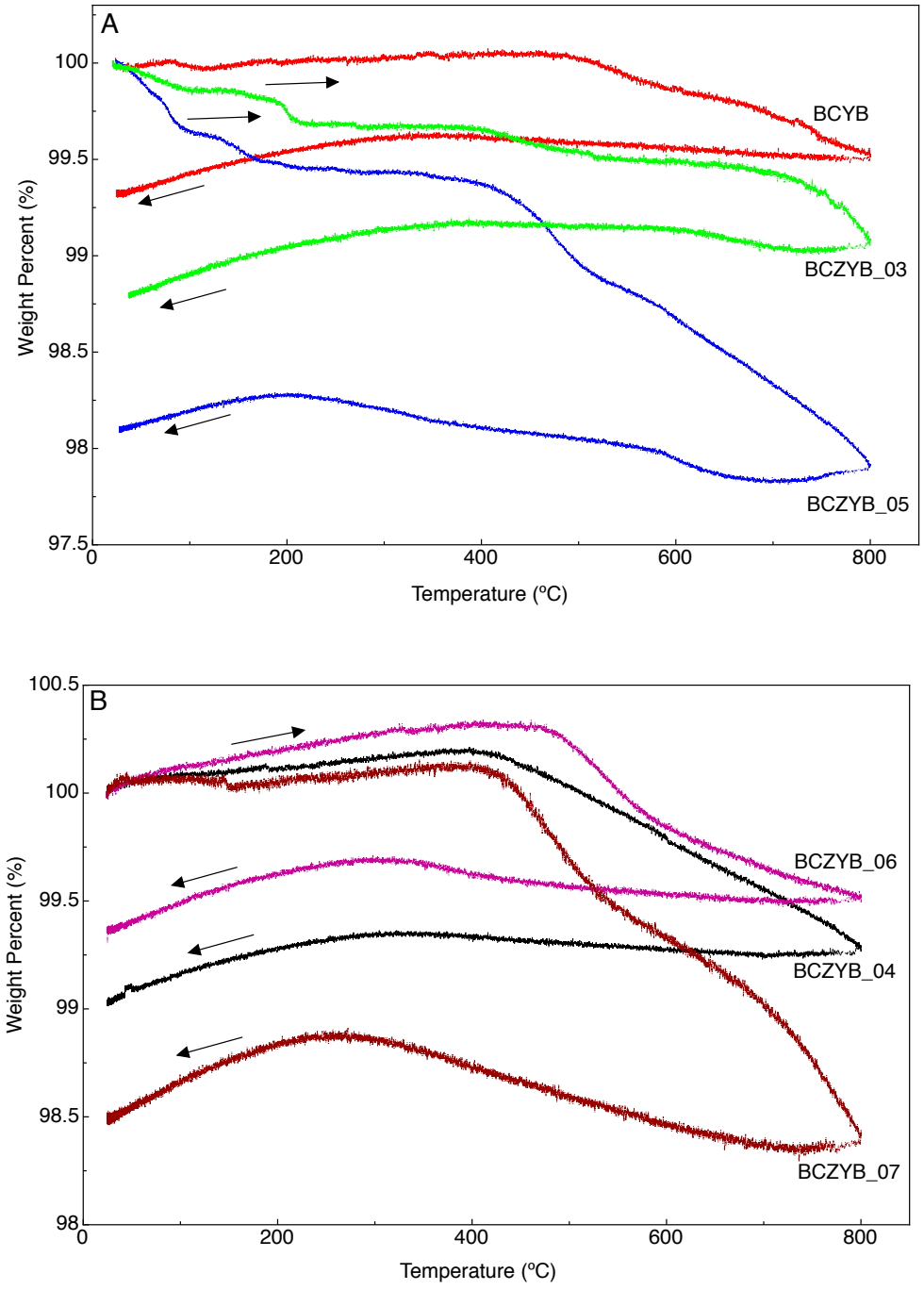

Figure 4.29 (A) and (B) TG curves of BCYs in 5% H_2-Ar from RT to 800 ºC

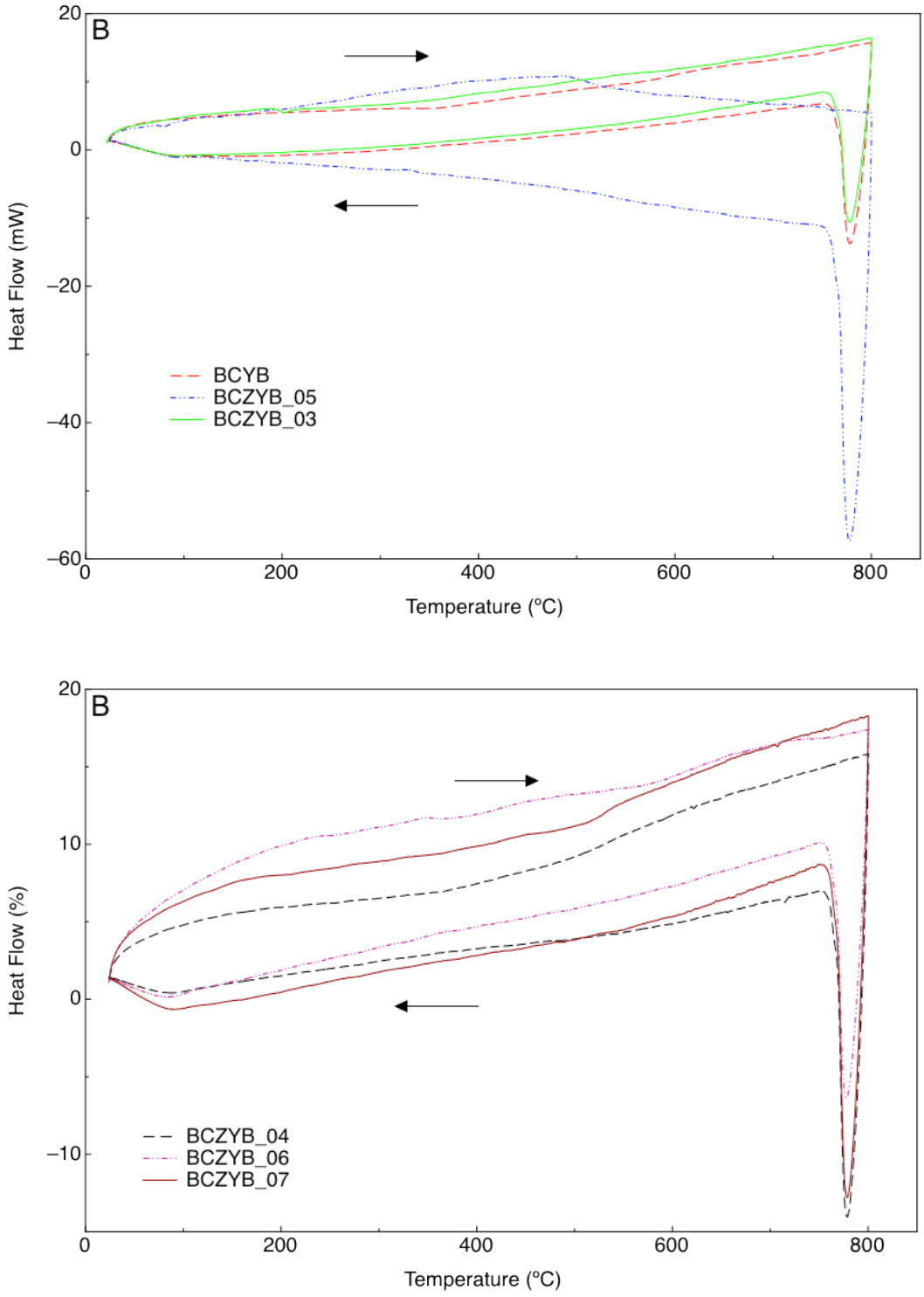

Figure 4.30 (A) and (B) DSC curves of BCYs in 5% H_2-Ar from RT to 800 ºC

Analyses in wet 5% H_2-Ar were carried out up to 750 ºC at a rate of 5 ºC.min^{-1} and the results are shown in Figures 4.31 and 4.32 for the TG traces and XRD stability patterns respectively. All compounds exhibit an overall weight loss across the temperature range with total weight losses after return to room temperature of over 1%

for BCZYB_03, 1% for BCZYB_04 and just above 1% for BCZYB_05. These results contrast with those obtained in non-humidified un-dried 5% H_2-Ar as in comparison samples BCZYB_03 to _05 either lost more or have an unchanged weight once back at room temperature. Thus, all samples do, to some extent, retain water molecules. The uptake of water had however a major effect on the structure of the compounds as confirmed by XRD analysis after water treatment, and all compounds exhibited – in addition to the orthorhombic phase – the presence of barium carbonate as shown in Figure 4.32.

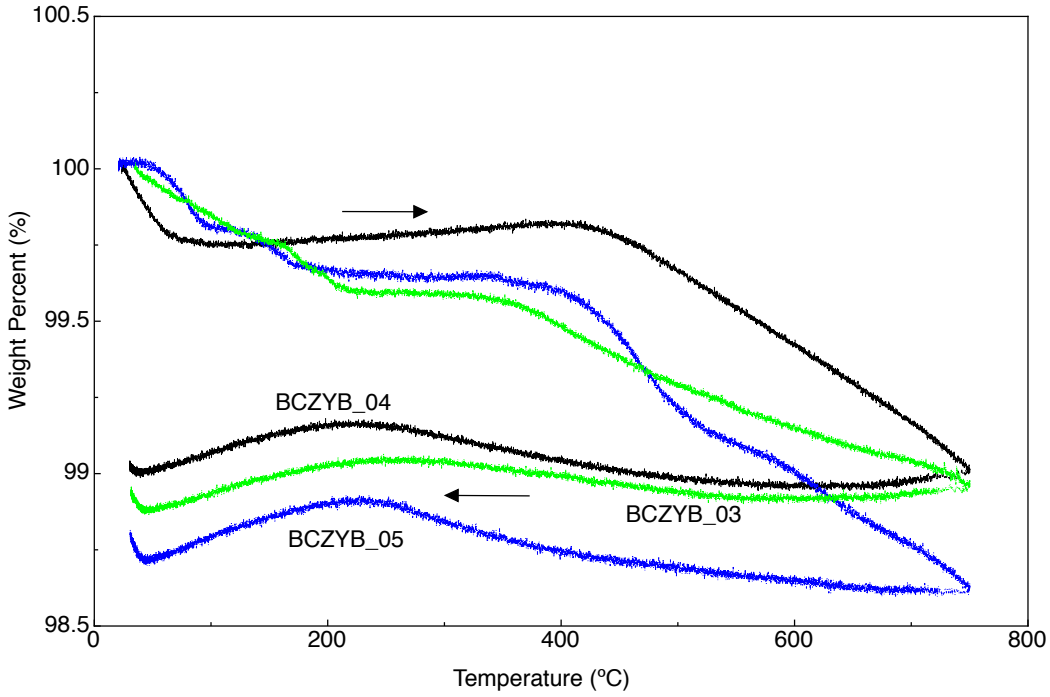

Figure 4.31 TG curves of BCs in wet 5% H_2-Ar from RT to 750 ºC

As the presence of elemental carbon cannot be rationalise from the measurement carried out in wet 5% H_2-Ar (as the presence of CO_2 should be suppressed), it is likely to result from an impurity already present in the sample and intensified by treatment in reduced atmosphere. This may be in the form of a phase too low quantitatively to be detected by XRD, or from the transformation of an amorphous phase into a crystalline one, or else. Moreover, the fact that these phases are not observed to such extent in the XRD patterns after conductivity measurement (see section 4.4.1.) suggests that the water atmosphere is equally unlikely to be the sole cause of the appearance of these phases as electrical properties were measured in wet atmosphere for periods far in excess to thermal analyses durations. This latter point

would also indicate that the physical state of the measured sample influences the phase content as well, as conductivity measurements are carried out with highly dense pellets compare to powder for thermal analyses.

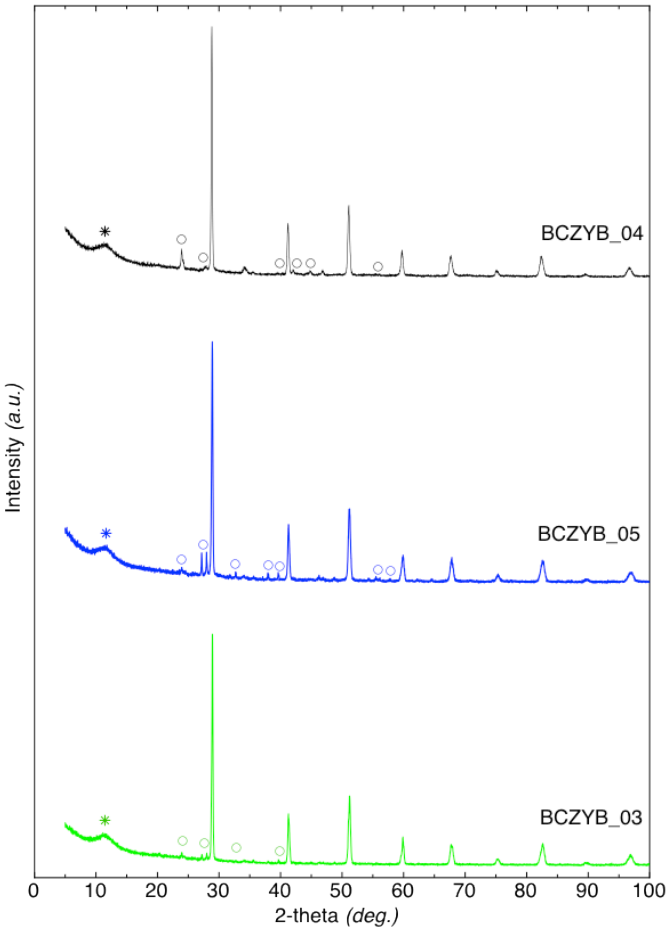

Figure 4.32 XRDs of BCYs after TG/DSC analysis in wet 5% H_2-Ar (* grease support, ○ $BaCO_3$)

From all the above, these samples should therefore be considered as structurally stable in water-containing atmosphere even though the presence of impurities is observed as effects observed during conductivity measurements (as discussed later) do not support the theory of a total uncontrolled degradation of the barium cerate orthorhombic phase.

4.4.3. Microstructure

In order to verify the microstructural behaviour of the compounds after sintering and after reduction, SEM pictures of selected compositions were taken for comparison

and are shown in Figure 4.33 (all pictures are taken from the centre of the pellets, horizontally and vertically speaking). The pictures on the left – corresponding to the microstructure after sintering – exhibit a well sintered structure of plain particles forming a fused network of crystals (especially visible for BCZYB_06, B) while right hand side pictures – taken after conductivity measurements – show generally cracked and dispersed parts with obvious closed pores in combination to a well-sintered fused network as background. This latter observation is particularly true for BCZYB_06 (B and E) and BCYB (C and F) while BCZYB_03 (A and D) could be considered unchanged as no structural difference as evident as in the case of other compositions is noticeable.

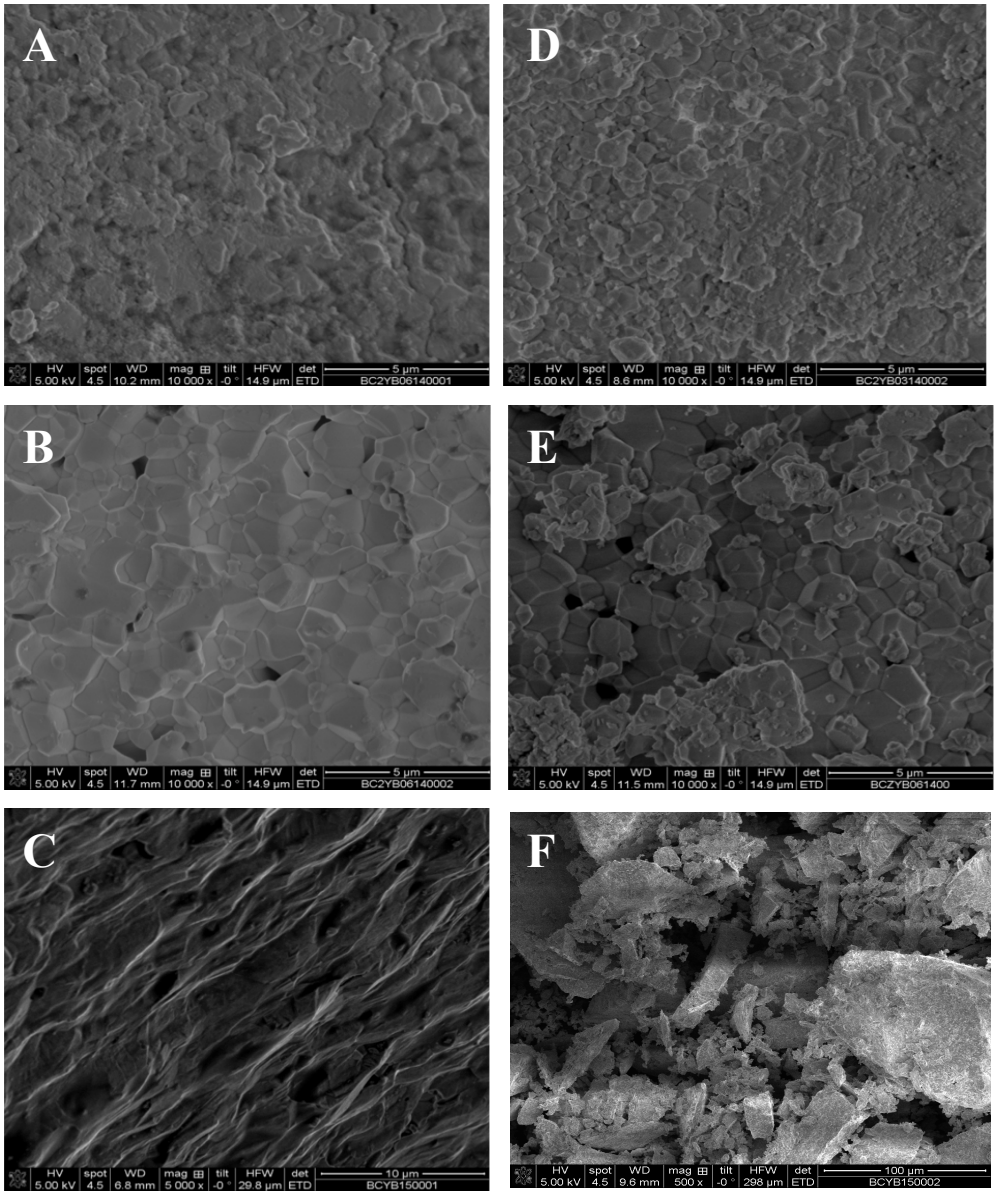

Figure 4.33 SEM images of BCYs after sintering (A to C) and after conductivity measurement (D to F)

4.4.4. Infrared spectroscopy

As for each barium cerate compound, the instability in presence of CO_2 leading to the formation of barium carbonate is the largest issue to be tackled with when synthesising that type of compounds. In order to ascertain the presence and/or absence of barium carbonate after conductivity measurements, IR scans were measured with results shown in Figure 4.34 and 4.35 for scans after conductivity and sintering respectively.

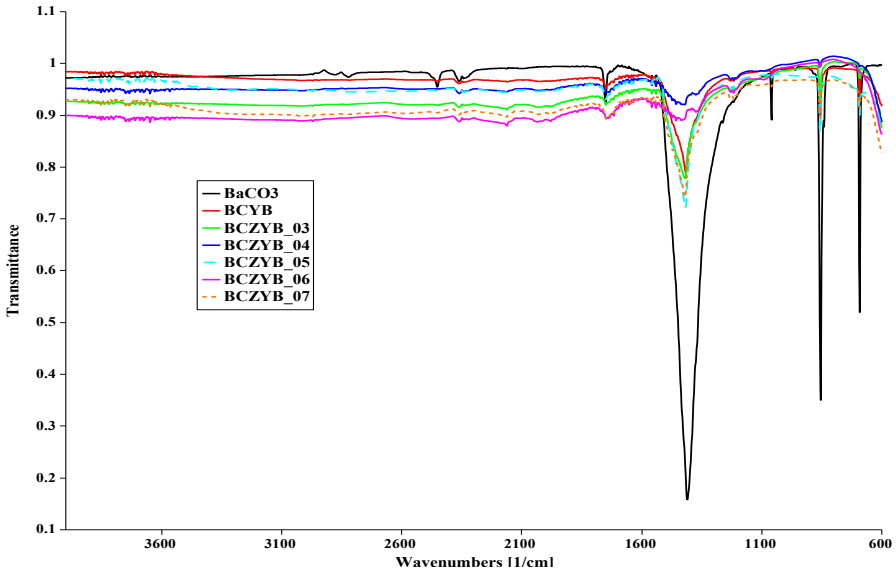

Figure 4.34 IR scans of Bi-doped BCY's after conductivity measurement

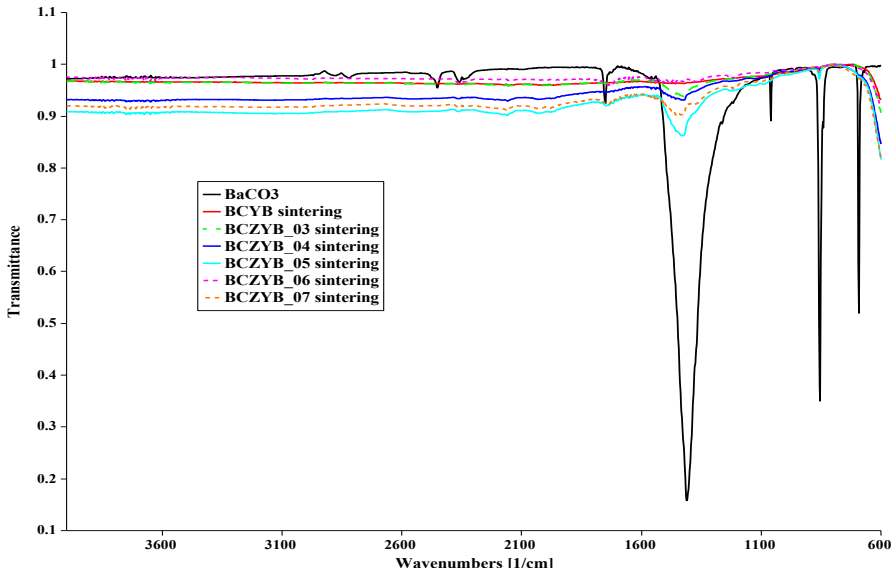

Figure 4.35 IR scans of Bi-doped BCY's after sintering

It can be seen, using a blank of barium carbonate as comparative sample, that the major C=O and C–O bands are present in all compounds studied after conductivity, although in a minor proportion for two of the compositions. From Figure 4.35, it can be seen that carbonates are in fact still present after sintering in at least two compounds, minor in two others and absent from the two remaining. Although not detected during phase refinement and XRD analyses, this brings additional information as to why barium carbonate peaks are observed in XRD after conductivity measurements by suggesting that an impurity intensification process by long-lasting firing in air at high temperature is plausible rather than a destructive phase transformation of the barium cerate structure and suggests $BaCeO_3$ is crystallising during the high temperature treatment.

4.4.5. Conductivity

Values obtained from the conductivity measurements – performed in air, dry and wet 5% H_2-Ar – were used to plot Arrhenius type plots of the conductivity against inverse temperature and are shown in Figures 4.36 and 4.37 for air and dry and wet hydrogen respectively.

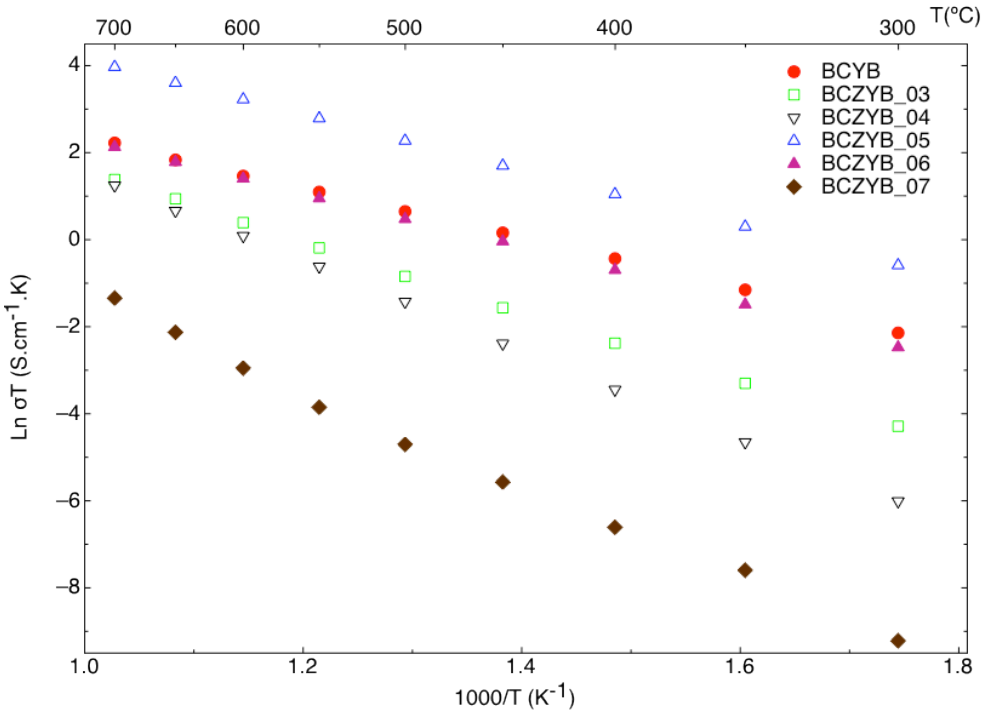

Figure 4.36 Total conductivity plot in ambient air of BCYs (filled symbol compositions not measured in reduced atmosphere)

Filled symbols in Figure 4.36 correspond to particular compositions (BCYP, BCZYB_06 and BCZYB_07) whose conductivities were not measured in reduced atmosphere due to mechanical degradation of the pellets, mainly caused by the reduction of bismuth causing a fundamental lattice change in the structure and inducing cracking.

This behaviour is observed experimentally by a progressive increase of the impedance measured under reducing conditions at 700 °C. Rationalising why these compounds do not have sufficient mechanical strength in reduced atmosphere solely because of the bismuth content reduction is however not evident. Indeed, the three compositions that sustain reducing atmosphere conditions have a bismuth content greater than two of the compositions that fail to achieve sufficient mechanical integrity. A series of factors must therefore have a role to play in the variations of mechanical strength of the different compositions as no straightforward link can be established between the amount of bismuth contained in the structure and cracking. The electrical properties of these compositions in air are very close to one another for the two compounds that only differ on the presence of zirconium in the structure (BCYP: $BaCe_{0.7}Y_{0.2}Bi_{0.1}O_{3-\delta}$ and BCZYP_06: $BaCe_{0.6}Zr_{0.1}Y_{0.2}Bi_{0.1}O_{3-\delta}$) and reach total conductivity values common to barium cerates and zirconates at 9.4 x 10^{-3} $S.cm^{-1}$ at 700 °C for the zirconium-free compound (comparable with values obtained by Malavasi *et al.* for $BaCe_{0.8}Y_{0.2}O_{2.9}$)[211] while the lower conductivity of sample BCZYB_07 ($BaCe_{0.5}Zr_{0.1}Y_{0.2}Bi_{0.2}O_{3-\delta}$) can be ascribed to the lower density attained after sintering as well as a lower content of cerium in the structure despite an increase in bismuth that would in principle boost electrical properties. Open symbol compositions shown in Figure 4.37 did exhibit similar properties in the same range of total conductivity values with a maximum for sample BCZYB_05 of 5.5 x 10^{-2} $S.cm^{-1}$ at 700 °C attained after over 80 hrs of measurement at 700 °C (Figure 4.38) and show an increase in electronic conductivity dominance over time (Figure 4.39, evolving from a characteristic two semi-circle response to a depressed constant phase element before exhibiting an inductance combined with an ionic response and finally a pure inductance characteristic of metallic compounds), most likely due to bismuth reduction and/or loss of oxygen at high temperatures. In addition and in contrast to other reports on barium cerates[211], there is no evident slope change in the conductive behaviour of the Bi-doped yttrium barium cerates for what ambient atmosphere is concerned. In a reducing atmosphere, as

can be seen in Figure 4.37 for both wet and dry, a change in slope is noticeable between 500 and 600 °C with the exception of sample BCZYB_05 in wet reducing atmosphere, which exhibits a change in slope around 400 °C. Sample BCZYB_05 exhibits higher conductivity in wet 5% H_2-Ar indicating proton conduction and highlighted by the increased conductivity over time in humidified atmosphere at 700 °C (Figure 4.38).

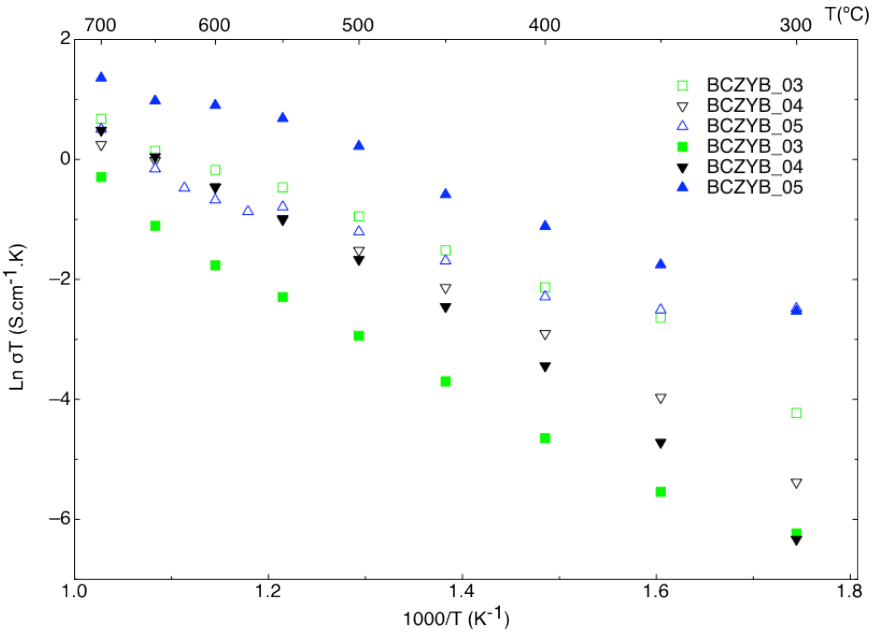

Figure 4.37 Total conductivity plot of BCYs in dry (open) and wet (filled) 5% H_2-Ar

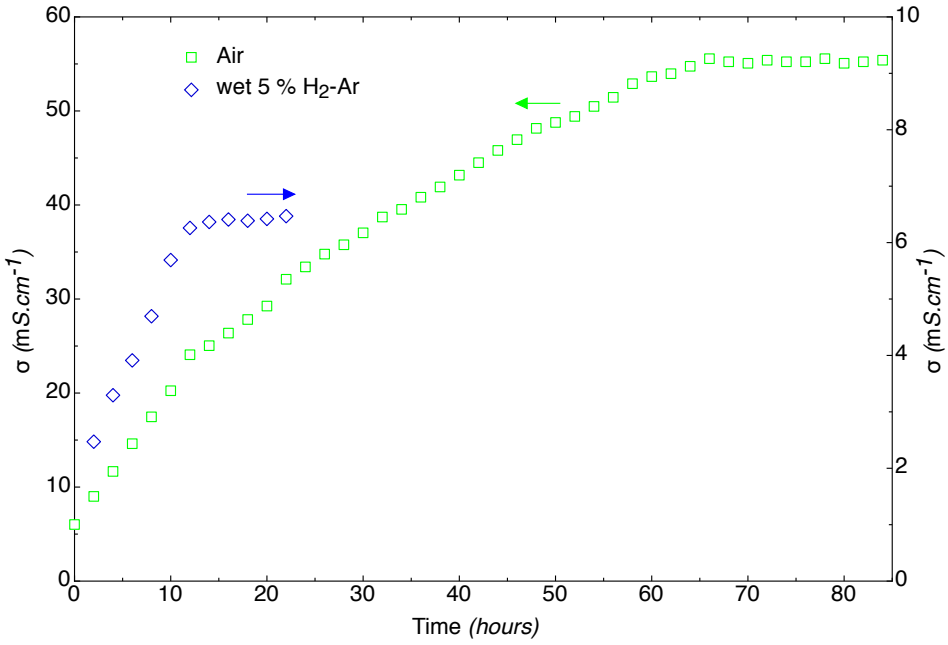

Figure 4.38 Total conductivity stabilisation plot of BCZYB_05 ($BaCe_{0.6}Zr_{0.1}Y_{0.1}Bi_{0.2}O_{3-\delta}$)at 700 ºC in air and in wet 5% H_2-Ar

The total conductivities of all samples in reducing atmosphere were found to be lower than the values obtained in air with samples exhibiting lower, similar or higher conductance in wet compare to dry reduced atmosphere (also noted during thermal analysis between non-humidified and wet reduced atmosphere). The presence of the barium carbonate phase detected after thermal analysis should – if a result of structural degradation rather than impurity intensification – have a direct diminishing effect on conductivity from the insulating nature of the $BaCO_3$ phase. This is however not observed as stability of the conductivity is demonstrated at high temperature thus, the noticed phenomena are most certainly linked to the nature of the conduction with diverse predominance of mixed ionic/electronic conduction and diverse behaviour concerning water uptake and stability, as illustrated in Figures 4.31 and 4.32.

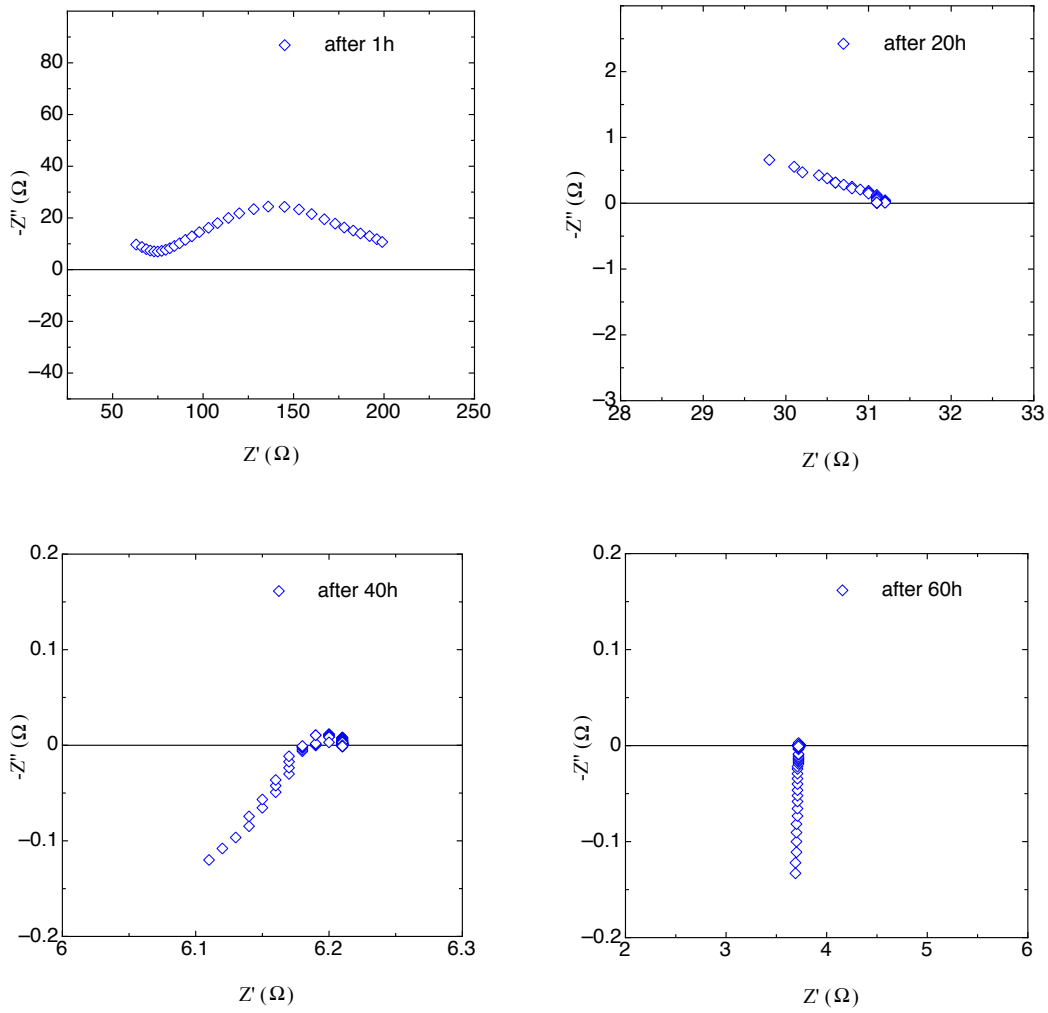

Figure 4.39 Evolution of impedance spectra of BCZYP_05 during stabilisation loop at 700 ºC in air

4.5. Cobalt addition to Pr-doped barium yttrium cerates

4.5.1. Crystal structure

Using a previous study as a reference[210], a series of samples where cobalt was added to praseodymium-doped BCY were successfully synthesised. Rietveld refinements were carried out with both structural and profile parameters being varied. Initial structural and spatial parameters for the orthorhombic perovskite structure with space group *I mma* (74) were used as mentioned in the literature [211]. Wyckoff sites assigned to Ba, Ce (and Y, Pr, Co) and O were 4*e*, 4*b* and *8g* and 4*e* respectively. Barium and oxygen were always considered –during the refinement processes– with full occupancies, whereas *B*-site atoms occupancies were varied in accordance with the stoichiometry. Profile refinements were performed using GSAS [136] after space group determination with HighScore Plus. An experimental and calculated profile for BCYP_05 is shown in Figure 4.40 as example and the refinement and lattice parameters for all compounds are listed in Table 4.6.

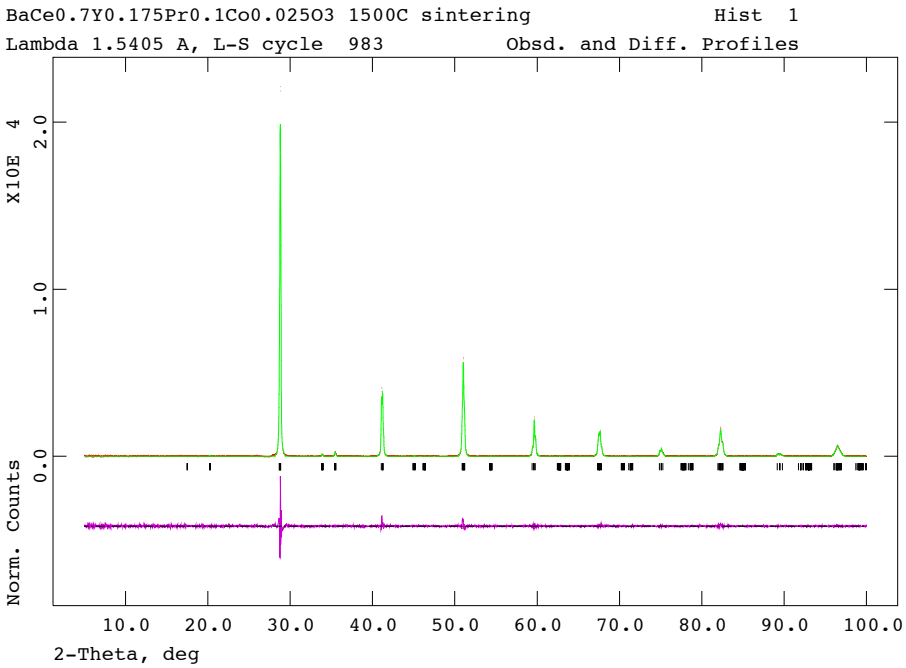

Figure 4.40 GSAS plot of $BaCe_{0.7}Y_{0.175}Pr_{0.1}Co_{0.025}O_{3-\delta}$

Based on the studied system (BCYP) single phase structures are obtained for 2.5% Co addition with presence of an impurity detected at a cobalt level of 5% (Figure 4.41) indicating that the incorporation of cobalt in Pr-doped BCY is limited to below

5%. Incorporation into the lattice is also confirmed from refinement parameters shown in Table 4.6 as if taking BCYP_05 as an example, its composition only differs from BCYP by the presence of 2.5% Co instead of yttrium and considering that the ionic radius of cobalt (in any oxidation state) is lower than that of yttrium (III) – ranging from 0.53 to 0.745 Å for 6-coordinated Co(IV) and Co(II) respectively compared with 0.9 Å for 6-coordinated Y(III)[167] – the reduction in lattice volume observed is thus related to the decrease in average radii of the *B*-site proving cobalt incorporation into the lattice.

	BCYP	**BCYP_04**	**BCYP_05**
Space Group	*Imma*(74)	*Imma* (74)	*Imma* (74)
a (Å)	6.2136 (5)	6.2002 (3)	6.1963 (3)
b (Å)	8.7504 (8)	8.7579 (4)	8.7518 (4)
c (Å)	6.2370 (6)	6.2192 (3)	6.2169 (3)
V (Å^3)	339.1 (1)	337.7 (1)	337.1 (1)
wRp (%)	9.68	9.27	8.36
Rp (%)	7.49	6.81	6.32
DWd	1.039	1.062	1.135
χ^2	2.126	2.485	2.050
ρ_{calc} (g.cm^{-3})	6.1746	6.2871	6.1961
ρ_{exp} (g.cm^{-3})	6.1663	6.2783	6.1938

Table 4.6 Refinement parameters for BCs compounds

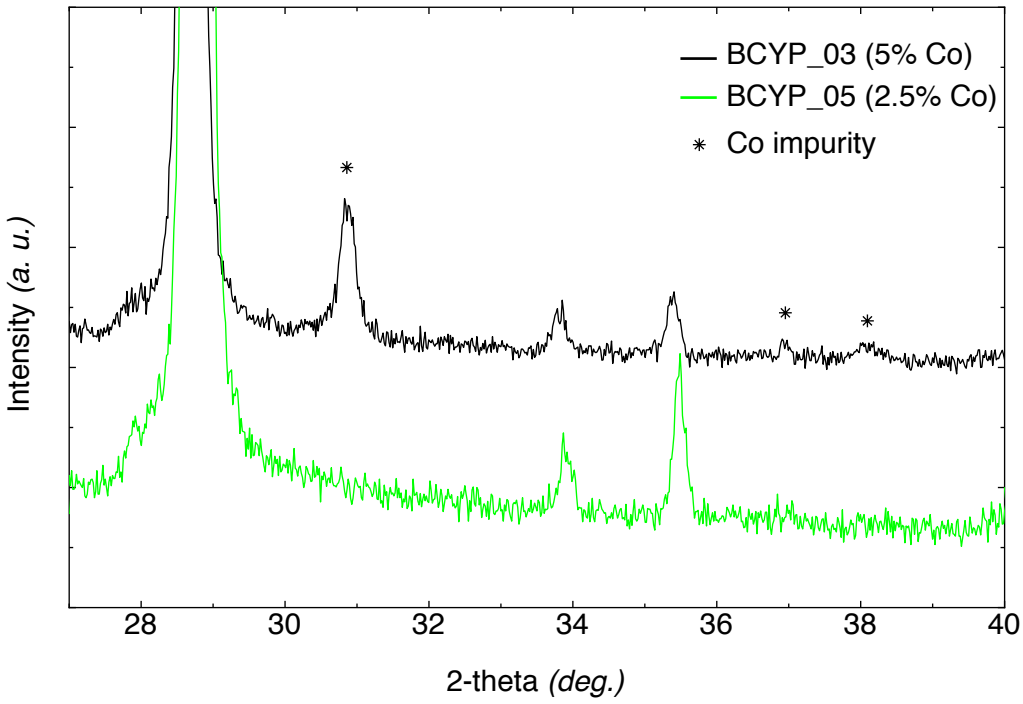

Figure 4.41 Raw XRDs comparing purity depending on cobalt level

XRD analysis was carried out after the conductivity measurements to monitor possible structural variations of the perovskite phase upon exposure to reduced and humidified atmosphere. As shown in Figure 4.42, all cobalt samples retained their orthorhombic form without changes and/or presence of impurities.

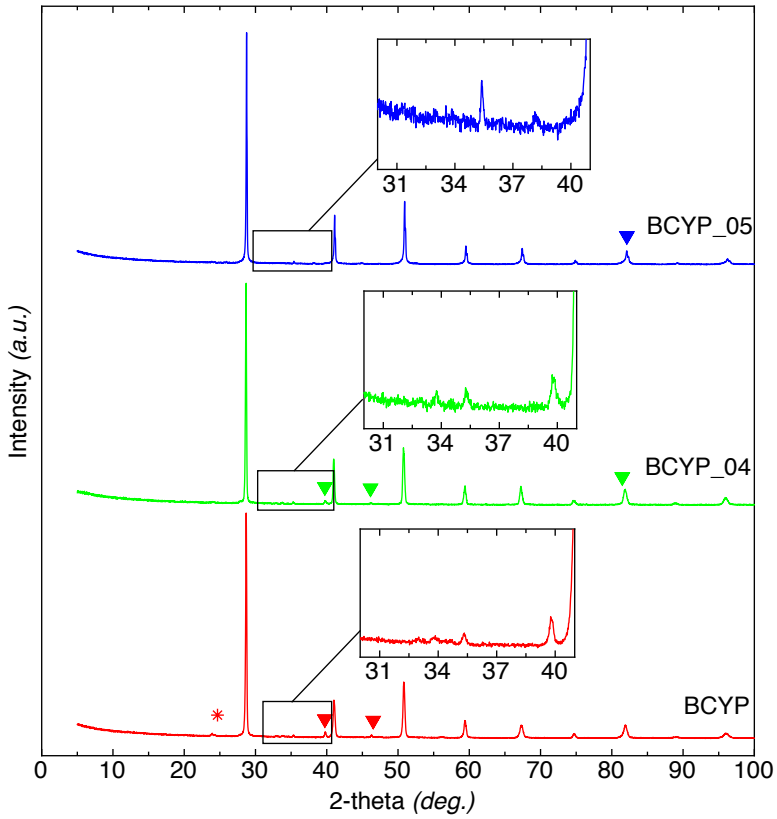

Figure 4.42 XRDs of BCYs after conductivity measurement (▼electrodic Pt, * unidentified peak)

4.5.2. Thermal analysis

Being able to sustain thermal cycles is a pre-requisite for any high temperature conducting materials thus TG/DSC curves of the sintered compounds were measured in flowing air and 5% H_2-Ar. Analyses in air were carried out up to 1000 ºC at a rate of 5 ºC min^{-1} and the results are shown in Figure 4.43. All samples are stable up to the measured temperature with weight losses not exceeding 1% and with the disappearance of the first order phase transitions observed with the Co-free sample [210] with the addition of cobalt in the structure. Clearly the addition of cobalt – which in both III and IV+ oxidation state has an ionic radius much smaller than all other *B*-site cations present [167] – has the effect of stabilising the obtained structure by a contraction and

rigidification of the lattice leaving little room left for the occurrence of distortions and transitions.

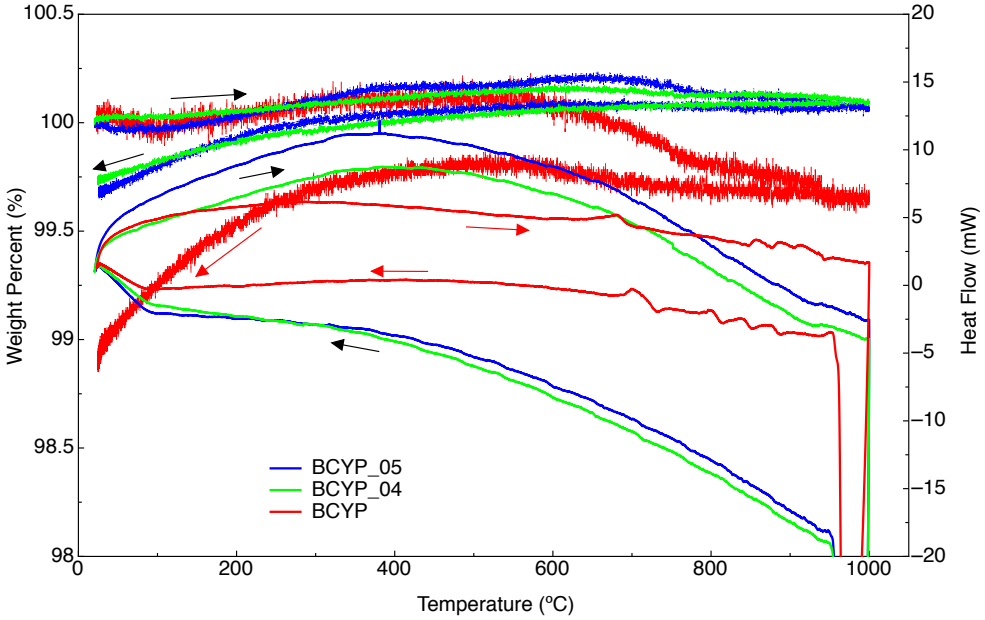

Figure 4.43 TG/DSC curves of BCYs in air from RT to 1000 ºC

Measurements in non-humidified and humidified 5% H_2-Ar were carried out up to 800 ºC and 750 ºC respectively at a rate of 5 ºC min^{-1} and results are shown in Figure 4.44 for the TG traces.

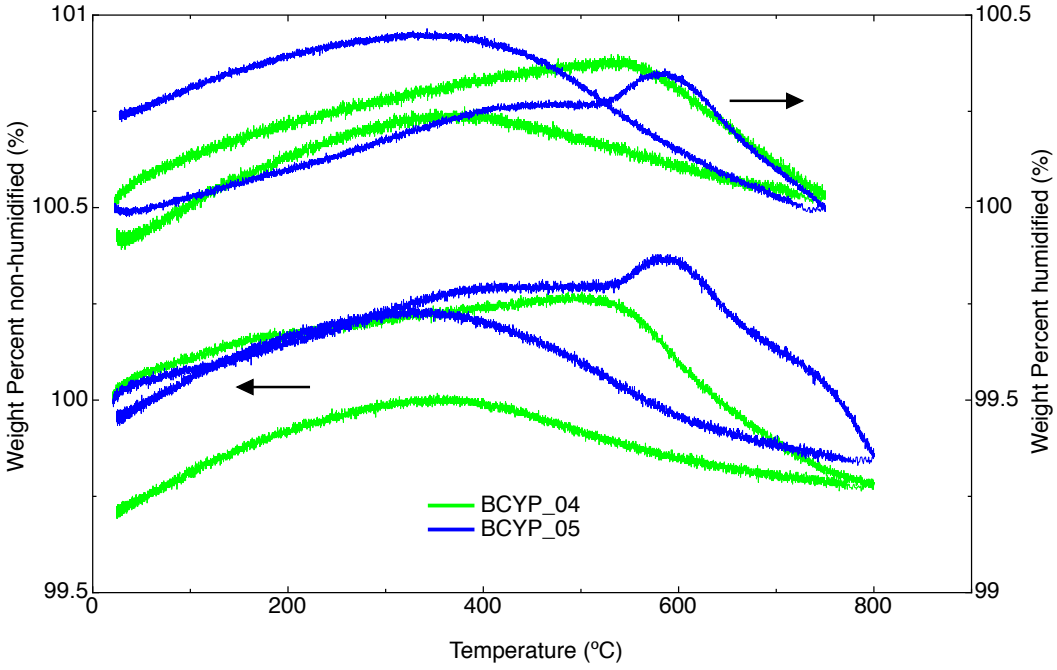

Figure 4.44 TG curves of BCYs in 5% H_2-Ar from RT to 800 ºC

Stability is demonstrated in non-humidified reducing atmosphere as weight losses of pre-analysis weights do not exceed 0.26% with the loss of oxygen vacancies between 500 and 600 ºC depending on the composition. In humidified atmosphere, a similar pattern is observed however a clear weight gain (around 0.25% for both compounds) is noticeable in comparison to the non-humidified analyses indicating water uptake, a phenomenon already reported for other barium cerates/zirconates[199, 209, 212, 213]. XRD analysis was carried out for samples after thermal analyses in humidified reducing atmosphere and indicates stability in the presence of steam (not shown due to similarity with data from initial GSAS refinements, Figure 4.40 and Table 4.6).

4.5.3. Infrared spectroscopy

One main issue and recurrent challenge with barium cerate-based compounds remains the fact that the presence of carbon dioxide leads to the formation of barium carbonate. To verify the presence of this instability, IR scans of the studied compounds were taken on sample powders after the conductivity measurements and after sintering and are shown in Figure 4.45 and 4.46 respectively.

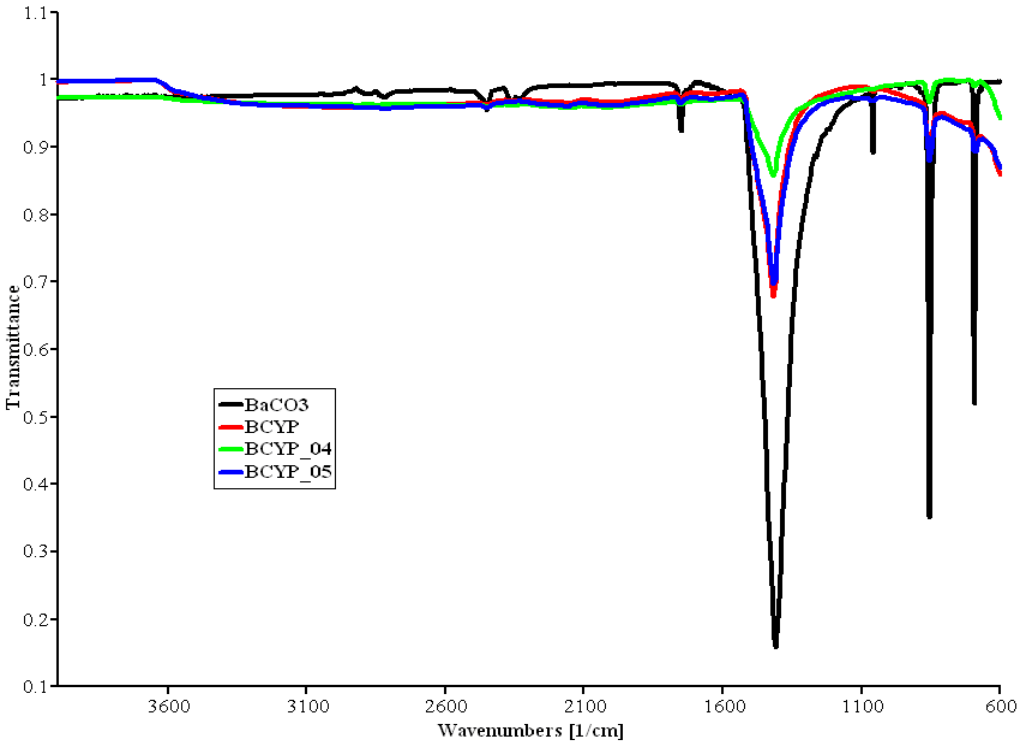

Figure 4.45 IR scans of Pr and Co-co-doped BCY's after conductivity measurement

With pure barium carbonate taken as reference sample, one can clearly see that the major C=O and C–O stretches exhibited by barium carbonate are present in all samples (Figure 4.45) while none are present after sintering (Figure 4.46). The intensity of the main carbonyl peak also provides information on how much carbonate seems to be formed depending on the composition as samples BCYP_04 and BCYP_05 for example have a large delta in the carbonyl peak intensity while having equal cobalt contents.

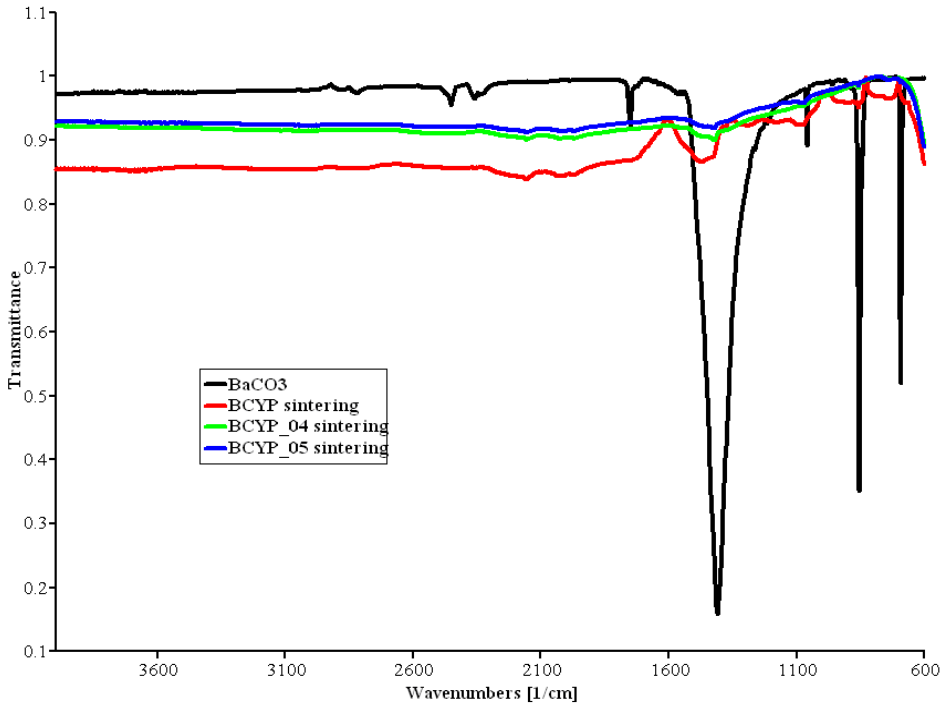

Figure 4.46 IR scans of Pr and Co-co-doped BCY's after sintering

4.5.4. Dilatometry

Considering the mechanical compatibility of these materials with other plausible cell components, thermal expansion measurements of dense ceramics were carried out in air using dilatometry. Figure 4.46 illustrates the $\Delta L/L_0$ values obtained using a 5 ºC min^{-1} heating rate in the 25 ºC to 1000 ºC range. The calculated thermal expansion coefficients were as follow, $12x10^{-6}$ K^{-1} for BCYP, $12.5x10^{-6}$ K^{-1} for BCYP_04 and $11.6x10^{-6}$ K^{-1} for BCYP_05. These are similar to the values reported for 8YSZ and LSGM[218] as well as the $10x10^{-6}$ K^{-1} found for 8YSZ synthesised through a low-temperature carbonated method as confirmation[169]. Shrinkage measurements were also carried out on BCYP_04 as this was the only sample requiring a temperature below

1500 ºC to achieve high density (Figure 4.47 where it is clear that sintering has occurred by 1400 ºC).

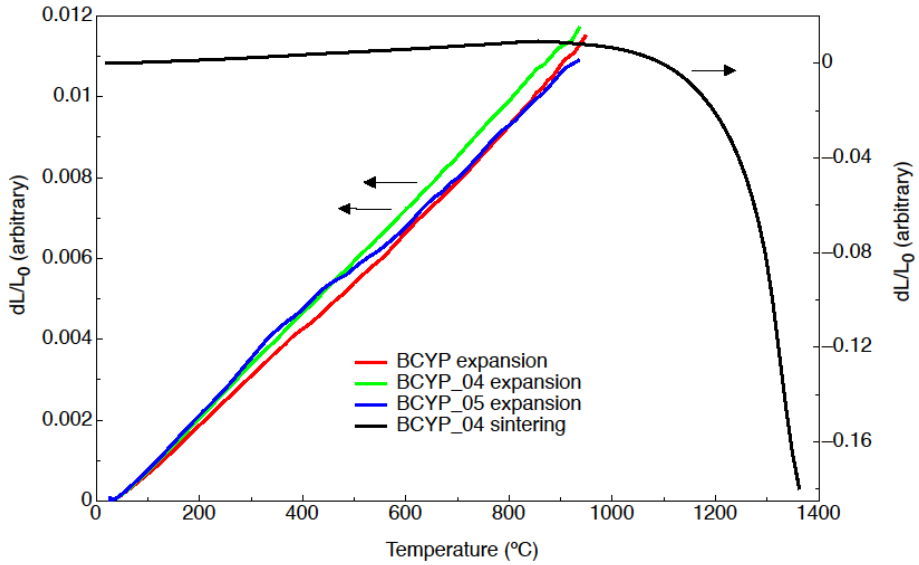

Figure 4.47 Dilatometric measurement in air up to 1000 ºC of $BaCe_{1-x-y-z}Y_xPr_yCo_zO_{3-\delta}$

4.5.5. Conductivity

Values obtained from the conductivity measurements were used to plot Arrhenius type plots of the conductivity against inverse temperature and are shown in Figure 4.48. It can be seen that compounds where cobalt was added have similar (BCYP_05) or slightly lower (BCYP_04) conductivity values as the cobalt free BCYP. Moreover, while conductivities in wet 5% H_2-Ar are lower than in dry 5% H_2-Ar for BCYP_04 ($BaCe_{0.75}Y_{0.075}Pr_{0.15}Co_{0.025}O_{3-\delta}$) under 600 ºC, in the case of BCYP_05 ($BaCe_{0.7}Y_{0.175}Pr_{0.1}Co_{0.025}O_{3-\delta}$) wet hydrogen values are higher than dry over the whole range of temperature and to an extent greater than that observed with BCYP (Figure 4.49 and 4.50) which would indicate an increased protonic conduction in that particular compound. This can be explained from the noticable water uptake shown in the TG curves between humidified and non-humidified reducing atmosphere. Being structurally very similar (differing only in the yttrium amount and the presence of cobalt), it is not surprising that values obtained for BCYP_05 are very close to those obtained for the cobalt-free compound, however a generally increased conductive behaviour is nonetheless observed across the different atmospheres favouring ionic conduction.

Cobalt is usually accepted as being a contributor towards electronic conduction (Figure 4.49 and 4.50). This is noted as both plots show *p*-type semi-conduction with almost fully joined responses for hydrogen in the case of BCYP with closed termini Warburg diffusion while BCYZP_05 has clearly segregated responses with non-finite Warburg diffusion.

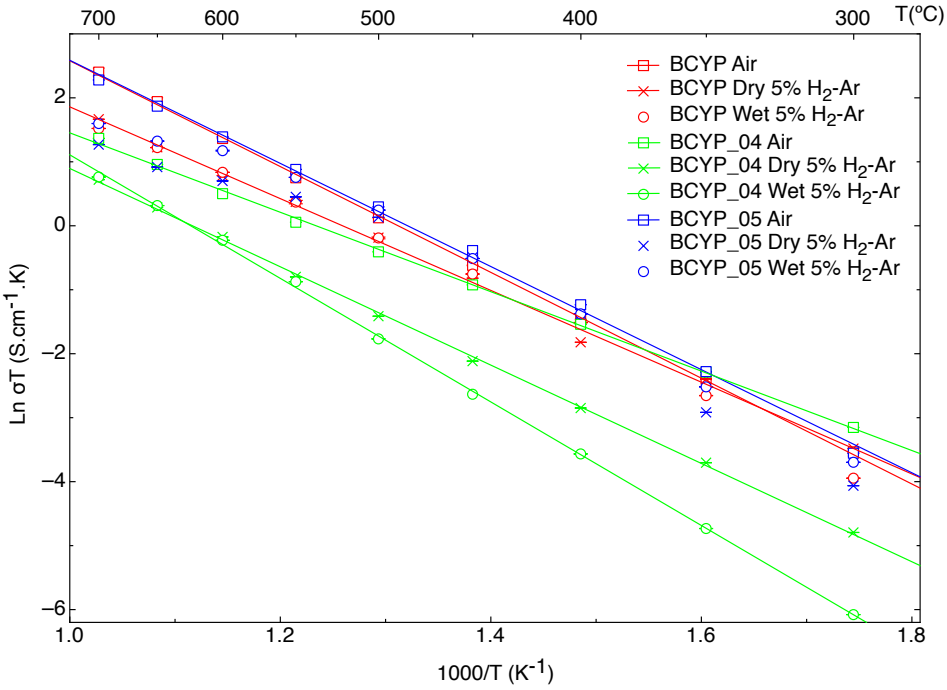

Figure 4.48 Total conductivity plot of BCYs in various atmospheres from 700 ºC to 300 ºC

Additionally and in contrast to other reports on barium cerates[211], there is no evident slope change in the conductive behaviour of the cobalt-containing samples except in reducing atmosphere for BCYP_05. Trend lines added on Figure 4.48 illustrate the absence of such change and were omitted for samples exhibiting a slope change for clarity with activation energies given in Table 4.7. A slope change does however occur around 500 ºC for BCYP_05 in dry and wet reducing atmosphere correlating with the sudden weight gain prior to the loss from oxygen vacancies formation shown in Figure 4.44 but without noticeable change in conductive state during impedance measurements (no metallic to semi-conductor transition or vice-versa).

Total conductivity values thus obtained at 700 ºC in air for samples BCYP, BCYP_04 and BCYP_05 are 0.0121, 0.00403 and 0.00985 S cm^{-1} respectively. The

conductivity of samples BCYP and BCYP_05 are therefore comparable to values obtained by Malavasi *et al.*[53] for $BaCe_{0.8}Y_{0.2}O_{2.9}$. In the case of dry and wet reducing atmosphere –in the same order– values obtained are 0.0055 and 0.0047S cm^{-1}, 0.0021 and 0.0022 S cm^{-1}, 0.0036 and 0.0051 S cm^{-1} respectively.

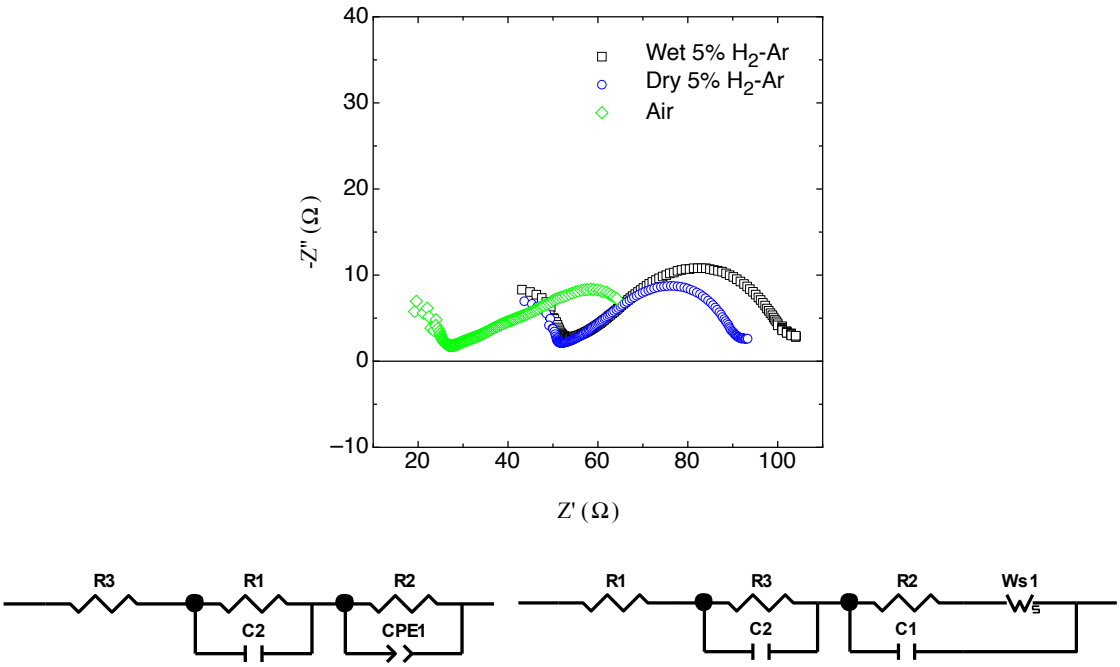

Figure 4.49 Impedance of BCYP in various atmosphere at 650 ºC and corresponding ECs for air (L) and 5% H_2-Ar (R)

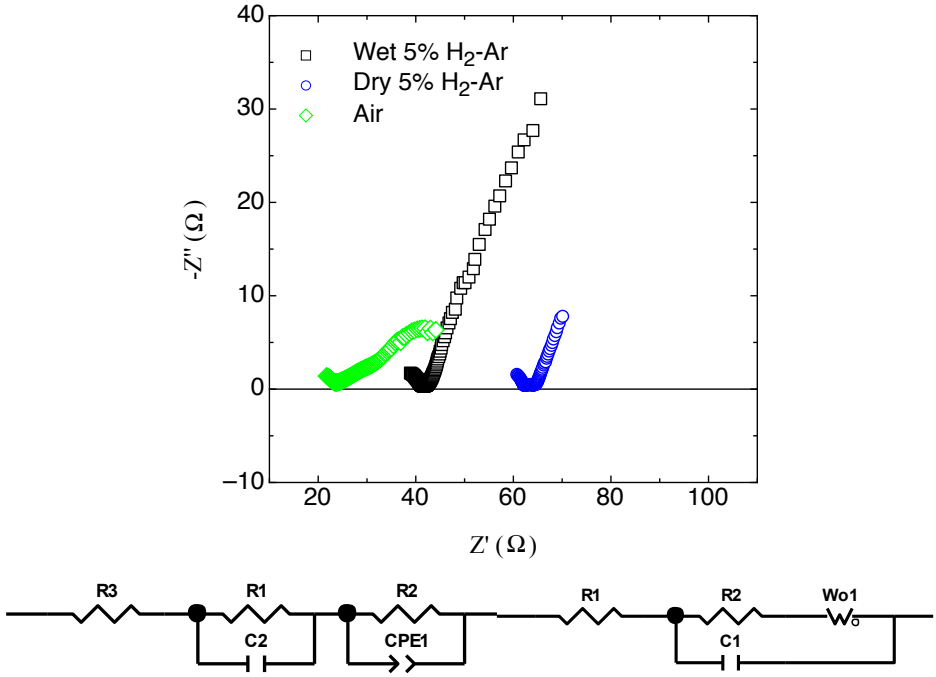

Figure 4.50 Impedance of BCZYP in various atmosphere at 650 ºC and corresponding ECs in air (L) and reducing atmosphere (R)

E_a in kJ mol^{-1} A in S K cm^{-1}			*BCYP*	*BCYP_04*	*BCYP_05*
Air		E_a	67.6 ± 0.2	50.5 ± 0.1	62.6 ± 0.1
		A	$4.2.10^4$ ± 1.0	$1.7.10^3$ ± 1.7	$2.3.10^4$ ± 1.1
dry 5% H_2-Ar	High Temp	E_a	59.6 ± 1.1	63.9 ± 0.6	34.2 ± 2.1
		A	$8.4.10^3$ ± 1.2	$5.3.10^3$ ± 1.1	228.9 ± 1.3
	Low Temp	E_a	NA	NA	$7.8.10^5$ ± 2.8
		A	NA	NA	84.4 ± 5.4
	Approx. Temp. Border (ºC)		NA	NA	500
wet 5% H_2-Ar	High Temp	E_a	54.1 ± 1.0	80.3 ± 0.7	37.2 ± 0.1
		A	$3.8.10^3$ ± 1.2	$4.7.10^4$ ± 1.2	489.9 ± 1.0
	Low Temp	E_a	78.0 ± 0.8	NA	73.7 ± 1.3
		A	$2.5.10^5$ ± 1.2	NA	$1.3.10^5$ ± 1.3
	Approx. Temp. Border (ºC)		450	NA	500

Table 4.7 Arrhenius constants and activation energies in $BaCe_{1-x-y-z}Y_xPr_yCo_zO_{3-\delta}$*

Activation energies in air were found to slightly decrease with the introduction of cobalt into the structure and generally fit values reported in the literature for similar compounds with ~0.7eV (68 kJ mol^{-1}) reported for $BaZr_{0.8}Y_{0.2}O_{3-\delta}$ in air[219] and 0.63eV (61 kJ mol^{-1}) for $BaZr_{0.9}Y_{0.1}O_{3-\delta}$ in dry Ar/O_2[220]. In doped $BaCeO_3$, activation energies for protonic conduction are generally lower than 50 kJ.mol^{-1} [221, 222] and raise to about 75 kJ mol^{-1} when hydroxide ions conduction via vacancies is pre-dominant[223] (a phenomenon often occurring when samples are exposed to saturated water atmosphere). Considering the case of hydrogen – both wet and dry – and using the two most neighbouring compositions (BCYP and BCYP_05), it is clear that cobalt addition has a

* *As in Table 3.5*

direct effect on the value of the activation energy with a diminution of 1.5 times between dry and humidified conditions.

In order to verify the conductive stability of the studied compositions, conductivity measurements at high temperature were carried out over a long period of time to reach a sustained equilibrium. A stabilisation plot is represented in Figure 4.51 and shows that a time of under 12 hrs is required at 700 ºC to obtain stabilised conductivity values for the cobalt containing compounds in air and several days of recordings for measurements in reduced atmosphere.

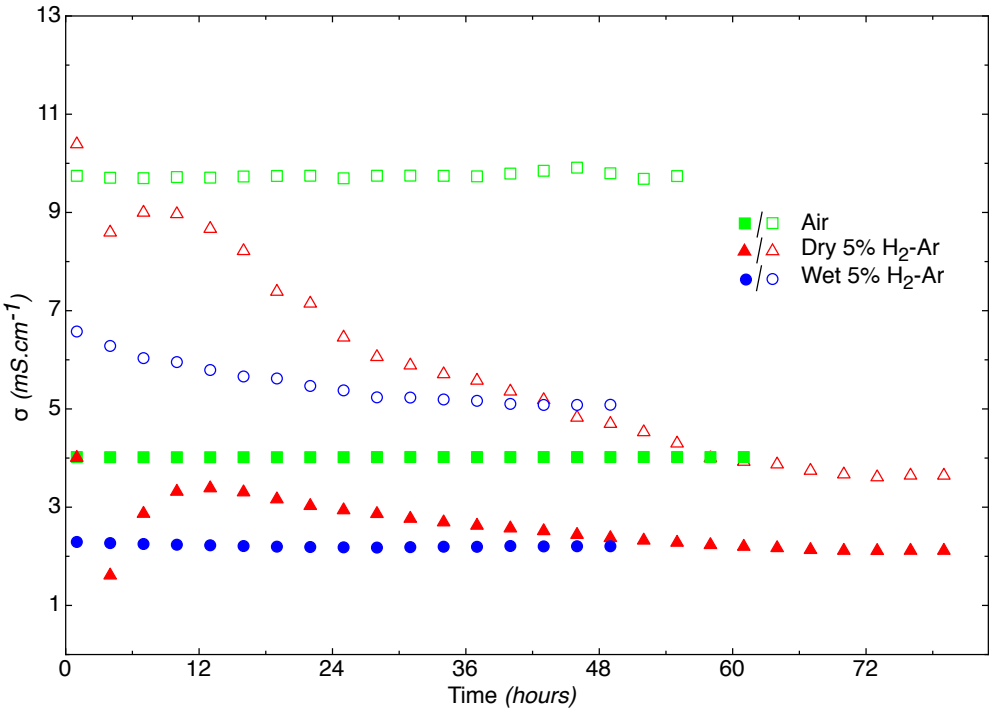

Figure 4.51 Total conductivity stabilisation plot of BCYP_04 (plain) and BCYP_05 (open) at 700 ºC

The fact that a stable value is obtained and sustained also indicates that the barium carbonate peaks detected in the IR scans after conductivity do not constitute an obstacle to high conductivity despite barium carbonate being an insulator. This may be due to either the formation of its latter reaches a negligible maximum (since below the XRD detection limit) due to limited exposure to carbon dioxide from atmospheric air during measurement and/or to its formation renders the compound passive and thus protects it from further reaction without affecting its conductivity and/or finally because it occurs due to adsorbed carbon dioxide onto the sample surface after conductivity due

to a greater time elapsed between conductivity measurement and IR scans than between conductivity measurement and XRD analysis. Thus, while the incorporation of cobalt allows conductivity levels to be maintained at a similar level than without it, when similar compositions are considered (BCYP and BCYP_05), the overall stability of Pr- and Y-co-doped $BaCeO_3$ is clearly improved by the incorporation of cobalt into the lattice.

4.6. Conclusions

Praseodymium-doped and bismuth-doped yttrium barium cerates were successfully synthesised by solid state reactions followed by quick sintering at 1500 ºC for 1 hr allowing densification over 96% to be obtained in the case of Pr-doped compounds and sintering at temperatures between 1400 and 1500 ºC for 1 to 6 hrs with densification over 98% obtained for Bi-doped compounds. Cobalt addition to praseodymium-yttrium co-doped barium cerates was also successfully achieved via solid state syntheses followed by sintering at 1400 ºC or 1500 ºC for only 1 hr achieving relative density > 98%.

All bismuth samples were found to retain their original orthorhombic phase after treatment in either air, dry and wet 5% H_2-Ar even though differences in mechanical strength were observed upon reduction that are not solely due to strains and stresses induced by bismuth ionic size variations. Conductivity values as high as 0.055 S cm^{-1} were obtained for sample $BaCe_{0.6}Zr_{0.1}Y_{0.1}Bi_{0.2}O_{3-\delta}$ and of 0.0094 S cm^{-1} for the Zr-free compound ($BaCe_{0.7}Y_{0.2}Bi_{0.1}O_{3-\delta}$) at 700 ºC in air. Compounds with sufficient structural strength to support reducing atmospheres were however found to exhibit dominant electronic conduction as is noticeable from the conductivity measurements with water uptake behaviours different per each composition, which contrasts with the effects obtained from the doping of barium yttrium cerates with other elements but is in line with the conclusions of Hui and Pijolat.[202] The presence of barium carbonate in samples after conductivity measurements however indicates that these materials are unstable in air. Praseodymium samples on the other hand were found to be stable in air, dry and wet hydrogen atmosphere with the highest conductivity values obtained for the Zr-free compound at 0.0121 S cm^{-1} at 700 ºC in air. Co-doping with Pr/Bi was found to be detrimental to the cerate normally higher conductivity despite the introduction of bismuth, that should have increased electrical capacity and is believed to be mostly related to structural constraints. Zr-containing Pr-doped samples were however found to have much higher conductivities in wet reducing atmosphere than in ambient air over almost the entire studied range of temperature suggesting a higher water uptake rendered possible by the introduction of praseodymium into the lattice of the perovskite structure – a phenomenon already observed for Pr-doped barium zirconates – which would greatly benefit ionic conduction of these types of materials especially for

applications such as high temperature solid oxide fuel cells or electrolysers. Cobalt addition to these Pr-containing compounds allows even larger amounts of water to be retained as suggested by the higher conductivities obtained in wet hydrogen compared to the values in dry hydrogen as well as to decrease the sintering burden overall without sacrificing too much the resulting conductivity.

5. Conclusions and Future work

Crystals of $Ce_{1-x}M_xVO_4$ (M = Ca, Sr with $0 \leq x \leq 0.7$ and $0 \leq x \leq 0.4$ respectively) were synthesised by a standard ceramic technique and solid solution limits were found to lie between 0.4125 and 0.425 and 0.175 and 0.2 respectively. All single phase samples were found to exhibit the tetragonal zircon type structure of space group $I\,4_1/amd$. Calculations were carried out and show that the lattice contraction on Sr/Ca-doping is most likely due to the change of charge of cerium ions from Ce^{3+} to Ce^{4+} introducing oxygen hyperstoichiometry. This, however, reaches a maximum plateau level at which point further doping does not yield more and more oxygen content. This particular condition permits the creation of different concentrations of oxygen vacancies during reduction (resulting in different conductivity values depending on dopant levels).

Conductivity measurements carried out in air and in reduced atmosphere have shown that the improvement in conductivity resulting from the doping is independent of the dopant level as well as of the temperature for the case of air and while $CeVO_4$ exhibits an increased conductivity in a reduced atmosphere, the conductivity for substituted compounds decreases except for sample $Ce_{0.7}Ca_{0.3}VO_4$ which exhibits low level ionic conduction in combination with dominant electronic conduction. The relatively low conductivity in a reducing atmosphere will however restrain the application of these materials as anodes for intermediate temperature solid oxide fuel cells. Additionally, average expansion coefficients are disadvantageous. Most doped samples are redox stable (stable to fundamental structural changes) at a temperature below 600 °C although some lattice expansion was observed which is related to the chemical reduction of both cerium and vanadium ions.

Single phase crystals of $Ce_{1-x}M_xVO_3$ (M = Ca, Sr with $0.1 \leq x \leq 0.4$ and $0 \leq x \leq 0.15$ respectively) were synthesised by a standard ceramic technique. All Sr-doped samples were found to exhibit the orthorhombic perovskite structure of space group *P*nma (62) while all Ca-doped samples exhibited an orthorhombic – *P*nma (62) – and/or monoclinic – $P2_1/c$ (14) – unit cells.

Impedance measurements carried out in air and in reduced atmosphere have shown that the conductivities of Ca/Sr-doped $CeVO_3$ are higher both in air and in dry 5% H_2-Ar compared to $CeVO_3$. This latter actually behaves in the same manner as its orthovanadate counterpart whereas the conductivity of the Ca/Sr-doped compounds

were found to be of three orders of magnitude higher in the metavanadate form compared to the orthovanadate counterpart. Moreover, while the oxidation of $CeVO_3$ reduced from $CeVO_4$ and $Ce_{0.9}Ca_{0.1}VO_3$ to $Ce_{0.9}Ca_{0.1}VO_4$ does not yield back the zircon structure, in the case of other Ca-doped $CeVO_3$ as well as $Ce_{0.85}Sr_{0.15}VO_3$, a reversible phase transition (with formation of calcium vanadium oxide for $x = 0.4$) has been established.

It was therefore concluded that due to the instability of $CeVO_3$ and $Ce_{0.9}Ca_{0.1}VO_3$ upon oxidation leading to a multiple of undesired phases and the formation of $Ca_3(VO_4)_2$ for $Ce_{0.6}Ca_{0.4}VO_3$, $Ce_{1-x}Sr/Ca_xVO_3$ compounds are not suitable *per se* as anode materials for IT-SOFCs, however the reversible phase transition observed for Ca/Sr-doped metavanadates to orthovanadates and the general character of the compounds investigated may be used for low temperature fuel cells (< 200 ºC as suggested by stability tests carried out in air for $Ce_{0.7}Ca_{0.3}VO_3$ reflecting usability in an oxygen-rich atmosphere) either as a single electrode or a symmetrical system and/or on an electrolyte-supported cell assembly. Challenges remain relative to the sintering and cell fabrication due to abnormal thermal expansion of the orthovanadate phase.

Praseodymium-doped and bismuth-doped yttrium barium cerates were successfully synthesised by solid state reactions followed by quick sintering at 1500 ºC in the case of Pr-doped compounds and sintering at temperatures between 1400 and 1500 ºC for Bi-doped compounds in order to obtain overall densities above 96%. Cobalt addition to praseodymium-yttrium co-doped barium cerates was also successfully achieved via solid state syntheses followed by sintering at 1400 ºC or 1500 ºC achieving relative density > 98%.

All bismuth samples were found to retain their original orthorhombic phase after treatment in either air or dry and wet 5% H_2-Ar even though differences in mechanical strength were observed upon reduction that are not solely due to strains and stresses induced by bismuth ionic size variations and could be due to thermal expansion coefficients. Compounds with sufficient structural strength to support reducing atmospheres were however found to exhibit dominant electronic conduction as is noticeable from the conductivity measurements as a function of water uptake behaviour different per each composition. This contrasts with the effects obtained from the doping of barium yttrium cerates with other elements, but is in line with the conclusions of Hui

and Pijolat.[202] The presence of barium carbonate in samples after conductivity measurements however indicates that these materials are unstable in air at high temperature with formation of carbonate phases.

Praseodymium samples on the other hand were found to be stable in air, dry and wet hydrogen atmosphere with the highest conductivity values obtained for the Zr-free compound at 0.0121 S cm^{-1} at 700 ºC in air, comparable to results obtained in other studies for the standard BCY. Co-doping with Pr/Bi was found to be detrimental to the cerate conductivity despite the introduction of bismuth that should have increased electrical conductance. This is believed to be mostly related to structural constraints. Zr-containing Pr-doped samples were however found to have much higher conductivities in wet reducing atmosphere than in ambient air over almost the entire studied range of temperature suggesting a higher water uptake rendered possible by the introduction of praseodymium into the lattice of the perovskite structure – a phenomenon already observed for Pr-doped barium zirconates by Fabbri *et al.*[199].

Cobalt addition to Zr-free Pr-doped BCY allows much larger amounts of water to be retained – as suggested by the higher conductivities obtained in wet hydrogen compared to the values in dry reducing hydrogen – as well as to decrease the sintering burden overall without sacrificing too much the resulting conductivity, which is in antagony with expectations as cobalt addition in other perovskite systems has been shown to drastically increase conductivity.

It was concluded from all the electrolyte compositions studied that Pr-, Bi-, Pr-Bi and Pr-Co doped barium yttrium cerates were not suitable as electrolytes for IT-SOFCs due to a decreased but still too elevated sintering temperature and some structural instability towards redox and atmospheric treatment; however properties discovered about water uptake and conductive behaviour in reduced atmospheres greatly benefit the ionic conduction of these types of materials, especially for applications such as high temperature solid oxide fuel cells or electrolysers.

Generally, results obtained during the electrode studies allowed many initial hypotheses to be answered. First, the hyperstoichiometry found for cerium orthovanadates forms another argument in contradiction with the studies carried out in 1999 by Picardi[156] and Krašovec[155] that found evidence of an orthovanadate structure containing solely Ce^{3+} and V^{5+} atoms (neutron and XPS measurements should be

carried out in the future to fully ascertain the state of cerium ions within the structure). Secondly, the assumption that doping onto the *A*-site of the metavanadate should also result in much higher conductivity values and led to the creation of entirely new compounds with promising properties. Indeed, one major issues faced at the moment by researchers in the fuel cell community is the fact that current cermet materials are too energy demanding in terms of operating temperature, performance and impurities. However, decreasing the range of operation without the implementation of new materials does not seem feasible mainly as currently known materials require such high temperature so as to be able to use more impure fuel gases (the lower the temperature of operation, the higher the purity of the fuel gases need to be if the materials used are not stable to impurities). At the other end of the operational range, PEMFCs are limited to temperature below water vapour as their electrolyte medium is based entirely on water. Hence, the recent interests in developing materials for a 300 ºC to 600 ºC operational range. Electrolytes based on copper-containing ceramics have been identified as suitable materials at such temperatures, however, there is no known electrode material today that can be used in conjunction to these electrolytes without also requiring high cost noble metal catalysts.

It is therefore believed that an entire temperature gap existing between PEMFCs and IT-SOFCs has been totally ignored and really constitutes the missing element in the future large scale implementation of fuel cell technology. In fact, diverse materials have been identified as being extremely stable and highly conductive in the range from RT to under 300 ºC (which is the case of the metavanadate compounds developed in this thesis). The main issue with these materials is the fact that there is no existing ceramic electrolyte that can effectively function in this temperature range as well as exhibiting decent cell performance.

Concerning the series of electrolyte studied, some improvements have been identified. Doping of the barium cerate with praseodymium has shown to be effective as a phase stabiliser without the use of zirconium (although this latter is usually universally accepted as being essential to stabilise the barium cerate phase in presence of water/carbon dioxide-rich environments) and addition of small amount of cobalt into the lattice (shown to substantially increase oxide ion conductivity in LSGM for

example) have allowed the sintering temperature to be decreased without any loss in densification.

Regarding future work, this should focus on polymer-oxide composite electrolytes based on alternative perovskite type oxides and/or developed vandates from this thesis and high temperature polymer membranes. This would permit to bridge the existing gap between the PEMFC and the SOFC and thus, develop a compatible electrolyte material permitting the metavanadate compounds to be used in symmetrical systems at much lower temperature (in order to provide a better match with the properties exhibited below 300 ºC).

Bibliography

1. J. Farman, B. Gardiner and J. Shanklin, *Nature*, 1985, **315**, 207-210.
2. J. Lee, N. Quan, J. Hwang, S. Lee, H. Kim, H. Lee and H. Kim, *J. Ind. Eng. Chem.*, 2006, **12**, 175-183.
3. R. Hagiwara, T. Nohira, K. Matsumoto and Y. Tamba, *Electrochem. Solid-State Lett.*, 2005, **8**, A231-A233.
4. V. I. Vedeneyev, L. V. Gurvich, V. N. Kondrat'yev, V. A. Medvedev and Y. L. Frankevich, *Bond energies, Ionization Potentials and Electron Affinities*, St. Martin's Press, New York, 1962.
5. G. Herzberg and A. Monfils, *J. Mol. Spectrosc.*, 1961, **5**, 482-498.
6. T. Schaffer, V. Hacker and J. Besenhard, *J. Power Sources*, 2006, **153**, 217-227.
7. H. Dohle, J. Divisek and R. Jung, *J. Power Sources*, 2000, **86**, 469-477.
8. X. Li, Y. He, B. Yin, Z. Miao and X. Li, *J. Power Sources*, 2008, **178**, 344-352.
9. S. Celik and M. Mat, *Int. J. Hydrogen Energy*, 2010, **35**, 2151-2159.
10. H. Dohle, J. Mergel and D. Stolten, *J. Power Sources*, 2002, **111**, 268-282.
11. J. Nordlund, C. Picard, E. Birgersson, M. Vynnycky and G. Lindbergh, *J. Appl. Electrochem.*, 2004, **34**, 763-770.
12. C.-H. Wan and C.-L. Chen, *Int. J. Hydrogen Energy*, 2009, **34**, 9515-9522.
13. W. He, *Energy Convers. Manage.*, 1998, **39**, 775-783.
14. B. Kang, J.-H. Koh and H. Lim, *J. Power Sources*, 2001, **94**, 51-62.
15. J. Milewski, T. Swiercz, K. Badyda, A. Miller, A. Dmowski and P. Biczel, *Int. J. Hydrogen Energy*, 2010, **35**, 2997-3000.
16. W. Nernst, *Z. Elektrochem.*, 1899, **6**, 41-43.
17. E. Baur and H. Preis, *Z. Elektrochem.*, 1937, **43**, 727-732.
18. A. R. West, *Basic Solid State Chemistry*, John Wiley & Sons, Chichester, 1988.
19. J. Goodenough, *Annu. Rev. Mater. Sci.*, 1971, **1**, 101-138.
20. R. N. Gurzhi, A. I. Kopeliovich and S. B. Rutkevich, *Physica B+C*, 1981, **107**, 145-146.
21. I. G. Kuleev, *Phys. Solid State*, 1999, **41**, 1608-1616.
22. K. Lehovec, *J. Chem. Phys.*, 1953, **21**, 1123-1128.
23. R. Parsons, *Pure Appl. Chem.*, 1974, **37**, 499-516.
24. R. O'Hayre, D. Barnett and F. Prinz, *J. Electrochem. Soc.*, 2005, **152**, A439-A444.
25. H. Yokokawa and N. Skai, *Handbook of Fuel Cells Fundamentals Technology and Applications*, John Wiley & Sons, Chichester, 2003.

26. H. Yokokawa, *Annu. Rev. Mater. Res.*, 2003, **33**, 581-610.
27. H. Yokokawa, T. Horita, N. Sakai, T. Kawada and M. Dokiya, *Solid State Ionics*, 1995, **78**, 203-210.
28. H. Yokokawa, T. Horita, N. Sakai, K. Yamaji, M. E. Brito, Y.-P. Xiong and H. Kishimoto, *Solid State Ionics*, 2006, **177**, 3193-3198.
29. S. Yamaguchi, K. Nakamura, T. Higuchi, S. Shin and Y. Iguchi, *Solid State Ionics*, 2000, **136-137**, 191-195.
30. D. Simwonis, F. Tietz and D. Stöver, *Solid State Ionics*, 2000, **132**, 241-251.
31. Y. Matsuzaki and I. Yasuda, *Solid State Ionics*, 2000, **132**, 261-269.
32. K. Haga, S. Adachi, Y. Shiratori, K. Itoh and K. Sasaki, *Solid State Ionics*, 2008, **179**, 1427-1431.
33. M. Mogensen, K. Jensen, M. Jørgensen and S. Primdahl, *Solid State Ionics*, 2002, **150**, 123-129.
34. Y. L. Liu and C. Jiao, *Solid State Ionics*, 2005, **176**, 435-442.
35. F. Cayan, M. Zhi, S. Pakalapati, I. Celik, N. Wu and R. Gemmen, *J. Power Sources*, 2008, **185**, 595-602.
36. F. Tietz, *Ionics*, 1999, **5**, 129-139.
37. M. Pihlatie, A. Kaiser and M. Mogensen, *Solid State Ionics*, 2009, **180**, 1100-1112.
38. B. Iwanschitz, J. Sfeir, A. Mai and M. Schutze, *J. Electrochem. Soc.*, 2010, **157**, B269-B278.
39. N. Q. Minh and T. Takahashi, *Science and Technology of Ceramic Fuel Cells*, Elsevier Science, Amsterdam, 1998.
40. P. Plonczak, M. Gazda, B. Kusz and P. Jasinski, *J. Power Sources*, 2008, **181**, 1-7.
41. A. Mai, V. Haanappel, S. Uhlenbruck, F. Tietz and D. Stöver, *Solid State Ionics*, 2005, **176**, 1341-1350.
42. S. Simner, J. Shelton, M. Anderson and J. Stevenson, *Solid State Ionics*, 2003, **161**, 11-18.
43. H. Lv, Y.-j. Wu, B. Huang, B.-y. Zhao and K.-a. Hu, *Solid State Ionics*, 2006, **177**, 901-906.
44. N. Oishi, A. Atkinson, N. P. Brandon, J. A. Kilner and B. C. H. Steele, *J. Am. Ceram. Soc.*, 2005, **88**, 1394-1396.
45. A. Maignan, C. Martin, D. Pelloquin, N. Nguyen and B. Raveau, *J. Solid State Chem.*, 1999, **142**, 247-260.
46. V. Caignaert, I. Mirebeau, F. Bourée, N. Nguyen, A. Ducouret, J.-M. Greneche and B. Raveau, *J. Solid State Chem.*, 1995, **114**, 24-35.
47. CrystalMaker®, *A crystal and molecular structures program for Mac and Windows*, **CrystalMaker Software Ltd**, **Oxford, England** http://www.crystalmaker.com 1994-2011.
48. C. Frontera, A. Caneiro, A. Carrillo, J. Oro-Sole and J. Garcia-Munoz, *Chem. Mater.*, 2005, **17**, 5439-5445.

49. D. O. Bannikov and V. A. Cherepanov, *J. Solid State Chem.*, 2006, **179**, 2721-2727.
50. R. Chiba, F. Yoshimura and Y. Sakurai, *Solid State Ionics*, 1999, **124**, 281-288.
51. P. Moon and H. Tuller, *Solid State Ionics*, 1988, **28-30**, 470-474.
52. F. Abraham, J. Boivin, G. Mairesse and G. Nowogrocki, *Solid State Ionics*, 1990, **40-41**, 934-937.
53. L. Malavasi, C. A. J. Fisher and M. S. Islam, *Chem. Soc. Rev.*, 2010, **39**, 4370-4387.
54. J. A. Labrincha, J. R. Frade and F. M. B. Marques, *JOURNAL OF MATERIALS SCIENCE*, 1993, **28**, 3809-3815.
55. J. A. Labrincha, J. R. Frade and F. M. B. Marques, *Solid State Ionics*, 1997, **99**, 33-40.
56. S. Badwal, F. Ciacchi and D. Milosevic, *Solid State Ionics*, 2000, **136-137**, 91-99.
57. T. Politova and J. Irvine, *Solid State Ionics*, 2004, **168**, 153-165.
58. S. Wang, T. Kato, S. Nagata, T. Kaneko, N. Iwashita, T. Honda and M. Dokiya, *Solid State Ionics*, 2002, **152-153**, 477-484.
59. K. Huang, M. Feng and J. B. Goodenough, *J. Am. Ceram. Soc.*, 1996, **79**, 1100-1104.
60. T. Ishihara, Y. Hiei and Y. Takita, *Solid State Ionics*, 1995, **79**, 371-375.
61. K. Yamaji, T. Horita, M. Ishikawa, N. Sakai and H. Yokokawa, *Solid State Ionics*, 1999, **121**, 217-224.
62. S. Yamaguchi and N. Yamada, *Solid State Ionics*, 2003, **162-163**, 23-29.
63. M. Oishi, K. Yashiro, K. Sato, J. Mizusaki, N. Kitamura, K. Amezawa, T. Kawada and Y. Uchimoto, *Solid State Ionics*, 2008, **179**, 529-535.
64. N. Zakowsky, S. Williamson and J. T. S. Irvine, *Solid State Ionics*, 2005, **176**, 3019-3026.
65. X. X. Xu, S. W. Tao and J. T. S. Irvine, *J. Solid State Chem.*, 2010, **183**, 93-98.
66. J. Guan, S. Dorris, U. Balachandran and M. Liu, *J. Electrochem. Soc.*, 1998, **145**, 1780-1786.
67. L. Yang, S. Wang, K. Blinn, M. Liu, Z. Liu, Z. Cheng and M. Liu, *Science*, 2009, **326**, 126-129.
68. F. A. Kröger and H. J. Vink, in *Solid State Physics*, eds. F. Seitz and D. Turnbull, Academic Press: San Diego, CA, 1956, pp. 273-301.
69. S. V. Bhide and A. V. Virkar, *J. Electrochem. Soc.*, 1999, **146**, 4386-4392.
70. S. V. Bhide and A. V. Virkar, *J. Electrochem. Soc.*, 1999, **146**, 2038-2044.

71. C. Zuo, S. Zha, M. Liu, M. Hatano and M. Uchiyama, *Adv. Mater.*, 2006, **18**, 3318-3320.
72. A. Atkinson, S. Barnett, R. J. Gorte, J. T. S. Irvine, A. J. McEvoy, M. Mogensen, S. C. Singhal and J. Vohs, *Nat. Mater.*, 2004, **3**, 17-27.
73. S. Tao and J. T. S. Irvine, *Chem. Rec.*, 2004, **4**, 83-95.
74. C. Sun and U. Stimming, *J. Power Sources*, 2007, **171**, 247-260.
75. A. Jacobson, *Chem. Mater.*, 2010, **22**, 660-674.
76. E. Tsipis and V. Kharton, *J. Solid State Electrochem.*, 2008, **12**, 1039-1060.
77. P. I. Cowin, C. T. G. Petit, R. Lan, J. T. S. Irvine and S. W. Tao, *Adv. Energy Mater.*, 2011, **1**, 314-332.
78. J. Yu, G. Park, S. Lee and S. Woo, *J. Power Sources*, 2007, **163**, 926-932.
79. C. Keep, R. Baker and J. France, *J. Catal.*, 1977, **47**, 232-238.
80. K. Nikooyeh, R. Clemmer, V. Alzate-Restrepo and J. Hill, *Appl. Catal., A*, 2008, **347**, 106-111.
81. J. Rasmussen and A. Hagen, *J. Power Sources*, 2009, **191**, 534-541.
82. E. Murray, T. Tsai and S. Barnett, *Nature*, 1999, **400**, 649-651.
83. P. Lohsoontorn, D. J. L. Brett and N. P. Brandon, *J. Power Sources*, 2008, **183**, 232-239.
84. Q. X. Fu, F. Tietz and D. Stöver, *J. Electrochem. Soc.*, 2006, **153**, D74-D83.
85. S. W. Tao and J. T. S. Irvine, *Nat. Mater.*, 2003, **2**, 320-323.
86. O. Marina, N. Canfield and J. Stevenson, *Solid State Ionics*, 2002, **149**, 21-28.
87. G. Kim, M. Gross, W. Wang, J. Vohs and R. Gorte, *J. Electrochem. Soc.*, 2008, **155**, B360-B366.
88. M. Gross, K. Carver, M. Deighan, A. Schenkel, B. Smith and A. Yee, *J. Electrochem. Soc.*, 2009, **156**, B540-B545.
89. X. Sun, S. Wang, Z. Wang, J. Qian, T. Wen and F. Huang, *J. Power Sources*, 2009, **187**, 85-89.
90. X.-F. Sun, R.-S. Guo and J. Li, *Ceram. Int.*, 2008, **34**, 219-223.
91. M. J. Escudero, J. T. S. Irvine and L. Daza, *J. Power Sources*, 2009, **192**, 43-50.
92. R. T. Baker, I. S. Metcalfe, P. H. Middleton and B. C. H. Steele, *Solid State Ionics*, 1994, **72**, 328-333.
93. B. Steele, *Nature*, 1999, **400**, 619-621.
94. S. Georges, G. Parrour, M. Henault and J. Fouletier, *Solid State Ionics*, 2006, **177**, 2109-2112.
95. A.-L. Sauvet, J. Guindet and J. Fouletier, *Ionics*, 1999, **5**, 150-155.
96. G. Pudmich, B. Boukamp, M. Gonzalez-Cuenca, W. Jungen, W. Zipprich and F. Tietz, *Solid State Ionics*, 2000, **135**, 433-438.

97. V. V. Kharton, E. V. Tsipis, I. P. Marozau, A. P. Viskup, J. R. Frade and J. T. S. Irvine, *Solid State Ionics*, 2007, **178**, 101-113.
98. S. Zha, P. Tsang, Z. Cheng and M. Liu, *J. Solid State Chem.*, 2005, **178**, 1844-1850.
99. S. W. Tao and J. T. S. Irvine, *J. Electrochem. Soc.*, 2004, **151**, A252-A259.
100. S. W. Tao, J. T. S. Irvine and J. A. Kilner, *Adv. Mater.*, 2005, **17**, 1734-1737.
101. S. P. Jiang, X. J. Chen, S. H. Chan, J. T. Kwok and K. A. Khor, *Solid State Ionics*, 2006, **177**, 149-157.
102. J. Liu, B. D. Madsen, Z. Ji and S. A. Barnett, *Electrochem. Solid-State Lett.*, 2002, **5**, A122-A124.
103. J. Wan, J. H. Zhu and J. B. Goodenough, *Solid State Ionics*, 2006, **177**, 1211-1217.
104. J. C. Ruiz-Morales, J. Canales-Vázquez, D. Marrero-López, J. T. S. Irvine and P. Núñez, *Electrochim. Acta*, 2007, **52**, 7217-7225.
105. S. W. Tao, J. Canales-Vazquez and J. Irvine, *Chem. Mater.*, 2004, **16**, 2309-2316.
106. S. Tao and J. T. S. Irvine, *J. Mater. Chem.*, 2002, **12**, 2356-2360.
107. Y.-H. Huang, R. Dass, Z.-L. Xing and J. Goodenough, *Science*, 2006, **312**, 254-257.
108. Y.-H. Huang, R. I. Dass, J. C. Denyszyn and J. B. Goodenough, *J. Electrochem. Soc.*, 2006, **153**, A1266-A1272.
109. Y. Ji, Y.-H. Huang, J.-R. Ying and J. Goodenough, *Electrochem. Commun.*, 2007, **9**, 1881-1885.
110. K. S. Knight, *Solid State Ionics*, 1994, **74**, 109-117.
111. J. Frenkel, *Z. Physik*, 1926, **35**, 652.
112. C. Herring, *J. Appl. Phys.*, 1950, **21**, 437-445.
113. P. L. Read and E. Katz, *Phys. Rev. Lett.*, 1960, **5**, 466-468.
114. E. D. Deviatkova, *Sov. Phys. Tech. Phys.*, 1957, **2**, 414-418.
115. E. D. Deviatkova, A. V. Petrov and I. A. Smirnov, *Sov. Phys. Solid State*, 1961, **3**, 970-973.
116. P. G. Klemens, *Proc. Phys. Soc. A*, 1955, **68**, 1113-1128.
117. P. G. Klemens, *J. Phys. Chem. Solids*, 1959, **8**, 345-347.
118. J. A. Krumhansl, *J. Phys. Chem. Solids*, 1959, **8**, 343-345.
119. T. A. Kontorova, *Sov. Phys. Solid State*, 1963, **4**, 2435.
120. E. V. Mielczarek and H. P. R. Frederikse, *Phys. Rev.*, 1959, **115**, 888-891.
121. A. Fick, *Anna. Phys.*, 1855, **170**, 59-86.
122. R. J. Friauf, *J. Phys. Chem.*, 1962, **66**, 2380-2383.
123. M. D. Weber and R. J. Friauf, *J. Phys. Chem. Solids*, 1969, **30**, 407-419.

124. W. D. Compton and R. J. Maurer, *J. Phys. Chem. Solids*, 1956, **1**, 191-199.
125. R. E. Howard, *Physical Review*, 1966, **144**, 650-661.
126. K. Compaan and Y. Haven, *Transactions of the Faraday Society*, 1956, **52**.
127. K. Compaan and Y. Haven, *Transactions of the Faraday Society*, 1958, **54**.
128. K. Compaan and Y. Haven, *Discussions of the Faraday Society*, 1957, **23**.
129. W. C. Röntgen, *Nature*, 1896, **53**, 274-276.
130. W. C. Röntgen, *Sitzungsber. Würzb. Phys.-Med. Gegell.*, 1895, Eine Neue Art von Strahlen.
131. M. Laing, *An Introduction to the Scope, Potential and Applications of X-ray Analysis*, IUCr, Chester, 2001.
132. C. Hammond, *The Basics of Crystallography and Diffraction*, Oxford University Press, Oxford, 2009.
133. W. L. Bragg, *Proc. Camb. Phil. Soc.*, 1913, **17**, 43-57.
134. L. Brügemann and E. K. E. Gerndt, *Nucl. Instrum. Methods Phys. Res., Sect. A*, 2004, **531**, 292-301.
135. H. M. Rietveld, *J. Appl. Cryst.*, 1969, **2**, 65-71.
136. A. C. Larson and R. B. Von Dreele, *General Structure Analysis System (GSAS), Los Alamos National Laboratory Report, LAUR-86*, 2004.
137. P. Scherrer, *Göttinger Nachrichten Gesell.*, 1918, **2**, 98.
138. A. D. Cross, *An introduction to practical infra-red spectroscopy*, Butterworth & Co Ltd, London, 1964.
139. J. Tauc, *Materials Research Bulletin*, 1968, **3**, 37-46.
140. B. A. Boukamp, in *Electrochemical Impedance Spectroscopy*, Impedance Analysis Workshop 03/02 Part I, St-Andrews, 2010, p. 7.
141. B. A. Boukamp, in *Electrochemical Impedance Spectroscopy*, Impedance Analysis Workshop 03/02 Part I, St-Andrews, 2010, p. 53.
142. B. A. Boukamp, in *Electrochemical Impedance Spectroscopy*, Impedance Analysis Workshop 03/02 Part I, St-Andrews, 2010, p. 33.
143. B. A. Boukamp, in *Electrochemical Impedance Spectroscopy*, Impedance Analysis Workshop 03/02 Part II, St-Andrews, 2010, p. 59.
144. W. Milligan and L. Vernon, *J. Phys. Chem.*, 1952, **56**, 145-147.
145. M. Carron, M. Mrose and K. Murata, *J. Am. Mineral.*, 1958, **43**, 985-989.
146. H. Fuess and A. Kallel, *J. Solid State Chem.*, 1972, **5**, 11-14.

147. C. E. Rice and W. R. Robinson, *Acta Crystallogr., Sect. B: Struct. Sci*, 1976, **B32**, 2232-2233.
148. B. Chakoumakos, M. Abraham and L. Boatner, *J. Solid State Chem.*, 1994, **109**, 197-202.
149. J. M. Stencel, *Raman Spectroscopy for Catalysts*, Van Nostrand Reinhold, New York, 1990.
150. S. Mahapatra, G. Madras and T. Row, *Ind. Eng. Chem. Res.*, 2007, **46**, 1013-1017.
151. S. Mahapatra, R. Vinu, D. Saha, T. Guru Row and G. Madras, *Appl. Catal., A*, 2009, **361**, 32-41.
152. W. Milligan, L. Watt and H. Rachford, *J. Phys. Chem.*, 1949, **53**, 227-234.
153. I. Rao and O. Palanna, *Bull. Mater. Sci.*, 1995, **18**, 593-597.
154. E. Baran and P. Aymonino, *Z. Anorg. Allg. Chem.*, 1971, **383**, 226-229.
155. U. Krasovec, B. Orel, A. Surca, N. Bukovec and R. Reisfeld, *Solid State Ionics*, 1999, **118**, 195-214.
156. G. Picardi, F. Varsano, F. Decker, U. Opara-Krasovec, A. Surca and B. Orel, *Electrochim. Acta*, 1999, **44**, 3157-3164.
157. M. Martinez-Huerta, J. Coronado, M. Fernandez-Garcia, A. Iglesias-Juez, G. Deo, J. Fierro and M. Banares, *J. Catal.*, 2004, **225**, 240-248.
158. S. Mahapatra, R. Vinu, T. Row and G. Madras, *Appl. Catal., A*, 2008, **351**, 45-53.
159. S. Varma, B. Wani and N. Gupta, *Mater. Res. Bull.*, 2002, **37**, 2117-2127.
160. E. Tsipis, V. Kharton and J. Frade, *J. Eur. Ceram. Soc.*, 2005, **25**, 2623-2626.
161. E. Tsipis, V. Kharton, N. Vyshatko, A. Shaula and J. Frade, *J. Solid State Chem.*, 2003, **176**, 47-56.
162. E. Tsipis, M. Patrakeev, V. Kharton, N. Vyshatko and J. Frade, *J. Mater. Chem.*, 2002, **12**, 3738-3745.
163. T. Hirata and A. Watanabe, *J. Solid State Chem.*, 2001, **158**, 264-267.
164. A. Watanabe, *J. Solid State Chem.*, 2000, **153**, 174-179.
165. S. Varma, B. Wani and N. Gupta, *Appl. Catal., A*, 2003, **241**, 341-348.
166. S. Varma, B. Wani, A. Sathyamoorthy and N. Gupta, *J. Phys. Chem. Solids*, 2004, **65**, 1291-1296.
167. R. D. Shannon, *Acta Crystallogr., Sect. A: Found. Crystallogr.*, 1976, **32**, 751-767.
168. E. V. Tsipis, C. N. Munnings, V. V. Kharton, S. J. Skinner and J. R. Frade, *Solid State Ionics*, 2006, **177**, 1015-1020.

169. S. Jiang, G. C. Stangle, V. R. W. Amarakoon and W. A. Schulze, *J. Mater. Res.*, 1996, **11**, 2318-2324.
170. C. E. Guillaume, *"The Nobel Prize in Physics 1920". Nobelprize.org. Nobel Media AB 2013. Web. 24 Oct 2013.* <http://www.nobelprize.org/nobel_prizes/physics/laureates/1920/%3E.
171. M. M. Abraham, L. A. Boatner, T. C. Quinby, D. K. Thomas and M. Rappaz, *Radioact. Waste Manage.*, 1980, **1**, 181-191.
172. B. C. Sales and L. A. Boatner, *Radioactive Waste Forms for the Future*, ed. W. Lutze and R. C. Ewing, Elsevier, New-York, 1988, p. 507.
173. H. Nguyen and J. Goodenough, *J. Solid State Chem.*, 1995, **119**, 24-35.
174. M. Reehuis, C. Ulrich, P. Pattison, M. Miyasaka, Y. Tokura and B. Keimer, *Eur. Phys. J. B*, 2008, **64**, 27-34.
175. M. Onoda and H. Nagasawa, *Solid State Commun.*, 1996, **99**, 487-491.
176. K. Yoshii and H. Abe, *J. Alloys Compd.*, 2002, **343**, 199-203.
177. S. Miyasaka, Y. Okimoto, M. Iwama and Y. Tokura, *Phys. Rev. B: Condens. Matter*, 2003, **68**, 100406.
178. F. Luo, W. Song, Z.-F. Li and C.-H. Yan, *Solid State Commun.*, 2004, **132**, 595-599.
179. A. Muñoz, J. Alonso, M. Casáis, M. Martínez-Lope, J. Martínez and M. Fernández-Díaz, *Phys. Rev. B: Condens. Matter*, 2003, **68**, 144429.
180. N. Danilovic, J.-L. Luo, K. Chuang and A. Sanger, *J. Power Sources*, 2009, **192**, 247-257.
181. C. Petit, R. Lan, P. Cowin, A. Kraft and S. Tao, *JOURNAL OF MATERIALS SCIENCE*, 2011, **46**, 316-326.
182. C. Petit, R. Lan, P. Cowin and S. Tao, *J. Solid State Chem.*, 2010, **183**, 1231-1238.
183. D. Saha, S. Mahapatra, T. Row and G. Madras, *Ind. Eng. Chem. Res.*, 2009, **48**, 7489-7497.
184. Y. Kimishima, M. Takahashi, K. Okada, H. Ishikawa and Y. Ichiyanagi, *J. Magn. Magn. Mater.*, 1995, **140-144**, 1185-1186.
185. L. N. Yannopoulos, *J. Phys. Chem.*, 1968, **72**, 3293-3296.
186. C. T. G. Petit, R. Lan, P. I. Cowin, J. T. S. Irvine and S. Tao, *J. Mater. Chem.*, 2011, **21**, 525-531.
187. H. Iwahara, Y. Asakura, K. Katahira and M. Tanaka, *Solid State Ionics*, 2004, **168**, 299-310.
188. S. M. Haile, G. Staneff and K. H. Ryu, *JOURNAL OF MATERIALS SCIENCE*, 2001, **36**, 1149-1160.
189. J. Wu, R. A. Davies, M. S. Islam and S. M. Haile, *Chem. Mater.*, 2005, **36**, 846-851.

190. C. Zuo, S. Zha, M. Liu, M. Hatano and M. Uchiyama, *Adv. Mater.*, 2006, **18**, 3318-3320.
191. S. B. C. Duval, P. Holtappels, U. Stimming and T. Graule, *Solid State Ionics*, 2008, **179**, 1112-1115.
192. C. Peng, J. Melnik, J. Li, J. Luo, A. Sanger and K. Chuang, *J. Power Sources*, 2009, **190**, 447-452.
193. C. Peng, J. Melnik, J.-L. Luo, A. Sanger and K. Chuang, *Solid State Ionics*, 2010, **181**, 1372-1377.
194. F. Gao, H. Zhao, X. Li, Y. Cheng, X. Zhou and F. Cui, *Journal of Power Sources*, 2008, **185**, 26-31.
195. F. Zhao, Q. Liu, S. Wang, K. Brinkman and F. Chen, *Int. J. Hydrogen Energy*, 2010, **35**, 4258-4263.
196. S. W. Tao and J. T. S. Irvine, *J. Solid State Chem.*, 2007, **180**, 3493-3503.
197. S. W. Tao and J. T. S. Irvine, *Advanced Materials*, 2006, **18**, 1581-1584.
198. R. Mukundan, P. Davies and W. Worrell, *J. Electrochem. Soc.*, 2001, **148**, A82-A86.
199. E. Fabbri, L. Bi, H. Tanaka, D. Pergolesi and E. Traversa, *Adv. Funct. Mater.*, 2011, **21**, 158-166.
200. Z. Tao, L. Bi, L. Yan, W. Sun, Z. Zhu, R. Peng and W. Liu, *Electrochemistry Communications*, 2009, **11**, 688-690.
201. Y.-P. Fu, C.-W. Tseng and P.-C. Peng, *J. Eur. Ceram. Soc.*, 2008, **28**, 85-90.
202. Z. Hui and P. Michele, *Journal of Materials Chemistry*, 2002, **12**, 3787-3791.
203. S. Ricote and N. Bonanos, *Solid State Ionics*, 2010, **181**, 694-700.
204. S. Ricote, N. Bonanos, H. J. Wang and R. Haugsrud, *Solid State Ionics*, 2011, **185**, 11-17.
205. J. Tong, D. Clark, M. Hoban and R. O'Hayre, *Solid State Ionics*, 2010, **181**, 496-503.
206. J. Tong, D. Clark, L. Bernau, A. Subramaniyan and R. O'Hayre, *Solid State Ionics*, 2010, **181**, 1486-1498.
207. L. Yang, S. Wang, X. Lou and M. Liu, *International Journal of Hydrogen Energy*, 2011, **36**, 2266-2270.
208. D. Medvedev, V. Maragou, T. Zhuravleva, A. Demin, E. Gorbova and P. Tsiakaras, *Solid State Ionics*, 2011, **182**, 41-46.
209. E. Fabbri, I. Markus, L. Bi, D. Pergolesi and E. Traversa, *Solid State Ionics*, 2011, **202**, 30-35.
210. C. T. G. Petit and S. Tao, *Solid State Sci.*, 2013, **17**, 115-121.
211. L. Malavasi, C. Ritter and G. Chiodelli, *Chem. Mater.*, 2008, **20**, 2343-2351.

212. A. Kruth and J. T. S. Irvine, *Solid State Ionics*, 2003, **162–163**, 83-91.
213. S. Ricote, N. Bonanos and G. Caboche, *Solid State Ionics*, 2009, **180**, 990-997.
214. Z. Hui and P. Michele, *J. Mater. Chem.*, 2002, **12**, 3787-3791.
215. L. Bi, S. Zhang, S. Fang, Z. Tao, R. Peng and W. Liu, *Electrochem. Commun.*, 2008, **10**, 1598-1601.
216. Z. Tao, Z. Zhu, H. Wang and W. Liu, *J. Power Sources*, 2010, **195**, 3481-3484.
217. L. Bi, S. Zhang, L. Zhang, Z. Tao, H. Wang and W. Liu, *Int. J. Hydrogen Energy*, 2009, **34**, 2421-2425.
218. A. Aguadero, J. A. Alonso, M. T. Fernández-Díaz, M. J. Escudero and L. Daza, *Journal of Power Sources*, 2007, **169**, 17-24.
219. P. Babilo, T. Uda and S. M. Haile, *Journal of Materials Research*, 2007, **22**, 1322-1330.
220. H. G. Bohn and T. Schober, *Journal of the American Ceramic Society*, 2000, **83**, 768-772.
221. X. Meng, N. Yang, J. Song, X. Tan, Z.-F. Ma and K. Li, *International Journal of Hydrogen Energy*, 2011, **36**, 13067-13072.
222. R. C. T. Slade and N. Singh, *Solid State Ionics*, 1991, **46**, 111-115.
223. R. C. T. Slade and N. Singh, *Solid State Ionics*, 1993, **61**, 111-114.